

Dynamics of Water and Aqueous Protons studied using Ultrafast Multi-dimensional Infrared Spectroscopy

by

Krupa Ramasesha

B.S. Chemistry
University of Wisconsin, Madison, 2006

Submitted to the Department of Chemistry
in partial fulfillment of the requirements for the degree of

Doctor of Philosophy

at the

MASSACHUSETTS INSTITUTE OF TECHNOLOGY

February 2013

© Massachusetts Institute of Technology 2013. All rights reserved.

Signature of Author: _____

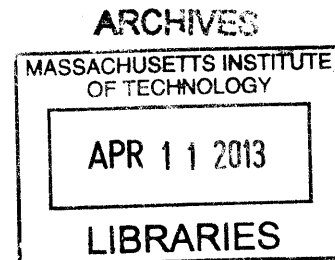
Krupa Ramasesha
December 17, 2012

Certified by: _____

Andrei Tokmakoff
Professor of Chemistry
Thesis Supervisor

Accepted by: _____

Robert W. Field
Professor of Chemistry
Chairman, Department Committee on Graduate Theses



This doctoral thesis has been examined by a Committee of the Department of Chemistry that included,

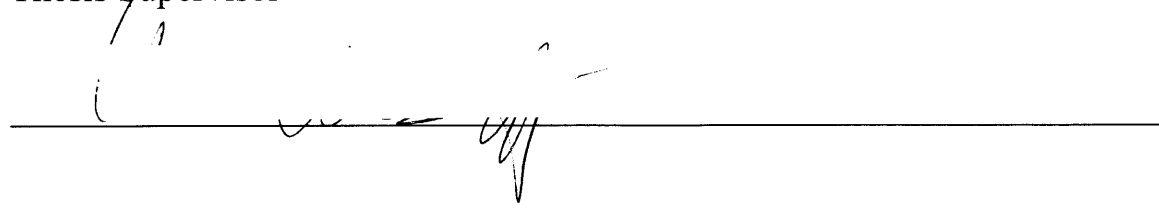
Professor Keith A. Nelson
Chair



Professor Troy Van Voorhis



Professor Andrei Tokmakoff
Thesis Supervisor



Dynamics of Water and Aqueous Protons studied using Ultrafast Multi-dimensional Infrared Spectroscopy

by

Krupa Ramasesha

Submitted to the Department of Chemistry on December 17, 2012
in partial fulfillment of the requirements for the degree of
Doctor of Philosophy

Abstract:

Liquid water consists of a highly dynamic network of hydrogen bonds, which evolves on timescales ranging from tens of femtoseconds to a few picoseconds. The fast structural evolution of water's hydrogen bond network is at the heart of numerous fundamental aqueous processes, such as proton transport, solvation, the hydrophobic effect and protein folding. In this thesis, I present our efforts in understanding the dynamics governing hydrogen bond switching and vibrational energy dissipation in water, and the transport of excess protons in strong acid solutions. We use ultrafast nonlinear infrared spectroscopy to study hydrogen bond and proton transfer dynamics in water and acids since vibrational frequencies, intensities and line shapes are closely associated with chemical structure and dynamics. We employed and characterized a new source of ultrafast broadband infrared pulses that span the entire mid-infrared region from 4000 cm^{-1} down to hundreds of cm^{-1} , with <70 fs pulse duration. We have demonstrated the use of these pulses in studying ultrafast vibrational dynamics in water and aqueous proton transfer dynamics in acids, where broad and feature-less vibrational transitions are present across the mid-infrared.

Rearrangements of the hydrogen bond network in liquid water involve rapid switching of hydrogen bonds, which is believed to be a concerted process where a water molecule undergoes large angle molecular reorientation as it exchanges hydrogen-bonding partners. To test this picture of hydrogen bond dynamics, we performed ultrafast 2D IR spectral anisotropy on the OH stretching vibration of HOD in D_2O to directly track the reorientation of water molecules as they change hydrogen bonding environments. Interpretation of the experimental data is assisted by modeling drawn from molecular dynamics simulations, and we quantify the degree of molecular rotation on changing local hydrogen bonding environment within the framework of restricted rotation models. Our results show evidence for concerted motions involving large angular deviations in the molecular dipole when a water molecule evolves from a strained configuration to a stable hydrogen bonded geometry.

In addition to its rapidly evolving hydrogen bonding network, the ability of liquid water to efficiently dissipate energy through ultrafast vibrational relaxation processes plays a key role in the stabilization of reactive intermediates and the outcome of aqueous chemical reactions. The ability of liquid water to efficiently dissipate energy through ultrafast vibrational relaxation plays a key role in the stabilization of reactive

intermediates and the outcome of aqueous chemical reactions. The vibrational couplings that govern energy relaxation in liquid H₂O remain difficult to characterize due to the complex interplay of inter- and intramolecular forces present in the liquid and the limitations of current methods to visualize these ultrafast motions simultaneously. Using ultrafast broadband infrared pulses, we performed 2D IR spectroscopy, pump-probe spectroscopy, and polarization anisotropy of H₂O by exciting the OH stretching transition in water and characterizing the response of the liquid from 1350-4000 cm⁻¹ with <70 femtosecond time resolution. These spectra reveal vibrational transitions at all frequencies simultaneous to the excitation, including cross peaks to the bend vibration and a continuum of induced absorptions to previously unobserved combination bands that are not present in linear spectra. These observations provide evidence for strong mixing of inter- and intra-molecular character and delocalization of the vibrations in liquid H₂O. Unlike traditional weak coupling models, it appears that excitation of OH stretch motion simultaneously drives bending and intermolecular motions as a result of strong anharmonic mixing. These delocalized vibrations, or excitons, have mixed stretch and bend character and evolve over several hundred femtoseconds, giving rise to a complex network of vibrational energy relaxation processes.

Protons are known to exhibit very high mobility in water compared to other ions due to the Grotthuss proton hopping mechanism, which describes proton transfer as a process where displacement of charge takes place through breaking and forming of O-H covalent bonds in water. Infrared spectra of strong acids are marked by broad and featureless transitions that span the entire mid-infrared due to a large distribution of rapidly exchanging solvated proton configurations. While previous research efforts have assigned different regions of the mid-infrared spectrum of acids to vibrations of the Eigen (H₉O₄⁺) and the Zundel (H₅O₂⁺) limiting structures of the solvated proton, experimental evidence for these assignments in solution and the dynamics that underlie the broad transitions have been largely absent. Using ultrafast broadband infrared pulses in pump-probe and 2D IR spectroscopy, we studied the evolution of frequency correlations across the entire mid-infrared spectrum of concentrated HCl in H₂O. Our results provide experimental evidence for the existence of Eigen and Zundel configurations of the solvated proton in HCl/H₂O with persistence times of at least 0.8 to 1 ps and 250 fs, respectively, and show that fleeting excursions of the proton from the Eigen configuration towards shared configurations are stabilized in less than 100 fs by electric field fluctuations of the solvating water molecules.

Thesis Supervisor: Andrei Tokmakoff
Title: Professor of Chemistry

To my parents...

For their unwavering support and encouragement

Acknowledgements

I could not have asked for a better graduate school experience than the last six and a half years in the Tokmakoff group. As I sit here writing this final part of my thesis, I am overwhelmed by nostalgia and a strong urge to hold on to my life here at MIT. I have many people to thank for making my time here so memorable. It was during the summer after my sophomore year as an undergraduate in UW-Madison when I heard Andrei Tokmakoff speak at the CMDS conference there. It was very clear that the work in his group was far too exciting to pass up and I instantly knew that I wanted to do graduate research in his group. Now, many years later, I feel truly fortunate to have had Andrei as my graduate research advisor. In addition to all the science that I have learnt from him, his courage to pursue some of the toughest problems through high-risk experiments has made the most impression on me. His optimism and support have been crucial in helping me cope with frustrating days in lab, and have been instrumental in allowing me to see some difficult experiments through. I am very grateful for his guidance and encouragement throughout graduate school.

I would like to thank the past and present members of “Team Water”, who have been extremely helpful over the last few years. Sean Roberts and Poul Petersen were remarkable teachers, who patiently taught me the nuts and bolts of nonlinear infrared spectroscopy and helped me learn the skills necessary to appease the Water Lab. Sean also introduced me to molecular dynamics simulations, which was crucial for the analysis of 2D IR anisotropy of water presented in Chapter 5 of this thesis, and Poul put together the broadband IR generation scheme in our lab, which kick-started our most recent work on water and acids. Becky Nicodemus and I worked together in the Karate Lab on some

early anisotropy experiments. I admired her attention to detail and perfection, and she was always my go-to person for questions on water literature. Over the last couple of years, I have had the pleasure of working with Aritra Mandal and Luigi De Marco, who have been instrumental in helping me set up broadband IR spectroscopy in the Water Lab. I have enjoyed discussing some cricket and Indian politics with Aritra over the years. Luigi and I work extremely well together, and I am thankful for all the lighthearted moments he has brought to some of the most frustrating days in lab.

Interacting with the protein folks has been both educative and very helpful. I would like to thank Adam Smith, Lauren DeFlores, Benjamin Dietzek, Ziad Ganim, Kevin Jones, Josh Lessing, Sam Peng, Mike Reppert, Paul Stevenson and Ann Fitzpatrick for all that they have taught me. Conversations with them have often led to a better understanding of my own project. They are wonderful people who have made working in the Tokmakoff group that much more memorable.

Thanks also go to friends from my year in the Chemistry department at MIT – Johanna, Harold, Misha, Tony, Nate, Barratt, Jeremy, Kit, Brian, Hee-Sun, Lee-Ping, Elise and Eric, with whom I have enjoyed discussing science, sharing frustrations and simply hanging out. I would also like to thank my closest friends at MIT outside the Chemistry department – Arvind, Sowmya, Ganesh, Anuja, Karthik, Murali, Aruna and Anna, for making my time at MIT so wonderful.

My parents are the reason I have made it this far. Being academics themselves, they have always put education at the forefront. My father, Ramasesha, is by far the best teacher I know, which surely stems from his innate passion for science. He made learning math and science a lot of fun, and always emphasized deep understanding of concepts.

He is a wonderful person, a great teacher and a fantastic scientist – truly a role model. I would consider myself lucky if I turned into half the academic that he is. My mother, Sheela, was the first woman to graduate with a Ph.D. from the Department of Chemistry at the Indian Institute of Science, during a time when women would rarely go to college. Her perseverance in the face of enormous hurdles and set-backs that often accompany a fundamental change in social mindset is a constant source of inspiration for me. It makes me realize that if one has the drive and focus like she does, nothing can deter. I am thankful for people like her who have opened doors for people like me. The courage, grace and the resolute optimism that she exhibits is truly inspiring. I dedicate this thesis to my parents for their unwavering support and encouragement, and for all that they have given up in order to make sure that I am never short of opportunities. My husband, Srihari, is my rock and source of inner peace. He has heroically stood by my side throughout graduate school. He has helped me through the many testing days, and has been the first to celebrate with me the occasional, but intense successes along the way. His love and support have been invaluable in helping me get here, and I consider myself extremely lucky to have him by my side. I am very grateful to my grandmothers, aunts Shamala, Tara and Shobha, and uncles Mouli and Rajagopal, for all their support and encouragement throughout my life. My closest cousins Mahesh, Prajit and Anand have always placed a high standard for academic success, which has driven me to do well. Thanks also to my mother-in-law, Sujaya, for her support during graduate school.

Table of Contents

| | |
|--|-----------|
| List of Figures | 14 |
| 1. Introduction | 23 |
| 1.1 Water's unique properties | 23 |
| 1.2 Probes of hydrogen bond dynamics in water | 30 |
| 1.3 Vibrational relaxation in liquid H ₂ O | 35 |
| 1.4 Aqueous proton transport in acids | 38 |
| 1.5 Thesis outline | 45 |
| References | 47 |
| 2. Calculation of the third-order nonlinear response function | 53 |
| 2.1 Introduction | 53 |
| 2.2 Nonlinear response function | 55 |
| 2.3 Approximations to the third-order response function | 63 |
| 2.3.1 Condon approximation | 63 |
| 2.3.2 Semiclassical approximation | 64 |
| 2.3.3 Second cumulant approximation | 68 |
| 2.4 Third-order nonlinear spectroscopy | 69 |
| 2.4.1 Three pulse vibrational echo peak shift (PS) | 72 |
| 2.4.2 Two-dimensional infrared spectroscopy (2D IR) | 74 |
| 2.4.3 Pump-probe spectroscopy (PP) | 78 |
| Acknowledgements | 80 |

| | |
|---|------------|
| References | 80 |
| 3. A phenomenological approach to modeling chemical dynamics in nonlinear and two-dimensional spectroscopy | 83 |
| 3.1 Introduction | 83 |
| 3.2 Approach | 86 |
| 3.2.1 Approximations to the response function | 86 |
| 3.2.2 Trajectory construction | 90 |
| 3.3 The non-Condon effect: Nonlinear IR spectroscopy of HOD/D ₂ O | 93 |
| 3.4 Range of applicability of trajectory mapping method | 98 |
| 3.4.1 Non-Gaussian dynamics: Spectroscopy of strong hydrogen bonds | 98 |
| 3.4.2 Chemical exchange | 104 |
| 3.5 Discussion and conclusions | 106 |
| Acknowledgements | 108 |
| References | 109 |
| 4. Generation and utilization of ultrafast mid-infrared pulses in nonlinear infrared spectroscopy | 113 |
| 4.1. Introduction | 113 |
| 4.2 Overview of experimental set-up | 117 |
| 4.3 Generation and characterization of 45 fs 3 μm pulses | 120 |
| 4.4 Acquisition of 2D IR and pump-probe spectra in the pump-probe beam geometry | 125 |
| 4.4.1 Data acquisition in the pump-probe geometry | 125 |
| 4.4.2 Sample | 133 |

| | |
|---|------------|
| 4.4.3 Processing of raw 2D IR data | 134 |
| 4.4.4 Extracting imaginary and phase 2D IR spectra | 137 |
| 4.5 Polarization scheme for 2D IR anisotropy measurements | 138 |
| 4.6 Summary | 142 |
| Acknowledgements | 143 |
| References | 143 |
| 5. Ultrafast 2D IR Anisotropy of Water Reveals Reorientation during Hydrogen-Bond Switching | 145 |
| 5.1 Introduction | 145 |
| 5.2 Methods | 148 |
| 5.2.1 Experimental | 148 |
| 5.2.2 Simulations and modeling | 151 |
| 5.3 Results and discussion | 152 |
| 5.3.1 Pump-probe anisotropy of HOD/D ₂ O | 152 |
| 5.3.2 2D IR anisotropy of HOD/D ₂ O | 158 |
| 5.3.3 Comparison to MD simulations | 168 |
| 5.4 Conclusions | 176 |
| Acknowledgements | 177 |
| References | 178 |
| 5.A. Appendix: Time-evolving angular-frequency correlations in HOD/D ₂ O from MD simulations | 182 |
| 5.B. Appendix: Temperature-dependent pump-probe anisotropy of HOD/D ₂ O | 188 |

| | |
|--|------------|
| 6. Generation of ultrafast broadband infrared pulses and measurement of broadband nonlinear spectra | 189 |
| 6.1 Introduction | 189 |
| 6.2 Overview of the experimental set-up | 193 |
| 6.3 Generation of BBIR pulses via filamentation in air | 197 |
| 6.3.1 BBIR spectral and spatial characterizations | 205 |
| 6.3.2 BBIR temporal characterization | 209 |
| 6.3.3 BBIR polarization characterization | 212 |
| 6.4 Spectroscopy with broadband infrared pulses | 213 |
| 6.5 Conclusions | 221 |
| Acknowledgements | 223 |
| References | 223 |
| | |
| 7. Water vibrations have strongly mixed intra- and inter-molecular character | 227 |
| 7.1 Introduction | 227 |
| 7.2 Experimental methods | 229 |
| 7.3 Results and discussion | 233 |
| 7.4 Summary | 245 |
| Acknowledgements | 246 |
| References | 246 |

| | |
|---|------------|
| 8. Fleeting excursions of protons in water give rise to the short-lived acid continuum and drive the exchange of Eigen and Zundel configurations | 249 |
| 8.1 Introduction | 249 |
| 8.2 Experimental methods | 259 |
| 8.3 Results and discussion | 261 |
| 8.4 Conclusions | 277 |
| Acknowledgements | 279 |
| References | 280 |
| 8.A. Appendix: Concentration dependence of third-order signal in HCl/H ₂ O | 283 |
| Curriculum Vitae | 285 |

List of Figures

| | |
|---|----|
| Figure 1-1: Geometric definition of a hydrogen bond..... | 25 |
| Figure 1-2: Correlation between ω_{OH} and R_{OO} and ω_{OH} and α (top), extracted from MD simulations of SPC/E water. The infrared spectrum of HOD/D ₂ O (bottom)..... | 31 |
| Figure 1-3: Large angle reorientation of a water molecule about a hydrogen bond switching event from molecular dynamics simulations of SPC/E water. | 34 |
| Figure 1-4: Illustrations of the Zundel (H_5O_2^+) and the Eigen (H_9O_4^+) complexes of the hydrated proton. | 39 |
| Figure 1-5: Linear infrared spectra of H ₂ O (blue) and 6M HCl in H ₂ O (red), normalized to the peak maximum at 3400 cm ⁻¹ | 44 |
| Figure 2-1: Variation of the transition dipole (in Debye) of the $\nu = 0$ to 1 transition of the OH stretch in HOD/D ₂ O with the fundamental OH stretching frequency (in cm ⁻¹)...... | 64 |
| Figure 2-2: Rephasing (left) and non-rephasing (right) contributions as a function of τ_1 and τ_3 for a two-level system. The carrier frequency is neglected here, and the plot shows only the time-domain envelope for the two contributions..... | 71 |
| Figure 2-3: The pulse sequence used in measuring the three-pulse vibrational echo for a waiting time τ_2 . This is a homodyne measurement, where the third-order signal is not interfered with a reference pulse, and hence lacks phase information..... | 73 |
| Figure 2-4: a) Three-pulse echo plotted as a function of τ_1 at different waiting times, calculated for correlated frequency and dipole trajectories. b) Three pulse echo peak shift calculated from the data in a), by finding the peak of the echo and plotting it as a function of waiting time..... | 74 |
| Figure 2-5: Pulse sequence for 2D IR spectroscopy. The third-order signal is overlapped with the local oscillator (E_{LO}) and the square of the sum of the signal and local oscillator is detected..... | 75 |

Figure 2-6: Rephasing (left), non-rephasing (middle) and correlation (right) spectra of the OH stretch of HOD/D₂O from MD simulations, calculated for $\tau_2 = 120$ fs. Only the $v = 0$ and $v = 1$ vibrational states of the OH stretch were included in this calculation.....76

Figure 2-7: Pulse sequence for pump-probe spectroscopy. Two interactions with E_{pump} creates a population state that evolves during the waiting time. E_{probe} interrogates the sample after τ_2 , and acts to heterodyne the third-order signal, which can then be detected using a spectrometer or a single-channel detector.....79

Figure 3-1: Procedure for calculating spectra using the trajectory mapping method.....91

Figure 3-2: Comparison of the normalized three-pulse echo peak shift calculated from our model, which includes the non-Condon effect, with the normalized experimental peak shift measurement (top left) of HOD/D₂O. The correlation functions that went into the peak shift calculations, which gave us the best fit with experimental results for both the Condon and non-Condon response function calculations (top right). The corresponding 2D IR spectra of HOD/D₂O with (bottom right) and without (bottom left) including the non-Condon effect.....97

Figure 3-3: (Top) Linear IR spectrum of aqueous hydroxide for different values of $\langle\delta\rangle$ (in Å), with constant distribution width of $\sigma = 0.3$ Å. Below, 2D IR spectra of hydroxide for two $\langle\delta\rangle$ values of 1.0 Å (middle) and 0.7 Å (bottom).....102

Figure 3-4: 2D IR spectra calculated for the under-damped (top) and over-damped (bottom) cases for the coupling of the OH stretch to the bath.....104

Figure 3-5: Waiting time series of 2D IR spectra calculated from Langevin simulations show the evolution of the diagonal peaks from being inhomogeneously broadened to being symmetric, along with the growth of the cross peaks signifying chemical exchange.....105

Figure 4-1: Overview of the experimental set-up. Arrows represent the direction of beam propagation and the filled circle is a periscope.....118

| | |
|---|-----|
| Figure 4-2: Spectra of the seed (red), the amplified 800 nm pulse (green) and the compressed laser output (blue), normalized to their maximum intensity..... | 119 |
| Figure 4-3: Tunability of the 3 μm spectrum from the home-built BBO/KNbO ₃ OPA..... | 122 |
| Figure 4-4: Second harmonic autocorrelation of the 3 μm pulses in AgGaS ₂ . The x-axis displays the relative time delay between two 3 μm pulses..... | 123 |
| Figure 4-5: Transient grating FROG of the 3 μm pulses from the third-order non-resonant response of CaF ₂ , dispersed on a MCT array detector..... | 124 |
| Figure 4-6: 2D IR spectroscopy in the box geometry (top) and in the pump-probe geometry (bottom). Subscripts <i>a</i> , <i>b</i> and <i>c</i> represent the three interactions of the sample with the infrared pulses..... | 127 |
| Figure 4-7: Detailed diagram of the set-up for acquiring 2D IR spectra in the pump-probe geometry. All the mirrors in the set-up are protected gold plane mirrors. BS: 3 mm thick CaF ₂ beamsplitters; WP: $\lambda/2$ MgF ₂ tilt waveplates, P: CaF ₂ wire-grid polarizers, S: sample, LO: local oscillator..... | 130 |
| Figure 4-8: Interferogram of the 3 μm pulses through a monochromator set at 3400 cm^{-1} (left). Fourier transform of the interferogram (right) shown in blue, while the red trace is the Gaussian fit to the transform to extract the center frequency..... | 133 |
| Figure 4-9: Projection of the 2D IR spectrum of HOD/D ₂ O at $\tau_2 = 250$ fs (red) onto the ω_3 dimension compared to the dispersed pump probe spectrum of the same sample at 250 fs (blue). To match this pair of spectra, the error in timing $\Delta\tau_1$ was found to be -2.2 fs..... | 134 |
| Figure 4-10: a) Time-frequency (τ_1 - ω_3) surface of HOD/D ₂ O at $\tau_2 = 250$ fs, upon correcting for errors in τ_1 and subtracting the constant pump-probe offset (left). A slice at $\omega_3 = 3400$ cm^{-1} (right) shows that the oscillations decay by the characteristic dephasing | |

time of the OH stretch in HOD/D₂O of ~150 fs. b) The Fourier transformed ($\omega_1-\omega_3$) 2D IR spectrum at $\tau_2 = 250$ fs.....136

Figure 4-11: The real (top left), imaginary (top right), absolute value (bottom left) and phase (bottom right) 2D IR spectra of HOD/D₂O at $\tau_2 = 250$ fs.....137

Figure 4-12: a) Beam diagram for 2D IR anisotropy measurements. b) Detection set-up for 2D IR anisotropy measurements.....139

Figure 4-13: Left: Absorptive (top) and absolute-value (bottom) 2D IR spectra of HOD in D₂O at $\tau_2 = 250$ fs, for ZZZZ and YYZZ polarizations. Right: Corresponding 2D IR anisotropy calculated from real absorptive and power spectra are shown on the right...142

Figure 5-1: (a) Raw ZZZZ and YYZZ dispersed pump-probe of HOD/D₂O plotted against waiting time (τ_2), before TSGS correction; (b) 3400 cm⁻¹ slice of the ZZZZ and YYZZ dispersed pump-probe, after correcting for TSGS. A three-point rolling average was performed for waiting times of <400 fs.....154

Figure 5-2: Experimental (left) and simulated (right) normalized pump-probe anisotropy of HOD/D₂O and the specified probe frequencies. Lower panel shows the amplitude of the inertial decay as a function of probe frequency.....155

Figure 5-3: Cartoon of restricted rotation model (top left). Potential of mean force for the hard cone (blue) and the harmonic cone (red) models (top right). Average angles and two standard deviations of the half-cone angle calculated from the inertial decay of measured and simulated pump-probe anisotropy (bottom), based on harmonic cone analysis.....157

Figure 5-4: 2D IR surfaces of HOD in D₂O in the ZZZZ and YYZZ polarization geometries, normalized to their maximum amplitudes, with linearly spaced contours. The ratio of the maximum amplitude of ZZZZ to ZZYY at 150 fs was 2.94.....159

Figure 5-5: Absorptive (left) and power (right) 2D IR spectra of HOD in D₂O at $\tau_2 = 250$ fs, for ZZZZ (top row) and YYZZ (second row) polarizations. Corresponding 2D IR

anisotropy calculated from real absorptive (bottom left) and power (bottom right) spectra.....160

Figure 5-6: 2D IR anisotropy spectra of HOD/D₂O calculated from absorptive ZZZZ and YZZZ 2D IR spectra from (a) experiment and (b) simulations, at four different waiting times.161

Figure 5-7: 2D IR anisotropy spectra for HOD in D₂O from (a) experiment and (b) simulation, at various waiting times.....162

Figure 5-8: (a) Experimental and (b) simulated waiting time behavior of the four quadrants of the 2D IR anisotropy calculated from 2D IR power spectra.165

Figure 5-9: Average angular deviations extracted from $\omega_1 = \text{“red”}$ and $\omega_1 = \text{“blue”}$ slices of 2D IR anisotropy from experiment (left) and simulation (right), at $\tau_2=100$ fs using the harmonic cone model. Average angles (top row) and two standard deviations (middle row) were calculated based on 2D IR anisotropy from power spectra. Average angles from 2D IR absorptive spectra are also shown (bottom row).....167

Figure 5-10: Comparison of different representations of 2D IR anisotropy from simulations at $\tau_2 = 300$ fs.172

Figure 5-A1: Time-evolution of the mean reorientation angle of the OH bond as a function of ω_1 and ω_3 plotted for six characteristic waiting times τ_2 . Angles are evaluated in degrees.....183

Figure 5-A2: Time-evolution of the standard deviation in reorientation angle of the OH bond as a function of ω_1 and ω_3 . Angles are evaluated in degrees.....184

Figure 5-A3: Time-evolution of the second Legendre polynomial orientational correlation function, P_2 , of the OH bond as a function of ω_1 and ω_3 . Here, P_2 is multiplied by 0.4 to convert it into anisotropy units.....186

Figure 5-B1: Pump-probe anisotropy of HOD/D₂O at different temperatures (left), calculated for the OH stretch fundamental. The decays were fit to a double exponential

plus offset, with long timescales (τ_{rot}) showing the following temperature dependence: 5 °C – 7 ps; 13 °C – 5.3 ps; 22 °C – 3.7 ps; 50 °C – 3.2 ps; 72 °C – 1.6 ps. Arrhenius plot of the temperature dependence of τ_{rot} (in picoseconds) (right), with error bars representing the standard deviation across three independent measurements.....188

Figure 6-1: Typical spectra from OPAs (shown in purple) compared to the many vibrational features present in H₂O (blue) and N-methylacetamide in dimethyl sulfoxide (red).....191

Figure 6-2: Overview of the experimental set-up for measuring broadband nonlinear spectra. Arrows represent the direction of beam propagation and the bold circles are periscopes.....194

Figure 6-3: Spectra (normalized to maximum intensity) of the 800 nm pulses at various stages in the laser are shown: after the Femtosource Oscillator (green), after the Coherent SSF spectral filter (red), after the stretcher (blue) and the compressed amplified final spectrum (black).....195

Figure 6-4: The $\omega/2\omega/3\omega$ broadband infrared generation scheme.....203

Figure 6-5: Spectrum of the BBIR dispersed onto a 64 element liquid N₂ cooled HgCdTe array detector, with a 6 μ m blazed 50 grooves/mm grating. The drop in intensity on the red edge of the spectrum is detector-limited, the feature at approximately 2300 cm⁻¹ is due to absorption from atmospheric CO₂, and absorption lines between 1400 cm⁻¹ and 1800 cm⁻¹ are due to atmospheric H₂O.....205

Figure 6-6: Dependence of the BBIR integrated intensity on the 800 nm power (left) for a BBIR spectrum resembling the one displayed in Figure 6-5.....206

Figure 6-7: Dependence of the BBIR integrated intensity and the noise on the medium used to purge the plasma (left).208

Figure 6-8: BBIR spectrum detected on the HgCdTe array detector after passing through 50 μ m pinhole placed at different points about the focal point at the sample position...209

| | |
|---|-----|
| Figure 6-9: Cross-correlation of the BBIR pulses with 45 fs 3 μm pulses in 500 μm thick InSb..... | 210 |
| Figure 6-10: Cross-correlation of the BBIR pulses with 3 μm pulses in a 1 mm thick CaF_2 window, showing a linear chirp across the mid-IR (left). The same cross-correlation is shown after numerically correcting for the chirp (right). The dotted blue line tracks the maximum of the cross correlation at every ω_3 to guide the eye..... | 211 |
| Figure 6-11: a) Spectrum of the broadband IR pulses at different polarization angles, unnormalized (left) and normalized (right). The polarization angles are relative to the polarization of the BBIR. b) Polarization dependence to the intensity of the BBIR at different frequencies, normalized to the value at 0° polarization angle..... | 213 |
| Figure 6-12: Beam diagram for the broadband 2D IR experiment (top). A cartoon of a broadband 2D IR spectrum of coupled oscillators at zero waiting time..... | 214 |
| Figure 6-13: The broadband 2D IR experimental set-up..... | 216 |
| Figure 6-14: Interferometric cross-correlation of the blue side of the BBIR and the 3 μm pulses..... | 219 |
| Figure 7-1: Spectra of the 3400 cm^{-1} pump and the broadband infrared probe pulses overlaid on the linear infrared spectrum of H_2O . The dip in the BBIR spectrum at $\sim 2300 \text{ cm}^{-1}$ is due to the atmospheric CO_2 | 229 |
| Figure 7-2: a) Broadband 2D IR spectrum of H_2O at $\tau_2 = 50 \text{ fs}$ using excitation pulses centered at 3400 cm^{-1} , with a $\sim 400 \text{ cm}^{-1}$ bandwidth. Color-coded arrows represent transitions illustrated in b). The grey bar represents response from atmospheric CO_2 . b) Intramolecular and intermolecular energy level diagrams representative of the bend-stretch coupling and vibrational delocalization pictures, respectively..... | 235 |
| Figure 7-3: Broadband 2D IR spectra at waiting times of 50 fs, 100 fs, 250 fs and 500 fs. The spectra are normalized to the maximum of the 50 fs surface. The low frequency parts | |

of the spectra at $\omega_3 < 2000 \text{ cm}^{-1}$ are magnified by a factor of four. The FTIR spectrum of H_2O is aligned with the ω_3 axis to guide the eye.....238

Figure 7-4: a) Broadband dispersed pump-probe spectrum of H_2O taken under magic angle polarization conditions (left). The feature at $\omega_3 \sim 2300 \text{ cm}^{-1}$ is due to the atmospheric CO_2 . Color bar represents a change in absorbance in units of ΔmOD . b) The first two components from a constrained singular value decomposition of the data presented in a) from 100 fs to 5 ps.....240

Figure 7-5: Slice at $\omega_3 = 3610 \text{ cm}^{-1}$ through the broadband dispersed pump-probe spectrum of H_2O . The line represents a double exponential fit through the data, which yielded timescales of 250 fs and 1 ps.....242

Figure 7-6: a) Broadband dispersed pump-probe spectra of H_2O at parallel and perpendicular polarizations, normalized to the maximum of the parallel spectrum. b) Time trace of pump-probe anisotropy as a function of waiting time integrated in ω_3 between 2900 cm^{-1} and 3000 cm^{-1}243

Figure 8-1: Illustration of the Grotthuss proton hopping mechanism.....250

Figure 8-2: Infrared spectra of H_2O and 6M HCl are shown along with spectra of the 3100 cm^{-1} and 3400 cm^{-1} excitation pulses and the BBIR probe pulse. Displayed on top of the spectra are cartoons of the Eigen (or hydronium), bend vibrations and the corresponding O---O separation (R_{OO}) distances. Cartoons of double-well proton transfer potentials are shown at the very top to illustrate the correlation between proton displacement and the corresponding vibrational frequencies.....255

Figure 8-3: a) 2D IR spectra of H_2O (left) and 6M HCl (right) at $\tau_2 = 50 \text{ fs}$ and 100 fs taken for pump pulses centered at 3200 cm^{-1} with a bandwidth of 400 cm^{-1} . b) $\omega_1 = 3350 \text{ cm}^{-1}$, 3200 cm^{-1} and 3100 cm^{-1} slices of the 2D IR broadband spectra of H_2O (top) and 6M HCl (bottom) at a waiting time of 100 fs.262

Figure 8-4: 2D IR spectra of 6M HCl at waiting times of 50 fs, 100 fs, 250 fs and 500 fs, for excitation pulse centered at 3200 cm^{-1} , with a bandwidth of 400 cm^{-1}264

Figure 8-5: Broadband dispersed pump-probe spectra of H₂O, 2M HCl, 4M HCl and 6M HCl using excitation pulses centered at 3400 cm⁻¹ (left) and 3100 cm⁻¹ (right) at $\tau_2 = 60$ fs. The linear infrared spectra of H₂O and 6M HCl, after subtracting the continuum absorption in the 6M HCl spectrum, are plotted on top to guide the eye. The grey dotted lines identify the position of the relevant bend peaks.....265

Figure 8-6: Broadband dispersed pump-probe spectra of H₂O, 2M HCl, 4M HCl and 6M HCl plotted from $\tau_2 = -100$ fs to 500 fs, for excitation pulses centered at 3100 cm⁻¹ with 400 cm⁻¹ bandwidth at FWHM.....267

Figure 8-7: Time traces at $\omega_3 = 3000$ cm⁻¹ (top) and $\omega_3 = 1750$ cm⁻¹ (bottom) of H₂O and 6M HCl for excitation pulses centered at 3100 cm⁻¹.....268

Figure 8-8: Broadband dispersed pump-probe spectra of H₂O, 2M, 4M and 6M HCl solutions plotted from $\tau_2 = -100$ fs to 500 fs, for excitation pulses centered at 3400 cm⁻¹.
.....269

Figure 8-9: a) Polarization dependent dispersed pump-probe of 6M HCl (left) and H₂O (right) using excitation pulses centered at 3100 cm⁻¹, normalized to the maximum of the parallel surfaces, respectively. b) Parallel minus perpendicular difference pump-probe spectra of 6M HCl (left) and H₂O (right). The difference spectra are normalized to their respective maxima.....270

Figure 8-10: A simple illustration to point out the different mechanisms by which the Eigen and Zundel species can exchange. Our data suggest the presence of the Eigen-to-Zundel-to-Eigen mechanism for proton transfer in acids, but does not show evidence for the absence of the Eigen-to-Eigen or Zundel-to-Zundel processes.....276

Figure 8-A1: Dispersed pump-probe signals for 3100 cm⁻¹ excitation at $\omega_3 = 2000$ cm⁻¹ (top) and $\omega_3 = 1745$ cm⁻¹ (bottom) as a function of acid concentration, normalized to the maximum of the induced absorption for each concentration, at the specified waiting times.....283

Chapter 1

Introduction

1.1 Water's unique properties

Water is the most abundant liquid on earth, owing partly to the fact that it is made of two of the three most common elements in the universe – hydrogen and oxygen. Water covers 70% of the earth's surface area, and is credited for creating and sustaining the rich flora and fauna both in the oceans as well as on land. The human body is also made up of as much as 65% water, which has proven to be an important solvent for biochemical reactions in all living organisms. Moreover, water's ability to exist in all three phases of matter under ambient conditions on earth, and its unique physical and thermodynamic properties such as large heat capacity and high boiling point, make it a key player in the regulation of global climate [1]. Water is not a mere spectator in any these geo- and biochemical processes, but an active participant owing to the peculiar nature in which it interacts with other molecules [1,2]. Several anomalous properties of water are well-known, from its high boiling point and expansion on freezing to its large surface tension and capillary activity. However, we lack fundamental understanding of how water engages in the complex chemistry that exists in nature.

Centuries of scientific research on water have revealed how intriguing this molecule actually is. Scientific investigations on water date back to the late 18th century, when water was first identified as being composed of the elements hydrogen and oxygen [2]. These studies were followed by experiments that determined its exact stoichiometric composition. With the advent of more sophisticated experimental and theoretical techniques in the twentieth century, such as molecular spectroscopy and computer modeling, much of the work over the last century has focused on understanding the electronic, vibrational and rotational properties of water. Early spectroscopic investigations were done on low pressure water vapor where interactions between water molecules are negligible. These studies were successful in measuring, with a high degree of accuracy, fundamental properties such as the geometry of the water molecule (bond lengths and angles), its ionization energies, vibrational normal modes and anharmonicities, and dipole and quadrupole moments of the three most abundant isotopologues of water – H₂O, HDO and D₂O. Subsequent studies on water vapor at higher pressures, along with electrostatic modeling of the interactions between molecules, revealed the ideal orientation of neighboring water molecules that led to the most favorable electrostatic interaction and gave insights into thermodynamic properties of water vapor like the second virial coefficient and the fraction of energy in various attractive and repulsive interactions between water molecules [2].

Water's unique properties arise from its interactions with other molecules in the condensed phases, called the hydrogen bonding interaction. A hydrogen bond is an intermolecular interaction that resembles, and is often modeled as, an electrostatic attraction between an electronegative (O) atom and an electropositive atom (H) [3]. In

liquid H₂O, the two H atoms can donate two hydrogen bonds and the two lone pairs on the O atom can accept two hydrogen bonds from other water molecules. Developing an adequate definition of the hydrogen bond that can accurately predict classical and quantum mechanical properties of liquid water remains an active area of research, pointing to the highly complex structure and dynamics that govern the unique properties of water. A commonly employed definition of a hydrogen bond for describing infrared spectroscopy involves imposing an arbitrary geometric cut-off in distance between neighboring O atoms ($R_{OO} < 3.5 \text{ \AA}$) and the angle between the O-H bond of a water molecule and the intermolecular O \cdots O vector, called the hydrogen bond angle (α or $\theta_{O-H\cdots O} < 30^\circ$) [4]. Figure 1-1 illustrates the cut-off distance and angle employed in the geometric hydrogen bond definition.

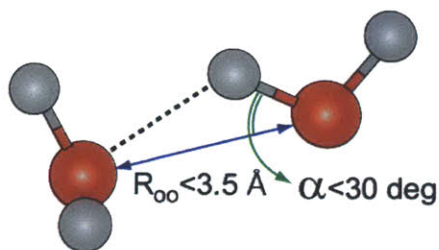


Figure 1-1: Geometric definition of a hydrogen bond between two water molecules. R_{OO} is the distance between the oxygen atoms of the two water molecules, and α is the angle made by an OH bond with a line segment connecting the two oxygen atoms.

Other hydrogen bond definitions include quantifying the electron occupancy of the anti-bonding OH orbitals [5,6], and a topological definition [7] that does not impose a

geometric cut-off but instead assigns hydrogen bonds based on the nearest O atoms. The delicate interplay between these attractive hydrogen bonds and the repulsive electrostatic interactions at short range give water a unique liquid structure consisting of a complex network of hydrogen bonds, which can explain some of its oddities such as the anomalous low density of ice compared to liquid water.

Water is a light molecule that can very rapidly move on timescales as short as tens of femtoseconds. Yet, its ability to accept and donate two hydrogen-bonds with its neighboring molecules means that it can form structured networks, such as those in ice. The hydrogen bond network of liquid water is strong enough to result in an elevated boiling point of water of 100 °C compared to other molecules with similar mass, since extra energy is needed to overcome the hydrogen bonding attraction between water molecules. In the absence of hydrogen bonds, a molecule as light as H₂O would have had a boiling point of -80 °C. On the other hand, the strength of a hydrogen bond is roughly 5 to 6 kcal/mol [3], making thermal fluctuations under ambient conditions sufficient to cleave these hydrogen bonds, leading to constant breaking and reforming of hydrogen bonds in liquid water. The difficulty in studying liquid water arises from the combination of both of these properties – fast motions of the light water molecule are coupled with the structural ordering imparted by hydrogen bonding, resulting in a complex structured liquid that rapidly evolves on fast femtosecond to picosecond timescales involving correlated rearrangements of hydrogen bonds.

The fastest nuclear motions in liquid water occur on timescales of tens of femtoseconds. These motions involve the intra-molecular vibrations such as the 10 fs period of an OH stretch vibration and the 20 fs period for an H₂O bend vibration.

Librations, or hindered inertial rotations of water molecules, have been shown to occur on a 50 fs timescale [8,9], while the intermolecular hydrogen bond stretch has a period of 200 fs [8,10]. The librational and translational bands of H₂O are extremely broad and appear in the far-infrared region of the spectrum centered approximately at 700 cm⁻¹ and 200 cm⁻¹, respectively. The hydrogen bond distortions about three oxygen centers, on the other hand, happen on a slightly slower 550 fs timescale [11,12]. The movement of water molecules on such fast timescales is crucial to its ability in mediating aqueous reactions. Therefore, predictions on how water behaves and its intimate role in chemical reactions have to be preceded by an understanding of the instantaneous configurations of hydrogen bonding networks and the dynamics that govern their evolution.

Water's ability to rapidly change its structure has made it an important component in many aqueous chemical processes. Due to the strong dipole moment of water and the pace at which water molecules can rearrange, charge transport in water is accompanied by fast hydrogen bond rearrangements that energetically stabilize the displaced charge [13]. Particular interest has been shown in studying the transport of excess protons and hydroxide in water, since early ionic conductance measurements showed that the mobility of H₃O⁺ was several times more than ions of similar size [13]. Grotthuss attributed this anomalously high mobility of protons to charge migration between water moieties [14]. This process, now known as the Grotthuss Mechanism, describes proton transfer as a chemical process of sequential proton hops from one water molecule to the next, via the cleavage and formation of O-H bonds along hydrogen bonds, resulting in long-range charge transport, and not long-range displacement of any particular proton [13]. This idea has been extended to conceptualize proton transport in biological

systems, for example across cell membranes, where water molecules are said to create water wires that guide the transport of charge.

Describing the behavior of water has been challenging both from theoretical and experimental perspectives. Ultrafast time-resolved spectroscopy, often in conjunction with classical molecular dynamics (MD) simulations and mixed quantum-classical models, has helped us elucidate important aspects of hydrogen bonding dynamics in water [15]. These MD simulations use classical force fields from various water models, such as the simple point charge (SPC) models, to propagate Newton's equations of motion. These water models describe the nature of the water molecules and the interactions between them. Several models have been proposed for describing the hydrogen bonding interaction between water molecules, and have been largely parameterized to reproduce bulk thermodynamics properties of water such as density, heat capacity and diffusion constants [16]. These models can be broadly classified into rigid and flexible water models. Rigid models assume that the intramolecular bond lengths and angles are fixed, and they only account for intermolecular interactions described by electrostatics. Flexible water models account for the fluctuations in both the intra- and intermolecular degrees of freedom, making them better equipped for calculating vibrational coupling between low frequency vibrations. However, for spectroscopic calculations thus far, the rigid water models have been most commonly used to describe high frequency OH stretching vibrations in water due to the ease with which they can be implemented [16]. Among the rigid water models, there are fixed charge models that assign fixed partial charges to the O and H atoms, and polarizable water models that allow for charge fluctuations based on the electrostatic

environment [16]. Intermolecular interactions in all of these models are described purely electrostatically and do not include quantum mechanical orbital overlap considerations. *Ab initio*-based force fields, such as the TTM force fields, have also been developed to describe water [17]. Intramolecular modes in these water models are described based on multidimensional molecular potential energy surfaces, and intermolecular interactions are parameterized based on *ab initio* calculations for water dimers [18,19]. These *ab initio* water models are flexible and implicitly include polarizability, and are used in conjunction with centroid and path integral molecular dynamics simulations to model hydrogen bonding dynamics and infrared spectroscopy [17–20]. However, due to added complexity and computational time associated with these calculations, *ab initio* techniques are yet to see the same level of popularity that classical methods enjoy for describing time-resolved spectroscopy of water.

Challenges from the experimental perspective have primarily originated from the difficulty in generating pulses short enough to study the fast motions of water molecules. Studying water requires laser pulses that are short enough to resolve the structural evolution of the hydrogen bond network on the femtosecond to picosecond timescales, and that are tuned to energies that can probe transitions in water most sensitive to the hydrogen bonding environment. Currently, ultrafast lasers are able to generate near-infrared pulses that are tens of femtoseconds in duration, short enough to probe the fast nuclear dynamics in liquids when tuned to appropriate frequencies. Optical parametric amplification techniques are used to tune the wavelength of laser outputs to frequencies ranging from the ultraviolet to the infrared regimes. However reliably generating pulses tuned to the OH stretching frequency at wavelengths of $\sim 3 \mu\text{m}$ without significantly

compromising pulse duration remains a challenge. Ultrafast laser spectroscopy of water serves as a reliable benchmark to compare and improve theoretical models of water. In return, comparison of experimental spectroscopic data with spectra calculated from simulations is a useful way to gain atomistic insight into the hydrogen bond dynamics in water.

1.2 Probes of hydrogen bond dynamics in water

In recent years, the interpretation of water IR spectroscopy has undergone tremendous advances as a result of mixed quantum-classical models that allow quantum mechanical transition frequencies to be predicted from classical simulations of the intermolecular motions of the liquid [16,21–26]. Molecular dynamics simulations of SPC/E (simple point charge extended; rigid model with fixed partial charges on the H and O atoms) water model showed that the OH stretch vibration (ω_{OH}) of water is a sensitive reporter of its local hydrogen bonding configuration [24,27,28]. The OH stretch frequency of a water molecule participating in a strong hydrogen bond is shifted to lower frequencies than that of a water molecule in a weak or broken hydrogen bond configuration. These studies correlated geometric parameters associated with hydrogen bonding, such as R_{OO} and α , with ω_{OH} from the SPC/E water model with frequencies calculated for the isotopically diluted HOD/D₂O system (Figure 1-2 top), and showed that the correlation coefficient with R_{OO} was 0.77 and with $\theta_{\text{OH}\cdots\text{O}}$ was 0.49 [24].

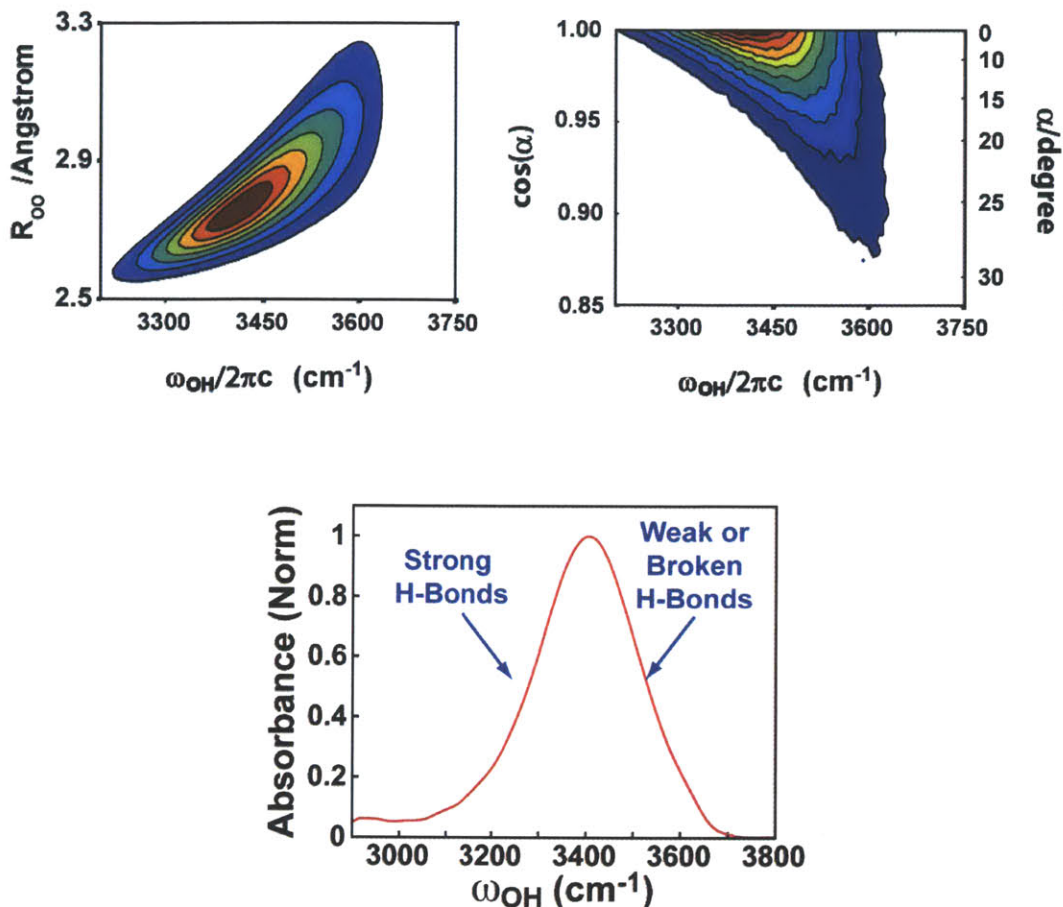


Figure 1-2: Correlation between ω_{OH} and R_{OO} and ω_{OH} and α (top), extracted from MD simulations of SPC/E water [24]. The infrared spectrum of HOD/D₂O (bottom).

While the correlation between ω_{OH} and the geometric parameters were good for low ω_{OH} , they found poor correlation for higher ω_{OH} , suggesting that there exists a broad range of geometric configurations for water molecules participating in weak hydrogen bonds. The correlation of ω_{OH} with the electric field of all the molecules in the simulation box projected along the OH bond was near-perfect, and the electric field of the nearest neighbor water molecule projected along the OH bond shows very good correlation, with a correlation coefficient of 0.89 [24]. This suggests that fluctuations in the electric field

of the environment strongly influence fluctuations in the hydrogen bond configuration. From these calculations, it was clear that ω_{OH} is a sensitive measure of hydrogen bonding environment and following the instantaneous fluctuations in ω_{OH} can tell us about the evolution of the hydrogen bonding network.

The linear infrared spectrum of HOD/D₂O is displayed at the bottom of Figure 1-2. The spectrum exhibits the OH stretching transition centered at 3400 cm⁻¹, which is inhomogeneously broadened to a full-width at half-maximum of ~250 cm⁻¹, reflecting the many hydrogen bond configurations in the liquid. OH stretch vibrations that absorb on the red side of the lineshape are due to HOD molecules in strong and linear hydrogen bonded configurations, while those that absorb on the blue side of the OH stretch lineshape are from HOD molecules in strained or broken hydrogen bond configurations.

Understanding hydrogen bond dynamics in water requires understanding the fast fluctuations of water molecules reflected in the evolution of the OH stretch frequency. The advent of ultrafast lasers has now allowed us to access the time-evolving structure of the hydrogen bond network of water on timescales of tens of femtoseconds to several picoseconds. Ultrafast two-dimensional infrared (2D IR) spectroscopy of the OH stretch vibration of HOD/D₂O is a powerful technique to probe the dynamics of hydrogen bond exchange in water, and interpretation of the data is aided by molecular dynamics simulations and mixed quantum-classical modeling of infrared spectra [15]. 2D IR and pump-probe experiments were done with 45 fs pulses centered at 3400 cm⁻¹ [29] to follow the evolution of frequencies within the OH stretch lineshape on fast timescales. 2D IR spectroscopy can follow the correlation between initial frequency and final frequency for a range of waiting times, allowing us to monitor changes to the OH stretch

frequency of water with time and deduce the underlying dynamics with the help of 2D IR spectra calculated from molecular dynamics simulations. Much of our understanding of the timescales for local and global changes to the structure of liquid water described in the previous section have been derived from earlier 2D IR, pump-probe and other nonlinear infrared spectroscopies along with MD simulations. From these studies, the global hydrogen bond rearrangement and collective reorientation of water molecules were measured to exhibit timescales of 1.5 ps and 3 ps, respectively [8].

These timescales tie into the dynamics of how water molecules exchange their hydrogen bonding partners. Two pictures emerge for describing the process of hydrogen bond exchange in water. One picture suggests that the exchange happens in a step-wise fashion, where a hydrogen bond is first broken and the dangling OH of a water molecule persists for timescales longer than the correlation time in water (~ 340 fs [8]) as it waits for a new hydrogen bond partner, and then forms a stable hydrogen bond with a different molecule. The other picture describes the hydrogen bond switch as being a concerted process, where the dangling hydrogen bond is only transiently visited during hydrogen bond exchange. Earlier 2D IR work on HOD/D₂O and MD simulations shed light on the relative persistence of strong and weakly hydrogen bonded configurations in water [30,31]. By analyzing the line shapes of 2D IR spectra, they concluded that the non-hydrogen bonded or strained configurations are visited only transiently during hydrogen bond exchange, and in fact persist for less than 100 fs. The experiments suggested that a non-hydrogen bonded configuration return to a stable hydrogen bonded state on a timescale of 60 fs, which is strikingly similar to the librational timescales in water. These studies indicated that the evolution of a non-hydrogen bonded water

molecule to a stable hydrogen bond configuration is driven by librational fluctuations, and that hydrogen bond switching is a concerted process involving exchange of the initial and final hydrogen bond acceptors [30].

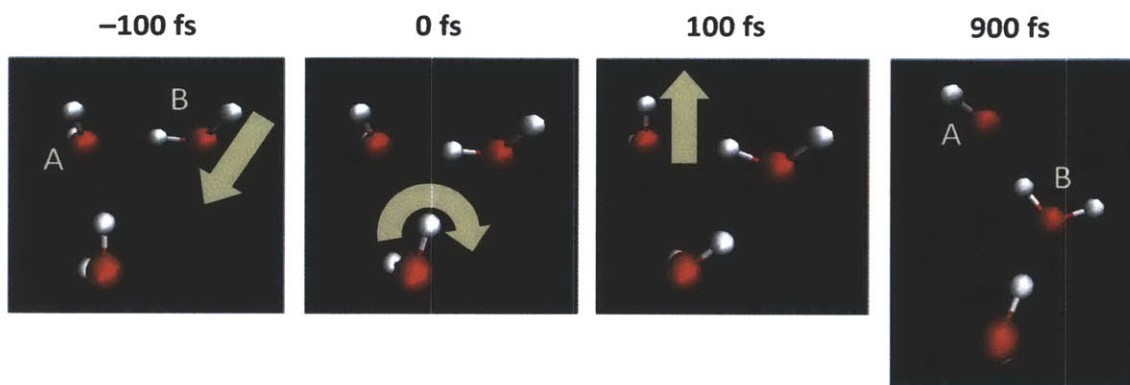


Figure 1-3: Large angle reorientation of a water molecule about a hydrogen bond switching event from molecular dynamics simulations of SPC/E water. The 0 fs frame represents the time when the switching happens, and the configuration at this time is referred to as a bifurcated hydrogen bond state.

MD simulations of the SPC/E water model (Figure 1-3) by Hynes and Laage [32,33] went on to provide evidence for the existence of inertial “jump” reorientation of water molecules that accompanies hydrogen bond switching, suggesting that the angular diffusion model cannot explain the large angular jumps they were observing in their simulations. These studies quantified the average angle for reorientation of a switching water molecule to be $\sim 68^\circ$, with the peak of the distribution of jump angles for various molecules in the simulation to be $\sim 50^\circ$. Other less probable switching mechanisms in simulations have also been described [7] using a different hydrogen bonding definition

for the same SPC/E water model, but all proposed mechanisms of hydrogen bond exchange involved a large angle reorientation of the switching water molecule. Furthermore, 2D IR experiments on switching of HBs to solvated ions [34,35] confirmed that hydrogen bond connectivity changes by large angle jump reorientation. In the first part of this thesis, I explore in detail the relationship between the initial and final ω_{OH} and the orientation of the HOD transition dipole through 2D IR anisotropy experiments. These measurements add an extra dimension to the spectroscopy, and can be interpreted through frequency-orientation correlations, giving us a direct measure of the orientational dynamics of hydrogen bond exchange [36].

1.3 Vibrational relaxation in liquid H₂O

In addition to the rapid rearrangement of the hydrogen bond network that mediates aqueous chemical reactions, the ability of water to energetically stabilize intermediates on ultrafast timescales through efficient vibrational energy dissipation is a major contributor to the role of water in aqueous chemistry. Solutes dissolved in liquid water are greatly influenced by the nature of the vibrations of the surrounding water molecules that help funnel excess energy into thermal vibrations of the system. The timescales and pathways for the relaxation of vibrational excitation in H₂O has been the subject of many experimental [37–47] and theoretical [48–52] investigations over the last several years. Using ultrafast narrowband infrared spectroscopy [39,42,45,46] and IR/Raman spectroscopy [37,44], previous experimental efforts have probed the relaxation of an OH stretch excitation in liquid H₂O. Understanding how vibrational energy is dissipated upon OH stretch excitation has constituted a large part of the efforts in understanding water.

The traditional picture for vibrational relaxation, where vibrational energy flows downhill through a set of weakly coupled intra-molecular normal modes and then to the low-frequency collective intermolecular vibrations of the surroundings, is often used to describe relaxation of the OH stretch excitation and the growth of the thermal spectrum in water. Work from other groups have suggested that upon the excitation of the OH stretch vibration in water at 3400 cm^{-1} , the energy first flows into the overtone ($3250\text{-}3300\text{ cm}^{-1}$) or the fundamental transition (1650 cm^{-1}) of the H_2O bend vibration that is either localized on one molecule or across two neighboring water molecules, and then into the collective librations and low frequency modes, resulting in heating of the liquid [39,44,46,47]. Using narrowband IR pump and incoherent anti-Stokes Raman probing of H_2O on sub-picosecond timescales, Dlott and co-workers [37,44] concluded that exciting the OH stretch transition at any frequency within the broad lineshape results in vibrational energy relaxation either to the $v = 0$ to 2 overtone transition of the bend centered at 3300 cm^{-1} that eventually excites one quantum of the $v = 0$ to 1 fundamental bend transition, or to two quanta of the fundamental bend transition on two adjacent water molecules [44]. From the anomalous temperature dependent trends in the vibrational relaxation timescale of the OH stretch from narrowband infrared pump-probe spectroscopy of H_2O , Lock and Bakker [46] postulated that the OH stretch relaxation happens through the $v = 0$ to 2 overtone transition of the bend. Using two-color infrared pump-probe spectroscopy, Lindner et al. [39] further suggested that upon exciting the OH stretching vibration in H_2O , the vibrational energy relaxation proceeds via a transiently populated $v = 0$ to 2 transition of the bend, followed by the splitting of the bend overtone transition to bend fundamental transitions over two molecules, each of which then relax

to populate the librational and low frequency modes. Attempts have also been made to explain vibrational relaxation as a process where the OH stretch excitation first undergoes resonant intermolecular energy transfer to excite OH stretch vibrations on surrounding water molecules, followed by energy dissipation to the low frequency modes [53]. Furthermore, using narrowband pump-probe anisotropy measurements on the OH stretch, Kraemer et al. [45] predicted the 80 fs anisotropy decay they measured to be from intermolecular OH energy transfer and the 250 fs population decay of the OH stretch to originate from intra-molecular stretch-to-bend relaxation.

An additional important consideration in liquid H₂O is the fact that the hydrogen bonding and intermolecular vibrational coupling give rise to the delocalization of the vibrational modes. Using temperature-dependent narrowband 2D IR and pump-probe anisotropy on H₂O, Kraemer et al. [45] concluded that the OH stretch excitation in water is delocalized over several water molecules. This is in agreement with molecular dynamics simulation work [48,50–52], which modeled the OH stretch delocalization through electrostatic interactions between water molecules and showed that the OH stretch vibrational eigenstates could be delocalized across as many as 6 water molecules. How this delocalization affects the timescale and pathways for energy relaxation, and the manner in which modes other than the OH stretch are delocalized are currently being investigated.

These earlier studies on water have attempted to decouple the contributions from intra- and inter-molecular pathways of energy relaxation in liquid H₂O, often resorting to the picture of sequential downhill energy relaxation as being the primary pathway for energy dissipation in water. These studies have probed water through a narrow frequency

window offered by narrowband infrared pulses generated by optical parametric amplifiers. In reality however, vibrational energy relaxation in liquid H₂O is slave to the complex interplay between intra-molecular and inter-molecular relaxation pathways, influenced by both vibrational coupling and hydrogen bonding interactions and requiring that we use a broader frequency window to probe vibrational dynamics of all mid-IR features of water. Using ultrafast broadband infrared pulses generated from a plasma, we probed vibrational coupling and relaxation in liquid H₂O through broadband 2D IR and broadband pump-probe spectroscopies, which are described in the second half of this thesis. Our results point to a strong mixing of inter- and intramolecular vibrational modes of water, giving rise to highly efficient pathways for ultrafast energy dissipation.

1.4 Aqueous proton transport in acids

Aqueous chemistry is ubiquitous in nature and occurs primarily under acidic or basic conditions, and aqueous reactions are governed by the transport of protons through liquid water. Aqueous proton transfer (PT) drives processes such as electrochemical reactions in fuel cells and biochemical reactions like charge transport across cell membranes and enzymatic catalysis. Ultrafast hydrogen bond rearrangements as well as rapid energy dissipation in water influence the transport of protons through the liquid. Despite its importance, the structure of the proton in liquid water and the dynamics of its transport are contested, and several unanswered questions remain. Is a proton in water localized on a single water molecule in the form of the covalently bound hydronium ion (H₃O⁺), and if so, is it more appropriate to characterize its structure as the Eigen ion (H₉O₄⁺) [54] where the hydronium is stabilized by being solvated by three water molecules? Or is the proton

more delocalized, where its charge is shared by two or more water molecules, such as in the Zundel species (H_5O_2^+) [55] where the proton is equally shared between two water molecules? Figure 1-4 shows cartoons of the Zundel and Eigen complexes of the hydrated proton. How do these structures interconvert and what is the role of the solvating water molecules in the transfer of protons?

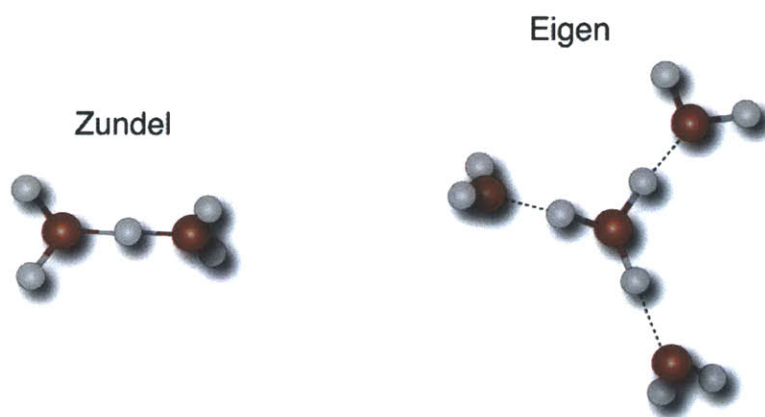


Figure 1-4: Illustrations of the Zundel (H_5O_2^+) and the Eigen (H_9O_4^+) complexes of the hydrated proton. The O---O distance for the two complexes have been calculated to be $\sim 2.4 \text{ \AA}$ and $\sim 2.6 \text{ \AA}$, respectively, which are shorter than the distance in bulk water ($\sim 2.8 \text{ \AA}$) [56].

While the proton hopping mechanism is a widely accepted picture for proton transport in acids and bases, it does not explain the driving force behind proton transfer and presents a highly simplistic view of the process. That the strength of a hydrogen bond and the barrier for proton transfer are similar in energy indicates that the reorganization of hydrogen bonds of the surrounding water molecules is linked to the transfer of proton

from a donor to an acceptor molecule [13]. The solvating water molecules move on fast enough timescales, that one has to consider the influence of water molecules in promoting proton transfer and rapidly stabilizing protonated configurations. The structures of solvated proton configurations involved in PT and their lifetimes, the mechanism of PT and the free energy barrier for proton motion are in need of experimental investigation. Due to the participation of several water molecules in the process, identifying a suitable reaction coordinate for describing PT is also nontrivial. The Grotthuss hopping mechanism has been the subject of several theoretical studies, leading to differing pictures of PT with few experimental observations to compare with. Previous theoretical investigations have proposed various mechanisms that each suggests the stability of the Zundel or Eigen configurations during proton transfer.

The proton transport mechanism involving primarily Zundel species describes PT events to occur in concert between successive Zundel entities [57,58]. The water molecules in the Zundel configuration are strongly hydrogen bonded, perhaps even covalently, resulting in a barrier-less transfer of proton from one water molecule to the other. The proton, therefore, undergoes rapid shuttling between the water molecules, simultaneous to the shuttling of a proton in the neighboring Zundel species, resulting in a concerted PT process. Zundel proposed that this concerted process is driven by distortions of the proton potential from a Morse-like potential for a proton localized on a single water molecule to a double well potential for a proton equally shared between two water molecules [55,59].

The PT mechanism involving primarily the Eigen species is said to occur as a step-wise process. First, a hydrogen bond between the first and second solvation shells of the

proton is ruptured under the influence of thermal fluctuations, leading to a reduction of the coordination number of the water molecule in the first solvation shell of the proton. The proton from the donor hydronium then hops to the acceptor water molecule, via the Zundel configuration. Bond-order analysis by Voth and co-workers show that this event is followed by hydrogen bond rearrangements around the donor molecule, resulting in an increase in the coordination number of the now deprotonated donor [60]. Hydrogen bonds around the protonated acceptor also undergo rearrangements as a means of stabilizing the excess charge. The collective hydrogen bond rearrangement has been identified as the rate-limiting step in this mechanism [56]. Voth and co-workers' studies of change in hydrogen bond angles during PT point to the question of causality of this process – whether the rupture of the hydrogen bond precedes the PT event or vice versa or if the two processes happen in tandem. This mechanism also suggests that PT in a particular local environment happens in sequence, where there is a time lag between successive PT events.

Empirical valence bond (EVB) MD simulations have hypothesized that the Eigen species is more stable and longer lived, with Zundel species forming the intermediate during PT [60]. Simulations by Voth and co-workers have suggested that proton transfer happens between a special pair of water molecules. In this picture, the symmetric Eigen species undergoes distortions that are driven by thermal fluctuations of the environment, resulting in one of the solvating water molecules to the hydronium forming a special pair with the hydronium ion. The special pair is marked by a smaller separation distance and a stronger pull of the proton from the hydronium core. This, they conclude, leads to the formation of the Zundel species with the proton equally shared between the special

pair [61]. Proton transfer is then complete when the proton hops over to the acceptor. These calculations predict lifetimes for Zundel and Eigen complexes to be approximately 370 fs and ~1-2 ps, respectively, with the entire PT event occurring on a timescale of a few picoseconds.

However, it is reasonable to assume that the Eigen and Zundel species form limiting cases in a realistic description of PT. Simulations by Parrinello and co-workers [62] suggest that solvated protons exist in several configurations that cannot be explicitly identified as either Eigen or Zundel. PT processes must hence be a combination of chemical exchanges between a range of different solvated proton configurations that can bear resemblance to Eigen or Zundel species. Given that the activation energy for PT is rather low at 2-3 kcal/mol [13], this seems like a more plausible explanation of proton transport. Experimental evidence would serve as a benchmark to compare against the different pictures of proton transfer that have emerged from various theoretical approaches.

So far, most experiments on PT in acids have been time-averaged measurements, such as gas phase spectroscopy on clusters [63–65], linear IR spectroscopy [55] and neutron scattering experiments [66]. Gas phase spectroscopy on various proton clusters has been successful in assigning infrared spectral features to specific vibrations of Zundel and Eigen species for a variety of isotope compositions [63–65]. Neutron scattering experiments have shown that the first peak in the O---O radial distribution function for acids appears at smaller distances than for pure water, indicating that the hydrogen bonds between a proton and a solvating water molecules is stronger than the hydrogen bond between two water molecules in the bulk [66]. Linear IR spectra of aqueous acids also

lead to similar conclusions based on the red-shifting of the OH stretching frequency of water in the presence of acids relative to bulk water, which is an indicator of a stronger hydrogen bond. Aqueous proton transfer in bases has been studied with ultrafast 2D IR spectroscopy by probing the evolution of the OH stretch vibration of dilute HOD in concentrated solutions of NaOD/D₂O [67,68]. These studies are currently being extended by using broadband infrared pulses to follow vibrations across the mid-infrared spectrum of aqueous hydroxide.

The linear infrared spectrum of H₂O consists of the broad OH stretching band at 3400 cm⁻¹, the H₂O bend mode at 1650 cm⁻¹, and a bend-libration combination band at 2150 cm⁻¹. Apart from these main features in the infrared spectrum, H₂O shows background absorption at all frequencies from the far to near infrared regimes arising from the highly coupled nature of the vibrations in H₂O. Several changes in the linear IR spectrum accompany the addition of strong acids to water, as shown in Figure 1-5. Compared to the linear infrared spectrum of neat liquid H₂O, HCl/H₂O spectra show strong enhancements on the low frequency side of the OH stretch. In HCl/H₂O, the OH stretch lineshape broadens on the red side and its peak shifts slightly to lower frequencies reflecting the strong hydrogen bonds between water molecules and protons. Water molecules directly hydrogen bonded to the chloride ion also contribute to the acid linear infrared spectrum and the OH stretch vibration of these water molecules are blue-shifted compared to bulk water due to a weaker hydrogen bonding interaction with the Cl⁻ ion. As acid concentration is increased, we also see a very broad “continuum” absorption that spans from 900 cm⁻¹ to 3400 cm⁻¹ due to a large distribution of rapidly interconverting hydrated proton configurations. Riding on top of the continuum is a feature at 1750 cm⁻¹

that appears as a shoulder to the H₂O bend on the blue side, and a distinct peak at 1200 cm⁻¹.

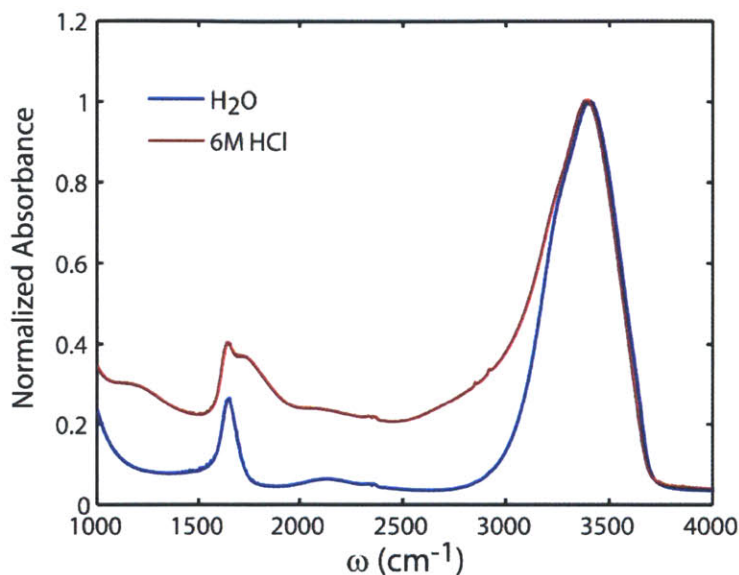


Figure 1-5: Linear infrared spectra of H₂O (blue) and 6M HCl in H₂O (red), normalized to the peak maximum at 3400 cm⁻¹.

Assignments of these spectral features have so far relied on gas phase spectroscopy of protonated clusters aided by DFT calculations and normal mode analysis [63–65], and empirical valence bond molecular dynamics simulations [69,70]. Based on gas phase spectroscopy and MD simulations, the infrared spectral features were assigned to specific vibrational modes of the Eigen and the Zundel limiting forms of the hydrated proton. These studies have assigned the broad 3200 cm⁻¹ to 3400 cm⁻¹ feature to the symmetric and asymmetric stretch of the water molecules flanking the shared proton in the Zundel species. The 1750 cm⁻¹ feature has been assigned to the bend vibration of the flanking water molecules and the 1200 cm⁻¹ feature to the intermolecular asymmetric stretching mode of the Zundel configuration. The Eigen configuration was assigned an even more

red-shifted OH stretching absorption between 2600 cm^{-1} to 3000 cm^{-1} from the symmetric OH stretching and the degenerate asymmetric stretching of the three equivalent protons of the hydronium, while the bending motion of the H_3O^+ species was shown to display a similar vibrational frequency to that of neat H_2O .

Few experiments have been performed investigating the intimate link between spectral assignments and the dynamics of proton transport in condensed phase. Due to highly overlapping and broad mid-IR absorption features that are characteristic of solvated protons in liquid water, linear spectra can offer little evidence for assignments of various features to specific solvated proton configurations and how they interconvert. Moreover, the nature of these vibrations change drastically from gas phase proton clusters to solvated protons in acid solutions, since terms such as symmetric and asymmetric stretch mean very little in the condensed phase, where vibrations are delocalized across several water molecules and the coupling between intra- and intermolecular vibrations result in significant mixing of vibrational modes. Building on our picture of vibrational coupling and relaxation in H_2O , we studied the dynamics of proton transfer in water and the associated assignments of the infrared spectral features using ultrafast broadband infrared spectroscopy of various concentrations of $\text{HCl}/\text{H}_2\text{O}$.

1.5 Thesis outline

This thesis details our efforts in elucidating the dynamics of hydrogen bond switching and vibrational relaxation in water, and their role in the transport of protons in aqueous acids.

In Chapter 2, I describe the steps involved in deriving the nonlinear response function and the approximations that go into calculating nonlinear infrared spectra starting with a time-dependent Hamiltonian, and end with the method of calculating nonlinear spectra from molecular dynamics simulations. Chapter 3 presents an alternate phenomenological approach from what currently exists, which uses the trajectory mapping method for calculating nonlinear spectra. In this methodology, we generate trajectories of a relevant internal coordinate and map the internal variable to experimental observables such as transition dipole moments and transition frequencies. We then use the mixed quantum-classical approach to calculate the third order response function and linear and nonlinear spectra. We illustrate this method using three examples that are poorly addressed using traditional phenomenological approaches for modeling spectroscopy. This trajectory mapping method allows us to correlate the observed spectra with simple internal variables for describing dynamics.

Chapter 4 describes in detail the experimental apparatus used for the measurement of 2D IR and pump-probe spectra of HOD/D₂O, including the generation and characterization of short 3 μm pulses and the calibration of delay stages that control the relative timing between replicas of these pulses to obtain reliable 2D IR spectra. The chapter ends by outlining the procedure for processing raw experimental data. In Chapter 5, I present our 2D IR anisotropy results on HOD/D₂O, their comparison to 2D IR anisotropy spectra obtained from molecular dynamics simulations, and the analysis of experimental and simulated spectra using restricted rotation modeling to extract hydrogen bond exchange angles. These experiments provided direct evidence for large angle reorientation during hydrogen bond switching in water.

Chapter 6 details the experimental set-up for the generation and utilization of ultrafast broadband mid-infrared pulses, in conjunction with the 3 μm pulses described in Chapter 4. This chapter goes through the spectral, temporal and spatial characterization of the broadband infrared pulses, and how they can be used in broadband 2D IR and broadband pump-probe experiments. Chapter 7 presents the results and interpretation of the broadband pump-probe and broadband 2D IR experiments on neat liquid H_2O . The chapter provides evidence and arguments that support the idea that water vibrations result from strong inter- and intra-molecular vibrational coupling, giving rise to highly efficient vibrational relaxation pathways that earlier work has not been able to measure or explain. Finally, Chapter 8 presents broadband 2D IR and broadband pump-probe spectroscopy of HCl in H_2O , which shows that aqueous proton transfer is driven by electric field fluctuations of the solvent environment primarily originating from librational and translational motions of solvating water molecules.

References

- [1] P. Ball, *Life's Matrix: A Biography of Water* (University of California Press, Berkeley, 2001).
- [2] D. Eisenberg and W. Kauzmann, *The Structure and Properties of Water* (Oxford University Press, New York, 1969).
- [3] F. H. Stillinger, *Science* (New York, N.Y.) **209**, 451 (1980).
- [4] A. Luzar and D. Chandler, *Phys. Rev. Lett.* **76**, 928 (1996).

- [5] B. M. Auer, R. Kumar, J. R. Schmidt, and J. L. Skinner, Proc. Natl. Acad. Sci. U.S.A. **104**, 14215 (2007).
- [6] R. Kumar, J. R. Schmidt, and J. L. Skinner, J. Chem. Phys. **126**, 204107 (2007).
- [7] R. H. Henchman and S. J. Irudayam, J. Phys. Chem. B **114**, 16792 (2010).
- [8] C. J. Fecko, J. J. Loparo, S. T. Roberts, and A. Tokmakoff, J. Chem. Phys. **122**, 54506 (2005).
- [9] J. J. Loparo, C. J. Fecko, J. D. Eaves, S. T. Roberts, and A. Tokmakoff, Phys. Rev. B **70**, 1 (2004).
- [10] C. J. Fecko, J. D. Eaves, J. J. Loparo, A. Tokmakoff, and P. L. Geissler, Science **301**, 1698 (2003).
- [11] E. W. Castner, Y. J. Chang, Y. C. Chu, and G. E. Walrafen, J. Chem. Phys. **102**, 653 (1995).
- [12] I. Ohmine, J. Phys. Chem. **99**, 6767 (1995).
- [13] N. Agmon, Chem. Phys. Lett. **244**, 456 (1995).
- [14] C. J. T. d. Grotthuss, Ann. Chim. LVIII **54**, (1806).
- [15] S. T. Roberts, K. Ramasesha, and A. Tokmakoff, Acc. Chem. Res. **42**, 1239 (2009).
- [16] J. R. Schmidt, S. T. Roberts, J. J. Loparo, A. Tokmakoff, M. D. Fayer, and J. L. Skinner, Chem. Phys. **341**, 143 (2007).
- [17] F. Paesani, S. S. Xantheas, and G. A. Voth, The Journal of Physical Chemistry. B **113**, 13118 (2009).
- [18] F. Paesani and G. A. Voth, The Journal of Chemical Physics **132**, 014105 (2010).
- [19] F. Paesani, J. Phys. Chem. A **115**, 6861 (2011).
- [20] P. L. Silvestrelli, M. Bernasconi, and M. Parrinello, Chem. Phys. Lett. **277**, 478 (1997).
- [21] J. L. Skinner, Mol. Phys. **106**, 225 (2008).
- [22] B. M. Auer and J. L. Skinner, J. Chem. Phys. **128**, 224511 (2008).

- [23] J. D. Eaves, J. J. Loparo, C. J. Fecko, S. T. Roberts, A. Tokmakoff, and P. L. Geissler, *Proc. Natl. Acad. Sci. U.S.A.* **102**, 13019 (2005).
- [24] J. D. Eaves, A. Tokmakoff, and P. L. Geissler, *J. Phys. Chem. A* **109**, 9424 (2005).
- [25] J. B. Asbury, T. Steinel, C. Stromberg, S. A. Corcelli, C. P. Lawrence, J. L. Skinner, and M. D. Fayer, *J. Phys. Chem. A* **108**, 1107 (2004).
- [26] T. Hayashi, T. L. C. Jansen, W. Zhuang, and S. Mukamel, *J. Phys. Chem. A* **109**, 64 (2005).
- [27] C. P. Lawrence and J. L. Skinner, *J. Chem. Phys.* **118**, 264 (2003).
- [28] K. B. Møller, R. Rey, and J. T. Hynes, *J. Phys. Chem. A* **108**, 1275 (2004).
- [29] C. J. Fecko, J. J. Loparo, and A. Tokmakoff, *Opt. Commun.* **241**, 521 (2004).
- [30] J. D. Eaves, J. J. Loparo, C. J. Fecko, S. T. Roberts, A. Tokmakoff, and P. L. Geissler, *Proceedings of the National Academy of Sciences of the United States of America* **102**, 13019 (2005).
- [31] J. J. Loparo, S. T. Roberts, and A. Tokmakoff, *J. Chem. Phys.* **125**, 194522 (2006).
- [32] D. Laage and J. T. Hynes, *J. Phys. Chem. B* **112**, 14230 (2008).
- [33] D. Laage and J. T. Hynes, *Science* **311**, 832 (2006).
- [34] M. Ji and K. J. Gaffney, *J. Chem. Phys.* **134**, 044516 (2011).
- [35] M. Ji, M. Odellius, and K. J. Gaffney, *Science* **328**, 1003 (2010).
- [36] K. Ramasesha, S. T. Roberts, R. A. Nicodemus, A. Mandal, and A. Tokmakoff, *J. Chem. Phys.* **135**, 054509 (2011).
- [37] A. Pakoulev, Z. Wang, and D. D. Dlott, *Chem. Phys. Lett.* **371**, 594 (2003).
- [38] J. Lindner, D. Cringus, M. S. Pshenichnikov, and P. Vöhringer, *Chem. Phys.* **341**, 326 (2007).
- [39] J. Lindner, P. Vöhringer, M. S. Pshenichnikov, D. Cringus, D. A. Wiersma, and M. Mostovoy, *Chem. Phys. Lett.* **421**, 329 (2006).
- [40] Z. Wang, A. Pakoulev, Y. Pang, and D. D. Dlott, *J. Phys. Chem. A* **108**, 9054 (2004).
- [41] O. F. A. Larsen and S. Woutersen, *J. Chem. Phys.* **121**, 12143 (2004).

- [42] M. L. Cowan, B. D. Bruner, N. Huse, J. R. Dwyer, B. Chugh, E. T. J. Nibbering, T. Elsaesser, and R. J. D. Miller, *Nature* **434**, 199 (2005).
- [43] N. Huse, S. Ashihara, E. T. J. Nibbering, and T. Elsaesser, *Chem. Phys. Lett.* **404**, 389 (2005).
- [44] J. C. Deak, S. T. Rhea, L. K. Iwaki, and D. D. Dlott, *J. Phys. Chem. A* **104**, 4866 (2000).
- [45] D. Kraemer, M. L. Cowan, A. Paarmann, N. Huse, E. T. J. Nibbering, T. Elsaesser, and R. J. D. Miller, *Proc. Natl. Acad. Sci. U.S.A.* **105**, 437 (2008).
- [46] A. J. Lock and H. J. Bakker, *J. Chem. Phys.* **117**, 1708 (2002).
- [47] S. Ashihara, N. Huse, A. Espagne, E. T. J. Nibbering, and T. Elsaesser, *J. Phys. Chem. A* **111**, 743 (2007).
- [48] T. L. C. Jansen, B. M. Auer, M. Yang, and J. L. Skinner, *J. Chem. Phys.* **132**, 224503 (2010).
- [49] T. Yagasaki and S. Saito, *J. Chem. Phys.* **134**, 184503 (2011).
- [50] B. M. Auer and J. L. Skinner, *J. Chem. Phys.* **128**, 224511 (2008).
- [51] A. Paarmann, T. Hayashi, S. Mukamel, and R. J. D. Miller, *J. Chem. Phys.* **130**, 204110 (2009).
- [52] C. Falvo, B. Palmieri, and S. Mukamel, *J. Chem. Phys.* **130**, 184501 (2009).
- [53] S. Woutersen and H. J. Bakker, *Nature* **402**, 507 (1999).
- [54] M. Eigen, *Angew. Chem.* **3**, 1 (1964).
- [55] R. Janoschek, E. G. Weidemann, H. Pfeiffer, and G. Zundel, *J. Am. Chem. Soc.* **94**, 2387 (n.d.).
- [56] T. J. F. Day, A. V. Soudackov, M. Čuma, U. W. Schmitt, and G. A. Voth, *J. Chem. Phys.* **117**, 5839 (2002).
- [57] R. Vuilleumier and D. Borgis, *J. Chem. Phys.* **111**, 4251 (1999).
- [58] M. E. Tuckerman, K. Laasonen, M. Sprik, and M. Parrinello, *J. Chem. Phys.* **103**, 150 (1995).
- [59] D. Borgis, G. Tarjus, and H. Azzouz, *J. Chem. Phys.* **97**, 1390 (1992).

- [60] H. Lapid, N. Agmon, M. K. Petersen, and G. A. Voth, *J. Chem. Phys.* **122**, 14506 (2005).
- [61] C. Knight and G. A. Voth, *Accounts of Chemical Research* **45**, 101 (2012).
- [62] D. Marx, M. E. Tuckerman, J. Hutter, and M. Parrinello, **397**, 601 (1999).
- [63] J. M. Headrick, E. G. Diken, R. S. Walters, N. I. Hammer, R. A. Christie, J. Cui, E. M. Myshakin, M. A. Duncan, M. A. Johnson, and K. D. Jordan, *Science (New York, N.Y.)* **308**, 1765 (2005).
- [64] K. R. Asmis, N. L. Pivonka, G. Santambrogio, M. Brümmer, C. Kaposta, D. M. Neumark, and L. Wöste, *Science (New York, N.Y.)* **299**, 1375 (2003).
- [65] J.-W. Shin, N. I. Hammer, E. G. Diken, M. A. Johnson, R. S. Walters, T. D. Jaeger, M. A. Duncan, R. A. Christie, and K. D. Jordan, *Science (New York, N.Y.)* **304**, 1137 (2004).
- [66] A. Botti, F. Bruni, S. Imberti, M. A. Ricci, and A. K. Soper, *J. Chem. Phys.* **121**, 7840 (2004).
- [67] S. T. Roberts, P. B. Petersen, K. Ramasesha, A. Tokmakoff, I. S. Ufimtsev, and T. J. Martinez, *Proc. Natl. Acad. Sci. U.S.A.* **106**, 15154 (2009).
- [68] S. T. Roberts, K. Ramasesha, P. B. Petersen, A. Mandal, and A. Tokmakoff, *J. Phys. Chem. A* **115**, 3957 (2011).
- [69] J. Xu, Y. Zhang, and G. A. Voth, *J. Phys. Chem. Lett.* **2**, 81 (2011).
- [70] J. Kim, U. W. Schmitt, J. A. Gruetzmacher, G. A. Voth, and N. E. Scherer, *J. Chem. Phys.* **116**, 737 (2002).

Chapter 2

Calculation of the third-order nonlinear response function

2.1 Introduction

Measuring frequency fluctuations on ultrafast timescales is critical to understanding the dynamics of aqueous systems, since vibrational frequencies in condensed phase are sensitive reporters of the local structural environment. Nonlinear infrared spectroscopy is a powerful time-resolved technique that can measure frequency fluctuations on fast timescales. Through multiple light-matter interactions, nonlinear infrared spectroscopy has the ability to initially tag specific vibrational transitions and follow their evolution as a function of time. As a result, it can disentangle multiple contributions to congested and broad infrared line shapes that are present in systems such as water. This technique provides direct control over many time variables and can hence monitor the correlation between initial (excited) and final (detected) states of a system.

The simplest of such correlations is described by the frequency correlation function $C(t) = \langle \delta\omega(t)\delta\omega(0) \rangle$, where $\delta\omega(t) = \omega(t) - \langle \omega \rangle$. It represents the probability of measuring a frequency $\omega(t)$ at a certain time provided the frequency was at $\omega(0)$ at time zero. Nonlinear spectroscopy can probe phenomena such as spectral diffusion, where an initially excited vibration changes its frequency as the oscillator samples different parts of its environment. This manifests in a nonlinear infrared spectrum as a loss of frequency correlation. Furthermore, nonlinear spectroscopy can probe chemical exchange, where, for instance, an oscillator that is initially non-covalently bound to another molecule shifts its frequency at a later time when the bound complex cleaves. This technique can also measure vibrational coupling by exciting a vibration at a certain frequency and detecting it at a different frequency at zero time delay. With careful analysis of nonlinear spectra, we can also deduce whether the coupled vibrational mode is correlated or anti-correlated with the excited mode. Combined with polarization sensitive probing, nonlinear spectra can also reveal orientational correlations.

In this thesis, I discuss the use of third-order nonlinear spectroscopy, or four-wave mixing, to understand vibrational dynamics in water and aqueous acids. Third-order spectroscopy uses a sequence of three resonant pulses to coherently excite vibrations in a sample to drive the emission of the third order polarization. The third-order polarization can be detected as a function of time or frequency or both to gather information about the system. There are various flavors of third-order infrared spectroscopy that each measures different properties of the system. Pump-probe spectroscopy, by far the most commonly used third-order technique, can track the relaxation of non-equilibrium vibrational populations and can probe the relaxation of orientational correlations when coupled to

polarization-sensitive detection. Three pulse echo peak shift spectroscopy on the other hand can measure the decay of the frequency correlation function, and can hence report on the spectral diffusion dynamics. The most powerful of these techniques is two-dimensional infrared (2D IR) spectroscopy [1–3], which can resolve both the excitation and detection frequencies with high time resolution and can hence measure spectral diffusion, vibrational coupling and chemical exchange dynamics with high fidelity.

However, deducing microscopic dynamics from ultrafast nonlinear vibrational spectra is complicated, and often relies on either molecular dynamics simulations with mixed quantum-classical modeling of spectra or fits to experimental spectra using phenomenological models. Methodologies for extracting experimental observables such as transition dipole moment and transition frequencies from microscopic quantities are required for making this connection. In this chapter, I present a discussion of the third-order nonlinear response function starting from a time-dependent Hamiltonian for the system. In the process, I also outline various approximations that can be used in calculating the response function, and discuss their effects on the calculated spectroscopy. This chapter will serve as background material for the subsequent chapters of the thesis, where I use spectroscopic modeling and concepts presented in this chapter to analyze nonlinear infrared spectra of water and acids.

2.2 Nonlinear response function

A response function is a measure of how a system reacts to interactions with an electromagnetic field, which is reflected in changes to the dipole moment and vibrational

frequencies of the system. Interactions of the liquid with infrared light fields result in transitions between vibrational states that evolve with time. In order to describe these interactions, we first start by writing down the time-dependent Hamiltonian of the process [4]:

$$H_{total}(t) = H_{sample} + H_{int}(t) \quad (2-1)$$

Here, H_{sample} describes the liquid, and H_{int} describes the interaction of the light field with the liquid. The part of the liquid that we probe using the light fields can then be defined as the system. We can consider its surroundings that do not directly interact with the electromagnetic field to be the bath, and assume an interaction between the system and the bath. In this formulation, we neglect the quantum Hamiltonian of the light field and just focus on the influence of the light field on the sample. Now, H_{sample} can be expressed as [5]:

$$H_{sample} = H_S + H_B + H_{SB}, \quad (2-2)$$

where, H_S is the system Hamiltonian which is a function of the system coordinates, H_B is the bath Hamiltonian which is a function of the bath coordinates, and H_{SB} describes the system-bath interactions. Many of the models commonly used in nonlinear spectroscopy treat the system and the bath phenomenologically. Analytically solvable expressions of spectroscopic observables are deduced by using models such as the Spin-Boson and Brownian Oscillator to treat a two-level system coupled to a quantum harmonic bath [4,6–8]. However, these models are limited by the approximations that go into them, such as assuming that the frequency fluctuations of the system follow Gaussian statistics (second cumulant approximation) and that the system transition dipole moment is

independent of the bath degrees of freedom (Condon approximation). Moreover, they do not rigorously treat relaxation processes, since the system states are assumed to be independently coupled to a harmonic bath. These models often do not offer direct atomistic insight to the observed spectroscopy, making it harder to use them as interpretive tools. To overcome these limitations, we use the Hamiltonian described in equation 2-2 to calculate spectroscopy from classical molecular dynamics simulations. This approach treats the system to be the only quantum mechanical quantity and its Hamiltonian is written as a gas-phase Morse oscillator. Its interaction with the bath is treated perturbatively [5] or using frequency maps from density functional theory calculations [9–15] on clusters extracted from simulations. The bath is treated classically and H_B is derived from the force field used in the simulations. In the simulation work presented in Chapter 5, the interaction between the system and the bath, H_{SB} is electrostatic and is treated as a perturbation to the system Hamiltonian.

We now use the dipole approximation to describe the light-matter interaction Hamiltonian, H_{int} . Such an approximation allows us to treat the dipole moment as being driven by the electric field of the incident electromagnetic pulses [16]. The H_{int} term can therefore be represented as a dot product:

$$H_{int}(t) = -\boldsymbol{\mu}(t) \cdot \mathbf{E}(\mathbf{r}, t) \quad (2-3)$$

In equation 2-3, $\boldsymbol{\mu}(t)$ is the transition dipole operator that is both a function of system and bath coordinates, and $\mathbf{E}(\mathbf{r}, t)$ is the oscillating electric field of the interacting light pulses as a function of spatial and temporal coordinates.

We now invoke the Liouville-von Neumann equation to express the time-dependence of the density matrix of the system, ρ .

$$i\hbar \frac{\partial \rho(t)}{\partial t} = [H_{total}, \rho(t)] \quad (2-4)$$

The $\rho(t)$ and $H_{int}(t)$ can be expressed in the interaction picture as,

$$\rho_I(t) = \exp\left(\frac{iH_{sample}t}{\hbar}\right) \rho(t) \exp\left(-\frac{iH_{sample}t}{\hbar}\right), \quad (2-5a)$$

$$\text{and, } H_I(t) = \exp\left(\frac{iH_{sample}t}{\hbar}\right) H_{int}(t) \exp\left(-\frac{iH_{sample}t}{\hbar}\right) \quad (2-5b)$$

This allows us to re-write equation 2-4 as,

$$i\hbar \frac{\partial \rho_I(t)}{\partial t} = [H_I(t), \rho_I(t)], \quad (2-6)$$

This equation can be solved by integrating both sides with respect to time and iteratively substituting the result into itself, until the desired order in the density matrix is achieved.

In general, the n th order contribution to the density matrix can be written as [16],

$$\rho_I^{(n)}(t) = \left(\frac{-i}{\hbar}\right)^n \int_{-\infty}^t dt_n \int_{-\infty}^{t_n} dt_{n-1} \dots \int_{-\infty}^{t_2} dt_1 \left[H_I(t_n), \left[\dots, \left[H_I(t_1), \rho_I^{(0)} \right] \right] \right] \quad (2-7)$$

This density matrix represents the response of the liquid to n interacting light fields separated in time with respect to each other, and contains n nested commutators with the equilibrium density matrix. A full solution to equation 2-6 is the sum of all the orders of the time-dependent density matrix.

Now, the first and third-order density matrices, $\rho^{(1)}(t)$ and $\rho^{(3)}(t)$ can be expressed as:

$$\rho_i^{(1)}(t) = \left(\frac{-i}{\hbar} \right) \int_{-\infty}^t dt_1 [H_I(t_1), \rho_i^{(0)}] \quad (2-8)$$

$$\rho_i^{(3)}(t) = \left(\frac{-i}{\hbar} \right)^3 \int_{-\infty}^t dt_3 \int_{-\infty}^{t_3} dt_2 \int_{-\infty}^{t_2} dt_1 [H_I(t_3), [H_I(t_2), [H_I(t_1), \rho_i^{(0)}]]] \quad (2-9)$$

Here, $\rho_i^{(0)} = \rho_{eq}$, the equilibrium density matrix. The nonlinear polarization of the sample can be expressed as a sum of all the orders in the polarization. In the time domain, the nonlinear polarization is a trace over the density matrix of the relevant order and the dipole moment operator in the interaction picture [16]:

$$\mathbf{P}(t) = \sum_{i=0}^{\infty} \mathbf{P}^{(i)}(t) = \text{Tr}(\mu_i(t)\rho_i^{(0)}(t)) + \text{Tr}(\mu_i(t)\rho_i^{(1)}(t)) + \text{Tr}(\mu_i(t)\rho_i^{(2)}(t)) + \text{Tr}(\mu_i(t)\rho_i^{(3)}(t)) + \dots \quad (2-10)$$

Equation 2-11 shows the frequency domain representation of nonlinear polarization, where each order of the polarization is a product of the susceptibility (χ) and the electric field (\mathbf{E}) to the power equal to the order of the term.

$$\mathbf{P}(\omega) = \sum_{i=0}^{\infty} \mathbf{P}^{(i)} = \chi(\omega)^{(0)} + \chi(\omega)^{(1)} \cdot \mathbf{E}(\omega) + \chi(\omega)^{(2)} \cdot \mathbf{E}(\omega)^2 + \chi(\omega)^{(3)} \cdot \mathbf{E}(\omega)^3 + \dots \quad (2-11)$$

By substituting equation 2-8 and 2-9 into equation 2-10, and using the expression for H_{int} shown in equation 2-3, the linear and third-order terms in the polarization can be expressed as [6],

$$P^{(1)}(t) = \int_0^{\infty} dt_1 \mathbf{R}^{(1)}(t_1) \mathbf{E}(t-t_1) \quad (2-12)$$

$$P^{(3)}(t) = \int_0^{\infty} dt_3 \int_0^{\infty} dt_2 \int_0^{\infty} dt_1 \mathbf{R}^{(3)}(t_3, t_2, t_1) \mathbf{E}_a(t-t_3) \mathbf{E}_b(t-t_3-t_2) \mathbf{E}_c(t-t_3-t_2-t_1), \quad (2-13)$$

where, $\mathbf{R}^{(1)}(t_1)$ and $\mathbf{R}^{(3)}(t_3, t_2, t_1)$ are the first and third-order response functions, respectively, and \mathbf{E} is the electric field envelope of the infrared pulses. We ignore $P^{(2)}$ since it has a negligible contribution in isotropic media. \mathbf{E}_a , \mathbf{E}_b and \mathbf{E}_c denote the three interaction time points separated in time by t_1 and t_2 , and t_3 is the delay between the third interaction with the sample and the time of detection. The electric field wavevectors are \mathbf{k}_a , \mathbf{k}_b and \mathbf{k}_c respectively, which are each defined by the \mathbf{k} vectors of the perturbing electric field, $\mathbf{E}(\mathbf{r}, t) = E(\mathbf{r}) \cdot \exp[-i(\omega t - \mathbf{k} \cdot \mathbf{r})] + c.c.$ Based on the geometry and time ordering of the a , b and c pulses, the third-order polarization is emitted in a phase matched direction along the resultant vector upon the appropriate addition of the \mathbf{k} vectors, $\mathbf{k}_{\text{sig}} = \pm \mathbf{k}_a \pm \mathbf{k}_b \pm \mathbf{k}_c$. Equation 2-13 accounts for the finite duration of the driving optical pulses by rigorously including the field envelopes in the description of the polarization. For delta function pulses, the integrals in equation 2-13 disappear, and the third order polarization turns out to be proportional to the third-order response function.

By comparing equations 2-13 and 2-11, it is interesting to note that the response function can be thought of as the time domain analog of the susceptibility of the system. Using equations 2-11 and 2-13, the third-order response function can be written as [16],

$$\mathbf{R}^{(3)}(t_3, t_2, t_1) = \left(\frac{i}{\hbar}\right)^3 \theta(t_1)\theta(t_2)\theta(t_3) \left\langle \left[\left[\left[\boldsymbol{\mu}(t_3 + t_2 + t_1), \boldsymbol{\mu}(t_2 + t_1) \right], \boldsymbol{\mu}(t_1) \right], \boldsymbol{\mu}(0) \right] \right\rangle \quad (2-14)$$

and the first order response function is simply,

$$\mathbf{R}^{(1)}(t_1) = \left(\frac{i}{\hbar}\right) \theta(t_1) \left\langle \left[\boldsymbol{\mu}(t_1), \boldsymbol{\mu}(0) \right] \right\rangle \quad (2-15)$$

Here, the angular brackets represent an ensemble average over the system and bath degrees of freedom and $\theta(t)$ are step functions to impose causality in the field-matter interactions. The emitted signal field is related to the time derivative of the third-order polarization, which can directly be detected or can be heterodyned with a reference pulse to extract phase information.

Expanding the commutator in equation 2-14 yields eight terms, four of which are unique terms and the remaining four are complex conjugates. Equation 2-16 below shows the four unique contributions to the third order response for a set of eigenstates of H_S represented by the subscripts of i, j, k and l to the $\boldsymbol{\mu}$ variables, and P_i denotes the equilibrium probability that the population occupies state i . Each $\boldsymbol{\mu}$ term denotes the matrix element corresponding to the eigenstates of H_S denoted in the subscripts, and angular brackets now denote an ensemble average over the bath degrees of freedom and the summation is over the system eigenstates.

$$\begin{aligned}
\mathbf{R}_1 &= \sum_{i,j,k,l} P_i \left\langle \boldsymbol{\mu}_{ij}(t_1+t_2+t_3) \boldsymbol{\mu}_{jk}(t_1+t_2) \boldsymbol{\mu}_{kl}(t_1) \boldsymbol{\mu}_{li}(0) \right\rangle \\
\mathbf{R}_2 &= \sum_{i,j,k,l} P_i \left\langle \boldsymbol{\mu}_{ij}(t_1) \boldsymbol{\mu}_{jk}(t_1+t_2) \boldsymbol{\mu}_{kl}(t_1+t_2+t_3) \boldsymbol{\mu}_{li}(0) \right\rangle \\
\mathbf{R}_3 &= \sum_{i,j,k,l} P_i \left\langle \boldsymbol{\mu}_{lk}(t_1) \boldsymbol{\mu}_{kj}(t_1+t_2+t_3) \boldsymbol{\mu}_{ji}(t_1+t_2) \boldsymbol{\mu}_{il}(0) \right\rangle \\
\mathbf{R}_4 &= \sum_{i,j,k,l} P_i \left\langle \boldsymbol{\mu}_{lk}(t_1+t_2) \boldsymbol{\mu}_{kj}(t_1+t_2+t_3) \boldsymbol{\mu}_{ji}(t_1) \boldsymbol{\mu}_{il}(0) \right\rangle
\end{aligned} \tag{2-16}$$

By expanding each of the time-dependent dipole matrix elements to include the propagator (or time-evolution operator), $\boldsymbol{\mu}_{ij}(t) = e^{iH_i t/\hbar} \boldsymbol{\mu}_{ij} e^{-iH_j t/\hbar}$, we can re-write equation 2-16 as:

$$\begin{aligned}
\mathbf{R}_1 &= \sum_{i,j,k,l} P_i \left\langle e^{iH_i(t_1+t_2+t_3)/\hbar} \boldsymbol{\mu}_{ij} e^{-iH_j t_3/\hbar} \boldsymbol{\mu}_{jk} e^{-iH_k t_2/\hbar} \boldsymbol{\mu}_{kl} e^{-iH_l t_1/\hbar} \boldsymbol{\mu}_{li} \right\rangle \\
\mathbf{R}_2 &= \sum_{i,j,k,l} P_i \left\langle e^{iH_i t_1/\hbar} \boldsymbol{\mu}_{ij} e^{iH_j t_2/\hbar} \boldsymbol{\mu}_{jk} e^{iH_k t_3/\hbar} \boldsymbol{\mu}_{kl} e^{-iH_l(t_1+t_2+t_3)/\hbar} \boldsymbol{\mu}_{li} \right\rangle \\
\mathbf{R}_3 &= \sum_{i,j,k,l} P_i \left\langle e^{iH_i t_1/\hbar} \boldsymbol{\mu}_{lk} e^{iH_k(t_2+t_3)/\hbar} \boldsymbol{\mu}_{kj} e^{-iH_j t_3/\hbar} \boldsymbol{\mu}_{ji} e^{-iH_l(t_1+t_2)/\hbar} \boldsymbol{\mu}_{il} \right\rangle \\
\mathbf{R}_4 &= \sum_{i,j,k,l} P_i \left\langle e^{iH_i(t_1+t_2)/\hbar} \boldsymbol{\mu}_{lk} e^{iH_k t_3/\hbar} \boldsymbol{\mu}_{kj} e^{-iH_j(t_2+t_3)/\hbar} \boldsymbol{\mu}_{ji} e^{-iH_l t_1/\hbar} \boldsymbol{\mu}_{il} \right\rangle
\end{aligned} \tag{2-17}$$

For systems with a large number of accessed vibrational states, it becomes cumbersome to rigorously solve these equations. Experimentally manipulating phase matching conditions to isolate certain signals is an effective way to reduce the number of contributions to the response function and hence simplify calculations. However, it is also useful to make certain mathematical approximations [6,8,17–19] to the third-order response function. These approximations should be made based on the specific nature of the system. In the next section, I will outline the three of the most commonly used

approximations for calculating the response function, and discuss their validity for systems such as water and acids.

2.3 Approximations to the third-order response function

2.3.1 Condon approximation

The Condon approximation [6] assumes that the dipole matrix elements in 2-17 are independent of the bath degrees of freedom. This allows us to move the dipole operators outside of the ensemble average shown in equation 2-17, simplifying the response function calculation. While this is often a reasonable assumption to make in the case of electronic spectroscopy, previous work has shown that the Condon approximation is inappropriate to use for describing vibrational spectroscopy of systems such as water, since vibrations like the OH stretch are strongly influenced by the bath degrees of freedom reflected in the local hydrogen bonding environment [13,20–22].

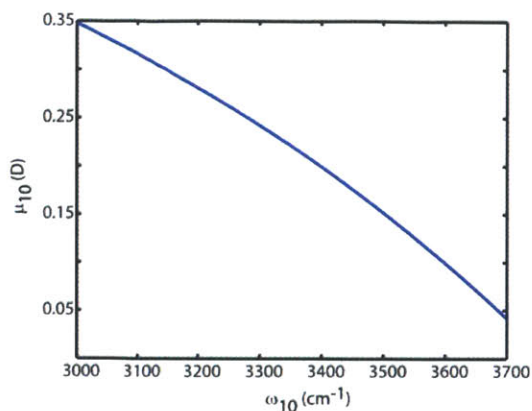


Figure 2-1: Variation of the transition dipole (in Debye) of the $v = 0$ to 1 transition of the OH stretch in HOD/D₂O with the fundamental OH stretching frequency (in cm⁻¹) [15]:

$$\mu_{10} = 1.8336 - (1.2973 \times 10^{-3})\omega_{10} + (4.7136 \times 10^{-7})\omega_{10}^2 - (6.8016 \times 10^{-11})\omega_{10}^3$$

In HOD/D₂O, it has been shown that the strength of the transition dipole varies greatly across the OH stretch lineshape owing to the non-Condon effect. Figure 2-1 displays the variation of the transition dipole of the $v = 0$ to 1 transition of the OH stretch vibration in HOD/D₂O with the OH stretching frequency. The magnitude of the transition dipole moment increases significantly with decreasing OH stretch frequency. We therefore rarely use this approximation for describing dynamics in water, since it yields nonlinear infrared spectra that look qualitatively different from experimental spectra.

2.3.2 Semiclassical approximation

The semiclassical approximation is useful to invoke when spectroscopic observables are calculated from semiclassical (or mixed quantum-classical) methods used in conjunction with classical molecular dynamics (MD) simulations. This approximation

assumes that the molecular dynamics are classical and that we can equate classical configurations with quantum frequencies and dipoles. Using this approximation, the spectroscopy can be described by classical frequency and dipole trajectories from MD simulations instead of having to calculate the response functions from the vibrational eigenstates of the system, which tends to be computationally expensive for systems with many degrees of freedom. In order to understand the semiclassical approximation, let us first look at the time-evolution operator in more detail. The time-evolution operator, $U(t, t_0)$ can be defined as the operator that acts upon a wavefunction at time t_0 to retrieve the wavefunction at time t [6]:

$$|\psi(t)\rangle = U(t, t_0)|\psi(t_0)\rangle \quad (2-18)$$

When equation 2-18 is substituted into the time-dependent Schrodinger equation, we obtain the following:

$$\frac{\partial}{\partial t} U(t, t_0) = -\frac{i}{\hbar} H_{\text{int}}(t)U(t, t_0) \quad (2-19)$$

Solving equation 2-19 keeping in mind that H_{int} is a time-dependent operator means that the solution to this equation is a time-ordered exponential in the Hamiltonian,

$$U(t, t_0) = \exp_+ \left[-\frac{i}{\hbar} \int_{t_0}^t dt' H_{\text{int}}(t') \right].$$

Equation 2-17 can be expanded in terms of time-

ordered exponentials, by inserting the identity operator, $\exp\left(\frac{-iH_t t}{\hbar}\right)\exp\left(\frac{iH_t t}{\hbar}\right) = 1$,

where necessary and using the equation [6],

$$\exp\left(\frac{-iH_i t}{\hbar}\right)\exp\left(\frac{iH_j t}{\hbar}\right) = \exp_+\left[-\frac{i}{\hbar}\int_0^t dt' H_{ij}(t')\right], \quad (2-20)$$

where, $H_{ij} = H_j - H_i$. Each of the response functions in 2-17 will then contain four time-ordered exponentials, making it extremely cumbersome to calculate.

The semiclassical approximation replaces the time-ordered exponential functions with ordinary exponentials, and substitutes each term in the response function by its classical analog therefore simplifying the response functions greatly and allowing us to input frequency and dipole trajectories from classical MD simulations directly. The third-order response functions can now be written as [6,19,23],

$$\begin{aligned} \mathbf{R}_1 &= \sum_{i,j,k,l} \rho_{ii}(0) \langle \mu_{ij}(t_1+t_2+t_3) \mu_{jk}(t_1+t_2) \mu_{kl}(t_1) \mu_{il}(0) \phi_{ijkl}^{(1)} \rangle \\ \mathbf{R}_2 &= \sum_{i,j,k,l} \rho_{ii}(0) \langle \mu_{ij}(t_1) \mu_{jk}(t_1+t_2) \mu_{kl}(t_1+t_2+t_3) \mu_{il}(0) \phi_{ijkl}^{(2)} \rangle \\ \mathbf{R}_3 &= \sum_{i,j,k,l} \rho_{ii}(0) \langle \mu_{lk}(t_1) \mu_{kj}(t_1+t_2+t_3) \mu_{ji}(t_1+t_2) \mu_{il}(0) \phi_{ijkl}^{(3)} \rangle \\ \mathbf{R}_4 &= \sum_{i,j,k,l} \rho_{ii}(0) \langle \mu_{lk}(t_1+t_2) \mu_{kj}(t_1+t_2+t_3) \mu_{ji}(t_1) \mu_{il}(0) \phi_{ijkl}^{(4)} \rangle \end{aligned} \quad (2-21)$$

where, $\mu(t)$ are the classical dipole trajectories and the $\phi_{ijkl}^{(n)}$ terms are called dephasing functions that are expressed as,

$$\begin{aligned}
\phi_{ijkl}^{(1)} &= \exp \left[-i \int_{t_1+t_2}^{t_1+t_2+t_3} \omega_{ji}(t') dt' - i \int_{t_1}^{t_1+t_2} \omega_{ki}(t') dt' - i \int_0^{t_1} \omega_{li}(t') dt' \right] \\
\phi_{ijkl}^{(2)} &= \exp \left[-i \int_{t_1+t_2}^{t_1+t_2+t_3} \omega_{lk}(t') dt' - i \int_{t_1}^{t_1+t_2} \omega_{kj}(t') dt' - i \int_0^{t_1} \omega_{li}(t') dt' \right] \\
\phi_{ijkl}^{(3)} &= \exp \left[-i \int_{t_1+t_2}^{t_1+t_2+t_3} \omega_{jk}(t') dt' + i \int_{t_1}^{t_1+t_2} \omega_{ki}(t') dt' + i \int_0^{t_1} \omega_{li}(t') dt' \right] \\
\phi_{ijkl}^{(4)} &= \exp \left[-i \int_{t_1+t_2}^{t_1+t_2+t_3} \omega_{jk}(t') dt' + i \int_{t_1}^{t_1+t_2} \omega_{lj}(t') dt' + i \int_0^{t_1} \omega_{li}(t') dt' \right]
\end{aligned} \tag{2-22}$$

Similarly, the first-order response function can be expressed as,

$$\mathbf{R}^{(1)} = \sum_{i,j} \rho_{ii}(0) \left\langle \mu_{ij}(t_1) \mu_{ji}(0) \exp \left[-i \int_0^{t_1} dt' \omega_{ji}(t') \right] \right\rangle \tag{2-23}$$

The semiclassical approximation treats the bath classically, and transition frequencies of the system are mapped onto classical variables such as the electric field of the bath, allowing us to generate frequency trajectories, $\omega(t)$. Classical instantaneous trajectories, $\omega(t)$ and $\mu(t)$, from MD simulations can serve as inputs to equations 2-21 through 2-23, allowing us to calculate nonlinear spectroscopy from simulations and compare with experimental spectra to gain atomistic insight and test simulation models [20,24–26]. It is also important to note that one can incorporate orientational information into equation 2-21 by obtaining the directionality of the dipole moment in the form of dipole trajectories along the x , y and z dimensions ($\mu_x(t)$, $\mu_y(t)$, $\mu_z(t)$) from MD simulations. This approach is used in Chapter 5 to calculate 2D IR and pump-probe anisotropy of HOD/D₂O, and is especially powerful for calculating polarization-sensitive nonlinear spectra [27], since

this obviates the need to treat orientation phenomenologically using spherical harmonics [8,28,29].

2.3.3 Second cumulant approximation

The second cumulant approximation is useful to make in the absence of classical trajectories, since truncating the time-ordered exponentials to second-order leads to expressions of the third-order response function that can be analytically solved based on experimental constraints [8].

This approximation uses the energy gap correlation function, which can be defined as,

$$C_{ge}(t-t_0) = \langle \delta\omega_{ge}(t)\delta\omega_{ge}(t_0) \rangle \quad (2-24)$$

where, $\omega_{ge} = \frac{E_e - E_g}{\hbar}$, and $\delta\omega_{ge}(t) = \omega_{ge}(t) - \langle \omega_{ge} \rangle$.

Upon invoking the Condon approximation and expanding the time-ordered exponential to second order, the first-order response function in equation 2-23 can be expressed as a function of the energy gap correlation function, average dipole moment and average transition frequencies, all of which can be constrained based on experiments [8]. After applying the Condon and second cumulant approximations, the first order response function can be written as,

$$\mathbf{R}^{(1)} = \sum_{i,j} \rho_{ii}(0) |\mu_{ji}|^2 \exp[-i\langle \omega_{ji} \rangle t_1 - g(t_1)] , \quad (2-25)$$

where, $g(t)$ is a quantum mechanical lineshape function,

$$g(t) = \int_0^t dt' (t-t') C_{ge} \quad (2-26)$$

Similar expressions for the third-order response can be found in the paper by Sung and Silbey [8].

One of the downsides of using this approximation is it assumes that Gaussian statistics govern the system fluctuations, and for systems that obey non-Gaussian dynamics, this formalism can allow us to calculate only average spectral diffusion timescales. This approximation is therefore not valid for water since the OH stretch frequencies undergo non-Gaussian fluctuations due to the fact that the OH stretch vibration is sensitive to its hydrogen bonding environment [5,30,31] and previous work has shown that water molecules participating in strained hydrogen bonds evolve rapidly compared to those in strong hydrogen bonds [24,25]. We therefore do not employ this approximation to describe vibrational dynamics in water presented in this thesis.

2.4 Third-order nonlinear spectroscopy

With the response function formalism at hand, we can now proceed to describe the various types of third-order nonlinear infrared spectroscopy. I will begin by using a simple two-level system, involving $v = 0$ and $v = 1$ vibrational states, as an example to describe the spectroscopy. After applying the semiclassical approximation, the third order response functions for a two-level system can be written as,

$$R_{\pm}^{(3)}(\tau_1, \tau_2, \tau_3) = \text{Re} \left[2 \left\langle \mu_{10}(\tau_1 + \tau_2 + \tau_3) \mu_{10}(\tau_1 + \tau_2) \mu_{10}(\tau_1) \mu_{10}(0) \exp \left[\pm i \int_0^{\tau_1} \omega_{10}(\tau) d\tau + i \int_{\tau_1 + \tau_2}^{\tau_1 + \tau_2 + \tau_3} \omega_{10}(\tau') d\tau' \right] \right\rangle \right] \quad (2-27)$$

The negative contribution to the response is from the rephasing signal, which is phase matched at $\mathbf{k}_R = -\mathbf{k}_a + \mathbf{k}_b + \mathbf{k}_c$, and the positive contribution is from the non-rephasing signal, $\mathbf{k}_{NR} = +\mathbf{k}_a - \mathbf{k}_b + \mathbf{k}_c$. If the three input light fields propagate along three corners of a square, the rephasing and non-rephasing signals propagate along the fourth corner. This beam geometry is called the boxcar or box geometry, which is commonly used to measure third-order signals. Switching the time ordering between the first two interactions helps us isolate the rephasing and non-rephasing contributions, where rephasing signals are emitted for $\tau_1 > 0$ and non-rephasing signals are emitted when $\tau_1 < 0$. The first pulse in these experiments creates a coherent superposition between $v = 0$ and $v = 1$ state (a “01” coherence). Oscillators exhibiting different vibrational frequencies (due to varying environments) first start vibrating in phase with a frequency related to the energy difference between the $v = 0$ and $v = 1$ states. Due to the distribution in vibrational frequencies, the oscillators dephase during τ_1 . At $t = \tau_1$, the second pulse then creates a population state either in $v = 1$ or $v = 0$, which decays with the characteristic vibrational energy relaxation time. During τ_2 (also called the waiting time), fluctuations of the solvent environment can lead to fluctuations in the $v = 0$ and $v = 1$ energies. If at $t = \tau_2$, the third pulse creates a “10” coherence that oscillates with the opposite phase during τ_3 relative to the τ_1 time period, the oscillators regain their phase relationship and emit a signal field called a vibrational echo at $t = \tau_3$. As the waiting time increases, the

rephasing signal becomes weaker since the phase of the different oscillators gets scrambled during τ_2 due to coupling with the bath. The non-rephasing signal contributes to the measured response when the first pulse and the third pulse both create a “01” coherence, such that the oscillators do not rephase by $t = \tau_3$. Figure 2-2 shows the rephasing and non-rephasing signals calculated for a two-level system. [It is worth noting here that in a pump-probe beam geometry, where the first two pulses are collinear with each other and the third-order signal is emitted along the direction of the third pulse, the rephasing and non-rephasing contributions cannot be separated.]

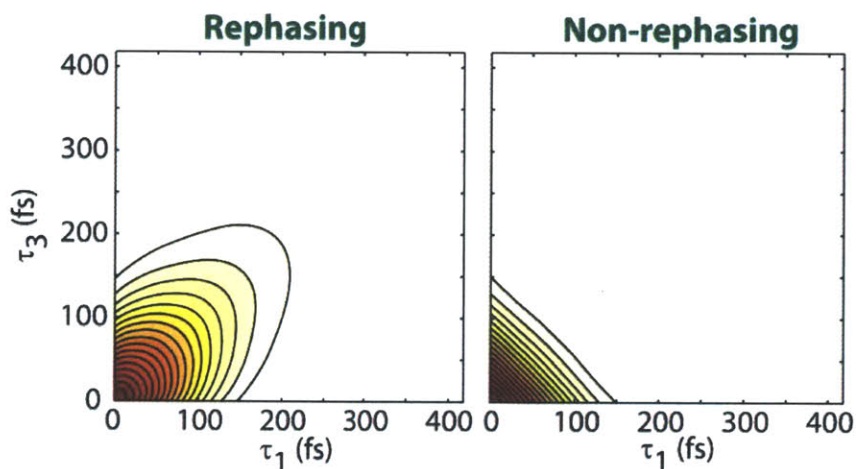


Figure 2-2: Rephasing (left) and non-rephasing (right) contributions as a function of τ_1 and τ_3 for a two-level system. The carrier frequency is neglected here, and the plot shows only the time-domain envelope for the two contributions. These were calculated using equation 2-21 by inputting MD simulation trajectories of ω_{10} and μ_{10} for HOD/D₂O at a waiting time of 120 fs. The non-Condon effect was included in this calculation [20].

Vibrations are inherently multi-level, and upon addition of other vibrational states, one has to consider more terms in the third-order response function due to additional Feynman pathways. For a three-level system, where the $v = 0, 1,$ and 2 states are accessed by the infrared pulses, the nonlinear response function contains an additional term:

$$R_{\pm}^{(3)}(\tau_1, \tau_2, \tau_3) = \text{Re} \left[2 \left\langle \mu_{10}(\tau_1 + \tau_2 + \tau_3) \mu_{10}(\tau_1 + \tau_2) \mu_{10}(\tau_1) \mu_{10}(0) \exp \left[\pm i \int_0^{\tau_1} \omega_{10}(\tau) d\tau + i \int_{\tau_1 + \tau_2}^{\tau_1 + \tau_2 + \tau_3} \omega_{10}(\tau') d\tau' \right] \right\rangle \right. \\ \left. - \left\langle \mu_{21}(\tau_1 + \tau_2 + \tau_3) \mu_{21}(\tau_1 + \tau_2) \mu_{10}(\tau_1) \mu_{10}(0) \exp \left[\pm i \int_0^{\tau_1} \omega_{10}(\tau) d\tau + i \int_{\tau_1 + \tau_2}^{\tau_1 + \tau_2 + \tau_3} \omega_{21}(\tau') d\tau' \right] \right\rangle \right] \quad (2-28)$$

In this case, the 1-2 transitions are anharmonically downshifted in frequency compared to the 0-1 transitions. The additional term in this expression accounts for the probed 1-2 induced absorption upon 0-1 excitation.

I will now describe three different kinds of third-order spectroscopies that are used in this thesis to study vibrational dynamics in water and acids – three pulse echo peak shift spectroscopy, two-dimensional infrared spectroscopy and pump-probe spectroscopy.

2.4.1 Three pulse vibrational echo peak shift (PS)

The three pulse echo peak shift technique is used for characterizing the spectral diffusion dynamics, and is most effective when applied to systems with a single vibrational transition such as the OH stretch vibration in HOD/D₂O [28]. The three pulse echo signal can be expressed as [32,33],

$$I_{echo}(\tau_1, \tau_2) \propto \int_{-\infty}^{\infty} |\mathbf{E}_{sig}(\tau_1, \tau_2, \tau_3)|^2 d\tau_3, \quad (2-29)$$

where, \mathbf{E}_{sig} is the time derivative of $\mathbf{P}^{(3)}$. In a PS measurement, the rephasing response is integrated along τ_3 and the location of the peak of echo is measured in τ_1 at different τ_2 . Figure 2-3 displays the pulse sequence used for measuring three-pulse vibrational echo. In the PS measurement, we do not scan the τ_3 delay but only the τ_1 and τ_2 delays, making it a fast and efficient way of extracting the spectral diffusion dynamics.

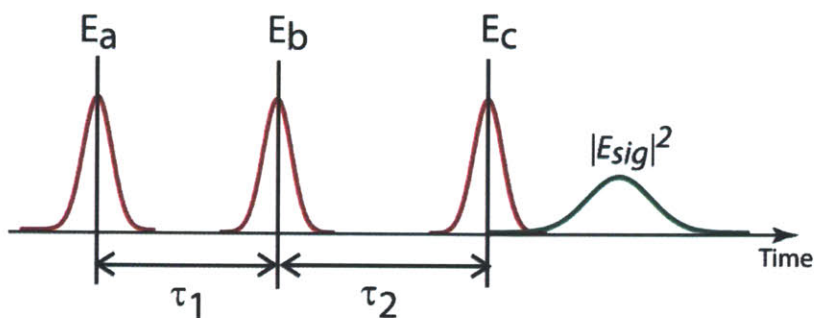


Figure 2-3: The pulse sequence used in measuring the three-pulse vibrational echo for a waiting time τ_2 . This is a homodyne measurement, where the third-order signal is not interfered with a reference pulse, and hence lacks phase information. The third-order signal is detected on a square law single-channel detector. In a PS measurement, the location of the peak of the vibrational echo in τ_1 is measured for different τ_2 values in order to map out the timescale for spectral diffusion.

The decay of the PS signal can be used to extract the frequency correlation function by iteratively finding the correlation function that yields a PS signal that best fits the experimental data [32]. In the past, the PS signal was calculated from an input correlation

function following the approach developed by Sung and Silbey [8], which makes both the Condon and the second cumulant approximations [28]. In Chapter 3, I will outline an alternative approach for calculating PS that stops at the semiclassical approximation, uses classical frequency and dipole trajectories, and includes non-Condon effects. Figure 2-4 displays the three pulse echo calculated for correlated frequency and dipole trajectories at different waiting times and the corresponding three pulse echo peak shift decay.

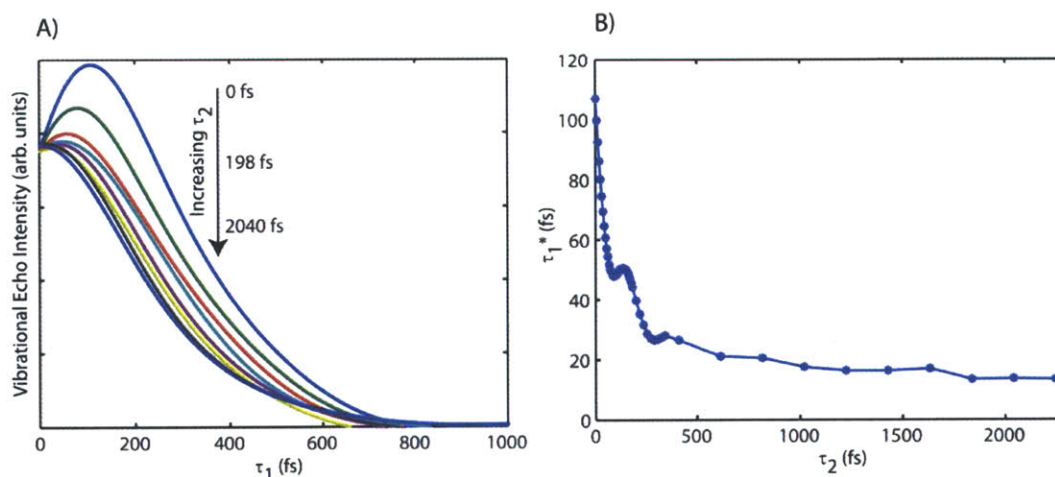


Figure 2-4: a) Three-pulse echo plotted as a function of τ_1 at different waiting times, calculated for correlated frequency and dipole trajectories. Rephasing signals were calculated from equation 2-21, and integrated across the τ_3 dimension to obtain the figure on the left. b) Three pulse echo peak shift calculated from the data in a), by finding the peak of the echo and plotting it as a function of waiting time.

2.4.2 Two-dimensional infrared spectroscopy (2D IR)

2D IR spectroscopy is a technique that uses three infrared pulses to drive the emission of the third-order signal. In this measurement, the third-order signal is interfered

with a reference pulse (called the local oscillator) to extract frequency and phase information. Effectively, all three time delays are scanned in this measurement, but the experiment is often implemented as a mixed time-frequency detection, where the heterodyned third-order signal is dispersed in frequency instead of scanning the third time delay [15,34], and only the first time delay is numerically Fourier transformed to the frequency domain. The pulse sequence for this experiment is displayed in Figure 2-5.

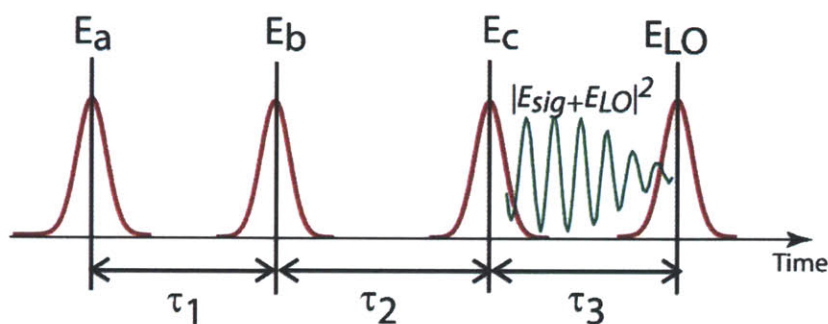


Figure 2-5: Pulse sequence for 2D IR spectroscopy. The third-order signal is overlapped with the local oscillator (E_{LO}) and the square of the sum of the signal and local oscillator is detected. Since this is a heterodyned measurement, we can extract phase information. The τ_3 dimension can be scanned and then Fourier transformed to obtain the ω_3 dimension of the 2D spectrum, or the ω_3 dimension can be generated by just spectrally dispersing the signal and local oscillator interference onto an array detector. In this thesis, we use the latter approach.

Upon adding the rephasing and non-rephasing contributions and Fourier transforming along the τ_1 and τ_3 dimensions we obtain a purely absorptive 2D IR spectrum (also known as correlation spectrum) in ω_1 and ω_3 as a function of the waiting time τ_2 [35].

Figure 2-6 shows the Fourier transformed rephasing and non-rephasing spectra of the OH stretch of HOD/D₂O from MD simulations, and the 2D IR correlation spectrum. Spreading the third order response across two frequency axes comes with an enormous advantage for studying spectral diffusion, vibrational coupling and chemical exchange dynamics.

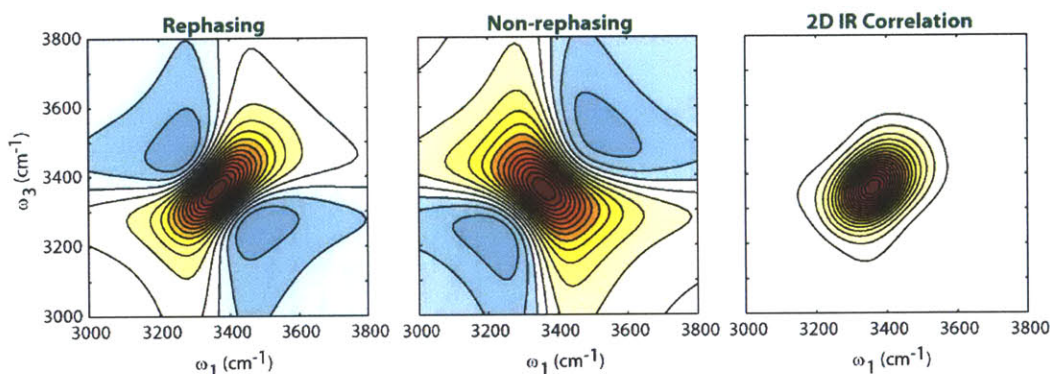


Figure 2-6: Rephasing (left), non-rephasing (middle) and correlation (right) spectra of the OH stretch of HOD/D₂O from MD simulations, calculated for $\tau_2 = 120$ fs. Only the $v = 0$ and $v = 1$ vibrational states of the OH stretch were included in this calculation.

A 2D IR spectrum is related to the joint probability of exciting an oscillator at a frequency ω_1 and detecting it at ω_3 after a waiting time τ_2 . For a three-level system, peaks in the 2D IR spectrum appear as doublets – the 0-1 ground state bleach and the 1-2 induced absorption are separated in the ω_3 dimension by the vibrational anharmonicity, and carry opposite signs. The diagonal peaks in a 2D IR surface represent the peaks present in a linear infrared spectrum. At waiting times less than the correlation time for

the system, these peaks appear diagonally elongated (inhomogeneous lineshape) since the frequencies in ω_1 are correlated with those in ω_3 . As the frequency correlation decays, at waiting times past the correlation time, we observe a homogeneous or symmetric lineshape representing a complete loss in ω_1 - ω_3 correlation. Spectral diffusion can be extracted from 2D IR spectra by calculating parameters such as the ellipticity of the lineshape, the anti-diagonal linewidth, the center line slope, or the slope of the nodal line between the 0-1 and 1-2 peaks as a function of waiting time [36]. Off-diagonal peaks in a 2D IR spectrum arise either due to vibrational coupling (when present at $\tau_2 = 0$) [3,10,37] or due to chemical exchange between distinct species [18,38], in which case the cross-peaks grow with waiting time. Analyzing how the cross-peak lineshapes compare to the diagonal peaks can tell us about whether two vibrations are correlated (diagonally elongated cross-peaks), anti-correlated (anti-diagonally elongated cross-peaks), or uncorrelated (homogeneous cross-peaks at early waiting times).

Orientational information can also be gathered from 2D IR spectroscopy by orienting the polarization of the first two beams parallel and perpendicular with respect to the third beam and the local oscillator. Using 2D IR surfaces in the parallel and perpendicular polarization geometries, we have, for the first time, been able to measure and analyze 2D IR anisotropy on water. 2D IR anisotropy can be calculated as,

$$r(\omega_1, \omega_3; \tau_2) = \frac{S_{\parallel}(\omega_1, \omega_3; \tau_2) - S_{\perp}(\omega_1, \omega_3; \tau_2)}{S_{\parallel}(\omega_1, \omega_3; \tau_2) + 2S_{\perp}(\omega_1, \omega_3; \tau_2)} \quad (2-30)$$

The quantity $r(\omega_1, \omega_3; \tau_2)$ is sensitive to both ω_1 and ω_3 at every waiting time [27]. In equation 2-23, S_{\parallel} and S_{\perp} corresponded to the third-order signal detected at parallel and

perpendicular relative polarizations, respectively. The method for measuring and analyzing 2D IR anisotropy is described in detail in Chapter 5.

2.4.3 Pump-probe spectroscopy (PP)

Pump-probe spectroscopy uses two beams to extract population and orientational dynamics of the system. The first, pump, beam causes two simultaneous interactions with the sample ($\tau_1 = 0$) immediately creating a population state, in the limit of delta function pulses. The probe beam then interrogates the sample after a waiting time τ_2 . This is a self-heterodyned measurement since the third order signal is emitted along the direction of the probe beam, and the probe field also acts as the local oscillator. Figure 2-7 shows the pulse ordering for a pump-probe experiment. PP spectroscopy is sensitive to population dynamics during the pump-probe waiting time delay, τ_2 . As τ_2 is increased, the intensity of the third order signal drops based on the characteristic vibrational energy relaxation timescale of the system. The pump-probe signal can either be detected using a spectrometer at different time delays, which offers frequency resolution in ω_3 , or can be detected using a single-channel detector that integrates over the detection frequency.

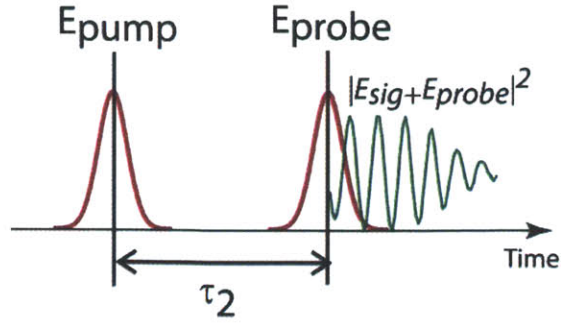


Figure 2-7: Pulse sequence for pump-probe spectroscopy. Two interactions with E_{pump} creates a population state that evolves during the waiting time. E_{probe} interrogates the sample after τ_2 , and acts to heterodyne the third-order signal, which can then be detected using a spectrometer or a single-channel detector.

We can obtain orientational information from pump-probe spectroscopy by rotating the polarization of the pump to be parallel and perpendicular to the polarization of the probe [27,39]. When the pump-probe signal is dispersed in frequency, the measurement allows us to calculate frequency-dependent pump-probe anisotropy,

$$r(\omega_3, \tau_2) = \frac{S_{\parallel}(\omega_3, \tau_2) - S_{\perp}(\omega_3, \tau_2)}{S_{\parallel}(\omega_3, \tau_2) + 2S_{\perp}(\omega_3, \tau_2)}, \quad (2-31)$$

which is proportional to the second Legendre polynomial orientational correlation

function, $P_2(\langle \boldsymbol{\mu}(\tau_2) \cdot \boldsymbol{\mu}(0) \rangle) = \left\langle \frac{3 \cos^2 \theta - 1}{2} \right\rangle$, where θ is the angle between the molecular

dipole vector at $\tau_2 = 0$ and the dipole vector at a subsequent time point. The decay of pump-probe anisotropy reflects the loss of orientational correlation. On the other hand, by orienting the pump polarization at 54.7° (magic angle) with respect to that of the probe, one can selectively diminish the contribution of reorientation to the observed pump-probe

signal [29]. This can be understood by realizing that the magic angle represents the intersection of the excited $\cos^2\theta$ angular distribution with an isotropic spherical angular distribution. The magic angle pump-probe therefore is sensitive only to the vibrational population dynamics.

Acknowledgements

I thank Michael Reppert for his comments and suggestions on the material presented in this chapter.

References

- [1] M. Cho, Chem. Rev. **108**, 1331 (2008).
- [2] D. M. Jonas, Ann. Rev. Phys. Chem. **54**, 425 (2003).
- [3] M. Khalil, N. Demirdoven, and A. Tokmakoff, J. Phys. Chem. A **107**, 5258 (2003).
- [4] S. Mukamel and R. F. Loring, J. Opt. Soc. Am. B **3**, 595 (1986).
- [5] J. D. Eaves, A. Tokmakoff, and P. L. Geissler, J. Phys. Chem. A **109**, 9424 (2005).
- [6] S. Mukamel, *Principles of Nonlinear Optical Spectroscopy* (Oxford University Press, New York, 1995).
- [7] G. R. Fleming and M. Cho, Ann. Rev. Phys. Chem. **47**, 109 (1996).
- [8] J. Sung and R. J. Silbey, J. Chem. Phys. **115**, 9266 (2001).

- [9] T. L. C. Jansen, T. Hayashi, W. Zhuang, and S. Mukamel, *J. Chem. Phys.* **123**, 114504 (2005).
- [10] T. Hayashi and S. Mukamel, *J. Phys. Chem. B* **111**, 11032 (2007).
- [11] T. Hayashi, T. L. C. Jansen, W. Zhuang, and S. Mukamel, *J. Phys. Chem. A* **109**, 64 (2005).
- [12] B. M. Auer, R. Kumar, J. R. Schmidt, and J. L. Skinner, *Proc. Natl. Acad. Sci. U.S.A.* **104**, 14215 (2007).
- [13] S. A. Corcelli and J. L. Skinner, *J. Phys. Chem. A* **109**, 6154 (2005).
- [14] T. L. C. Jansen and J. Knoester, *J. Phys. Chem. B* **110**, 22910 (2006).
- [15] S. T. Roberts, *Hydrogen Bond Rearrangements and the Motion of Charge Defects in Water Viewed Using Multidimensional Ultrafast Infrared Spectroscopy*, Ph.D Thesis, Massachusetts Institute of Technology, 2009.
- [16] A. Tokmakoff, *Time-Dependent Quantum Mechanics and Spectroscopy*; Massachusetts Institute of Technology, 2003-2011, pp License: Creative Commons BY, n.d.
- [17] M. Cho, *Chem. Rev.* **108**, 1331 (2008).
- [18] K. Kwak, J. Zheng, H. Cang, and M. D. Fayer, *J. Phys. Chem. B* **110**, 19998 (2006).
- [19] J. G. Saven and J. L. Skinner, *J. Chem. Phys.* **99**, 4391 (1993).
- [20] J. J. Loparo, S. T. Roberts, R. A. Nicodemus, and A. Tokmakoff, *Chem. Phys.* **341**, 218 (2007).
- [21] J. R. Schmidt, S. A. Corcelli, and J. L. Skinner, *J. Chem. Phys.* **123**, 044513 (2005).
- [22] S. T. Roberts, P. B. Petersen, K. Ramasesha, A. Tokmakoff, I. S. Ufimtsev, and T. J. Martinez, *Proc. Natl. Acad. Sci. U.S.A.* **106**, 15154 (2009).
- [23] A. M. Walsh and R. F. Loring, *J. Chem. Phys.* **94**, 7575 (1991).
- [24] J. J. Loparo, S. T. Roberts, and A. Tokmakoff, *J. Chem. Phys.* **125**, 194522 (2006).
- [25] J. D. Eaves, J. J. Loparo, C. J. Fecko, S. T. Roberts, A. Tokmakoff, and P. L. Geissler, *Proc. Natl. Acad. Sci. U.S.A.* **102**, 13019 (2005).

- [26] J. R. Schmidt, S. T. Roberts, J. J. Loparo, A. Tokmakoff, M. D. Fayer, and J. L. Skinner, *Chem. Phys.* **341**, 143 (2007).
- [27] K. Ramasesha, S. T. Roberts, R. A. Nicodemus, A. Mandal, and A. Tokmakoff, *J. Chem. Phys.* **135**, 054509 (2011).
- [28] C. J. Fecko, J. J. Loparo, S. T. Roberts, and A. Tokmakoff, *J. Chem. Phys.* **122**, 54506 (2005).
- [29] A. Tokmakoff, *J. Chem. Phys.* **105**, 1 (1996).
- [30] C. P. Lawrence and J. L. Skinner, *J. Chem. Phys.* **118**, 264 (2003).
- [31] K. B. Møller, R. Rey, and J. T. Hynes, *J. Phys. Chem. A* **108**, 1275 (2004).
- [32] T. Joo, Y. Jia, J.-Y. Yu, M. J. Lang, and G. R. Fleming, *J. Chem. Phys.* **104**, 6089 (1996).
- [33] P. Hamm, M. Lim, and R. M. Hochstrasser, *Phys. Rev. Lett.* **81**, 5326 (1998).
- [34] S. T. Roberts, J. J. Loparo, K. Ramasesha, and A. Tokmakoff, *Opt. Commun.* **284**, 1062 (2011).
- [35] M. Khalil, N. Demirdöven, and A. Tokmakoff, *Phys. Rev. Lett.* **90**, 2 (2003).
- [36] S. T. Roberts, J. J. Loparo, and A. Tokmakoff, *J. Chem. Phys.* **125**, 084502 (2006).
- [37] Z. Ganim, H. S. Chung, A. W. Smith, L. P. Deflores, K. C. Jones, and A. Tokmakoff, *Acc. Chem. Res.* **41**, 432 (2008).
- [38] K. Kwac, C. Lee, Y. Jung, J. Han, K. Kwak, J. Zheng, M. D. Fayer, and M. Cho, *J. Chem. Phys.* **125**, 244508 (2006).
- [39] J. J. Loparo, C. J. Fecko, J. D. Eaves, S. T. Roberts, and A. Tokmakoff, *Phys. Rev. B* **70**, 1 (2004).

Chapter 3

A phenomenological approach to modeling chemical dynamics in nonlinear and two-dimensional spectroscopy

3.1 Introduction

Ultrafast spectroscopy is the most widely used experimental approach for studying the dynamics of molecules in condensed phases. The interpretation of these experiments has relied heavily on nonlinear spectroscopy models which use perturbation theory to describe the dynamics in terms of multi-point correlation functions in the dipole operator. The most useful models to have been embraced by experimentalist and theoretician alike provide the ability to directly calculate the measured experimental observables, allowing interpretation and fitting of the data. Unfortunately, in several cases, the assumptions built into these models are proving to be too restrictive to properly describe nonlinear and two-dimensional infrared spectroscopy. To provide a realistic interpretation of such data, mixed quantum-classical models that use classical molecular dynamics (MD) simulations

to describe the dynamics are being widely developed. These models map the classical coordinates of the MD simulation onto a quantum Hamiltonian for the spectroscopic degrees of freedom and provide direct insight into how specific dynamics influence the spectroscopy. However, they usually add a layer of complexity that makes them impractical for experimentalists. The goal of this chapter is to present a simple and intuitive approach to modeling nonlinear spectroscopy that describes the system and dynamics phenomenologically but calculates observables from trajectories and mapping variables as performed in mixed quantum-classical calculations.

The most popular approach to modeling nonlinear spectroscopy are the class of models that include the Brownian oscillator model and spin-boson model, which were popularized by Mukamel [1], and are often implemented with the aid of double-sided Feynman diagrams. This method treats the interaction of one or more quantum degrees of freedom with a quantum harmonic bath [1–4]. Within that framework, it provides exact analytical expressions for observables in nonlinear spectroscopy, given variables that describe the system and the frequency correlation function or spectral density for the bath. The high temperature limit and specific forms of the bath lead to simple analytic descriptions of homogeneous and inhomogeneous broadening and spectral diffusion.

Analytical models typically rely on a series of approximations, including bilinear coupling of the system to a harmonic bath, the second cumulant approximation, and the Condon approximation. Perhaps the most restrictive is the use of the cumulant expansion to second order, also known as the Gaussian approximation. This allows the signal to be described exactly for Gaussian fluctuations or disorder in the system coordinate, which finds greatest use for the description of fluctuations about a free energy minimum. Barrier

crossings, kinetics, and other non-Gaussian chemical dynamics are not accounted for, but are often added in an *ad hoc* manner. Bilinear coupling to a bath provides the ability to solve this problem analytically, but it only describes pure dephasing processes. Population relaxation and orientational relaxation must still be added in a manner that is uncorrelated with the pure dephasing. Finally, the Condon approximation states that the external electromagnetic field couples to a dipole operator that is a function of the system coordinates but not the bath. These approximations are proving to be too restrictive for many recent applications of nonlinear and two-dimensional infrared spectroscopy, which has spurred investigations into alternative methods of extracting such information from experiment [5–7].

The past decade has also seen the growth of spectroscopic models based on the semi-classical approximation that draw from classical MD simulations. A number of variations for these mixed quantum-classical models exist, but they share in common a classical treatment of the molecular dynamics and the construction of a time-dependent quantum Hamiltonian for the spectroscopic degrees of freedom by mapping from one or more coordinates of the classical simulation [8–12]. These approaches may be used for spectroscopy of excitonic states and for reactive systems. They provide an atomistic interpretation of spectroscopic observables by nature of their direct correlation with underlying molecular dynamics. These advantages come at the cost of considerable effort for developing models and implementing the simulations, which makes them less accessible to experimentalists.

Existing models have proven very useful for many problems in nonlinear spectroscopy, and continue to be the favorite for the analysis of condensed phase

dynamics. However, the advent of two-dimensional spectroscopy, and the growth of infrared vibrational spectroscopy in particular, has highlighted the need for a new class of models to analyze the spectroscopy of dynamics in complex and reactive systems. Previously, a few approaches to stochastically model vibrational dynamics using semi-classical methods have been put forth to describe linear [13] and nonlinear infrared spectroscopy [14–17]. Here we describe a phenomenological approach, which draws on the semi-classical approximation and can be used to describe the nonlinear spectroscopy of barrier crossings, non-Gaussian dynamics, and the non-Condon effect. It draws from mixed quantum-classical modeling, using stochastic trajectories for one or more system coordinates that are constructed in a phenomenological manner, and mapping variables that relate these internal coordinates to the spectroscopic observables. This trajectory mapping method provides an avenue to interpreting nonlinear and two-dimensional spectroscopy in the optical and infrared regimes in terms of known dynamics of internal coordinates.

3.2 Approach

3.2.1 Approximations to the response function

The common description of spectroscopy emerges from a Hamiltonian $H = H_0 + V(t)$ where H_0 is the Hamiltonian for the matter and $V(t) = -\mathbf{m} \cdot \mathbf{E}$ describes the electromagnetic field \mathbf{E} interacting with the matter through the quantum mechanical dipole operator \mathbf{m} [1,18]. Within linear response theory, time-domain spectroscopy depends on response functions, which are expressed as multipoint correlation functions in

m. In the case of linear spectroscopy, the response function is related to $\langle \mathbf{m}(t) \cdot \mathbf{m}(0) \rangle$, and the time-evolution of the dipole moment $\mathbf{m}(t)$ for all degrees of freedom can be obtained directly from *ab initio* molecular dynamics simulations [19] or a classical representation of the dipole operator [20]. To reduce computational cost and complexity, one typically focuses only on the specific degrees of freedom that are resonant with \mathbf{E} . This amounts to separating the spectroscopic degrees of freedom (“system” Q) from the remaining ones (“bath” q), which we account for by partitioning $H_0 = H_S + H_B + H_{SB}$, where H_{SB} describes the interaction between the “system” and the “bath”. In the case of vibrational spectroscopy, one can expand \mathbf{m} in Q and q . For instance, when including the permanent dipole, transition dipole moment, and linear non-Condon corrections to the transition dipole we have,

$$\mathbf{m} = \mathbf{m}_0 + \frac{\partial \mathbf{m}}{\partial Q} Q + \sum_{\alpha} \frac{\partial^2 \mathbf{m}}{\partial Q \partial q_{\alpha}} Q q_{\alpha} \quad (3-1)$$

Then, we can write dipole correlation functions in terms of the transition dipole moment $\bar{\mu}_{ab}(t) = \langle a | \mathbf{m}(t) | b \rangle$ where matrix elements are taken in the eigenstates of H_S , and the time dependence results from H_B . The linear response function for a two-level system with system states a and b becomes,

$$R^{(1)}(\tau) = \text{Re} \left\langle \bar{\mu}_{ab}(\tau) \bar{\mu}_{ba}(0) \exp \left[-i \int_0^{\tau} \omega_{ba}(\tau') d\tau' \right] \right\rangle \quad (3-2)$$

Here the time-dependent transition energy

$\omega_{ab}(t) = (\langle a | H_S + H_{SB} | a \rangle - \langle b | H_S + H_{SB} | b \rangle) / \hbar$, and the angular brackets denote a trace

over the bath degrees of freedom. For nonlinear vibrational spectroscopy, the result for rephasing (−) and non-rephasing (+) contributions to the third-order response function is [4]

$$\begin{aligned} R_+^{(3)} &= \sum_{abcd} \langle \bar{\mu}_{ab}(\tau_3 + \tau_2 + \tau_1) \bar{\mu}_{bc}(\tau_2 + \tau_1) \bar{\mu}_{cd}(\tau_1) \bar{\mu}_{da}(0) f_{abcd}^{(+)} \rangle \\ R_-^{(3)} &= \sum_{abcd} \langle \bar{\mu}_{cd}(\tau_3 + \tau_2 + \tau_1) \bar{\mu}_{bc}(\tau_2 + \tau_1) \bar{\mu}_{ab}(\tau_1) \bar{\mu}_{da}(0) f_{abcd}^{(-)} \rangle \end{aligned} \quad (3-3)$$

$$\begin{aligned} f_{abcd}^{(+)} &= \exp \left[-i \int_{\tau_2 + \tau_1}^{\tau_3 + \tau_2 + \tau_1} \omega_{ba}(\tau) d\tau - i \int_{\tau_1}^{\tau_2 + \tau_1} \omega_{ca}(\tau) d\tau - i \int_0^{\tau_1} \omega_{da}(\tau) d\tau \right] \\ f_{abcd}^{(-)} &= \exp \left[-i \int_{\tau_2 + \tau_1}^{\tau_3 + \tau_2 + \tau_1} \omega_{dc}(\tau) d\tau - i \int_{\tau_1}^{\tau_2 + \tau_1} \omega_{db}(\tau) d\tau - i \int_0^{\tau_1} \omega_{da}(\tau) d\tau \right] \end{aligned} \quad (3-4)$$

Further simplification of Eq. (3-2) requires that we neglect the dependence of the transition moment on the bath (Condon approximation) and neglect orientational factors (isotropic approximation). Then for the specific case of Gaussian dynamics one can make the cumulant approximation and truncate at second order to obtain an expression of the following form,

$$R^{(1)}(\tau) = |\mu_{ab}|^2 e^{-i\omega_{ab}\tau} \exp \left[-\int_0^\tau \int_0^{\tau'} \langle \delta\omega_{ab}(\tau'') \delta\omega_{ab}(\tau') \rangle d\tau' d\tau'' \right] \quad (3-5)$$

where, $\delta\omega_{ab}$ is the deviation of ω_{ab} from its mean value. Response functions in the second cumulant approximation can be derived analytically for the specific form of a system bilinearly coupled to a harmonic bath. This leads to the commonly used phenomenological models, such as the Brownian oscillator model [1,4].

Mixed quantum-classical models apply a semi-classical approximation to Eqs. (3-2)–(3-4). This replaces the time propagator $e^{-iH_B t/\hbar}$ with classical dynamics for the bath

variables q , and replaces the trace over the bath with an equilibrium average over phase space. For the quantum operator $\mathbf{m}(Q, q, t)$, only the system coordinate Q remains quantized, and the orientation and magnitude of the dipole moment and the dynamics depend on the classical degrees of freedom \tilde{q}_α . In practice, use of this approximation in nonlinear spectroscopy has been handled in different ways, but practical considerations have dictated that $\omega_{ab}(t)$ and $\bar{\mu}_{ab}(t)$ are not separately calculated for each time step. Instead, within an adiabatic approximation, one can use a mapping that correlates these variables with the bath coordinates q . For instance,

$$\omega_{ab} = \omega_{ab}^0 \left(1 + \sum_{\alpha} a_{\alpha} \tilde{q}_{\alpha} + \dots \right) \quad (3-6)$$

$$\bar{\mu}_{ab} = \bar{\mu}_{ab}^0 \left(1 + \sum_{\alpha} b_{\alpha} \tilde{q}_{\alpha} + \dots \right) \quad (3-7)$$

Here a_{α} and b_{α} are the mapping coefficients between the bath and the transition frequency $a_{\alpha} = (\partial\omega_{ab}/\partial\tilde{q}_{\alpha})/\omega_{ab}^0$ or transition dipole moment $b_{\alpha} = (\partial\bar{\mu}_{ab}/\partial\tilde{q}_{\alpha})/\bar{\mu}_{ab}^0$, and ω_{ab}^0 and $\bar{\mu}_{ab}^0$ are their values in the absence of interactions with the bath. This expansion is only shown to the linear term, but the nonlinear terms in this expansion will be used where this method is most useful. The mapping may be to local or collective bath coordinates, and to as many degrees of freedom as are necessary to obtain a highly correlated single-valued mapping of $\omega_{ab}(q)$ and $\bar{\mu}_{ab}(q)$. Examples of these mappings include correlating ω_{ab} with the electric field of the bath acting on the system coordinate [8,11,21–23] and with bond length [24,25]. The construction of these maps is independent of the dynamics, and has been performed using perturbation theories for the

system-bath interaction [21,26], DFT calculations on clusters and model systems [8,12,27,28], and empirical methods [29]. In the case of multiple interacting degrees of freedom, the site energies and couplings of the system Hamiltonian can all be constructed by mapping procedures [30].

3.2.2 Trajectory construction

The semi-classical approximation to Eqs. (3-3) and (3-4) allows one to calculate spectroscopic observables from trajectories for the transition energy gap $\omega_{ab}(t)$ and the transition dipole moment $\bar{\mu}_{ab}(t)$. If one can obtain trajectories for the dynamics of the system, this approach provides a clear physical interpretation to the spectrum. However, added complexity exists if these must be obtained by performing molecular dynamics simulations, which introduces more difficulties in the analysis of data. Instead, we propose that classical trajectories with specified dynamical characteristics for one or more stochastic variables of the bath be constructed and used with mapping to the spectroscopic quantities to calculate or fit the experimental observables using the semi-classical approximation.

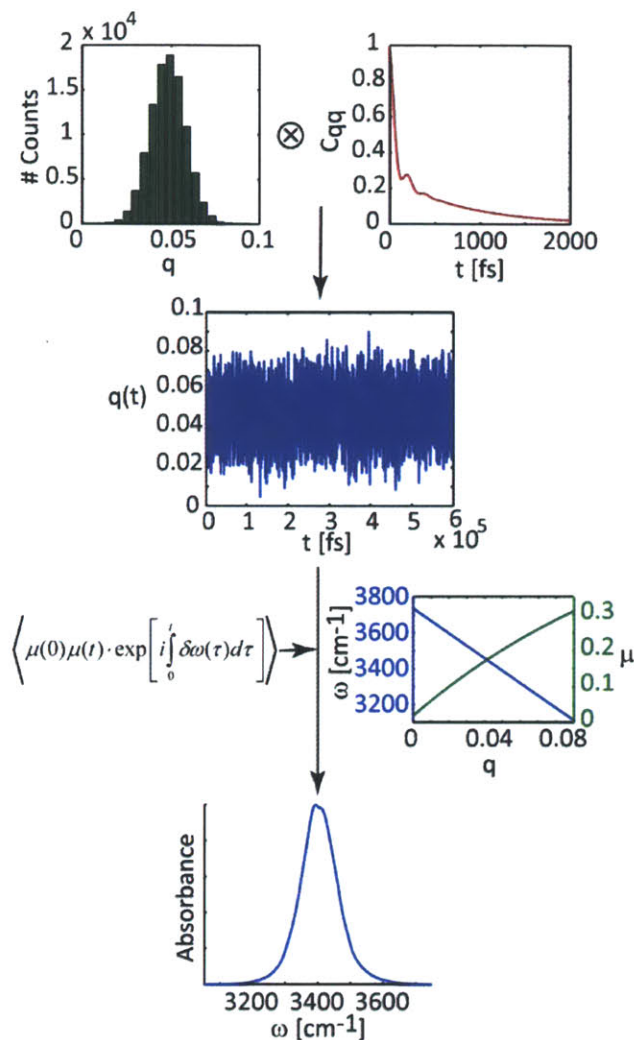


Figure 3-1: Procedure for calculating spectra. We identify the stochastic variable best suited for the problem, propose a random distribution for the variable and convolve it with a correlation function to arrive at the instantaneous correlated trajectory of the stochastic variable. We then generate a mapping between the variable and spectroscopic quantities like transition dipole and frequency. This mapping gives rise to a correlated frequency and transition dipole trajectory, which we use to calculate response functions and spectra. In this illustration, the stochastic variable q corresponds to the collective electric field of solvating D_2O molecule projected onto the O-H bond of an HOD molecule.

To illustrate this method, we make use of two approaches of constructing trajectories in the internal stochastic variable of the bath q to which we attribute the dynamics. In the first method, illustrated in Figure 3-1, the phenomenological inputs are an equilibrium distribution function for q , $P(q)$, and a correlation function for the stochastic variable $c_q(t) = \langle q(t)q(0) \rangle$. A trajectory is generated by convoluting a vector of random values for q , $v(i)$, chosen randomly from $P(q)$, with the correlation function. A specified $c_q(t)$ is also saved in discrete form in a vector of equal length, where a time spacing Δt between points is understood. If we now associate the index of $v(i)$ with a time point $t_i = i \Delta t$, then a trajectory for q with the time-dependent properties of $c_q(t)$ can be obtained by convoluting,

$$q(t) = \int dt' c_q(t-t') v(t'). \quad (3-8)$$

In practice, we perform this convolution using fast Fourier transform methods. The time-ordered sequence of values for q can be translated into trajectories for the transition energy $\omega_{ab}(t)$ and transition dipole moment $\bar{\mu}_{ab}(t)$ on the basis of a mapping from q . A related approach is to use a transformation matrix that contains correlation information to convert Gaussian random fluctuations in the system-bath Hamiltonian into a correlated trajectory [16].

The second method involves generating a trajectory by using Langevin dynamics on a potential of mean force for the stochastic variables of interest, $F(q) = -kT \ln P(q)$. The dynamics are propagated on the potential of mean force as a function of q . With trajectories for the stochastic variable $q(t)$, trajectories for the spectroscopic variables

$\omega_{ab}(t)$ and $\bar{\mu}_{ab}(t)$ can be obtained using appropriate mapping [31]. Alternatively, Langevin dynamics can be run on a higher dimensional potential of mean force that explicitly accounts for the statistical relationship between $q(t)$ and $\omega_{ab}(t)$. These surfaces may have multiple minima for the purpose of describing barrier crossing kinetics.

To illustrate the utility and ease of the trajectory mapping method we calculated linear and nonlinear infrared vibrational spectra for three problems that are not easily addressed with existing phenomenological or analytical models, explained in detail in Ref. [32]. We used two approaches for trajectory construction [32], and provided a description of the frequency and dipole maps. With frequency and dipole trajectories in hand, we calculate the $R^{(1)}$ and $R^{(3)}$ using their semi-classical forms (Eqs. (3-2)–(3-4)). Additional details for how we calculate nonlinear and two-dimensional spectra are described in more detail in Ref. [27]. In the case of 2D IR spectra, the time domain responses were windowed, zero-padded and Fourier transformed in τ_1 and τ_3 to give rephasing and non-rephasing spectra, which were summed to give 2D IR spectra [33].

3.3 The non-Condon effect: Nonlinear IR spectroscopy of HOD/D₂O

Ultrafast infrared spectroscopy of the OH stretch vibration has been widely used to understand hydrogen bond dynamics in liquid water [34,35]. The sensitivity of the OH stretch frequency to its local hydrogen bonding environment has made it a powerful observable to probe the evolution of the hydrogen bond network [21,26,36]. Moreover, molecular dynamics simulations using various water models, in conjunction with semi-classical approaches of calculating spectroscopy, have been extensively used to

understand hydrogen bond dynamics in water [21,36–38]. Water is a highly anharmonic system and exhibits non-Gaussian dynamics, making traditional approaches to modeling the nonlinear response problematic. In particular, experiments and molecular dynamics simulations have indicated that the non-Condon variation in the transition dipole moment with OH stretch frequency is a particularly strong effect that may mask the underlying hydrogen bond dynamics in infrared spectroscopy [29,39,40].

We used the phenomenological approach outlined above to study the non-Condon effect in nonlinear spectra of the OH stretch in HOD/D₂O. We focused on the results from three-pulse echo peak shift (PS) measurement [41], which can measure the OH stretch frequency correlation function, giving insight into the timescales involved in HB dynamics. In their original analysis, Fecko et al. [41] fit their experimentally measured three-pulse peak shift decay to a Brownian oscillator model to extract the OH frequency correlation function [4]. This analysis accounted for finite pulse length, population relaxation, thermally-shifted ground state, and molecular reorientation.

To explore the effects of the Condon approximation on the extracted OH frequency correlation function, we fit the PS data with the trajectory mapping model that included variation of the OH transition dipole moment with OH frequency, but retained a Gaussian distribution of OH frequencies. Although evidence has indicated that water's dynamics are non-Gaussian, we chose a Gaussian distribution to illustrate the specific manner in which non-Condon behavior influences nonlinear spectroscopy. Comparison of the correlation functions that best fit the PS data with or without non-Condon corrections shows the importance of including this effect. We generated a Gaussian frequency distribution for the $\nu = 0-1$ transition centered at 3400 cm^{-1} , with its width scaled to

match the full-width of the experimental linear infrared spectrum of HOD/D₂O. We then convoluted random frequencies within this distribution with frequency correlation functions that had the same general form as in previously published work [41], but with varying decay timescales, and decay and oscillation amplitudes. We found the calculated spectra and PS to be very sensitive to the parameters governing the short time relaxation, and we iteratively varied the parameters of the input correlation function to find best agreement of the calculated PS with the experimental PS data. The resulting frequency trajectories were each 600 ps long, with a 6 fs time step between successive frequencies. The corresponding dipole trajectories were scaled by their non-Condon relationship to the transition frequencies [42], as shown below:

$$\mu_{10} = 1.8336 - (1.2973 \times 10^{-3})\omega_{10} + (4.7136 \times 10^{-7})\omega_{10}^2 - (6.8016 \times 10^{-11})\omega_{10}^3 \quad (3-9)$$

Here ω_{10} is specified in cm^{-1} and μ_{10} is in D. We also generated a ω_{21} distribution that was fully correlated with the ω_{10} distribution, with a fixed anharmonicity of ω_{10} - $\omega_{21}=180 \text{ cm}^{-1}$. We then calculated the third-order response from Eqs. (3-3) and (3-4) for a three-level system [29],

$$R_{\pm}^{(3)}(\tau_1, \tau_2, \tau_3) = \text{Re} \left[2 \left\langle \bar{\mu}_{10}(\tau_1 + \tau_2 + \tau_3) \bar{\mu}_{10}(\tau_1 + \tau_2) \bar{\mu}_{10}(\tau_1) \bar{\mu}_{10}(0) \exp \left[\pm i \int_0^{\tau_1} \omega_{10}(\tau) d\tau + i \int_{\tau_1 + \tau_2}^{\tau_1 + \tau_2 + \tau_3} \omega_{10}(\tau') d\tau' \right] \right\rangle \right. \\ \left. - \left\langle \bar{\mu}_{21}(\tau_1 + \tau_2 + \tau_3) \bar{\mu}_{21}(\tau_1 + \tau_2) \bar{\mu}_{10}(\tau_1) \bar{\mu}_{10}(0) \exp \left[\pm i \int_0^{\tau_1} \omega_{10}(\tau) d\tau + i \int_{\tau_1 + \tau_2}^{\tau_1 + \tau_2 + \tau_3} \omega_{21}(\tau') d\tau' \right] \right\rangle \right] \quad (3-10)$$

For calculations of the peak shift and 2D IR spectra, we averaged response functions across three dipole and frequency trajectories for waiting times <400 fs, and across five

trajectories for waiting times >400 fs. We then proceeded to calculate the peak shift decay for the various trial input correlation functions, by projecting the negative (rephasing) contribution in Eq. (3-10) onto the τ_1 axis and plotting the maximum of this projected three-pulse echo at different waiting times, τ_2 . The normalized calculated PS that included the non-Condon behavior, which best follows the behavior of the experimentally measured PS is shown in Figure 3-2. The calculated PS displays the salient features of the measured PS [41], showing a double exponential decay with timescales of ~ 75 ps and 1 ps with a weak recurrence at ~ 130 fs. However, since real pulse envelopes are critical to obtaining absolute peak shift values and were not included in our calculations, the calculated PS shows a higher zero-time peak shift of 95 fs, as opposed to the 28 fs seen in experiments.

The general nature of the extracted correlation function – double exponential decay with a weak oscillation – is similar to the one obtained by Fecko et al. The short time decay amplitude for the non-Condon case is smaller than seen in Ref. [41]. Since we did not include real pulse effects, the short time component of the correlation function shows a longer decay than the correlation function deduced in Ref. [41]. The oscillation in the input correlation function calculated here is of lower amplitude compared to the correlation function from Fecko, et al. Figure 2 shows the input trial correlation function, with and without the non-Condon effect, used to generate the best fit of the measured PS.

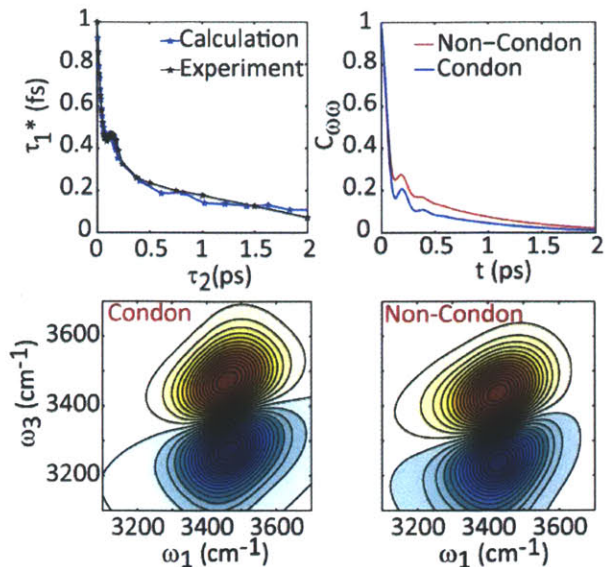


Figure 3-2: Comparison of the normalized three-pulse echo peak shift calculated from our model, which includes the non-Condon effect, with the normalized experimental peak shift measurement (top left) of HOD/D₂O [41]. The correlation functions that went into the peak shift calculations, which gave us the best fit with experimental results for both the Condon and non-Condon response function calculations (top right). The corresponding 2D IR spectra of HOD/D₂O with (bottom right) and without (bottom left) including the non-Condon effect.

The correlation function that best fits the experimental PS for the Condon case displays a larger amplitude fast time drop and a slightly larger amplitude oscillation, compared to the correlation function employed after accounting for the non-Condon effect. Skinner and co-workers calculated frequency correlation functions and peak shifts for Condon, non-Condon and cumulant cases from MD simulations of SPC/E water model, and found that the non-Condon peak shift and correlation function showed a larger amplitude fast decay and a stronger under-damped oscillation compared to the latter two scenarios [40]. We tested to see if the PS calculated using our method displayed similar behavior for the

two cases and found that for a given input correlation function, we see the same trend seen by Schmidt, et al. for the Condon and the non-Condon PS calculations – a larger amplitude fast drop, a stronger oscillation and a smaller zero-time value for the non-Condon PS compared to the Condon case. It appears that the absence of the Condon approximation influences the short time amplitude as well as the amplitude of the oscillation in the extracted frequency correlation function, although the qualitative behavior is the same.

Extending these calculations to 2D IR spectroscopy, Fig. 2 shows the 2D IR spectra of HOD/D₂O calculated upon convoluting the random OH frequencies in a Gaussian distribution with trial correlation functions that fit the experimental PS best for both the Condon and non-Condon cases, respectively. As expected, the 2D IR spectrum with the non-Condon effect clearly shows shifts in intensity to lower frequencies compared to the Condon 2D IR spectra, due to the enhanced transition dipole strengths at lower frequencies that characterize the non-Condon behavior. These calculations are consistent with the spectra obtained from molecular dynamics simulations [10,29,38,40].

3.4 Range of applicability of trajectory mapping method

3.4.1 Non-Gaussian dynamics: Spectroscopy of strong hydrogen bonds

The difficulties with current efforts to model vibrational spectroscopy are in striking evidence in the study of strongly hydrogen bonding systems, such as carboxylic acid dimers [43], N-H-O hydrogen bonds [44], and aqueous acids and bases [45]. Here, one must consider several factors that emerge for highly anharmonic potentials – a large non-

Condon effect, the importance of direct 0-2 transitions that are typically not allowed in the weakly anharmonic case, and unusual “negative anharmonicities” where $\omega_{21} > \omega_{10}$.

The anomalously fast diffusion of protons in water, both in aqueous acids and bases, has been attributed to the Grotthuss hopping mechanism of protons from a proton donor to an acceptor [46]. In the case of hydroxide, this proton donor is the hydrogen bonded water molecule. The hydrogen bond rearrangements that facilitate the stabilization of the proton donor and acceptor molecules, as well as the nature and lifetimes of hydrated proton species that participate in its transport, are currently being investigated using ultrafast nonlinear IR spectroscopy [27,45]. Molecular dynamics simulations of these systems have the additional challenge of accounting for the breaking and formation of covalent O-H bonds during Grotthuss proton transport.

Our previous 2D IR experiments to understand proton transfer in aqueous bases were performed on dilute HOD in concentrated NaOD in D₂O solutions, by probing the evolution of the OH stretch vibrational frequency during proton transfer from HOD to OD⁻ [27,45]. We have also described a mixed quantum-classical cluster-based mapping model that draws from a multistate empirical valence bond (MS-EVB) MD simulation of aqueous hydroxide [47]. For every snapshot in these simulations around a successful proton transfer event, an HOD molecule in the first solvation shell of the OD⁻ ion, along with all water molecules within ~10 Å distance from the HOD molecule, were selected as a cluster. DFT calculations were performed on these clusters by stretching the OH bond in steps of 0.1 Å and tracing the corresponding potential energy curve [42]. As the proton moves from the donor molecule to the acceptor, the curve evolves from a Morse-like potential when the proton is localized on the donor or acceptor, to a symmetric double-

well when the proton is equally shared between two molecules. The potential energy curves from these DFT calculations were fit to an 8th degree polynomial, and the discrete variable representation method was used to calculate the transition frequencies and their corresponding transition dipole moments, thus generating a mapping of these quantities to the internal coordinate for the cluster [42]. In the past, we used the EVB simulations of Martinez and coworkers [47,48] and identified a collective solvation coordinate as the internal variable and used DFT-based electronic structure calculations to map this variable onto the spectroscopic quantities [27].

For the example presented in Ref. [32], we investigated the spectroscopy that arises from large amplitude fluctuations in the hydrogen bond length between donor and acceptor. For these purposes, the most intuitive stochastic internal variable is the differential distance of the proton from donor and acceptor oxygen atoms, $\delta = \left| \mathbf{r}_{O_aH} - \mathbf{r}_{O_dH} \right|$, since it directly reports on the position of the proton as it transfers from a water molecule to a hydroxide ion. Small δ values correspond to the case where a proton is equally shared between two molecules, leading to a symmetric double-well potential and larger δ values correspond to a localized proton and a Morse-like potential. Using the same cluster-based mapping method as described above, we also extracted the associated δ for each of the clusters and mapped these onto the corresponding ω and μ . The broad symmetric double-well potential of the shared proton species (small δ) results in a significant red-shift in the transition frequencies, an enhancement of transition dipole strength, and requires that one- and two-quantum transitions to higher vibrational states, $v = 2, 3$ and 4 , be considered for mid-IR spectroscopy in the $1000\text{-}4000\text{ cm}^{-1}$ region.

For the purposes of using the trajectory mapping model, the proton transfer variable δ was used as the internal stochastic variable. A Gaussian distribution in δ was generated and convoluted with a bi-exponential correlation function. Drawing on the nonlinear mapping between δ and transition dipoles and frequencies, we deduced the instantaneous transition dipole and frequency trajectories for all relevant one-quantum and two-quantum transitions. From these trajectories we calculated the third-order response functions from Eqs. (3-3) and (3-4). Since we explicitly calculated the variation of the transition dipole with δ and ω , we rigorously include non-Condon effects in calculating spectra. In practice, these integrals are evaluated for $v = 0$ to 4, leading to 30 Feynman diagrams that include pathways that exclusively involve one- or two-quantum transitions, as well as those that involve mixed one- and two-quantum transitions, and coherence during the waiting period τ_2 . As shown in Figure 3-3, the calculated 2D IR spectra red-shifted with decreasing values of δ , and showed evidence for exchange features that reflected fast fluctuations of the proton.

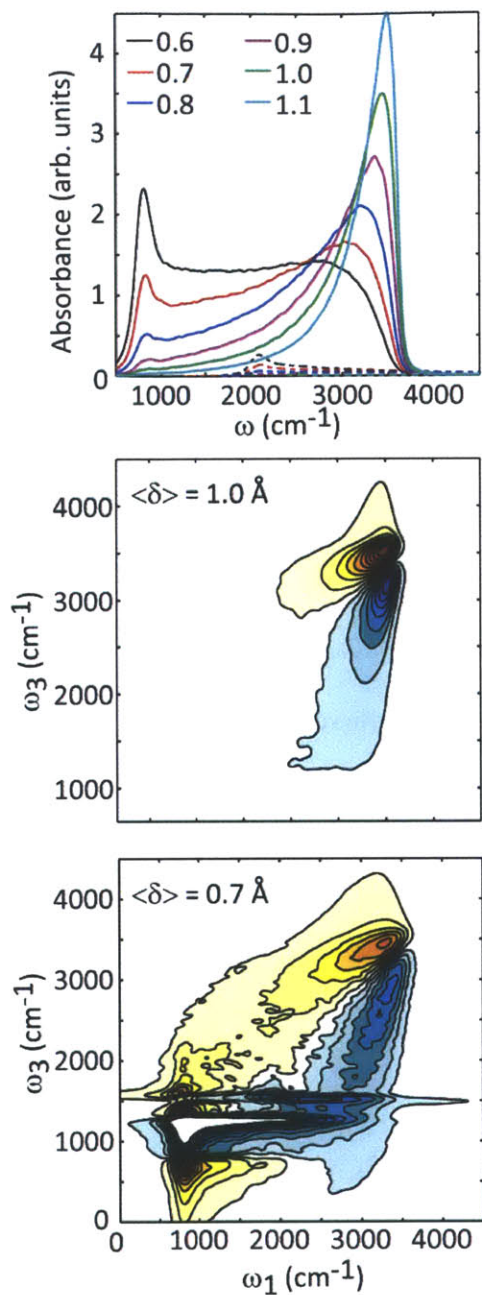


Figure 3-3: (Top) Linear IR spectrum of aqueous hydroxide for different values of $\langle\delta\rangle$ (in \AA), with constant distribution width of $\sigma = 0.3 \text{\AA}$. Below, 2D IR spectra of hydroxide for two $\langle\delta\rangle$ values of 1.0 \AA (middle) and 0.7 \AA (bottom).

As another example presented in Ref. [32], we calculated 2D IR spectra of a model applicable to molecules linked by strong hydrogen bonds, such as carboxylic acid dimers.

Pump-probe and peak shift spectroscopies on strongly hydrogen bonded dimers have shown evidence for strong modulation of the high frequency OH or NH vibrations at the dimer interface by inter-dimer low-frequency (bath) modes [43,44]. We explored how varying fluctuations in these low frequency vibrations that impose different dephasing criteria on the high frequency vibrations affect the 2D IR line shapes of the high frequency mode.

We considered the $v = 0, 1,$ and 2 states of an OH stretch vibration coupled to a low frequency mode, and varied their coupling between underdamped and overdamped limits. We chose a Gaussian frequency distribution for the $v = 0-1$ transition of the OH stretch vibration. We then generated a ω_{21} distribution that was fully correlated with the ω_{10} distribution, offset in frequency by a fixed anharmonicity of $\omega_{21}-\omega_{10}=200 \text{ cm}^{-1}$. The system-bath interaction was represented through the analytical expressions for the complex Brownian oscillator correlation functions given by Mukamel [1], and the damping rate was varied to examine their effect on the calculated spectra. For each case, we calculated the third-order response function using Eqs. (3-3) and (3-4) that included both the $v = 0-1$ and $v = 1-2$ transitions and the non-Condon scaling of the dipole moment according to Eq. (3-9). As expected, the 2D IR spectrum for the under-damped case showed structured vibronic progression, while the spectrum for the over-damped case showed a broad doublet. The calculated spectra are shown in Figure 3-4.

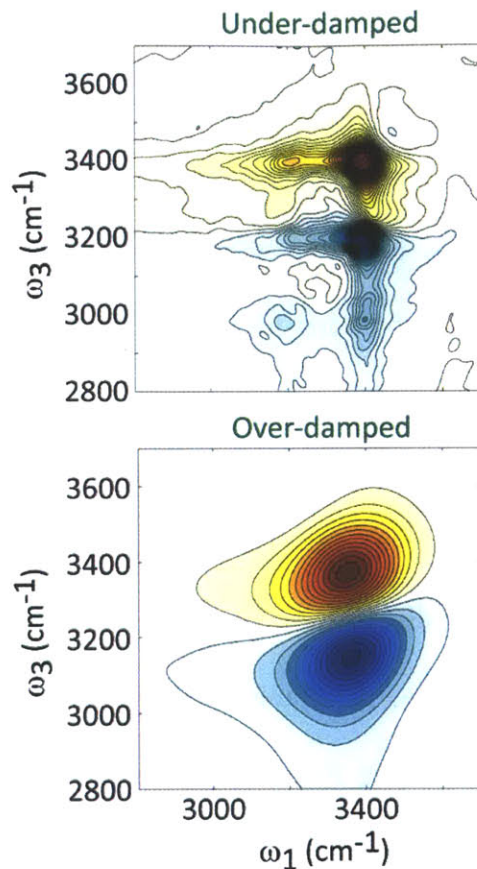


Figure 3-4: 2D IR spectra calculated for the under-damped (top) and over-damped (bottom) cases for the coupling of the OH stretch to the bath. The 2D IR spectrum for the under-damped case has been truncated to show the lower 75% of the contours to emphasize the low-intensity peaks.

3.4.2 Chemical exchange

As the final example presented in Ref. [32], we modeled barrier crossings in a chemical exchange experiment using a trajectory generated from a Langevin simulation on a potential of mean force.¹ With the exception of the work presented in Ref. [31], most chemical exchange models assume a separation of timescales between the dephasing dynamics of the spectroscopic transition and the slower kinetics for the reaction, leading

to standard kinetic equations and explicit treatment of only one time variable in the experiment [24,49–53]. In the example in Ref. [32], vibrational dephasing and the two-state kinetics were intertwined.

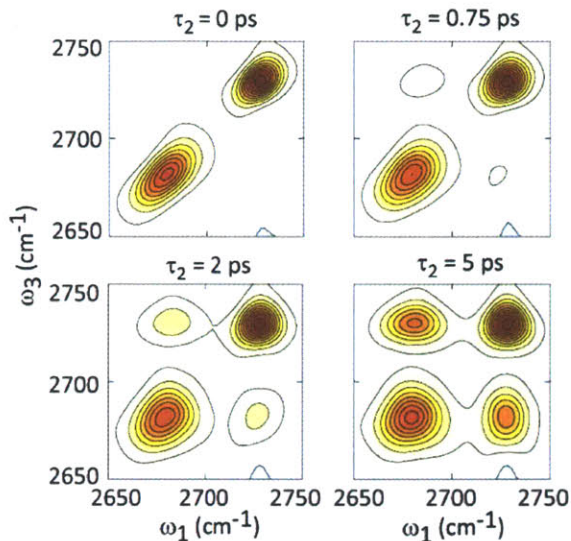


Figure 3-5: Waiting time series of 2D IR spectra calculated from Langevin simulations show the evolution of the diagonal peaks from being inhomogeneously broadened to being symmetric, along with the growth of the cross peaks signifying chemical exchange. The parameters used in solving the Langevin equations are: $c_\omega = 2 \text{ cm}^{-1} \text{ s}^{-1}$, $c_\xi = 10^{-6} \text{ s}^{-1}$, $T_\omega = 0.030$, $T_\xi = 0.000025$, and $\langle \lambda^{-2} \rangle = 3 \times 10^{-15}$ (units of cm^{-2} in the ω -equation and unitless in the ξ -equation).

Our model was parameterized to reproduce the spectroscopy and two-state exchange kinetics between two configurations of a solute that can form either zero or one hydrogen bond to the solvent [51,52]. The hydrogen bonded complex and free molecule give rise to two distinct absorption peaks in the linear IR spectrum with different center frequencies and widths. Frequency trajectories were constructed by solving the Langevin equation for

a two dimensional potential of mean force. 2D IR spectra, displayed in Figure 3-5, were then calculated at different waiting times using Eqs. (3-3) and (3-4), and showed evidence for the growth of exchange cross peaks with waiting time.

3.5 Discussion and conclusions

The trajectory mapping method provides a phenomenological approach to modeling nonlinear spectroscopy in cases where the Gaussian approximation and the Condon approximation are not appropriate, or in cases where there are nonlinear relationships between internal dynamical variables of the bath and the spectroscopic variables ω and μ . One sets probability distributions for one or more internal dynamical variables, describes their stochastic or deterministic evolution through trajectory construction, maps the dynamical variable onto the spectroscopic variables, and evaluates the semi-classical nonlinear response function. Experimental observables can add constraints on the inputs to this model, like the width of the frequency distribution and the relevant correlation function for a given system, thus allowing the model to be used for fitting experimental spectra and deducing the underlying dynamics of the microscopic variables.

Here we concentrated on three classes of problem: (1) fitting of data to account for non-Condon effects, (2) non-Gaussian dynamics and highly nonlinear relationships between the system and bath variables, and (3) barrier crossing and complex non-Gaussian dynamics on an arbitrary potential of mean force. However, there are several other examples and different types of spectroscopy that can be addressed within the trajectory mapping approach. Generally speaking, the classes of problems for which we feel this method will find most use include the following:

(1) Heterogeneous dynamics: Cases in which a dynamical property of the system depends on an evolving bath coordinate can be treated with trajectory mapping. For instance an inhomogeneous system may exhibit a frequency-dependent population relaxation, which can be addressed by mapping frequency to an instantaneous relaxation rate $k_{ab}(t)$. One can integrate over this time-varying relaxation rate in the response function, i.e. $\exp(-\int k_{ba}(\tau)d\tau)$ in the case of the linear response function, Eq. (3-2) [54].

(2) Correlated dynamics: The dynamics for varying relaxation processes of the system can now be treated as correlated when appropriate. For instance, orientational relaxation is often treated independent of vibrational or electronic degrees of freedom. Correlated vibrational and orientational dynamics can be obtained from Langevin simulations on a potential of mean force that represents their statistical relationship, and mapped onto spectroscopic variables.

(3) Multiple coupled vibrations: Although the examples presented here involve mapping to the dynamics of one system coordinate, an arbitrary number of coupled system coordinates can in principle be incorporated and the dynamics calculated non-perturbatively. Using either convolution or Langevin simulations, one can construct trajectories in internal variables that influence the frequency of oscillators (site energies) and the coupling between them. These variables can then be mapped onto a time-dependent system Hamiltonian in the site basis. The resulting trajectory in the system eigenstates and dipole moments in turn can be directly evaluated or integrated to include non-adiabatic effects [2].

The trajectory mapping method also has drawbacks, which constrain how and when it is used. Since this involves numerical integration over one or more trajectories,

constructing trajectories and calculating the response functions is more taxing than other phenomenological approaches. This means that it will be most useful as an interpretive tool for testing hypotheses regarding dynamics, whereas fitting data through error minimization will be time-consuming. Also, this approach requires a map relating stochastic internal variables to spectroscopic quantities. While the non-Condon scaling of the transition dipole with frequency can be deduced empirically [29], maps that relate microscopic quantities like bond distances or electric fields with transition dipole and frequencies require more expensive computations, either in the form of electronic structure calculations or molecular dynamics simulations or both. Moreover, dynamics in most complex systems cannot readily be attributed to one or two microscopic quantities, and therefore, it cannot substitute for classical and *ab initio* simulations. Finally, we note that trajectory mapping, as presented here, uses entirely classical descriptions of the bath, and we have ignored the action of the system on the bath or detailed balance.

The strength of the trajectory mapping approach lies in its flexibility to use a variety of inputs for stochastic quantities and mapping parameters, allowing us to directly assess their effects on the calculated spectra. This flexibility, combined with the ability to constrain the inputs to the model from a variety of spectroscopic techniques, can prove to be a powerful and inexpensive tool to understand chemical dynamics from infrared spectroscopy.

Acknowledgements

This chapter is a modified version of Ref. [32]. Aritra Mandal calculated spectra using trajectory mapping for aqueous hydroxide (first part of section 3.4.1), Andrew Horning

calculated spectra for strongly hydrogen bonded dimers (second part of section 3.4.1) and Luigi De Marco performed Langevin simulations to calculate spectra for a chemical exchange system (section 3.4.2). We thank Ziad Ganim for suggesting the convolution approach expressed in Eq. (3-8). We thank Sean Roberts for providing frequencies, dipoles and δ values for aqueous hydroxide. This work was supported by a grant from the Department of Energy (DE-FG02-99ER14988). I thank Michael Reppert for a careful reading of the manuscript.

References

- [1] S. Mukamel, *Principles of Nonlinear Optical Spectroscopy* (Oxford University Press, New York, 1995).
- [2] S. Mukamel and R. F. Loring, *J. Opt. Soc. Am. B* **3**, 595 (1986).
- [3] G. R. Fleming and M. Cho, *Ann. Rev. Phys. Chem.* **47**, 109 (1996).
- [4] J. Sung and R. J. Silbey, *J. Chem. Phys.* **115**, 9266 (2001).
- [5] S. Garrett-Roe and P. Hamm, *J. Chem. Phys.* **130**, 164510 (2009).
- [6] S. Garrett-Roe and P. Hamm, *J. Chem. Phys.* **128**, 104507 (2008).
- [7] S. Roy, M. S. Pshenichnikov, and T. L. C. Jansen, *J. Phys. Chem. B* **115**, 5431 (2011).
- [8] T. Hayashi, T. L. C. Jansen, W. Zhuang, and S. Mukamel, *J. Phys. Chem. A* **109**, 64 (2005).
- [9] T. Hayashi and S. Mukamel, *J. Phys. Chem. B* **111**, 11032 (2007).

- [10] B. M. Auer, R. Kumar, J. R. Schmidt, and J. L. Skinner, Proc. Natl. Acad. Sci. U.S.A. **104**, 14215 (2007).
- [11] S. A. Corcelli and J. L. Skinner, J. Phys. Chem. A **109**, 6154 (2005).
- [12] T. L. C. Jansen and J. Knoester, J. Phys. Chem. B **110**, 22910 (2006).
- [13] J. R. Schmidt and S. A. Corcelli, J. Chem. Phys. **128**, 184504 (2008).
- [14] T. L. C. Jansen, T. Hayashi, W. Zhuang, and S. Mukamel, J. Chem. Phys. **123**, 114504 (2005).
- [15] F. Sanda and S. Mukamel, The Journal of Chemical Physics **125**, 014507 (2006).
- [16] A. G. Dijkstra, T. L. C. Jansen, R. Bloem, and J. Knoester, J. Chem. Phys. **127**, 194505 (2007).
- [17] T. L. C. Jansen, W. Zhuang, and S. Mukamel, J. Chem. Phys. **121**, 10577 (2004).
- [18] A. Tokmakoff, Time-Dependent Quantum Mechanics and Spectroscopy; Massachusetts Institute of Technology, 2003-2011, pp License: Creative Commons BY, n.d.
- [19] P. L. Silvestrelli, M. Bernasconi, and M. Parrinello, Chem. Phys. Lett. **277**, 478 (1997).
- [20] F. Paesani, S. S. Xantheas, and G. A. Voth, J. Phys. Chem. B **113**, 13118 (2009).
- [21] J. D. Eaves, A. Tokmakoff, and P. L. Geissler, J. Phys. Chem. A **109**, 9424 (2005).
- [22] J. Wang, W. Zhuang, S. Mukamel, and R. M. Hochstrasser, J. Phys. Chem. B **112**, 5930 (2008).
- [23] C. Liang, T. L. C. Jansen, and J. Knoester, J. Chem. Phys. **134**, 044502 (2011).
- [24] M. Cho, Chem. Rev. **108**, 1331 (2008).
- [25] J. Stenger, D. Madsen, J. Dreyer, E. T. J. Nibbering, P. Hamm, and T. Elsaesser, J. Phys. Chem. A **105**, 2929 (2001).
- [26] K. B. Møller, R. Rey, and J. T. Hynes, J. Phys. Chem. A **108**, 1275 (2004).
- [27] S. T. Roberts, P. B. Petersen, K. Ramasesha, A. Tokmakoff, I. S. Ufimtsev, and T. J. Martinez, Proc. Natl. Acad. Sci. U.S.A. **106**, 15154 (2009).
- [28] B. M. Auer and J. L. Skinner, J. Chem. Phys. **128**, 224511 (2008).

- [29] J. J. Loparo, S. T. Roberts, R. A. Nicodemus, and A. Tokmakoff, *Chem. Phys.* **341**, 218 (2007).
- [30] Z. Ganim, H. S. Chung, A. W. Smith, L. P. Deflores, K. C. Jones, and A. Tokmakoff, *Acc. Chem. Res.* **41**, 432 (2008).
- [31] T. L. C. Jansen and J. Knoester, *J. Chem. Phys.* **127**, 234502 (2007).
- [32] K. Ramasesha, L. De Marco, A. D. Horning, A. Mandal, and A. Tokmakoff, *J. Chem. Phys.* **136**, 134507 (2012).
- [33] M. Khalil, N. Demirdoven, and A. Tokmakoff, *J. Phys. Chem. A* **107**, 5258 (2003).
- [34] S. T. Roberts, K. Ramasesha, and A. Tokmakoff, *Acc. Chem. Res.* **42**, 1239 (2009).
- [35] H. J. Bakker and J. L. Skinner, *Chem. Rev.* **110**, 1498 (2010).
- [36] C. P. Lawrence and J. L. Skinner, *J. Chem. Phys.* **118**, 264 (2003).
- [37] C. J. Fecko, J. D. Eaves, J. J. Loparo, A. Tokmakoff, and P. L. Geissler, *Science* **301**, 1698 (2003).
- [38] J. J. Loparo, S. T. Roberts, and A. Tokmakoff, *J. Chem. Phys.* **125**, 194522 (2006).
- [39] A. Piryatinski and J. L. Skinner, *J. Phys. Chem. B* **106**, 8055 (2002).
- [40] J. R. Schmidt, S. A. Corcelli, and J. L. Skinner, *J. Chem. Phys.* **123**, 044513 (2005).
- [41] C. J. Fecko, J. J. Loparo, S. T. Roberts, and A. Tokmakoff, *J. Chem. Phys.* **122**, 54506 (2005).
- [42] S. T. Roberts, *Hydrogen Bond Rearrangements and the Motion of Charge Defects in Water Viewed Using Multidimensional Ultrafast Infrared Spectroscopy*, Ph.D Thesis, Massachusetts Institute of Technology, 2009.
- [43] K. Heyne, N. Huse, E. T. J. Nibbering, and T. Elsaesser, *Chem. Phys. Lett.* **369**, 591 (2003).
- [44] P. B. Petersen, S. T. Roberts, K. Ramasesha, D. G. Nocera, and A. Tokmakoff, *J. Phys. Chem. B* **112**, 13167 (2008).
- [45] S. T. Roberts, K. Ramasesha, P. B. Petersen, A. Mandal, and A. Tokmakoff, *Journal of Physical Chemistry A* **115**, 3957 (2011).

- [46] C. J. T. d. Grotthuss, *Ann. Chim.* LVIII **54**, (1806).
- [47] I. S. Ufimtsev, A. G. Kalinichev, T. J. Martinez, and R. J. Kirkpatrick, *Phys. Chem. Chem. Phys.* **11**, 9420 (2009).
- [48] I. S. Ufimtsev, A. G. Kalinichev, T. J. Martinez, and R. J. Kirkpatrick, *Chem. Phys. Lett.* **442**, 128 (2007).
- [49] Y. S. Kim and R. M. Hochstrasser, *J. Phys. Chem. B* **110**, 8531 (2006).
- [50] Y. S. Kim and R. M. Hochstrasser, *Proc. Natl. Acad. Sci. U.S.A.* **102**, 11185 (2005).
- [51] J. Zheng and M. D. Fayer, *J. Phys. Chem. B* **112**, 10221 (2008).
- [52] K. Kwak, J. Zheng, H. Cang, and M. D. Fayer, *J. Phys. Chem. B* **110**, 19998 (2006).
- [53] K. Kwac, C. Lee, Y. Jung, J. Han, K. Kwak, J. Zheng, M. D. Fayer, and M. Cho, *J. Chem. Phys.* **125**, 244508 (2006).
- [54] Y.-S. Lin, P. A. Pieniazek, M. Yang, and J. L. Skinner, *J. Chem. Phys.* **132**, 174505 (2010).

Chapter 4

Generation and utilization of ultrafast mid-infrared pulses in nonlinear infrared spectroscopy

4.1. Introduction

The ability to measure the time-dependent changes to vibrational frequencies and lineshapes helps us understand the evolution of molecular configurations in condensed phase, since most vibrational transitions in liquids are sensitive to their local environments [1–4]. Liquid water evolves on timescales of tens of femtoseconds to several picoseconds, which range from inertial constrained motions of water molecules to global rearrangements of hydrogen bond networks [5,6]. Studying water therefore requires pulses that are both short enough to resolve fast dynamics and that are tuned to vibrational frequencies that can best report on the structural evolution of the liquid. It is now well-established that the OH stretch vibration of liquid water (specifically, dilute HOD in D₂O) is sensitive to its local hydrogen bonding environment [1,3]. The OH stretch vibration of HOD/D₂O is centered at 3400 cm⁻¹ and has a broad lineshape of ~270 cm⁻¹ full-width at half-maximum. The width of the OH stretch lineshape reflects the

inhomogeneous broadening due to water molecules experiencing different hydrogen bonding environments. Water molecules in strong hydrogen bonds exhibit a red-shifted OH stretch frequency, while those in weak or strained hydrogen bond configurations absorb on the blue side of the lineshape. Therefore, monitoring frequency shifts within the OH stretch lineshape on a fast enough timescale can help us understand hydrogen bonding dynamics. By measuring these frequency shifts in conjunction with polarization measurements of orientational dynamics can further illuminate the mechanism of hydrogen bond exchange by monitoring rotational fluctuations of water molecules.

Using short 800 nm pulses as an input to a home-built mid-infrared optical parametric amplifier (OPA) [7], our group has been able to generate sub-50 fs pulses in the 3 μm region, which affords us both the ability to probe the OH stretch vibration as well as sufficient time resolution to study the fast nuclear dynamics in water. The OPA has been engineered to use very few transmissive optics and to carefully control the thickness of the optics in order to minimize the dispersion of the mid-IR pulses and reliably generate short pulses. In order to study the time-evolution of vibrational frequencies, we use ultrafast nonlinear infrared spectroscopy techniques such as pump-probe (PP) spectroscopy, two-dimensional infrared (2D IR) spectroscopy and anisotropy measurements. We utilize the sub-50 fs 3 μm pulses with 400 cm^{-1} of bandwidth full-width at half-maximum to excite the OH stretch vibration of dilute HOD in D_2O and report on the local hydrogen bonding environment. The output from the home-built OPA can excite all of the sub-ensembles under the broad OH lineshape, and can hence be used to track how these sub-ensembles evolve with time with sufficient time resolution.

2D IR spectroscopy uses replicas of these mid-IR pulses to sequentially excite the system to drive the emission of resonant third-order signal. The first pulse creates a coherent superposition between $v = 0$ and $v = 1$ vibrational states; after a time delay τ_1 , the second pulse breaks the coherence and creates a population state which decays with the inherent vibrational relaxation timescale; after a time delay τ_2 , the third pulse recreates coherence oscillations in τ_3 . The goal of 2D IR spectroscopy is to correlate the frequency of oscillations in τ_3 with those in τ_1 as a function of the waiting time τ_2 . Fourier transforming the oscillations in τ_1 and τ_3 give us a 2D IR spectrum across the ω_1 and ω_3 dimensions, as a function of waiting time τ_2 . This spectrum is therefore related to a mapping of how vibrations in ω_1 (excitation dimension) are correlated with vibrations in ω_3 (detection dimension) at different waiting times, and can be qualitatively thought of as a joint probability, $P(\omega_3, \tau_2; \omega_1)$. Since our $3 \mu\text{m}$ pulses excite the entire OH stretch lineshape in HOD/D₂O, 2D IR spectroscopy allows us to correlate the initial and final hydrogen bond configurations to extract timescales for the decay of frequency correlation at different OH stretch frequencies.

Pump-probe spectra on the other hand are essentially 2D IR surfaces that are integrated across the ω_1 dimension, and hence lack the ability to resolve the excitation dimension. PP spectroscopy uses two fractions of the OPA output, one to pump the OH stretch lineshape to immediately create a non-equilibrium population state, and the other to probe the evolution of the population over a series of time delays. Extracting frequency correlation from PP spectroscopy would require the use of tunable narrowband pulses that excite and probe a range of vibrational sub-ensembles to map out the two-

dimensional surface over many measurements [8]. However, narrowband infrared spectroscopy comes at the cost of time-resolution. We use broadband PP spectroscopy, using the <50 fs 3 μm pulses to pump and probe the entire OH stretch band, as a faster way of extracting timescales for population growth or decay. We disperse the time-resolved pump-probe signal onto an array detector in order to measure the timescales over which the initially prepared vibrational excitations end up at different detected frequencies.

2D IR anisotropy [9–11] provides an additional dimension to the measurement compared to 2D IR spectra. By orienting the polarization of the first two interactions parallel and perpendicular to the third interaction, we can construct the anisotropy,

$$r = \frac{S_{\parallel} - S_{\perp}}{S_{\parallel} + 2S_{\perp}},$$

where S_{\parallel} and S_{\perp} are the parallel (ZZZZ) and perpendicular (YYZZ) 2D

IR surfaces, respectively. Such a measurement tells us the anisotropy for every (ω_1, ω_3) point as a function of τ_2 . This is hence related to a joint probability, $P(r, \omega_3, \tau_2; \omega_1)$, of measuring a particular orientational anisotropy of the HOD transition dipole provided the OH stretch vibration was excited at ω_1 and detected at ω_3 after a waiting time τ_2 . Pump-probe anisotropy cannot extract the joint anisotropy-frequency correlation, but can provide an easy way of measuring the timescale for anisotropy decay at different detection frequencies. Pump-probe and 2D IR experiments, along with the anisotropy measurements, complement one another by providing different pieces of information on the system. Since anisotropy is a double-difference measurement, it is extremely sensitive to drifts in experimental parameters. We therefore put together a set-up that can simultaneously acquire ZZZZ and YYZZ surfaces.

In this chapter, I will first present an overview of the set-up used for 2D IR and pump-probe experiments on HOD/D₂O. I will then describe the functioning of the home-built OPA used to generate 45 fs 3 μm pulses. Subsequent sections of the chapter will present the optical layout for the 2D IR experiments, and the nuts and bolts of 2D IR and pump-probe data acquisition and data processing, with emphasis on anisotropy measurements that are presented in Chapter 5.

4.2 Overview of experimental set-up

Figure 4-1 shows the overview of the experimental set-up required for the nonlinear infrared experiments on HOD/D₂O. We use a Femtolasers Femtopower Compact Pro Ti:Sapphire multi-pass amplifier system to generate 800 nm pulses for pumping the home-built OPA. The amplifier is seeded by a Femtolasers Femtosource Scientific Pro Ti:Sapphire chirped mirror oscillator (450 mW mode-locked power, 80-100 nm bandwidth at full-width at half-maximum, 10 fs pulse duration and 76 MHz repetition rate), which is pumped with the 4 W output from a Nd:YVO₄ Spectra Physics Millennia Vs continuous wave laser. A Faraday isolator is placed after the oscillator to prevent back reflection off the subsequent mirrors and the amplified spontaneous emission to re-enter the oscillator cavity. Figure 4-2 shows the spectrum of the oscillator seed pulse.

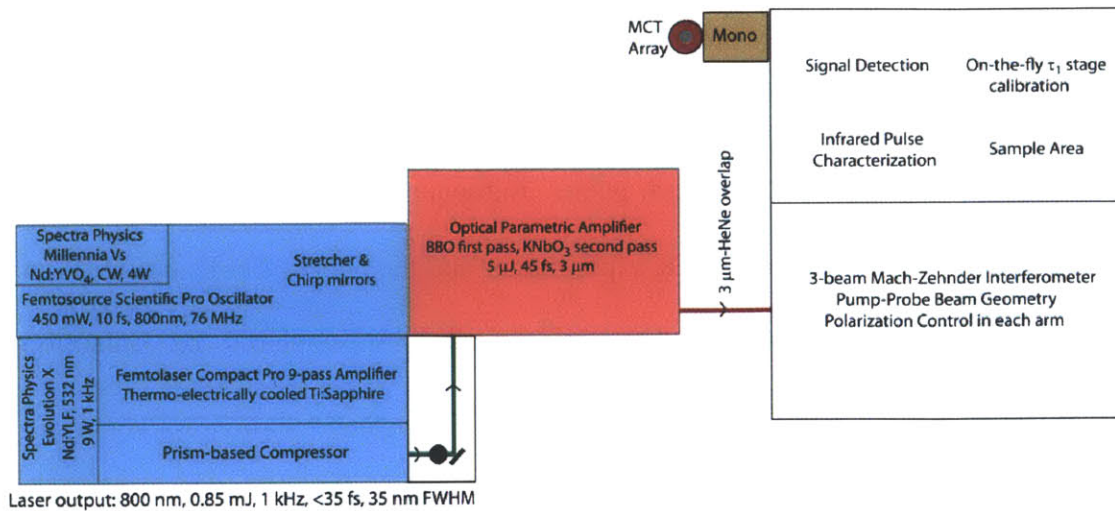


Figure 4-1: Overview of the experimental set-up. Arrows represent the direction of beam propagation and the filled circle is a periscope.

The oscillator MHz pulse train is then sent through a 5 cm long slab of Schott glass to stretch the pulse, and third order dispersion from the glass slab is compensated for by multiple reflections off of chirped mirrors. The stretched pulse then enters the multi-pass amplifier, which contains a thermo-electrically cooled Ti:Sapphire crystal housed in a vacuum enclosure with Brewster windows. The amplifier is pumped by a Spectra Physics Nd:YLF Evolution X laser (1 kHz, 8.5 W, 532 nm). The stretched seed pulse train is amplified by passing through the Ti:Sapphire crystal in the amplifier nine times. The first two passes result in a peak amplification of 40:1 and the next two passes further amplify the pulse train by a factor of 2000:1, resulting in an overall amplification factor of 10^5 after four passes. The pulses are then sent through a Pockels cell (Lasermetrics) that picks out the most intense pulse in the MHz pulse train, and down-shifts the repetition rate to 1 kHz to match the repetition rate of the pump laser. The pulse is then sent through the

Ti:Sapphire crystal five more times, resulting in an overall output of 0.8 to 0.9 mJ/pulse after the amplifier.

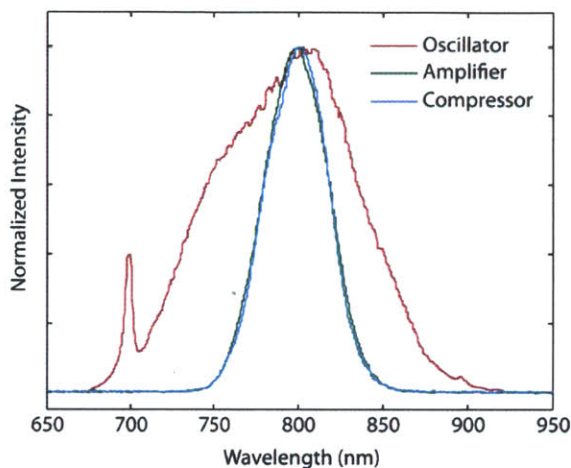


Figure 4-2: Spectra of the seed (red), the amplified 800 nm pulse (green) and the compressed laser output (blue), normalized to their maximum intensity.

The beam size is increased using an expanding telescope to about 1.5 to 2 cm in diameter before sending it to the compressor to minimize self-phase modulation in the hot-spot of the beam profile. A prism-based compressor is used to compress the pulse down to 30 to 35 fs at full-width at half-maximum. We placed a waveplate before the compressor in order to be able to tune the power output of the laser. Figure 4-2 also displays the spectrum of the amplified and compressed 800 nm pulse.

Approximately 500 mW of the laser output is used to pump the home-built β -barium borate (BBO) and potassium niobate (KNbO_3) based OPA used to generate the 45 fs 3 μm pulses [7]. The OPA output is first sent through a 3 mm thick piece of anti-reflection

coated germanium window to compensate for the dispersion in the OPA and to filter out the visible and near-IR output from the OPA. A HeNe tracer beam is first spatially overlapped with the 3 μm beam on the same Ge window for alignment purposes. This is done by flipping up a mirror right before the 3 μm beam enters the interferometer, jogging both the HeNe and 3 μm beams to a far field detector, and overlapping them both in the near and far fields by cutting into the beam and monitoring the loss in intensity on the far field detector. The final two mirrors in the OPA are tweaked for near and far field HeNe – 3 μm overlap, respectively. The flipper mirror is then moved out of the way and the 3 μm beam enters the interferometer where it is split into three beams for 2D IR and pump-probe spectroscopy. The detailed layout of the interferometer is presented in section 4.4 of this chapter.

The 3 μm pulses are first characterized in time via second harmonic autocorrelation, and in frequency by dispersing the beam onto a 2 x 64 element liquid nitrogen cooled array HgCdTe (MCT) array detector. The 3 μm beams are then focused into the sample using off-axis parabolic mirrors. Another off-axis parabolic mirror then collimates the beams and several mirrors are used to direct the signal into the MCT array detector. The signal is focused into the array detector using a ~ 20 cm focal length and 2 inch diameter CaF_2 lens.

4.3 Generation and characterization of 45 fs 3 μm pulses

The two-pass OPA used for experiments on HOD/D₂O is described in detail in Ref. [7], and I will only provide a brief outline of the set-up here. The 500 mW <35 fs

800 nm output from the Femtolaser system is first incident on a fused silica window that is anti-reflection coated on one side. The window reflects roughly 4% of the beam, which is sent through a $\lambda/2$ waveplate and thin film polarizer to finely control the intensity, and then onto a concave spherical mirror that focuses the beam into a sapphire plate for white light seed generation. The white light seed is then sent to another spherical mirror to collimate the beam and then focused using a fused silica convex lens into a 1 mm thick Type I BBO crystal cut at $\theta = 29.2^\circ$ and $\phi = 0^\circ$ (Casix). The 800 nm beam that is transmitted through the fused silica window is incident on a 37% reflectance beamsplitter. The reflected 800 nm arm is sent onto a translation stage and then through a fused silica lens to focus into the BBO crystal. The white light seed and the 800 nm beam are overlapped spatially and temporally for the first stage of 1.1 μm signal and 3 μm idler generation in the BBO crystal. The BBO absorbs the 3 μm idler frequencies, but transmits the 1.1 μm signal. The output from the first pass is incident on a dichroic optic that selectively reflects only the 1.1 μm but transmits the residual 800 nm.

The second pass of the OPA uses the remaining 800 nm beam that transmits through the beamsplitter, and shrinks the spot size of the beam by using a transmissive telescope. The beam is then sent onto a translation stage for controlling the second pass timing, and then into a 1 mm thick Type II KNbO₃ crystal. The 1.1 μm output from the first pass and the 800 nm beam are spatially and temporally overlapped in the crystal to generate 1.1 μm signal and 3 μm idler, which in this case, is not absorbed by the KNbO₃ crystal. Some of the visible frequencies are eliminated by reflecting the second pass output off an 800 nm high reflector. The energy of the 3 μm output from the OPA upon pumping it with

450-500 mW <35 fs 800 nm pulses is about 5 $\mu\text{J}/\text{pulse}$. A transmissive telescope collimates the OPA output to a size of ~ 1 cm in diameter. The output is then overlapped with the HeNe on a 2 mm thick germanium plate, whose positive group velocity dispersion at 3 μm also compensates for the negative dispersion developed in the CaF_2 transmissive optics in the interferometer [7,12].

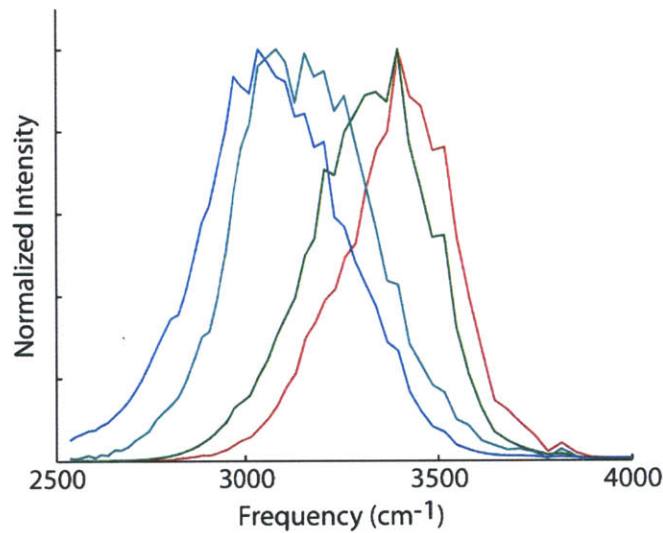


Figure 4-3: Tunability of the 3 μm spectrum from the home-built BBO/ KNbO_3 OPA.

Figure 4-3 displays the spectral tunability of the 3 μm OPA output. The peak frequency of the 3 μm OPA spectrum is modestly tunable, primarily by rotating the angle of the KNbO_3 crystal and compensating for walk-off by tweaking the second pass timing. The bandwidth of the spectrum, on the other hand, is tuned by rotating the BBO crystal and changing the first pass timing along with the 800 nm pulse compression. The OPA is best suited to deliver pulses that are centered at 3400 cm^{-1} with a 350 to 400 cm^{-1}

bandwidth at full-width at half-maximum. For temporal characterization, we perform second harmonic autocorrelation, where the beams from the 2D IR interferometer are focused pair-wise using bare gold off-axis parabolic mirrors (Janos Tech) into a 300 μm thick Type I silver gallium sulfide (AgGaS_2) crystal cut at $\theta = 37.4^\circ$ and $\phi = 45^\circ$ [7]. The relative time delay is scanned by using translation stages, and the resulting second harmonic autocorrelation is spatially isolated using an iris and sent into an indium gallium arsenide (InGaAs) photodiode (Thorlabs). The resulting autocorrelation is displayed in Figure 4-4, and shows a 45 fs time duration of the 3 μm pulses.

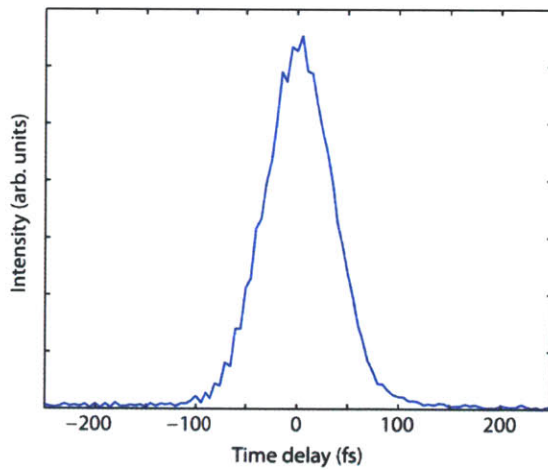


Figure 4-4: Second harmonic autocorrelation of the 3 μm pulses in AgGaS_2 . The x-axis displays the relative time delay between two 3 μm pulses.

In order to characterize the temporal chirp in the 3 μm pulses, we performed transient grating frequency-resolved optical gating (FROG) of the 3 μm pulses in a 1 mm thick CaF_2 window, shown in Figure 4-5. In this measurement, we focused three timed-

up 3 μm pulses in CaF_2 and scanned one of the pulses in time using a motorized delay stage. The resulting third-order non-resonant response from CaF_2 peaks when the three pulses are perfectly timed up, and tapers down as the timing is detuned. The third-order non-resonant response obtained from these three pulses was dispersed onto the MCT array detector and the spectrum of the response was plotted as a function of time delay to obtain the FROG. Chirp in the 3 μm pulses manifests itself as either a linear slope in the time dimension of the FROG (linear chirp) or a horse-shoe shaped curve in the time dimension (higher order chirp). The close-to vertical and compact shape of the FROG displayed in Figure 4-5 shows that the 3 μm pulses are short with little to no linear or higher order chirp.

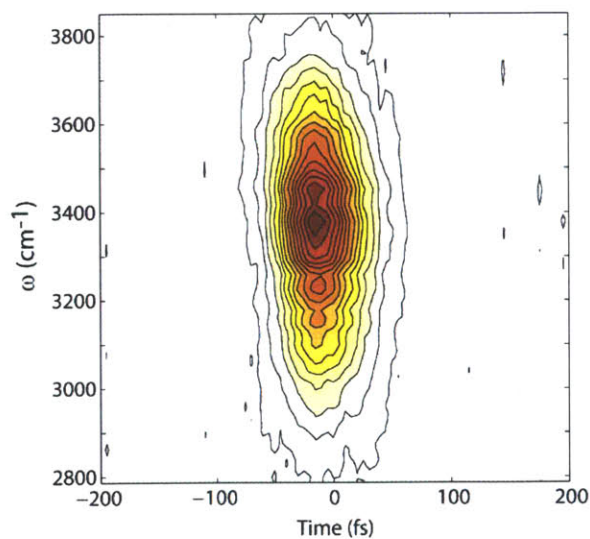


Figure 4-5: Transient grating FROG of the 3 μm pulses from the third-order non-resonant response of CaF_2 , dispersed on a MCT array detector.

Tuning the 3 μm pulse spectrum to lower or higher frequencies with respect to 3400 cm^{-1} requires that we add additional material in the beam to compensate for the chirp in the pulses. Based on the 3 μm autocorrelation and FROG measurements, we insert 1 mm to 2 mm thick anti-reflection coated ZnSe or CaF_2 windows in the 3 μm beam before the 2D IR interferometer to add positive or negative dispersion, respectively, and ultimately obtain 45 fs transform-limited 3 μm pulses for 2D IR experiments [7,12].

4.4 Acquisition of 2D IR and pump-probe spectra in the pump-probe beam geometry

4.4.1 Data acquisition in the pump-probe geometry

2D IR spectroscopy is traditionally performed in the box geometry (Figure 4-6 top), which uses five replicas of the mid-IR OPA pulses. When viewed along the plane perpendicular to beam propagation, three of these are excitation pulses that form three corners of a box and the third order signal is phase-matched to emit along the fourth corner. The fourth replica is used as a local oscillator to interfere with the signal after the sample to extract phase information, and the fifth replica is the “tracer” beam aligned along the signal direction that is used only for signal alignment purposes and is blocked during data acquisition.

The local oscillator is spatially and temporally overlapped with the resonant third-order signal on a 50/50 beamsplitter, and dispersed onto the MCT array detector to

generate the ω_3 dimension in the 2D IR spectrum. The intensity detected on the MCT array is an interferogram, which can be expressed as:

$$I = |E_{Sig} + E_{LO}|^2 = |E_{Sig}|^2 + |E_{LO}|^2 + 2|E_{Sig}||E_{LO}|\cos(\phi_{Sig} - \phi_{LO}) \quad (4-1)$$

This process, known as heterodyning, allows us to extract the phase of the signal, which is required for 2D IR measurements. The detected intensity is the square of the sum of the signal (E_{Sig}) and the local oscillator (E_{LO}) electric fields. The $|E_{Sig}|^2$ term is usually small and can be neglected, and the $|E_{LO}|^2$ term can be subtracted by using an optical chopper. The intensity detected on the array is therefore related to the cosine of the difference between the phase of the signal (ϕ_{Sig}) and that of the local oscillator (ϕ_{LO}). Translating the first two excitation pulses with respect to each other in time (τ_1) generates the rephasing and the non-rephasing spectra that are then summed and Fourier transformed along τ_1 to obtain a 2D IR correlation spectrum. The inaccuracies in the timing between the signal and the local oscillator (τ_3) and between the first two interactions (τ_1) are then corrected for during data processing by adding a constant phase factor along the ω_1 and ω_3 dimensions, since any errors in the pulse timings can distort the 2D IR lineshape by introducing artifacts. The error in τ_3 timing can be substantial, on the order of 20 fs, since finding the exact timing between the signal and the local oscillator tends to be quite difficult.

In order to considerably simplify the 2D IR set-up as well as minimize errors in pulse timings, we performed all measurements that I present in this thesis using the pump-probe beam geometry [13,14], illustrated in the lower part of Figure 4-6. In such a set-up, the OPA output is split into three beams to form the three excitation pulses.

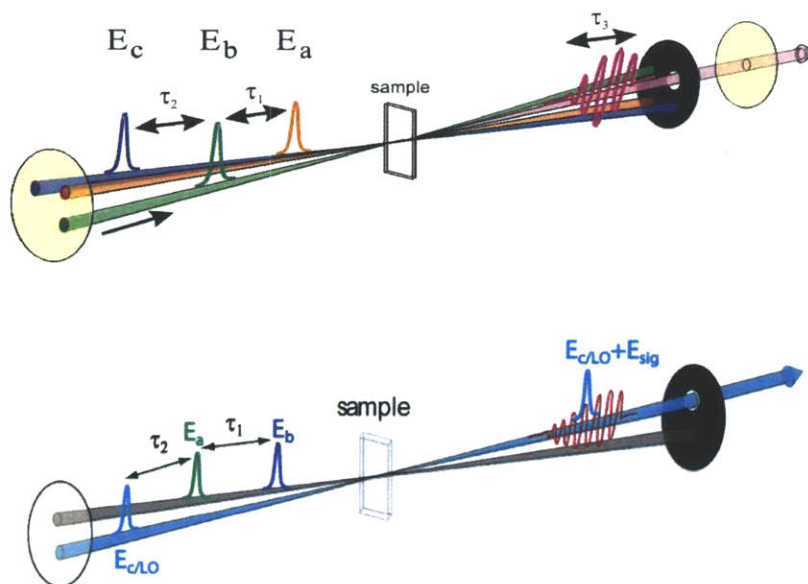


Figure 4-6: 2D IR spectroscopy in the box geometry (top) and in the pump-probe geometry (bottom). Subscripts a , b and c represent the three interactions of the sample with the infrared pulses.

In the pump-probe geometry, the first two interactions (called the “pump” interactions) are collinear with respect to each other and the third interaction (called the “probe”) is spatially separated from the pump beams. The third-order signal in such a geometry is generated along the direction of propagation of the probe, which acts to self-heterodyne the emitted third-order signal. This beam geometry therefore does not require an external local oscillator beam. The pump interactions are scanned with respect to each other in time to generate the τ_1 dimension and the probe plus signal are then dispersed onto an array detector to create the ω_3 dimension to obtain the 2D IR time-frequency correlation spectrum. Since the signal in the pump-probe geometry is inherently timed up

with the third interaction/local oscillator, errors in τ_3 timing are absent in this measurement, and one has to correct for errors in only the τ_1 timing. The second harmonic autocorrelation is accurate enough that the errors in τ_1 timing are usually within 10 fs. Switching from 2D IR spectroscopy to pump-probe spectroscopy in the pump-probe geometry is as simple as blocking one of the pump pulses and scanning the other pump pulse with respect to the probe in time, and dispersing the pump-probe signal onto the MCT array detector. The advantages of the pump-probe geometry are offset by the fact that one cannot separately measure the rephasing and non-rephasing contributions to the spectra. Moreover, the local oscillator/probe intensity cannot be controlled independently of the signal intensity, and would hence require attenuating the probe plus signal intensity after the sample in order to lie within the saturation threshold of the array detector. Therefore, for systems with very low third-order signal, the pump-probe geometry would result in lower signal-to-noise compared to the box geometry. However, since measuring reliable 2D IR lineshapes that are free from distortions is crucial to our analysis of the broad features in water and aqueous systems, we employed the pump-probe geometry for 2D IR data acquisition.

Figure 4-7 displays the optical layout of the pump-probe 2D IR interferometer used in measuring 2D IR spectra of HOD/D₂O. The 5 μ J, 45 fs, 3 μ m pulses from the OPA were first incident on the uncoated surface of a one-side anti-reflection coated CaF₂ window, which reflects \sim 5% of the 3 μ m pulse energy and transmits the rest. The reflected arm served as the probe beam, and was sent onto a gold retro-reflector mounted on a motorized translation stage (Aerotech) to scan the waiting time τ_2 . The beam that is transmitted through the CaF₂ window was incident on a 50/50 CaF₂ beamsplitter (anti-

reflection coated on one side), which equally split the beam into two replicas that served as the pump interactions. The reflected arm from the beamsplitter was sent onto a gold retro-reflector mounted on a motorized translation stage to scan the coherence time τ_1 with respect to the transmitted arm. The transmitted beam was sent onto a fixed retro-reflector. The two pump beams were then spatially recombined on another 50/50 CaF₂ beamsplitter. All the three arms were made to pass through the same amount of CaF₂ material in order to match the dispersion of the pulses. Each of the three arms of the interferometer contained a tilt MgF₂ $\lambda/2$ waveplate (Alphas) and an anti-reflection coated CaF₂ wire-grid polarizer (Molelectron) to control the relative polarizations of the pulses. The pump and probe pulses were vertically offset from each other. The beams were focused into the sample using an off-axis bare gold parabolic mirror (101.6 mm effective focal length; Janos Tech). The spot size at the sample position was approximately 100 μm . The pulses were timed up at the sample position using second harmonic autocorrelation described in the previous section.

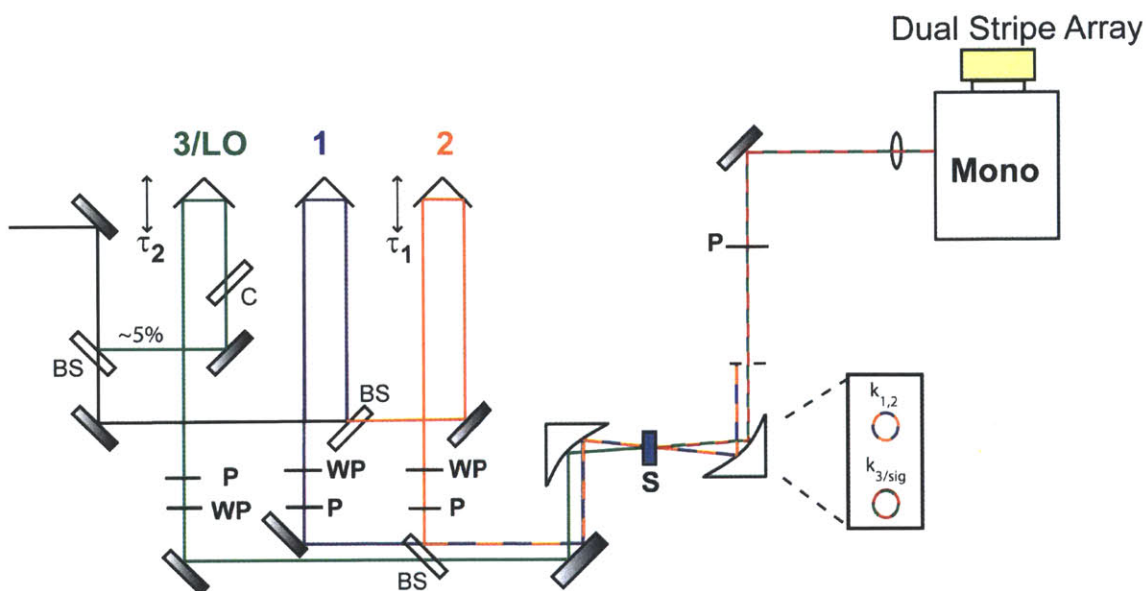


Figure 4-7: Detailed diagram of the set-up for acquiring 2D IR spectra in the pump-probe geometry. All the mirrors in the set-up are protected gold plane mirrors. BS: 3 mm thick CaF₂ beamsplitters; WP: $\lambda/2$ MgF₂ tilt waveplates, P: CaF₂ wire-grid polarizers, S: sample, LO: local oscillator.

Another off-axis gold parabolic mirror after the sample was used to collimate the probe plus signal beam, which was then sent through a CaF₂ lens to focus into the spectrometer. The spectrometer was equipped with a 75 grooves/mm grating blazed for 4 μm , in order to disperse the signal onto a 64 element liquid nitrogen cooled MCT array detector. The spectrum collected on the array provides the ω_3 dimension.

We scan the τ_1 stage in steps of 2 fs from -100 fs to 400 fs to trace out the coherence oscillations. Since the τ_1 axis has to be numerically Fourier transformed to obtain the broadband 2D IR spectra in the frequency domain, it is important to make sure that the error in the τ_1 delays is minimized to avoid side-bands and other artifacts in the Fourier

transformed 2D IR spectra. Motorized translation stages used to scan optical time delays usually offer a reproducibility of ~ 50 nm. Errors in stage position or timing translate to the mixing of real and imaginary 2D IR spectra, resulting in distortions to the 2D IR lineshape. We therefore perform an interferometric stage calibration procedure to correct for errors in the timing between the two arms before Fourier transforming the time-frequency raw data. The errors in stage position are systematic and stem from round-off issues in the stage encoder that tells the stage where to park for every time delay. These systematic errors can be corrected for by calibrating the stage position with an optical interferogram. We calibrated the τ_1 axis by performing quadrature detection [15,16] using the co-propagating HeNe beams in the two arms of the interferometer, directly following the method previously used for on-the-fly calibration of translation stages in a fast scanning 2D IR [17,18]. The calibration was set up by placing a $\lambda/2$ waveplate in one arm and a $\lambda/4$ waveplate to induce circular polarization in the other arm after the 3 μm beam was split into two arms in the Mach-Zehnder interferometer. After the beams were recombined on the second 50/50 beamsplitter, the combined beam was sent into a beam cube that split the beam into the S and P polarization, which were each sent into a photodiode (Thorlabs DET210). As the τ_1 stage is translated, the interferogram collected on the photodiodes are $\pi/2$ out-of-phase with each other due to the phase shift introduced by the $\lambda/4$ waveplate. The accumulated phase between the two arms was extracted by taking the inverse tangent of the ratio of the interferogram at P polarization (sine wave) to the interferogram at S polarization (cosine wave). The error in position was then calculated from the following expression [17]:

$$dx = \frac{\lambda_{\text{HeNe}}}{4\pi} d\phi, \quad (4-2)$$

and correspondingly, the error in time was calculated using

$$dt = \frac{\lambda_{\text{HeNe}}}{4\pi c} d\phi. \quad (4-3)$$

Here, λ_{HeNe} is the wavelength of the HeNe laser, which is 632.8 nm, c is the speed of light and $d\phi$ is the accumulated phase error. We then generated a look-up table for the τ_1 stage that contained a column with finely sampled stage positions and another column with the corresponding position error associated with every stage position. During data acquisition, the systematic error in the τ_1 stage was automatically corrected for on-the-fly by allowing the data acquisition program to access the look-up table and subtract the error associated with every point in the stage motion. While acquiring 2D IR spectra, we also performed on-the-fly interferometric calibration of the τ_1 dimension using the 3 μm infrared beams from the back reflection of the combining beamsplitter in the Mach-Zehnder interferometer, and sending the interferogram through a monochromator positioned at the peak of the 3 μm spectrum [19]. The interferogram is detected on a single-channel liquid N₂ cooled InSb detector (Infrared Systems).

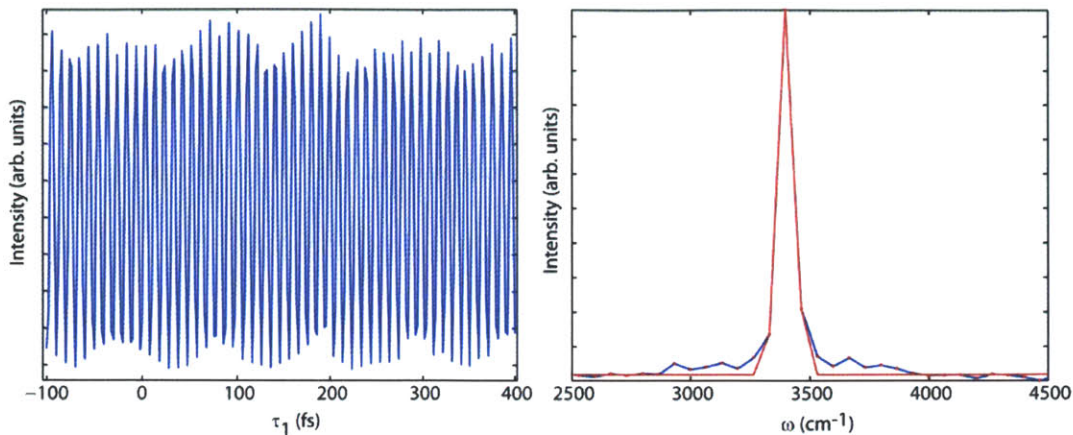


Figure 4-8: Interferogram of the 3 μm pulses through a monochromator set at 3400 cm^{-1} (left). Fourier transform of the interferogram (right) shown in blue, while the red trace is the Gaussian fit to the transform to extract the center frequency.

In this procedure, we correct for minor drifts in the τ_1 timing after the fact, by multiplying a phase factor in the time domain, which results in the exact monochromator frequency when the interferogram is Fourier transformed. Figure 4-8 displays the infrared interferogram with the monochromator set to 3400 cm^{-1} , and its Fourier transform. Note that the Fourier transform shows only one peak with suppressed side-bands, since the stage was already calibrated using HeNe quadrature detection.

4.4.2 Sample

The sample cell used in 2D IR spectroscopy of HOD/D₂O consisted of two 1 mm thick CaF₂ windows that contained ~1% by volume of H₂O in D₂O with a path length of 100 μm . This translates to an optical density of the OH stretch absorption at 3400 cm^{-1} to range between 0.2 and 0.4. Since CaF₂ windows show a large third-order non-resonant

response when the 3 μm pulses are overlapped, the 2D IR data taken with CaF_2 windows contain contributions from purely resonant signal after a waiting time of 100 fs. For acquiring 2D IR spectra at $\tau_2 < 100$ fs, we use 100 nm thick Si_2N_3 windows (Norcada), which shows negligible non-resonant signal at early waiting times [20].

4.4.3 Processing of raw 2D IR data

The error in timing between the pulses after performing second harmonic autocorrelation is usually within ± 5 fs, and we correct for this error by multiplying the ω_1 dimension of the 2D IR spectrum by a phase correction factor, $\phi = \exp(i\omega_1\Delta\tau_1)$, where $\Delta\tau_1$ is the error in timing between the pump pulses.

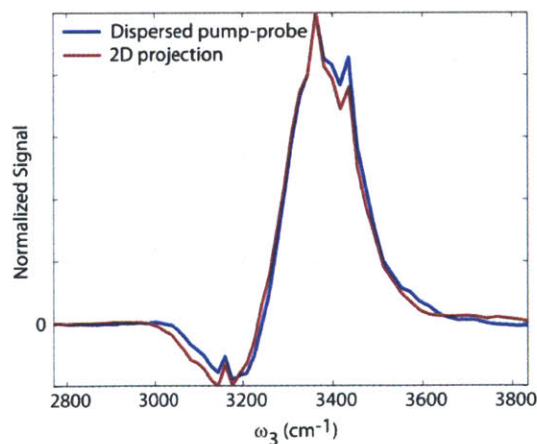


Figure 4-9: Projection of the 2D IR spectrum of HOD/D₂O at $\tau_2 = 250$ fs (red) onto the ω_3 dimension compared to the dispersed pump probe spectrum of the same sample at 250 fs (blue). To match this pair of spectra, the error in timing $\Delta\tau_1$ was found to be -2.2 fs.

Upon invoking the projection-slice theorem, we float the $\Delta\tau_1$ parameter in the phase correction factor such that the projection of the 2D IR surface onto the ω_3 dimension matches the dispersed pump-probe spectrum at the same waiting time, as illustrated in Figure 4-9 [21,22].

The raw time-frequency data and the Fourier transformed 2D IR spectrum after correcting for errors in τ_1 timing are shown in Figure 4-10. By scanning the non-chopped arm in time, we get a constant pump-probe offset to the oscillations in τ_1 [19]. So, before numerically Fourier transforming the oscillations, we subtract the constant pump-probe offset. (If the chopped arm is scanned in time, we obtain a time-varying pump-probe signal which is harder to correct for). We then multiply the time-frequency data by a Hanning window in the τ_1 dimension to suppress the noise, zero-pad the data, and use a fast Fourier transform algorithm to obtain the 2D IR spectrum. The 2D IR spectrum of HOD/D₂O appears as a doublet since our 3 μm pulses are broad enough to be resonant with three vibrational states of the OH stretch. The peak shown in red is due to the $v = 1$ to 0 stimulated emission and the peak in blue is due to the anharmonically downshifted $v = 1$ to 2 induced absorption.

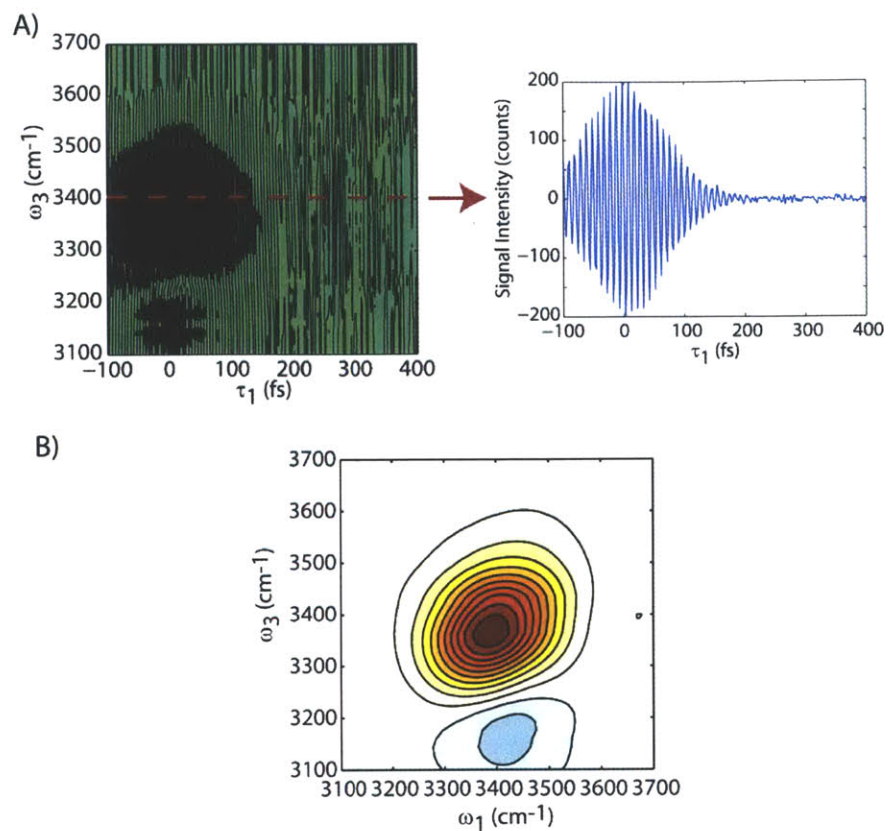


Figure 4-10: a) Time-frequency (τ_1 - ω_3) surface of HOD/D₂O at $\tau_2 = 250$ fs, upon correcting for errors in τ_1 and subtracting the constant pump-probe offset (left). A slice at $\omega_3 = 3400$ cm⁻¹ (right) shows that the oscillations decay by the characteristic dephasing time of the OH stretch in HOD/D₂O of ~ 150 fs. b) The Fourier transformed (ω_1 - ω_3) 2D IR spectrum at $\tau_2 = 250$ fs.

4.4.4 Extracting imaginary and phase 2D IR spectra

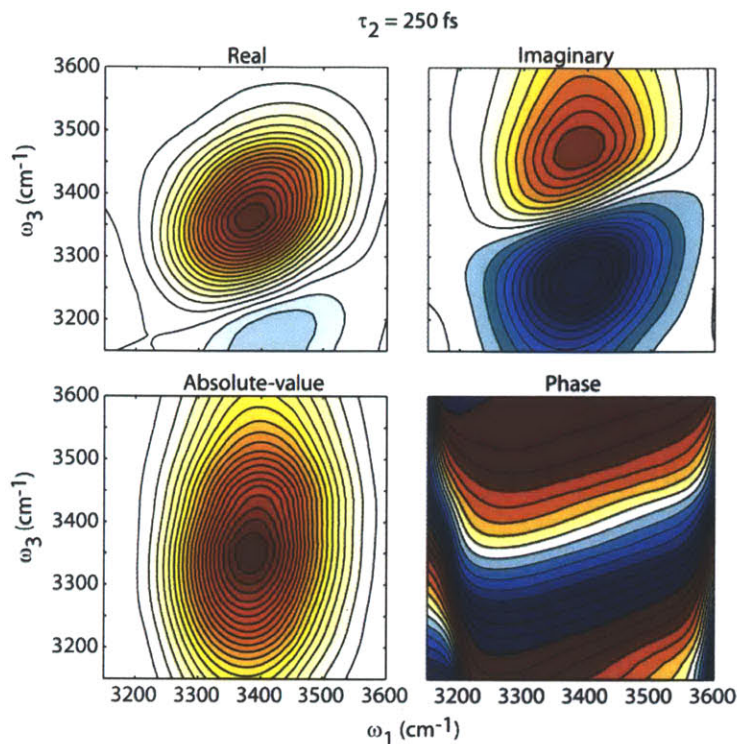


Figure 4-11: The real (top left), imaginary (top right), absolute value (bottom left) and phase (bottom right) 2D IR spectra of HOD/D₂O at $\tau_2 = 250$ fs.

A Kramers-Kronig assumption was used to evaluate the imaginary part of the 2D spectrum and the 2D power spectrum [13,23], as shown in Figure 4-11. We obtained these spectra by inverse Fourier transforming the measured 2D IR correlation spectrum into the time domain, invoking causality and eliminating the data at $\tau_3 < 0$, and Fourier transforming back into the frequency domain to extract the real and imaginary parts of the spectrum. We can then construct the phase spectrum by taking the arc tangent of the ratio of the real spectrum to the imaginary spectrum, $S_\phi = \tan^{-1} \left(\frac{\text{Re}(S_{corr})}{\text{Im}(S_{corr})} \right)$, and the

absolute value (power) spectrum by taking the square root of the sum of the square of the real and imaginary spectra, $S_{abs} = \sqrt{[\text{Re}(S_{corr})]^2 + [\text{Im}(S_{corr})]^2}$. Similarly, by taking linear combinations of the real and imaginary spectra with different phases, the rephasing and the non-rephasing spectra can also be extracted from the 2D correlation spectra measured in the pump-probe geometry [19].

4.5 Polarization scheme for 2D IR anisotropy measurements

Acquiring reliable 2D IR and pump-probe anisotropy of HOD/D₂O requires that the errors that stem from laser fluctuations, changing optical density of the sample (from absorption of atmospheric H₂O) and stage timing drifts be minimized. Since 2D IR anisotropy is a double difference measurement, even small uncertainties or noise can get magnified in the spectrum. We therefore manipulated the polarizations of the input beams in order to allow us to collect ZZZZ and YZZZ spectra simultaneously, therefore eliminating noise related to long time drifts in OPA output power, sample optical density and timing uncertainties [9].

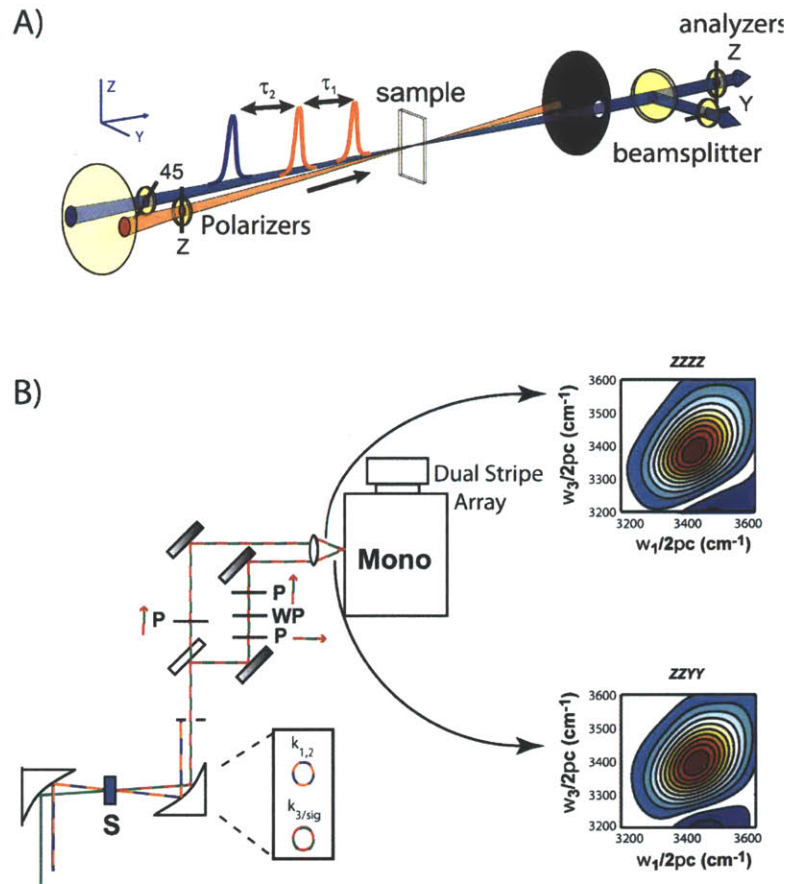


Figure 4-12: a) Beam diagram for 2D IR anisotropy measurements. The polarization of the probe beam is rotated by 45° with respect to the pump polarizations. After the sample, the ZZZZ and YZZZ components are detected by splitting the probe plus signal into two replicas and placing polarizers parallel and perpendicular to the pump polarization, respectively. b) Detection set-up for 2D IR anisotropy measurements. After the analyzing polarizer in the perpendicular arm of the probe, a waveplate-polarizer pair is used to rotate the probe to 0° to ensure that the detected spectra are free of artifacts due to the polarization dependence of the grating diffraction efficiency. Both the arms are then focused using a CaF₂ lens and dispersed on one stripe of a 2 x 64 element MCT array detector.

Figure 4-12a shows the beam diagram for the 2D IR anisotropy set-up we constructed for balanced and simultaneous detection of the *ZZZZ* and *YYZZ* surfaces. We orient the polarizations of the pump beams to be parallel to each other at 0° , and that of the probe beam at 45° relative to the pump polarizations. We calibrated these polarizations at the sample position to account for any scrambling of the polarization caused by the focusing off-axis parabolic mirror. The rest of the interferometer was identical to what was described in the previous section. As shown in Figure 4-12b, we placed a 50/50 beamsplitter after the collimating parabolic. We then placed a polarizer set parallel (0°) to the pump polarization in one arm for collecting the *ZZZZ* 2D IR surfaces, and a polarizer set perpendicular (90°) to the pump polarization in the other arm to collect the *YYZZ* 2D IR surfaces. In the perpendicular arm, we also placed a $\lambda/2$ waveplate and polarizer to rotate the polarization back to 0° to minimize artifacts in the detected signal due to the polarization dependent efficiency of the diffraction grating in the spectrometer. Each of the two arms was then dispersed in a spectrometer equipped with 75 grooves/mm grating and imaged onto one stripe of a 2×64 element liquid nitrogen cooled MCT array (Infrared Systems) with a $16 \text{ cm}^{-1}/\text{pixel}$ resolution, which provided the ω_3 dimension of the 2D IR spectrum. Before acquisition of 2D IR anisotropy surfaces, it was made sure that the probe beams on both stripes of the array had equal intensity. After data collection, the difference in pixel sensitivity between the two stripes was corrected for by dividing the ω_3 dimension in the *ZZZZ* and *YYZZ* surfaces by the respective probe spectra. At any given waiting time, the error in τ_1 was found to be the same for both the *ZZZZ* and *YYZZ* surfaces since they were acquired simultaneously. At every waiting time, the pump-probe or 2D anisotropy was obtained from the corresponding parallel and

perpendicular detected spectra using, $r = (S_{ZZZZ} - S_{YYZZ}) / (S_{ZZZZ} + 2S_{YYZZ})$. 2D anisotropy surfaces were calculated for each (ω_1, ω_3) point for both real and power spectra.

Displayed in Figure 4-13 are the ZZZZ and YYZZ real and power 2D IR spectra, and the corresponding 2D IR anisotropy spectra. Since the 2D IR correlation spectrum consists of a node between the 0-1 and the 1-2 transitions, the 2D anisotropy shows singularities in the nodal region. Since the absolute value spectra do not contain the node, the 2D anisotropy calculated from the power spectra does not show these nodal distortions. However, the 2D anisotropy from the power spectra also include contributions from the imaginary 2D anisotropy spectra, which represent anisotropy changes to the dispersion of the sample, and are therefore harder to analyze. Chapter 5 describes our findings from 2D IR and pump-probe anisotropy measurements on HOD/D₂O, and discusses our approach to analyzing 2D IR anisotropy from power spectra.

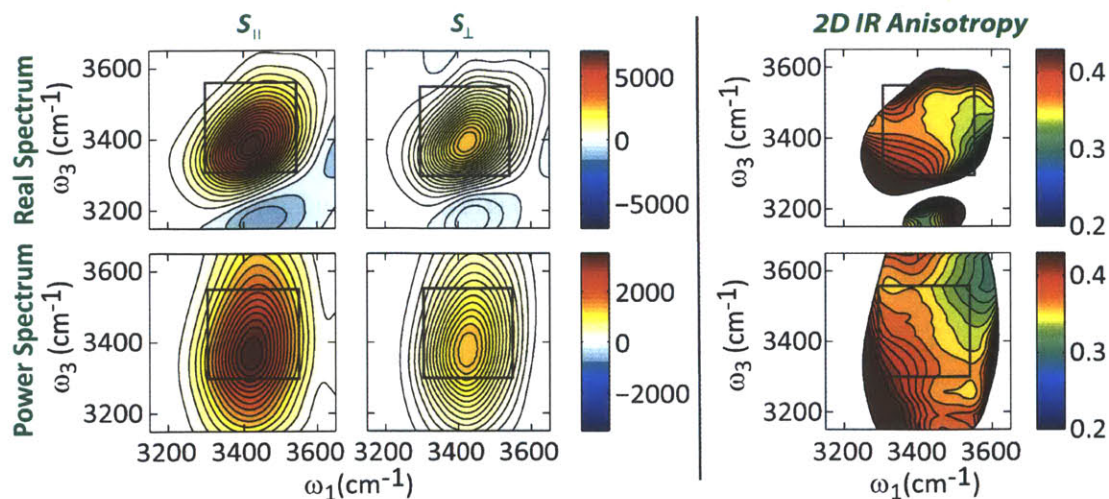


Figure 4-13: Left: Absorptive (top) and absolute-value (bottom) 2D IR spectra of HOD in D₂O at $\tau_2 = 250$ fs, for ZZZZ and YYZZ polarizations. Right: Corresponding 2D IR anisotropy calculated from real absorptive and power spectra are shown on the right. Contours represent a change in anisotropy of 0.01. The anisotropy calculated below a threshold of 5% of the maximum of the magic angle 2D IR spectrum is not plotted.

4.6 Summary

2D IR and pump-probe spectroscopy have proved to be an effective way of understanding frequency and orientational correlations in HOD/D₂O, and in conjunction with molecular dynamics simulations, have helped us to better understand the dynamics of hydrogen bond exchange. Using ultrafast 800 nm pulses to pump a home-built OPA, we generated 45 fs 3 μm pulses to probe the evolution of the OH stretch vibration with time. This chapter outlined the characteristics of the 3 μm pulses, the optical layouts of the 2D IR interferometer in the pump-probe beam geometry for 2D anisotropy measurements, and the detection and data processing involved in generating 2D IR

spectra. The next chapter will present results and analysis of 2D IR anisotropy spectra of HOD/D₂O.

Acknowledgements

I would like to thank Rebecca Nicodemus for helpful suggestions during the process of building the pump-probe interferometer for 2D IR anisotropy measurements. I would also like to thank Aritra Mandal for help with acquiring 2D IR surfaces of HOD/D₂O. This work was supported by the U.S Department of Energy (DE-FG02-99ER14988).

References

- [1] C. P. Lawrence and J. L. Skinner, *J. Chem. Phys.* **118**, 264 (2003).
- [2] K. B. Møller, R. Rey, and J. T. Hynes, *J. Phys. Chem. A* **108**, 1275 (2004).
- [3] J. D. Eaves, A. Tokmakoff, and P. L. Geissler, *J. Phys. Chem. A* **109**, 9424 (2005).
- [4] Z. Ganim, H. S. Chung, A. W. Smith, L. P. Deflores, K. C. Jones, and A. Tokmakoff, *Acc. Chem. Res.* **41**, 432 (2008).
- [5] C. J. Fecko, J. J. Loparo, S. T. Roberts, and A. Tokmakoff, *J. Chem. Phys.* **122**, 54506 (2005).
- [6] J. J. Loparo, C. J. Fecko, J. D. Eaves, S. T. Roberts, and A. Tokmakoff, *Phys. Rev. B* **70**, 1 (2004).
- [7] C. J. Fecko, J. J. Loparo, and A. Tokmakoff, *Opt. Commun.* **241**, 521 (2004).
- [8] V. Cervetto, J. Helbing, J. Bredenbeck, and P. Hamm, *J. Chem. Phys.* **121**, 5935 (2004).

- [9] K. Ramasesha, S. T. Roberts, R. A. Nicodemus, A. Mandal, and A. Tokmakoff, *J. Chem. Phys.* **135**, 054509 (2011).
- [10] M. Ji and K. J. Gaffney, *J. Chem. Phys.* **134**, 044516 (2011).
- [11] G. Stirnemann and D. Laage, *J. Phys. Chem. Lett.* **1**, 1511 (2010).
- [12] N. Demirdöven, M. Khalil, O. Golonzka, and A. Tokmakoff, *Opt. Lett.* **27**, 433 (2002).
- [13] J. A. Myers, K. L. M. Lewis, P. F. Tekavec, and J. P. Ogilvie, *Opt. Express* **16**, 17420 (2008).
- [14] L. P. Deflores, R. A. Nicodemus, and A. Tokmakoff, *Opt. Lett.* **32**, 2966 (2007).
- [15] L. Lepetit, G. Chériaux, and M. Joffre, *J. Opt. Soc. Am. B* **12**, 2467 (1995).
- [16] V. Greco, G. Molesini, and F. Quercioli, *Rev. Sci. Instr.* **66**, 3729 (1995).
- [17] S. T. Roberts, J. J. Loparo, K. Ramasesha, and A. Tokmakoff, *Opt. Commun.* **284**, 1062 (2011).
- [18] S. T. Roberts, *Hydrogen Bond Rearrangements and the Motion of Charge Defects in Water Viewed Using Multidimensional Ultrafast Infrared Spectroscopy*, Ph.D Thesis, Massachusetts Institute of Technology, 2009.
- [19] R. A. Nicodemus, *Hydrogen Bond Reorganization and Vibrational Relaxation in Water Studied with Ultrafast Infrared Spectroscopy*, Ph.D Thesis, Massachusetts Institute of Technology, 2011.
- [20] S. T. Roberts, P. B. Petersen, K. Ramasesha, A. Tokmakoff, I. S. Ufimtsev, and T. J. Martinez, *Proc. Natl. Acad. Sci. U.S.A.* **106**, 15154 (2009).
- [21] D. M. Jonas, *Ann. Rev. Phys. Chem.* **54**, 425 (2003).
- [22] J. D. Hybl, A. Albrecht Ferro, and D. M. Jonas, *J. Chem. Phys.* **115**, 6606 (2001).
- [23] R. A. Nicodemus, K. Ramasesha, S. T. Roberts, and A. Tokmakoff, *J. Phys. Chem. Lett.* **1**, 1068 (2010).

Chapter 5

Ultrafast 2D IR Anisotropy of Water Reveals Reorientation during Hydrogen-Bond Switching

5.1 Introduction

The rapidly evolving structure of liquid water's hydrogen bond (HB) network is at the heart of aqueous physical processes, such as ion solvation, the hydrophobic effect, proton transport, chemical reactivity, and biological processes. While there is consensus over most time and spatially averaged characteristics of water, the underlying HB dynamics responsible for water's anomalous properties remain difficult to describe. Water's directional HB network undergoes femtosecond local fluctuations and picosecond structural reorganization [1]. It is believed that HB rearrangement is a cooperative event involving the reorganization of multiple hydrogen bonded molecules [2], a concept originally framed as transitions between "inherent structures" [3,4]. Although difficult to verify, experiments recently provided evidence that a HB donor molecule switches between HB acceptors in a single concerted process, passing through a bifurcated transition state [5–7]. Further, simulations of water models [8–10] and experiments on switching of HBs to solvated ions [11,12] indicate that

hydrogen bond connectivity changes by large angle jump reorientation. Classical molecular dynamics (MD) simulations describe the fluctuations in HB donor and acceptor coordination number that enable the formation of a bifurcated HB transition state, and exhibit an average jump angle of 68° [8]. Other less probable switching mechanisms in simulations have also been described [13], but all proposed mechanisms of HB exchange involve a large angle reorientation of the switching water molecule.

Here we present experimental evidence for the picture of ultrafast HB switching by large angle reorientation in water. To describe the degree of reorientation of a water molecule while shifting HB environments, we use ultrafast two-dimensional infrared (2D IR) spectroscopy of the OH stretching vibration of dilute HOD in D_2O [14,15]. The OH stretch vibrational frequency ($\langle\omega_{OH}\rangle = 3400\text{ cm}^{-1}$) is a sensitive reporter of HB environment, with lower (red) frequencies ($\omega_{OH} < 3400\text{ cm}^{-1}$) corresponding to water molecules in strong, linear hydrogen bonded configurations, and higher (blue) frequencies ($\omega_{OH} > 3500\text{ cm}^{-1}$) corresponding to those in broken or strained hydrogen bonded configurations (non-HB or NHB) [14–16]. 2D IR spectroscopy provides the ability to correlate time-evolving spectral features and chemical exchange with ultrafast time resolution. Previous 2D IR experiments have shown that water molecules in NHB configurations undergo inertial relaxation to stable HB configurations within 150 fs, indicating a concerted hydrogen bond switching process and the absence of dangling HBs in water [5]. While ω_{OH} shows reasonable correlation with hydrogen bond length, its correlation with hydrogen bond angle is weak, especially for the large angles that exist during HB switching [15]. Therefore, we employ polarization-sensitive 2D IR

measurements to characterize changes in OH transition dipole orientation during HB fluctuations and rearrangements [17].

The recent proposal that HB rearrangement involves large angle molecular reorientation, leads to the prediction that time-dependent ω_{OH} spectral shifts during hydrogen bond exchange should be correlated with inertial OH rotation [7,9]. Information on ultrafast molecular reorientation is commonly obtained in the form of a rotational anisotropy, $r(\tau) = 0.4 P_2 \langle \boldsymbol{\mu}(\tau) \cdot \boldsymbol{\mu}(0) \rangle$, that is extracted from polarization sensitive experiments, where P_2 is the second Legendre polynomial orientational correlation function and $\boldsymbol{\mu}(\tau)$ is the orientation of the molecular dipole at a given time τ . Simulations and pump-probe (PP) measurements have revealed a dependence of the inertial anisotropy decay on detection frequency [14,18–21]. However, pump-probe anisotropy measurements cannot correlate anisotropy with both initial and final hydrogen bond configuration with high enough time resolution to follow hydrogen bond switching. To overcome these obstacles, we made measurements of the 2D IR spectral anisotropy as a function of both excitation and detection frequency to study the inertial orientational dynamics of water. Earlier measurements of the 2D anisotropy of aqueous ions [11,12] and calculations of the 2D anisotropy of water [7,9] have revealed the advantage of the technique in understanding the rotational dynamics of water. 2D IR anisotropy is related to the joint probability of exciting the OH oscillator at a frequency ω_1 and observing an anisotropy r at frequency ω_3 , after a waiting time τ_2 . The results presented here provide clear signatures of heterogeneous reorientational motion on timescales <400 fs. Simulation of the experiment with a well characterized water model allows us to interpret the origin of the spectrally varying anisotropy in terms of specific dynamic events.

Further, we quantify the average angular changes experienced by different configurations during the inertial period, providing evidence that the rapid return of NHB configurations to hydrogen bonded geometries is associated with large angle reorientation.

5.2 Methods

5.2.1 Experimental

Experiments used a home-built optical parametric amplifier which generates 45 fs pulses centered at 3400 cm^{-1} , having a 350 cm^{-1} bandwidth with pulse energy of $5\text{ }\mu\text{J}$, as detailed in Ref. [22]. For the double-differential 2D IR anisotropy measurements, we constructed a pump-probe Fourier transform 2D interferometer [23] that provided simultaneous balanced detection of parallel (ZZZZ) and perpendicular (YYZZ) spectra. A $\sim 5\%$ reflection of the IR beam was split to make the probe pulse, which was sent to a delay stage for scanning the waiting time (τ_2). The remaining IR beam was equally split and recombined in a Mach-Zehnder interferometer to create the collinear pump pair for the 2D experiment. One of the pump beams was sent to a delay stage (Aerotech), and stepped in 2 fs intervals until 400 fs, to generate the excitation (τ_1) axis. The other fixed pump beam was chopped at half the laser repetition rate. The beams were focused and crossed in the sample, with a spot size of $100\text{ }\mu\text{m}$ at the sample.

The HOD/D₂O sample was made by adding $\sim 1\%$ by volume of H₂O (de-ionized, 18 M Ω resistance) to D₂O (99.96% purity from Cambridge Isotope Laboratories, Inc.), such that the OH stretch absorbance at 3400 cm^{-1} was always kept below 0.4 to minimize re-absorption contributions to the signal. For acquiring 2D IR anisotropy, the HOD/D₂O

sample was held between 1 mm thick CaF₂ windows, with a path length of 100 μm. Due to non-resonant effects from CaF₂ windows, we show 2D IR anisotropy for $\tau_2 > 100$ fs. To acquire dispersed pump-probe spectra, we simply blocked the non-chopped pump beam and scanned the probe beam. For the dispersed pump-probe experiments, the sample was held between 100 nm thick Si₃N₄ windows (Norcada) to eliminate non-resonant signal, allowing us to access < 100 fs time delays.

Tunable zero-order half-waveplates (Alphas) and wire-grid polarizers (Molelectron) controlled the polarization of each beam, and were calibrated with respect to an analyzing polarizer placed at the sample position prior to data collection. The polarizations of the two pump beams were oriented at 0° (*Z*) and the probe was oriented at 45° with respect to the pump beams. After passing through the sample, the probe was split into two arms with a 50/50 beamsplitter. One arm passed through a polarizer oriented parallel (*Z*) to the pump beams to acquire *ZZZZ* surfaces, and the other arm passed through a polarizer oriented perpendicular to the pump beams (*Y*) to acquire *YYZZ* surfaces. Each of the two arms was dispersed in a monochromator and imaged onto one stripe of a 2 x 64 element liquid nitrogen cooled MCT array (Infrared Systems) with a 16 cm⁻¹/pixel resolution, which provided the ω_3 dimension of the 2D IR spectrum. After the analyzing polarizer in the perpendicular arm of the probe, a waveplate-polarizer pair was used to rotate the probe to 0° to ensure that the detected spectra were free of artifacts due to the polarization dependence of the grating diffraction efficiency. We also normalized for pixel sensitivities between the two stripes of the array before calculating anisotropy by multiplying the signal on one of the stripes by the ratio of the probe spectra from the two stripes.

The $ZZZZ$ and $YYZZ$ τ_1 - ω_3 surfaces were Fourier transformed in the τ_1 dimension to obtain the absorptive (real) 2D IR spectra. Prior to this transformation, the constant pump-probe background in the τ_1 dimension arising from the chopped pump beam and the probe beam was subtracted, and a Hanning window was applied in τ_1 to minimize noise. The error in determining τ_1 (± 5 fs) was corrected for by adding a phase factor [24] during Fourier transformation upon invoking the projection-slice theorem [25,26]. At any given waiting time, this τ_1 correction factor was found to be the same for both the $ZZZZ$ and $YYZZ$ surfaces since they were acquired simultaneously. At every waiting time, the pump-probe or 2D anisotropy was obtained from the corresponding parallel (S_{ZZZZ}) and perpendicular (S_{YYZZ}) detected spectra using, $r = (S_{ZZZZ} - S_{YYZZ}) / (S_{ZZZZ} + 2S_{YYZZ})$. A Kramers-Kronig assumption was used to obtain the imaginary part of the 2D spectrum and the 2D power spectrum [27,28]. 2D anisotropy surfaces were then calculated for each (ω_1, ω_3) point for both real and power spectra. In this paper, we present one set of data obtained from averaging 4-6 surfaces at every waiting time, for each polarization geometry. This data set is representative of all the 2D anisotropy spectra we have taken on this system.

We corrected for the thermally shifted ground state (TSGS) in the dispersed pump-probe data using a method very similar to those outlined in Refs. [29–31]. Using the $ZZZZ$ and $YYZZ$ dispersed pump-probe spectra at our longest waiting time of 8.5 ps, we calculated the isotropic TSGS spectrum. We let the TSGS spectrum grow mono-exponentially with a 2 ps timescale. We found that including an intermediate state [29] for the OH stretch relaxation had negligible effect on the <100 fs inertial dynamics. We subtracted the TSGS spectrum at every waiting time from both $ZZZZ$ and $YYZZ$ spectra

and proceeded to calculate dispersed pump-probe anisotropy from these corrected spectra. The librational dynamics we see on <100 fs timescale were insensitive to the picosecond timescale that characterized the growth of the TSGS. TSGS contributions to 2D IR anisotropy were found to be negligible at <1 ps waiting times, and therefore the 2D anisotropy data reported in this paper do not include this correction.

5.2.2 Simulations and modeling

To assist in the interpretation of experimental data, we modeled the 2D IR and pump-probe anisotropy of HOD/D₂O using molecular dynamics simulations of SPC/E water and a mixed quantum-classical model for the OH vibrational spectroscopy that has been described elsewhere [15]. From the simulations, we extract instantaneous frequencies $\omega_{\text{OH}}(t)$ and the projection of the OH bond orientation onto the $i = x, y$ and z coordinates. Similar to prior calculations [14,15,32], we assume that the OH transition dipole is oriented along the OH bond axis and we account for the non-Condon effects by scaling the magnitude of the OH transition dipole based on an empirical mapping between it and the frequency of the OH bond: $\mu_{i,ab} = \hat{i} \cdot \hat{\mu} \langle a | \mu(\omega_{ab}) | b \rangle$ [33]. The trajectories are used to calculate rephasing (−) and non-rephasing (+) third order response functions [34,35] according to the semiclassical approximation [33].

$$\begin{aligned}
R_{\pm,ijj}^{(3)}(\tau_1, \tau_2, \tau_3) = & \text{Re} \left[2 \left\langle \mu_{10,i}(\tau_1 + \tau_2 + \tau_3) \mu_{10,i}(\tau_1 + \tau_2) \mu_{10,j}(\tau_1) \mu_{10,j}(0) \right. \right. \\
& \times \exp \left[\pm i \int_0^{\tau_1} \omega_{10}(\tau) d\tau + i \int_{\tau_1 + \tau_2}^{\tau_1 + \tau_2 + \tau_3} \omega_{10}(\tau') d\tau' \right] \left. \right\rangle \\
& - \left\langle \mu_{21,i}(\tau_1 + \tau_2 + \tau_3) \mu_{21,i}(\tau_1 + \tau_2) \mu_{10,j}(\tau_1) \mu_{10,j}(0) \right. \\
& \left. \times \exp \left[\pm i \int_0^{\tau_1} \omega_{10}(\tau) d\tau + i \int_{\tau_1 + \tau_2}^{\tau_1 + \tau_2 + \tau_3} \omega_{21}(\tau') d\tau' \right] \right\rangle \left. \right] \quad (5-1)
\end{aligned}$$

These two terms describe the time-dependent coupled vibrational-orientational dynamics for the $v = 0-1$ and $v = 1-2$ energy gaps that are resonant with the sequence of pulses in our experiments. Parallel (S_{\parallel}) and perpendicular (S_{\perp}) 2D IR spectra are obtained by averaging all the parallel and perpendicular components of the signal, $S_{\parallel} = (S_{XXXX} + S_{YYYY} + S_{ZZZZ})/3$ and $S_{\perp} = (S_{YYZZ} + S_{XXZZ} + S_{YYXX})/3$. Both rephasing and non-rephasing signals for each geometry are summed, Fourier transformed with respect to τ_1 and τ_3 to obtain 2D IR spectra, and used to calculate 2D anisotropy surfaces.

5.3 Results and discussion

5.3.1 Pump-probe anisotropy of HOD/D₂O

As an initial characterization of the inertial OH reorientation, we performed dispersed pump-probe anisotropy experiments with broadband excitation. These measurements follow the reorientation of water molecules that initiate at all possible HB configurations and are detected at frequencies (ω_3) corresponding to certain HB environments, after a waiting time, τ_2 . Figure 5-1a displays the ZZZZ and YZZZ dispersed pump-probe spectra before TSGS correction, and Figure 5-1b shows slices of

the dispersed pump-probe at 3400 cm^{-1} , following TSGS correction. Figure 5-2 shows time traces of pump-probe anisotropy at three detection frequencies, from experiment and simulation. Much like the broadband pump-probe anisotropy with integrated detection, transients at all detection frequencies showed bimodal relaxation corresponding to the inertial reorientation of the HOD molecule followed by collective molecular reorientation. [36] We find that the timescales observed are independent of detection frequency, but the relative amplitude of the components varies. After correcting for the thermally shifted ground state as described earlier, the experimental data were fit to double exponential decays with fixed timescales of 70 fs and 2.7 ps. These timescales agree with earlier measurements of the integrated pump-probe anisotropy. [30,36] We find that the amplitude of the inertial decay (A) increases monotonically with detection frequency ω_3 (Figure 5-2, lower left panel), indicating that molecules detected in strained configurations have experienced more orientational randomization during the inertial time-period than those detected in strong hydrogen bond configurations. [14,30]

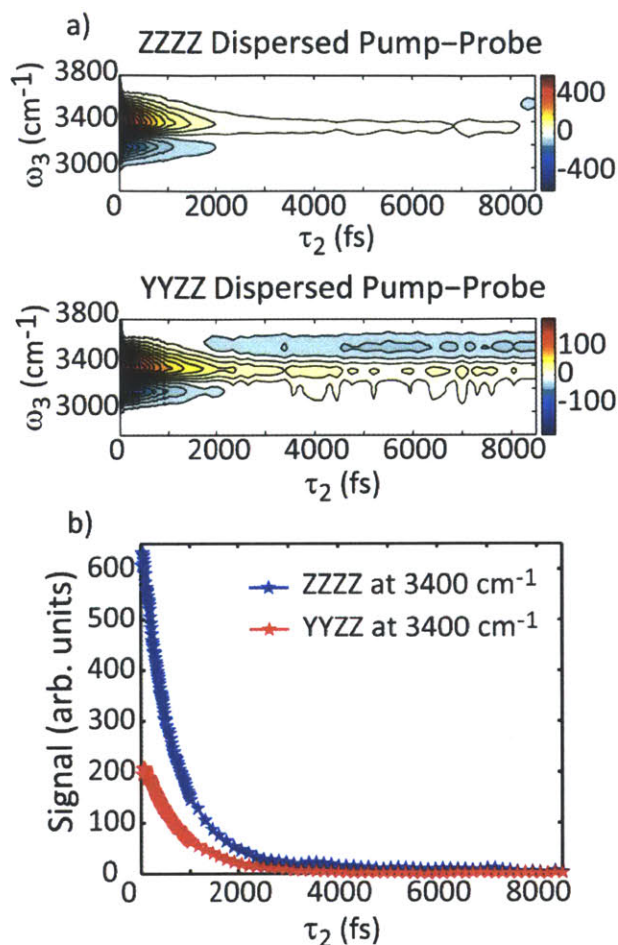


Figure 5-1: (a) Raw ZZZZ and YYZZ dispersed pump-probe of HOD/D₂O plotted against waiting time (τ_2), before TSGS correction; (b) 3400 cm $^{-1}$ slice of the ZZZZ and YYZZ dispersed pump-probe, after correcting for TSGS. A three-point rolling average was performed for waiting times of <400 fs.

Inertial reorientation includes rotational motion due to fluctuations about hydrogen bonded configurations and reorientation during hydrogen bond switching. Since these motions occur within a hindered environment, the orientational relaxation is incomplete until the global structure of the liquid reorganizes. We can quantify the degree of orientational motion of the OH transition dipole during the inertial period within the framework of restricted rotation models. [37–39]

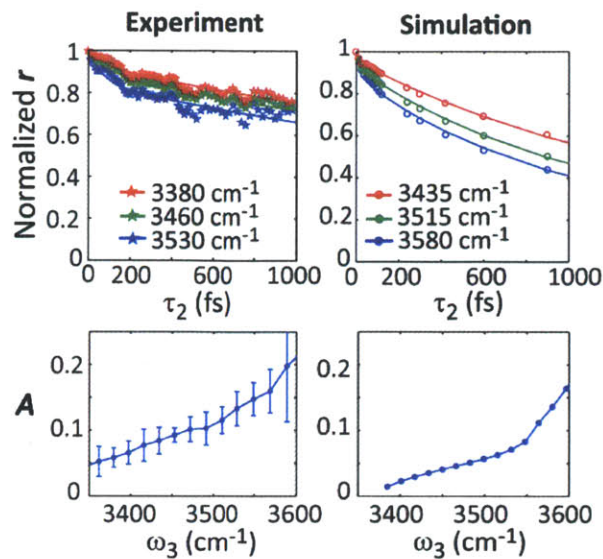


Figure 5-2: Experimental (left) and simulated (right) normalized pump-probe anisotropy of HOD/D₂O and the specified probe frequencies. The experimental traces were fit to a double exponential plus offset, with timescales of 70 fs and 2.7 ps, and pump-probe anisotropy from simulations were fit to the same function with timescales of 35 fs and 1.5 ps. For the experimental data, a rolling average was performed for short time delays, upon subtracting the hot ground state contribution from ZZZZ and YYZZ spectra; Lower panel shows the amplitude of the inertial decay as a function of probe frequency. Error bars in the experimental plot indicate the standard deviation across four independent measurements.

We study two models of restricted reorientation, which are described in terms of the restricted orientational probability distribution $p(\theta)$, that defines the angular configurations allowed during inertial relaxation. The upper panel of Figure 5-3 shows the potentials of mean force for the hard cone and the harmonic cone probability distributions. From these models, we obtain the generalized order parameter, S , which characterizes the extent of angular motion during the inertial period

$$S = \left[\int d\Omega p(\theta) P_2(\cos\theta) \right] / \left[\int d\Omega p(\theta) \right] \quad (5-2)$$

Here, Ω refers to spherical coordinates (θ, ϕ) and $\int d\Omega = \int d\phi \int \sin\theta d\theta$. In the harmonic cone model, [18] the degree of restricted rotation is characterized by θ_H as described by $p(\theta) = \exp[-\theta^2/2\theta_H^2]$. For the hard cone model [37–39], $p(\theta)$ imposes an abrupt angular cut-off to orientational excursions greater than the half-cone angle θ_0 . The generalized order parameter for the hard cone model can be simplified to,

$$S_{HC} = \frac{\int_0^{2\pi} d\phi \int_0^{\theta_0} \sin\theta \cdot P_2(\cos\theta) \cdot d\theta}{\int_0^{2\pi} d\phi \int_0^{\theta_0} \sin\theta \cdot d\theta} = \frac{\cos\theta_0(1 + \cos\theta_0)}{2} \quad (5-3)$$

Since the amplitude of the fast anisotropy decay, A , is the residual anisotropy following inertial relaxation, we equate $A=1-S^2$, and use S to determine θ_0 and θ_H for both restricted reorientation models. The average angular deviations during the inertial period can be obtained using the mean half-cone angle

$$\langle\theta\rangle = \left[\int d\Omega \theta p(\theta) \right] / \left[\int d\Omega p(\theta) \right], \quad (5-4)$$

whereas the extent of large excursions in angle can be quantified through the half-cone angle θ_0 , or through $2\theta_H$, the half-angle that contains 95% of inertial angular excursions. We found that the calculated $\langle\theta\rangle$ for both the harmonic cone and hard cone model were nearly identical, and that the deduced hard cone angle was the same as the two standard deviations in the harmonic cone model, $2\theta_H \approx \theta_0$. For this reason we only report angular changes in terms of the harmonic cone model.

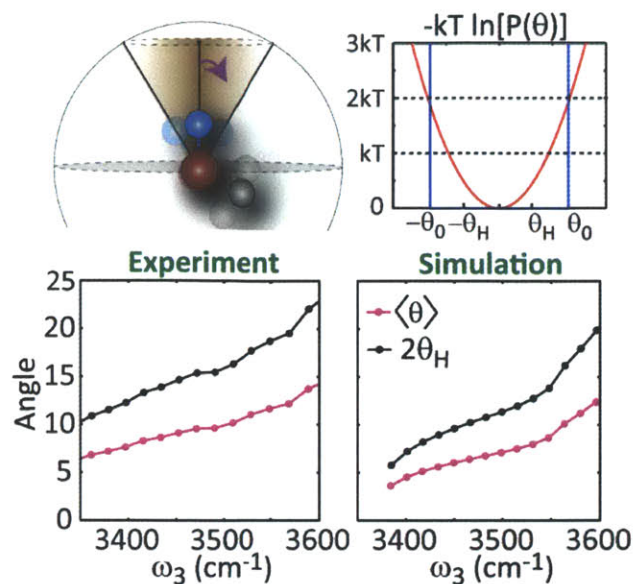


Figure 5-3: Cartoon of restricted rotation model (top left). Potential of mean force for the hard cone (blue) and the harmonic cone (red) models (top right). Average angles and two standard deviations of the half-cone angle calculated from the inertial decay of measured and simulated pump-probe anisotropy (bottom), based on harmonic cone analysis.

Figure 5-3 displays the average OH angular changes and large excursions during the inertial period as a function of detection frequency ω_3 . The experimental mean angular changes for the harmonic and hard cone models show a modest increase with ω_3 , from $\sim 7^\circ$ at 3380 cm^{-1} to $\sim 12^\circ$ at 3550 cm^{-1} , and the $2\theta_H$ excursions vary from $\sim 10^\circ$ to $\sim 23^\circ$ over the same range. The $2\theta_H$ values are lower than the angles that Bakker and co-workers calculated by applying a hard cone model to their narrowband pump-probe anisotropy of HOD/D₂O, where they report a 20-28° range. [20] However, the average harmonic cone angles are similar to those that Moilanen et al. calculated for the OD stretch of HOD/H₂O from broadband pump-probe measurements. [18] These observations demonstrate that, upon inertial relaxation, molecules detected in stable HB

configurations undergo reorientation to a lesser extent than those detected in strained configurations.

For free rotation, the harmonic cone angle can be related to the HOD moment of inertia I and the angular frequency ω_{rot} by $\theta_H^2 = k_B T / I \omega_{rot}^2$. [18] Using the value $I = 2.847 \times 10^{-47} \text{ kg m}^2$, angular frequencies are calculated to vary from $\sim 670\text{-}330 \text{ cm}^{-1}$, as a function of increasing detection frequency ω_3 . The frequency range agrees with the broad infrared signature of the HOD librational band. [40–44]

5.3.2 2D IR anisotropy of HOD/D₂O

A waiting time series of ZZZZ and YYZZ 2D IR spectra are displayed in Figure 5-4. Both polarizations show an asymmetrically broadened lineshape at early waiting times as described previously. [5,24] The increased antidiagonal line width for blue side excitation reflects the $<150 \text{ fs}$ spectral relaxation of NHB species toward stable hydrogen bond configurations, and the lack of any persistent dangling HB species. The differences in lineshapes between $S_{||}$ and S_{\perp} are subtle, with the most visible difference being the smaller slope of the node between the positive $v = 0\text{-}1$ and negative $v = 1\text{-}2$ transitions in perpendicular spectra. Since the nodal slope is a measure of loss of frequency correlation, [45–47] the difference between ZZZZ and YYZZ surfaces points to a correlation of frequency and orientational HB dynamics.

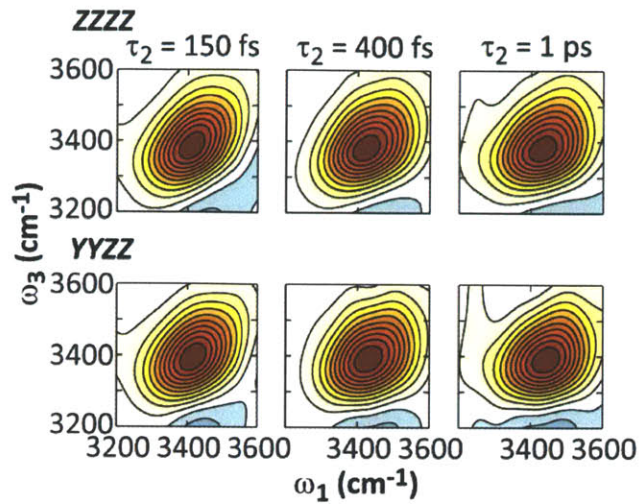


Figure 5-4: 2D IR surfaces of HOD in D₂O in the ZZZZ and YYZZ polarization geometries, normalized to their maximum amplitudes, with linearly spaced contours. The ratio of the maximum amplitude of ZZZZ to ZZYY at 150 fs was 2.94.

2D anisotropies can be calculated from a number of representations, of which those obtained from 2D IR absorptive and 2D IR power spectra for $\tau_2=250$ fs are compared in Figure 5-5. As a result of the positive and negative features in the absorptive spectrum, the resulting 2D anisotropy contains distortions that arise from the singularity along the nodal line. For this reason we also analyze the anisotropy obtained from 2D power spectra, which retains a similar anisotropy profile without the distortions near the node. Comparison of the anisotropy profiles, with contour lines placed at anisotropy intervals of 0.01, provide an estimate of the degree of uncertainty that exists in quantitatively interpreting the data. Representative 2D IR anisotropies obtained from measured real spectra are shown in Figure 5-6a for four waiting times. The anisotropy is color coded and the underlying lineshape of the isotropic spectrum, $S_{iso} = (S_{||}+2S_{\perp})/3$, is represented by solid contour lines. The corresponding anisotropies obtained from power spectra are

shown in Figure 5-7a. We analyze relaxation within four quadrants of the 2D anisotropy, which vary by excitation and detection frequency, referring to frequencies $<3400\text{ cm}^{-1}$ as “red” and frequencies $>3500\text{ cm}^{-1}$ as “blue”.

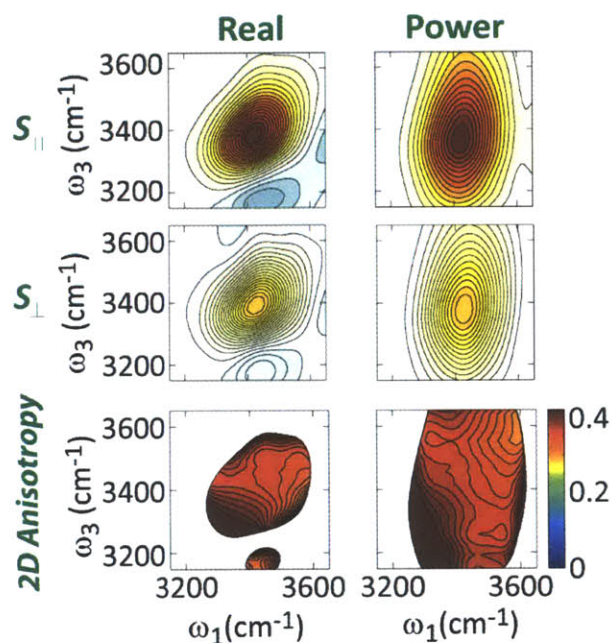


Figure 5-5: Absorptive (left) and power (right) 2D IR spectra of HOD in D₂O at $\tau_2 = 250$ fs, for ZZZZ (top row) and YYZZ (second row) polarizations. Corresponding 2D IR anisotropy calculated from real absorptive (bottom left) and power (bottom right) spectra. Contours represent a change in anisotropy of 0.01.

Formally the 2D anisotropy is related to a four-point joint correlation function in the OH dipole moment. [48,49] It remains a challenge to interpret nonlinear spectra in which rotational and vibrational degrees of freedom are coupled, since general models for this case have not yet been established.

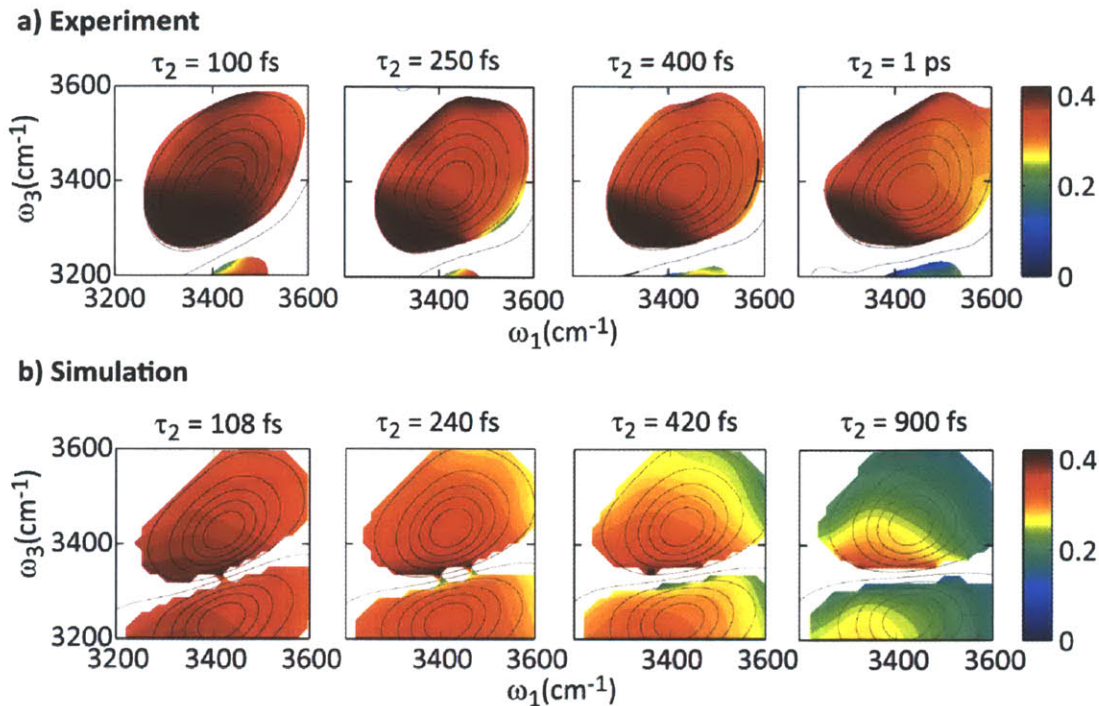


Figure 5-6: 2D IR anisotropy spectra of HOD/D₂O calculated from absorptive ZZZZ and YZZZ 2D IR spectra from (a) experiment and (b) simulations, at four different waiting times. Anisotropy is color-coded to represent a change of 0.01, and contour lines show the shape of the underlying isotropic spectra. These spectra have been truncated to eliminate (ω_1 , ω_3) data points where the magnitude of the isotropic response is less than 8% of its maximum value.

To initially simplify the analysis, we make the approximation that reorientational and vibrational dynamics during τ_1 and τ_3 are negligible, so that rotation can be completely described in terms of the two-point correlation function $\langle P_2[\mu(\tau_2) \cdot \mu(0)] \rangle$. We use restricted rotation modeling to provide quantitative estimates of the angular deviations of water molecules upon changing HB environment. To this end, we equate the residual anisotropy values from the four quadrants of the 2D anisotropy surface following the inertial decay ($\tau_2 = 100$ fs) to the square of the generalized order parameter, S^2 .

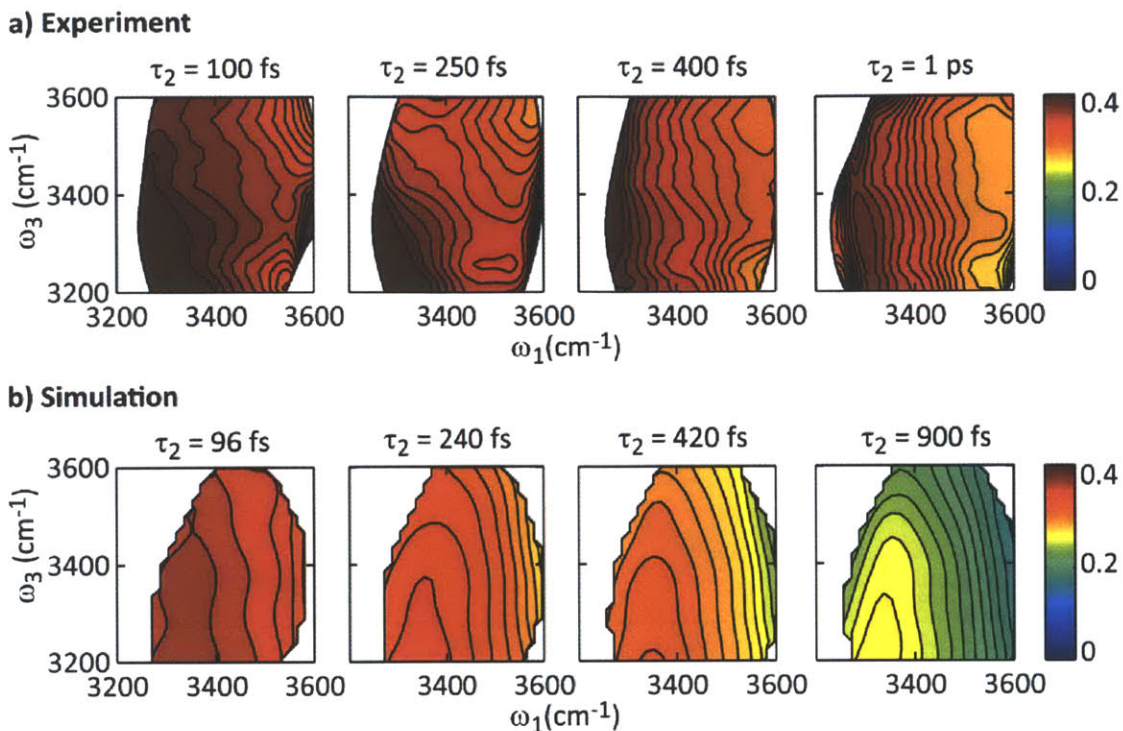


Figure 5-7: 2D IR anisotropy spectra for HOD in D₂O from (a) experiment and (b) simulation, at various waiting times. Each contour represents a change in anisotropy of 0.01. These spectra have been truncated to eliminate (ω_1 , ω_3) data points where the magnitude of the isotropic response is less than 10% of its maximum value.

Along the diagonal, the 2D anisotropy obtained from both real and power spectra drops from red to blue, indicating that water molecules in strong HB configurations are more orientationally constrained than those in strained and bifurcated configurations. The red-to-red ($\omega_1 = \text{red}$, $\omega_3 = \text{red}$) region corresponds to molecules that persist in stable HB configurations, and the value of $r = 0.4$ at $\tau_2 = 100$ fs indicates that these molecules do not reorient during the inertial period (within our experimental uncertainty in r of $\pm 5\%$). The blue-to-blue region, which corresponds to molecules that initiate and end in unstable configurations, shows the most orientational randomization.

Off-diagonal regions of the 2D anisotropy reflect orientational changes that accompany shifts in HB environment. In the blue-to-red region of the 2D anisotropy, we probe molecules that initiate in unstable configurations, including those undergoing HB switching, large amplitude librations, and hydrogen bond extension, and subsequently relax to a stable HB configuration. In this region of the 2D anisotropy from both real and power spectra, inertial relaxation is characterized by the anisotropy value of 0.37 for $(\omega_1, \omega_3) = (3550 \text{ cm}^{-1}, 3350 \text{ cm}^{-1})$ at $\tau_2 = 100 \text{ fs}$, which corresponds to average rotational relaxation of $\langle\theta\rangle \sim 10^\circ$. Since this corresponds to relaxation of an unstable NHB configuration to a HB configuration, the angle represents half the full extent of orientational excursion. Given that this angle averages over successful and non-successful switches and translational HB fluctuations, this implies that water molecules shifting from strained to stable hydrogen bonding environment reorient by a mean angle of at least 20° , with HB switching angles probably being considerably larger. The $\tau_2 = 100 \text{ fs}$ red-to-blue anisotropy calculated from power spectra, obtained for $(\omega_1, \omega_3) = (3350 \text{ cm}^{-1}, 3550 \text{ cm}^{-1})$ leads to $\langle\theta\rangle \sim 5^\circ$, which is smaller than the angles we obtained in the blue-red quadrant. The red-to-blue anisotropy calculated from real spectra show larger angles of $\sim 10^\circ$, but due to low signal-to-noise in this quadrant of the real spectra, we place large error bars on these numbers.

On longer timescales, the 1 ps blue-to-red anisotropy of 0.28 from power spectra indicates that OH dipoles initially in NHB configurations diffuse to sample an average half-cone angle of $\sim 18^\circ$ within the first picosecond. Blue-to-red anisotropy of 0.3 from real spectra, similarly translates to a $\langle\theta\rangle \sim 17^\circ$. However, those molecules initially excited

in strong HB configurations barely change their orientation ($r \sim 0.4$), indicating that there are a significant number of HBs that remain intact for a few picoseconds. Since the 1 ps waiting time is on the order of spectral diffusion timescales for the OH stretch of HOD/D₂O, the contour lines in the 2D anisotropy become almost parallel to the ω_3 axis and equally spaced in ω_1 , indicating that the rate of anisotropy decay is spectrally independent from this time forward. The vertical orientation of these contour lines means that at any given ω_1 , the anisotropy is the same across all ω_3 , suggesting that all water molecules behave similarly after about 1 ps.

Figure 5-8a shows the waiting time-dependent decay of the anisotropy in each quadrant. As expected, the red-to-red anisotropy remains high at even longer waiting times due to the persistence of stable HBs, while the blue-to-blue anisotropy is relatively low at all waiting times due to the transient NHB species. Anisotropies for molecules initiating blue are consistently lower than for those that initiate red. Figure 5-9 shows the comparison between the average and largest angles ($2\theta_H$) from the 100 fs 2D anisotropy surfaces using restricted rotation modeling. The angles extracted from the $\omega_1 = 3550 \text{ cm}^{-1}$ slice are larger than those from the $\omega_1 = 3350 \text{ cm}^{-1}$ slice of the 2D anisotropy. These results indicate that HB switching from a strained HB to a stable HB, on average, proceeds by an angular reorientation of $\geq 20^\circ$.

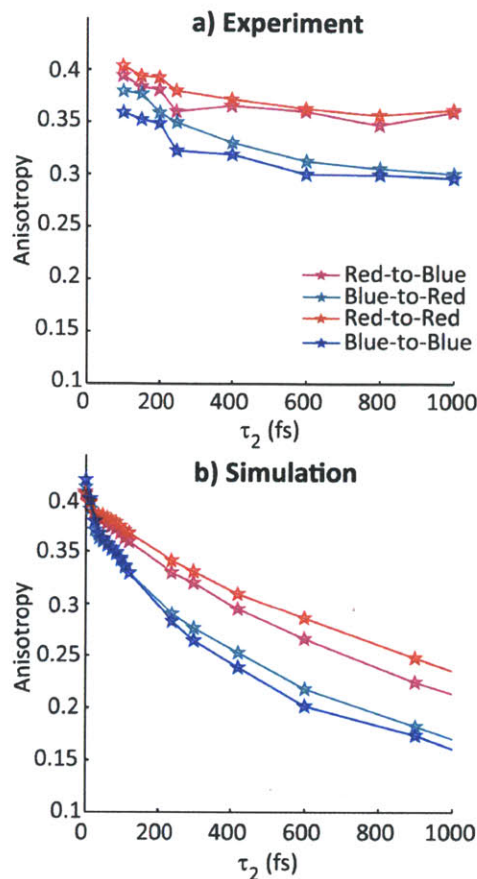


Figure 5-8: (a) Experimental and (b) simulated waiting time behavior of the four quadrants of the 2D IR anisotropy calculated from 2D IR power spectra. These quadrant anisotropies were calculated by integrating a 50 cm^{-1} -by- 50 cm^{-1} box in corresponding quadrants of the 2D anisotropy surface, and normalizing to the number of data points in the respective box. “Red” refers to $3350\text{-}3400 \text{ cm}^{-1}$ for experimental anisotropies and $3400\text{-}3450 \text{ cm}^{-1}$ for the simulated anisotropies (to account for the shifted OH stretch absorption in simulations). “Blue” refers to $3500\text{-}3550 \text{ cm}^{-1}$ for experiments and $3550\text{-}3600 \text{ cm}^{-1}$ for simulated anisotropies.

The frequency-dependent trends in our quadrant anisotropy results are consistent with the frequency-resolved narrow band pump-probe anisotropy trends that Bakker and co-workers observe, with red-to-red anisotropy being the highest and the blue-to-blue anisotropy being the lowest [19]. However, our results do not display the timescales

reported in their paper. Unlike the differences in picosecond timescales they report between the blue-to-blue and the red-to-red pump-probe anisotropies, we primarily see frequency dependence to anisotropy on much shorter inertial timescales. Our results are however consistent with broadband pump-probe anisotropy measurements by Moilenen et al. [18], where they also observe the largest frequency dependence in anisotropy to be during the <100 fs inertial time period. The frequency dependent trends we see in our simulations and experiments on HOD/D₂O are in contrast with the narrow band pump-broadband probe experiments on HOD/H₂O by Bakker et al. [20], where they report higher blue-to-blue anisotropy compared to blue-to-red anisotropy at a waiting time of 200 fs. Gaffney and co-workers have measured 2D difference spectra between parallel and perpendicular 2D IR spectra of aqueous ions in order to understand the kinetics of exchange via jump reorientation between ions and water molecules, and estimate these jump angles [11,12].

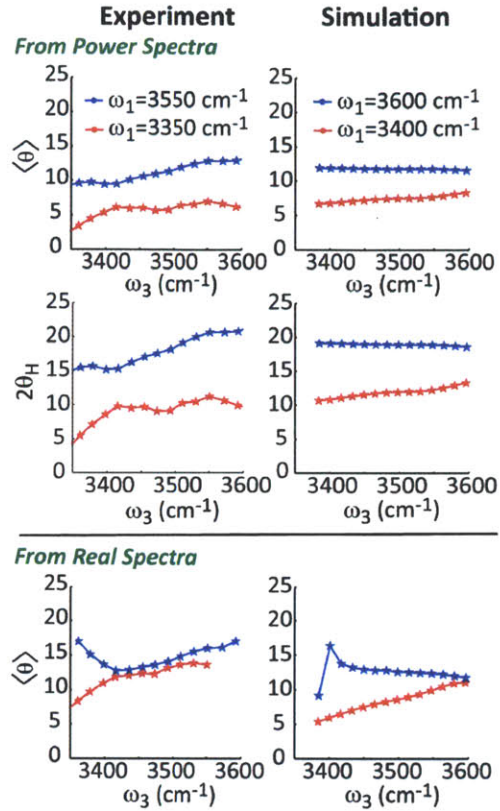


Figure 5-9: Average angular deviations extracted from $\omega_1 =$ “red” and $\omega_1 =$ “blue” slices of 2D IR anisotropy from experiment (left) and simulation (right), at $\tau_2=100$ fs using the harmonic cone model. Average angles (top row) and two standard deviations (middle row) were calculated based on 2D IR anisotropy from power spectra. Average angles from 2D IR absorptive spectra are also shown (bottom row). Average angles calculated from the hard cone model (not shown) are close-to identical to those calculated from the harmonic cone model. Also, we found that the hard cone angle $\theta_0 \approx 2\theta_H$.

They extract average jump angles of $\sim 50^\circ$ from their modeling of picosecond reorientation of water molecules switching to form HBs with ions. Since we adopt a different approach to extracting angles, and are primarily concerned with sub-picosecond inertial dynamics in water, we measure smaller cone angles for HB exchange in water.

5.3.3 Comparison to MD simulations

To better understand how the underlying hydrogen bond dynamics are reflected in the experiment, it is helpful to compare to the known dynamics of the SPC/E water model, which exhibits concerted hydrogen bond switching with jump reorientation [8]. The mixed quantum-classical spectroscopic model used here has qualitatively reproduced many of the features of the OH vibrational spectroscopy [5,15,46,50], although the timescales for spectral relaxation are significantly shorter (600 fs [15]) than those observed in experiments.

Figure 5-2 (top right) shows simulated frequency-dependent pump-probe anisotropy calculated using methods described in section IIb. Simulated pump-probe anisotropy shows a <50 fs inertial component and a 2.3 ps long time relaxation, which has been attributed to the collective reorientation of water molecules. Calculations of frequency-resolved P_2 and pump-probe anisotropy from MD simulations have been performed before using similar methodology [14,18,21,51]. These calculations have revealed that the frequency dependence to orientational relaxation exists primarily during <50 fs inertial timescales, with negligible frequency dependence to the picosecond rotation dynamics, reflecting the fact that spectral diffusion timescales are faster than timescales of collective reorientation. Moreover, Lin et al. have pointed out that including the non-Condon effect and the 1-2 transition in a full response function calculation of pump-probe anisotropy diminishes the amplitude of the <50 fs inertial decay and consequently, raises the anisotropy values at longer waiting times [51]. These calculations were shown to agree better with experimentally measured anisotropy compared to P_2 .

Similar to our analysis of experimental pump-probe anisotropy, we applied restricted rotation modeling to extract inertial angles from simulated pump-probe anisotropy. To be consistent with our analysis of the experimental data, we fit the simulated pump-probe anisotropy decay with a double exponential plus offset until a waiting time of 2.5 ps, with fixed timescales of 35 fs and 1.6 ps, varying only the amplitudes. Like in our experimental pump-probe anisotropy, the inertial decay amplitude increases with increasing detection frequency as displayed in the lower right panel of Figure 5-2. The bottom right panel of Figure 5-3 displays the calculated angles from simulated pump-probe anisotropy. The angles we extract from simulations vary in $\langle\theta\rangle$ from $\sim 3^\circ$ to $\sim 12^\circ$ and in $2\theta_H$ from $\sim 5^\circ$ to $\sim 20^\circ$, which are similar to the angles calculated from the experimental data. The resulting frequency dependence to the calculated inertial decay amplitudes shown in Figure 5-2 are also consistent with the trends calculated by Lin, et al. for the HOD/H₂O system. However, we see a steeper dependence of the inertial decay amplitude on detection frequency than reported in Ref. [51]. Laage and Hynes applied the hard cone model to <100 fs frequency dependent amplitudes from P_2 and calculated larger θ_0 ($2\theta_H$) – varying from 14° to 36° across the OH stretch band [21]. The differences in the angles reported in these studies is likely due to the variations in the definitions used for the inertial reorientation amplitude.

Figures 5-6b and 5-7b show the 2D IR anisotropy of HOD/D₂O obtained from real and power spectra, respectively, calculated from MD simulations. The results in Figure 5-6b are consistent with previous calculations of anisotropy obtained from absorptive spectra [7,9]. There are a number of qualitative similarities between the simulations and experiments, as well as some conspicuous quantitative differences. Both show that blue-

excitation followed by blue-detection leads to the lowest value anisotropies, while red-to-red anisotropies are highest. Similar to our experimental observations, the 2D anisotropy calculated from the power spectra are asymmetric about the diagonal, with slightly lower anisotropies observed in the blue-to-red quadrant compared to the red-to-blue quadrant. They share similar anisotropy contours, although the predicted values differ from experiment. The anisotropy values differ less from experiments at shorter waiting times than at longer waiting times. Also, for picosecond timescales, vertical contours are observed for blue-excitation, indicating that although some residual alignment still exists, memory of the initial frequency has vanished.

Figure 5-8 displays the experimental and simulated anisotropies from the four quadrants of the 2D anisotropy as a function of waiting time. Both experimental and simulated spectra tend toward the expected value of 0.4 at $\tau_2 = 0$, and show little indication of inertial response for time scales ≤ 100 fs. For both, the anisotropy decays observed for $\tau_2 < 400$ fs for red excitation is slower than for blue excitation, and relaxation for all quadrants occurs at the same rate by 1 ps. This confirms that the faster time scale of spectral diffusion acts to homogenize the observed relaxation considerably faster than orientational relaxation. It is also striking that the calculated 2D anisotropies show little <100 fs inertial response, when the calculated P_2 orientational correlation functions show a 25% decay within 100 fs [36], with higher inertial contributions for blue excitation [14,21].

The differences between experimental and simulated spectra are most prominent at longer waiting times, where simulations underestimate the anisotropy amplitudes. The magnitude of orientational fluctuations at short times and the rate of orientational

relaxation as viewed through the 2D anisotropy are both higher in simulated spectra than in experiment. There are also different anisotropy contours observed in simulations for $\tau_2 < 200$ fs, where inertial reorientation dominates.

It is clear from these results that both experiments and simulation show 2D anisotropies with off-diagonal asymmetry, especially in those derived from power spectra. Within linear response and microscopic reversibility arguments, one expects red-to-blue and blue-to-red anisotropies to be equal. However it is difficult to discount the possibility that red-to-blue orientational relaxation has more HB fluctuations persisting about the stable linear configuration than the blue-to-red relaxation, leading to a smaller distribution of angles during the inertial period. This asymmetry could also be a result of blue excitation containing a significant fraction of bifurcated configurations, many of them switching, that undergoes large angle reorientation to return to a stable configuration.

In practice, quantitative analysis of polarization dependent nonlinear experiments is also complicated by interference effects between the $v = 0-1$ and $v = 1-2$ resonances. We used the simulations to better understand how the 2D spectral anisotropy can be distorted in different representations of the data. The 2D anisotropy from real and power spectra were also calculated for just the $v = 0-1$ transition (two-level system) using only the first term in Eq. (5-1). Figure 5-10 compares the 2D anisotropy for the two-level and three-level systems calculated from real and power spectra. The 2D anisotropy derived from the real spectra using only the $v = 0-1$ transition is symmetric about the diagonal, as expected from the linear response approximation upon which these calculations are based. This is the most accurate representation of the orientational dynamics of the

model. However, for the same system, calculating the 2D anisotropy from power spectra breaks this symmetry as a result of the added contribution of the imaginary spectrum, which is not symmetric about the diagonal. This results in a higher red-to-blue anisotropy than what is measured in the blue-to-red quadrant.

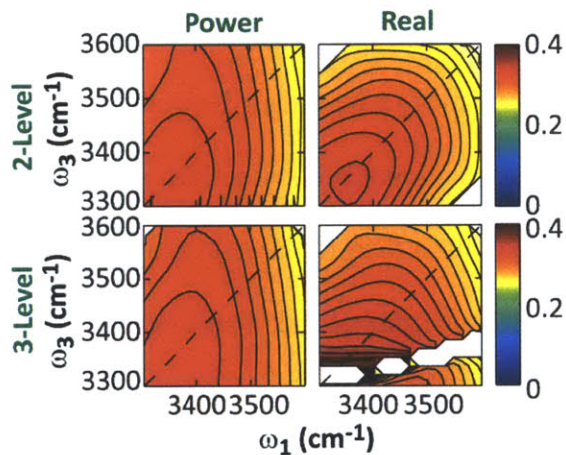


Figure 5-10: Comparison of different representations of 2D IR anisotropy from simulations at $\tau_2 = 300$ fs. 2D anisotropy for the two-level system (not including the $v = 1-2$ transition) are shown in the upper row, and 2D anisotropy for the three-level system are shown in the bottom row. 2D anisotropy for each system was calculated both from the absorptive (left) and power (right) 2D IR spectra. Each contour represents a change in anisotropy of 0.01.

We also see that the anisotropy values along the diagonal are accurate, and the blue-to-red quadrant more faithfully reproduces the off-diagonal anisotropy from the real spectrum. The 2D anisotropy for the full three-level system from both real and power spectra are inherently asymmetric about the diagonal owing to the contribution from the anharmonically shifted $v=1-2$ transition. For the three-level system, the red-to-blue quadrant in the real spectra and the diagonal axis accurately reproduce the underlying

dynamics seen in the two-level system. Since anisotropy calculated from power spectra for both the two- and three-level calculations are almost indistinguishable, the blue-to-red quadrant of the 2D anisotropy from power spectra most accurately reproduces the off-diagonal anisotropy in the two-level 2D anisotropy calculated from real spectra.

As another measure of how the experiment reflects the underlying angular changes, we applied the restricted orientation analysis to the 2D anisotropies calculated from simulations of the 2D IR real and power spectra at $\tau_2 = 96$ fs (Figure 5-9). Overall the average angular changes observed in experiments do not differ greatly from simulations. In both, average angular excursions for red and blue side excitation obtained from power spectra are roughly 6° and 12° , respectively. From the analysis of simulations, both real and power spectrum anisotropies predict similar inertial angular changes ($3\text{-}4^\circ$) across the OH lineshape. Like the experiments, the simulations predict an increase in average observed reorientation with detection frequency for red excitation in 2D experiments, and in pump-probe anisotropies. However, the blue-to-red anisotropy remains fairly flat across ω_3 . These similarities seen in Figure 5-9 indicate that overall there is reasonable agreement between the inertial orientational dynamics in experiments and simulations.

This agreement between 2D anisotropy cone angles obtained from experiment and simulation is perhaps the best indication that the large angle reorientation during concerted HB switching seen in SPC/E water is consistent with the frequency dependent 2D anisotropies observed in simulations and experiments. The similarities in average angles plotted in Figure 5-9 show that, while these estimates seem to be small compared to the large angle reorientation predicted by earlier work on SPC/E water that reported switching angles of 50° or more [8], the values obtained from spectroscopic data are

skewed by molecules that undergo translational or small-angle fluctuations. Unlike earlier simulation work that used geometric criteria to isolate switching events and extracted larger angles [8], our ability to window switching events is limited by the sensitivity of OH stretch frequencies to such events. Since the OH stretch frequency, especially on the blue-side of the lineshape, displays weaker correlation with HB angle and intermolecular separation distances [15], our analysis invariably includes fluctuations that do not involve successful switching of HB partners. We therefore find it useful to also look at two standard deviations in the harmonic cone model (Figure 5-9), which corresponds to 95% of the inertial angular excursions, since that better represents the larger rotations a water molecule initiating from a given configuration can undergo. The blue-to-red $2\theta_{\text{H}}$ half-angle of $\sim 15^\circ$ and a $3\theta_{\text{H}}$ half-angle of $\sim 23^\circ$ implies that $\sim 5\%$ of the molecules shifting from blue to red undergo full rotation of greater than 30° , with $\sim 0.3\%$ of excursions that we experimentally measure being larger than $\sim 46^\circ$.

Regardless of the agreement between the cone angles obtained from simulations and experiments in the present work, there are still several factors that are not accounted for in simulations, which must be kept in mind when comparing simulated and experimental spectra. One factor is that classical simulations do not treat librations quantum mechanically. Water's librational band in the infrared spans a range of frequencies (~ 300 - 1000 cm^{-1}) that lie well above $k_{\text{B}}T$. Including quantum effects in describing librations have proven important for modeling infrared spectra and dielectric response [52–54]. A recent study concluded that including nuclear quantum effects in simulation of water reorientation provided quantitatively accurate results for frequency and orientational correlations [55,56]. A second factor to remember is that our simulations model the

orientational relaxation of the OH bond vector of HOD/D₂O, while experiments track the rotation of the transition dipole moment of the HOD molecule. These are certainly not the same for the highly anharmonic OH stretch, and it has been seen that the angle between the transition dipole and the OH bond vector varies with the strength of the hydrogen bond [57,58]. While the variation in this angle might be small across the OH stretch lineshape in the liquid phase, including this effect might lead to better agreement with experimental observations. Finally, these simulations were performed with the SPC/E rigid water model, which does not account for the bend-rotation coupling in the molecule and might predict large HB reorientation angles as a way of compensating for the model's inflexibility.

Two-dimensional anisotropy experiments provide a further criterion by which to judge the accuracy of hydrogen bond dynamics of water models. Most water models are not parameterized to account for dynamics, and show quantitative differences in spectral diffusion and reorientation timescales [50]. A comparison of the model-dependent nature of calculated dynamical observables in a number of classical models have shown that the SPC/E model exhibits a better overall agreement with experiment at the qualitative level, but that polarizable models show closer agreement with experiment over timescales of structural relaxation [50,59]. More recently, *ab initio* based water models propagated with centroid molecular dynamics showed better agreement with experimental reorientational and OH frequency correlation functions than classical MD simulations of rigid water models [55,56].

In making comparisons, it is important to note that even though the 2D anisotropy provides the most detailed constraints on switching dynamics, it is still a statistically

averaged description of what may be a very heterogeneous process. Although one general mechanism for concerted switching has been characterized [8], other switching processes may be present to varying degrees. In fact, the analysis of the same SPC/E model using a different definition for a hydrogen bond, finds three distinct exchange processes of which 22% of switches do not follow the initially postulated jump reorientation [13]. Experimental averaging over orientational motion along varying trajectories invariably complicates the microscopic interpretation of the pump-probe and 2D anisotropy measurements.

5.4 Conclusions

We presented experimental and simulated 2D IR spectral anisotropy of the OH stretch of HOD/D₂O that directly reports on water reorientation during HB configurational changes. Experimental results show a frequency-dependent trend in anisotropy, whose behavior is consistent with the picture of large angle reorientation during concerted hydrogen bond switching. We observe that strongly HB water molecules can be orientationally constrained for a few picoseconds, whereas molecules in broken or strained environments rapidly orientationally randomize. Given that 2D IR anisotropy can correlate HB configurational fluctuations with anisotropy, these experiments have allowed us to quantitatively approximate the angular rotation during hydrogen bond exchange, within the framework of restricted rotation models. From these calculations, we observe large angular deviations in the molecular dipole, as water molecules shift from a strained configuration to a stable configuration. This transition from a NHB to a HB configuration is characterized by a distribution of angles due to

contributions from water molecules that undergo successful switches and those that do not. Average angles for water molecules relaxing from a NHB state to a stable HB state both from experiments and simulations were found to be 10° , leading to a full switching angle of at least 20° . Based on $3\theta_H$ values, we estimate the maximum angular deviations for a HB exchange event to be $\sim 46^\circ$. While these angles are smaller than the switching angles calculated from earlier simulation studies, our experiments are biased by the fraction of NHB molecules that do not successfully switch but undergo only translational and small-angle fluctuations to return to a HB state.

The increased orientational randomization of NHB molecules on inertial timescales as well as the rapid evolution of NHB molecules to a HB state observed in these experiments and simulations of the 2D anisotropy provide further confirmation that dangling hydrogen bonds do not persist in liquid water, that the HB structure remains largely tetrahedral on timescales of HB fluctuations, and that the concerted HB switching events involving multiple molecules proceed through a large change of HB angle.

Acknowledgements

Material presented in this chapter has been published in [60]. This work was supported by the U.S Department of Energy (DE-FG02-99ER14988) and the ACS Petroleum Research Fund (46098-AC6). I thank Sean Roberts for help with MD simulations, Rebecca Nicodemus for experimental help with collecting 2D IR and pump-probe anisotropy of HOD/H₂O (not presented in this chapter), and Carlos Baiz for a careful reading of the manuscript.

References

- [1] H. J. Bakker and J. L. Skinner, *Chem. Rev.* **110**, 1498 (2010).
- [2] I. Ohmine and H. Tanaka, *Chem. Rev.* **93**, 2545 (1993).
- [3] F. H. Stillinger and T. A. Weber, *J. Phys. Chem.* **87**, 2833 (1983).
- [4] F. H. Stillinger, *Science* **209**, 451 (1980).
- [5] J. D. Eaves, J. J. Loparo, C. J. Fecko, S. T. Roberts, A. Tokmakoff, and P. L. Geissler, *Proc. Natl. Acad. Sci. U.S.A.* **102**, 13019 (2005).
- [6] J. J. Loparo, S. T. Roberts, and A. Tokmakoff, *J. Chem. Phys.* **125**, 194522 (2006).
- [7] S. T. Roberts, K. Ramasesha, and A. Tokmakoff, *Acc. Chem. Res.* **42**, 1239 (2009).
- [8] D. Laage and J. T. Hynes, *J. Phys. Chem. B* **112**, 14230 (2008).
- [9] G. Stirnemann and D. Laage, *J. Phys. Chem. Lett.* **1**, 1511 (2010).
- [10] D. Laage and J. T. Hynes, *Science* **311**, 832 (2006).
- [11] M. Ji and K. J. Gaffney, *J. Chem. Phys.* **134**, 044516 (2011).
- [12] M. Ji, M. Odelius, and K. J. Gaffney, *Science* **328**, 1003 (2010).
- [13] R. H. Henchman and S. J. Irudayam, *J. Phys. Chem. B* **114**, 16792 (2010).
- [14] C. P. Lawrence and J. L. Skinner, *J. Chem. Phys.* **118**, 264 (2003).
- [15] J. D. Eaves, A. Tokmakoff, and P. L. Geissler, *J. Phys. Chem. A* **109**, 9424 (2005).
- [16] K. B. Møller, R. Rey, and J. T. Hynes, *J. Phys. Chem. A* **108**, 1275 (2004).
- [17] K. Ramasesha, R. A. Nicodemus, S. T. Roberts, A. Mandal, and A. Tokmakoff, in *Ultrafast Phenomena XVII*, edited by M. Chergui, D. Jonas, E. Riedle, R. Schloenlein, and A. Taylor (Oxford University Press, 2010), pp. 454–456.

- [18] D. E. Moilanen, E. E. Fenn, Y.-S. Lin, J. L. Skinner, B. Bagchi, and M. D. Fayer, Proc. Natl. Acad. Sci. U.S.A. **105**, 5295 (2008).
- [19] H. J. Bakker, S. Woutersen, and H.-K. Neinhuys, Chem. Phys. **258**, 233 (2000).
- [20] H. J. Bakker, Y. L. A. Rezus, and R. L. A. Timmer, J. Phys. Chem. A **112**, 11523 (2008).
- [21] D. Laage and J. T. Hynes, Chem. Phys. Lett. **433**, 80 (2006).
- [22] C. J. Fecko, J. J. Loparo, and A. Tokmakoff, Opt. Commun. **241**, 521 (2004).
- [23] L. P. Deflores, R. A. Nicodemus, and A. Tokmakoff, Opt. Lett. **32**, 2966 (2007).
- [24] J. J. Loparo, S. T. Roberts, and A. Tokmakoff, J. Chem. Phys. **125**, 194521 (2006).
- [25] J. D. Hybl, A. Albrecht Ferro, and D. M. Jonas, J. Chem. Phys. **115**, 6606 (2001).
- [26] M. Khalil, N. Demirdöven, and A. Tokmakoff, Phys. Rev. Lett. **90**, 2 (2003).
- [27] J. A. Myers, K. L. M. Lewis, P. F. Tekavec, and J. P. Ogilvie, Opt. Express **16**, 17420 (2008).
- [28] R. A. Nicodemus, K. Ramasesha, S. T. Roberts, and A. Tokmakoff, J. Phys. Chem. Lett. **1**, 1068 (2010).
- [29] Y. L. A. Rezus and H. J. Bakker, J. Chem. Phys. **125**, 144512 (2006).
- [30] C. J. Fecko, J. J. Loparo, S. T. Roberts, and A. Tokmakoff, J. Chem. Phys. **122**, 54506 (2005).
- [31] S. Yeremenko, M. S. Pshenichnikov, and D. A. Wiersma, Phys. Rev. A **73**, 2 (2006).
- [32] C. J. Fecko, J. D. Eaves, J. J. Loparo, A. Tokmakoff, and P. L. Geissler, Science **301**, 1698 (2003).

- [33] J. J. Loparo, S. T. Roberts, R. A. Nicodemus, and A. Tokmakoff, *Chem. Phys.* **341**, 218 (2007).
- [34] A. Piryatinski and J. L. Skinner, *J. Phys. Chem. B* **106**, 8055 (2002).
- [35] J. R. Schmidt, S. A. Corcelli, and J. L. Skinner, *J. Chem. Phys.* **123**, 044513 (2005).
- [36] J. J. Loparo, C. J. Fecko, J. D. Eaves, S. T. Roberts, and A. Tokmakoff, *Phys. Rev. B* **70**, 1 (2004).
- [37] C. C. Wang and R. Pecora, *J. Chem. Phys.* **72**, 5333 (1980).
- [38] G. Lipari and A. Szabo, *J. Am. Chem. Soc.* **104**, 4546 (1982).
- [39] G. Lipari and A. Szabo, *Biophys. J.* **30**, 489 (1980).
- [40] H. Tanaka and I. Ohmine, *J. Chem. Phys.* **87**, 6128 (1987).
- [41] I. Ohmine and S. Saito, *Acc. Chem. Res.* **32**, 825 (1999).
- [42] G. E. Walrafen, Y. C. Chu, and G. J. Piermarini, *J. Phys. Chem.* **100**, 10363 (1996).
- [43] G. E. Walrafen, *J. Chem. Phys.* **121**, 2729 (2004).
- [44] C. J. Fecko, J. D. Eaves, and A. Tokmakoff, *J. Chem. Phys.* **117**, 1139 (2002).
- [45] S. T. Roberts, J. J. Loparo, and A. Tokmakoff, *J. Chem. Phys.* **125**, 084502 (2006).
- [46] J. B. Asbury, T. Steinel, C. Stromberg, S. A. Corcelli, C. P. Lawrence, J. L. Skinner, and M. D. Fayer, *J. Phys. Chem. A* **108**, 1107 (2004).
- [47] P. Hamm, *J. Chem. Phys.* **124**, 124506 (2006).
- [48] A. Tokmakoff, *J. Chem. Phys.* **105**, 1 (1996).
- [49] A. Tokmakoff and M. D. Fayer, *J. Chem. Phys.* **103**, 2810 (1995).

- [50] J. R. Schmidt, S. T. Roberts, J. J. Loparo, A. Tokmakoff, M. D. Fayer, and J. L. Skinner, *Chem. Phys.* **341**, 143 (2007).
- [51] Y.-S. Lin, P. A. Pieniazek, M. Yang, and J. L. Skinner, *J. Chem. Phys.* **132**, 174505 (2010).
- [52] P. A. Bopp, A. A. Kornyshev, and G. Sutmann, *J. Chem. Phys.* **109**, 1939 (1998).
- [53] P. L. Silvestrelli, M. Bernasconi, and M. Parrinello, *Chem. Phys. Lett.* **277**, 478 (1997).
- [54] B. Guillot, *J. Chem. Phys.* **95**, 1543 (1991).
- [55] F. Paesani, *J. Phys. Chem. A* **115**, 6861 (2011).
- [56] F. Paesani, S. Yoo, H. J. Bakker, and S. S. Xantheas, *J. Phys. Chem. Lett.* **1**, 2316 (2010).
- [57] E. Whalley and D. D. Klug, *J. Chem. Phys.* **84**, 78 (1985).
- [58] J. R. Fair, O. Votava, and D. J. Nesbitt, *J. Chem. Phys.* **108**, 72 (1998).
- [59] E. Harder, J. D. Eaves, A. Tokmakoff, and B. J. Berne, *Proc. Natl. Acad. Sci. U.S.A.* **102**, 11611 (2005).
- [60] K. Ramasesha, S. T. Roberts, R. A. Nicodemus, A. Mandal, and A. Tokmakoff, *J. Chem. Phys.* **135**, 054509 (2011).

5.A. Appendix: Time-evolving angular-frequency correlations in HOD/D₂O from MD simulations

MD simulations form a framework by which we can more carefully analyze the time-dependent correlations between frequency and reorientation angle that underlies our time-resolved IR experiments. By extracting the instantaneous atomic positions of HOD and its two nearest neighbor D₂O molecules, and the instantaneous $\nu = 0$ to 1 transition frequencies and dipole orientations from MD simulations, we were able to calculate time-evolving angular correlations for water molecules initiating in strong and strained hydrogen bond configurations. Previous MD simulation work calculated the equilibrium joint probability distribution of hydrogen bond angles (α) as a function of the OH stretching frequency, and showed large variation in hydrogen bond angles for molecules forming weak hydrogen bonds at higher OH stretch frequencies compared to those in strong, linear hydrogen bonds with lower OH stretch frequencies [15] (shown in Section 1.2 of Chapter 1).

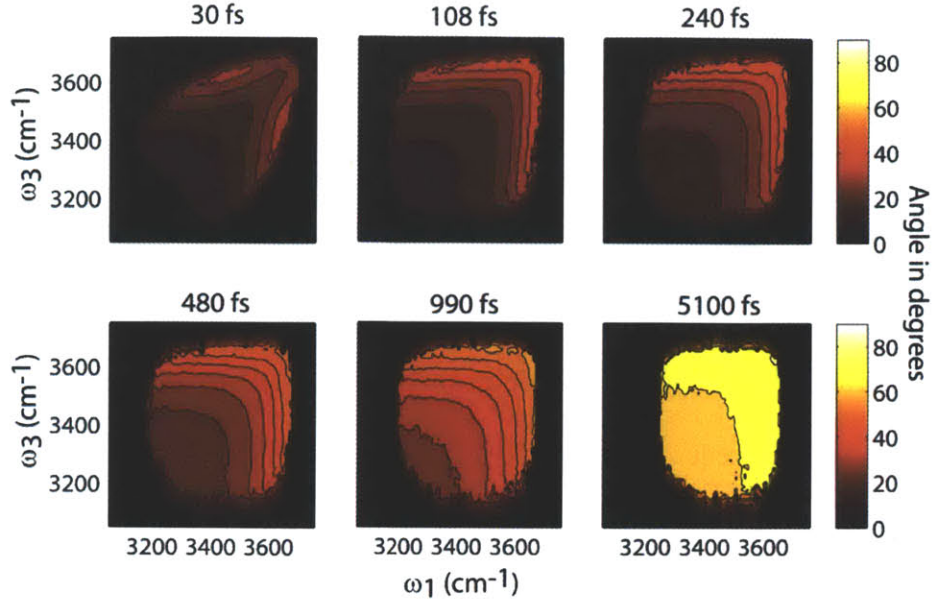


Figure 5-A1: Time-evolution of the mean reorientation angle of the OH bond as a function of ω_1 and ω_3 plotted for six characteristic waiting times τ_2 . Angles are evaluated in degrees.

In this appendix, we quantify time-evolving distributions of the reorientation angle θ , defined as:

$$\theta(\tau_2) = \cos^{-1}(\mathbf{r}_{OH}(\tau_2) \cdot \mathbf{r}_{OH}(0)), \quad (5-A1)$$

where, $\mathbf{r}_{OH}(t)$ is an instantaneous dipole unit vector that points along the OH bond of the HOD molecule. In order to understand how frequency shifts and angular excursions are correlated in time, we calculated the average reorientation angle θ of the OH bond for a waiting time τ_2 , provided the OH stretch is excited at frequency ω_1 and probed at ω_3 , $\langle \theta(\omega_3, \tau_2; \omega_1) \rangle$. For every waiting time τ_2 , this quantity was calculated by binning the initial and final frequencies across a time window with a width τ_2 , using an instantaneous $v = 0$ to 1 frequency trajectory, $\omega_{ID}(t)$, and the corresponding time window in a trajectory of the dipole unit vector $\mathbf{r}_{OH}(t)$ extracted from the same MD simulation run. Statistically

significant number of angle-frequency correlations was achieved by sliding the time window across an entire 1.5 ns long simulation trajectory to calculate joint probabilities at every waiting time, and then averaging the results across five unique MD simulation trajectories. Displayed in Figure 5-A1 are the waiting time series of the mean reorientation angles $\langle\theta\rangle$ as a function of ω_1 and ω_3 averaged across five 1.5 ns long MD simulation trajectories of a single HOD molecule in a box of 107 D₂O molecules. These spectra clearly show a frequency dependent trend to the angles – the higher the OH frequency, the larger the mean angles at early waiting times. At waiting times >5 ps, the angular and frequency correlations are scrambled, resulting in no OH frequency dependence to the reorientation angles.

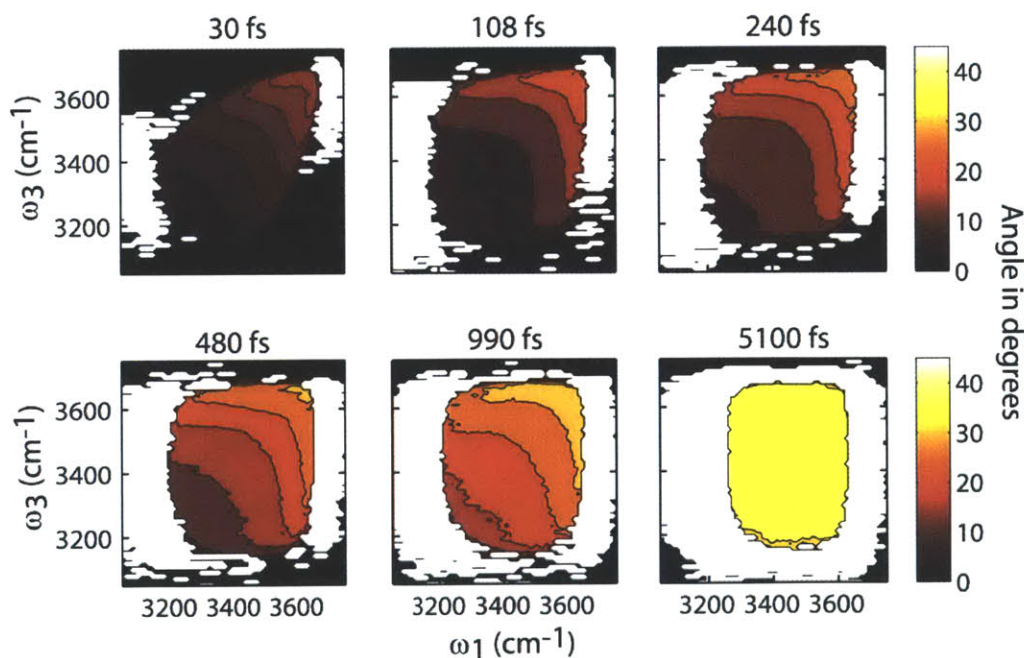


Figure 5-A2: Time-evolution of the standard deviation in reorientation angle of the OH bond as a function of ω_1 and ω_3 . Angles are evaluated in degrees.

Figure 5-A2 shows the standard deviations in the reorientation angles as a function of waiting time calculated for each simulation trajectory and then averaged across five unique trajectories. The standard deviation about the mean reorientation angle is substantial at all OH frequencies, and is particularly large for higher OH stretch frequencies where water molecules are in strained hydrogen bond configurations. At early waiting times, OH stretch vibrations that initiate on the red side of the lineshape show a smaller deviation in angle when detected at lower frequencies. This indicates that molecules that initiate in strong hydrogen bonds do not reorient much while sampling the low OH frequencies at short waiting times, suggesting that water molecules in strong hydrogen bonds are more constrained and sample a smaller cone angle. Water molecules that initiate in strong hydrogen bonds do reorient in order to shift to the blue side of the OH frequency distribution, and display a wider sampling of angles. However, even at early waiting times, water molecules that initiate on the blue side of the lineshape show large deviations in angles at all OH frequencies, in agreement with the fact that strained configurations are very short lived, resulting in faster sampling of angles across a wider cone. At waiting times of several picoseconds, the loss of frequency and angular correlation leads to a homogeneous angular distribution for molecules initiating on both the red and blue sides of the OH stretch lineshape.

Similarly, the second Legendre polynomial orientational correlation function, $P_2(\cos \theta)$, can also be calculated:

$$P_2(\cos \theta) = \left(\frac{3 \cos^2 \theta - 1}{2} \right) \quad (5-A3)$$

Here, θ is as defined in equation 5-A1. Figure 5-A3 displays $P_2(\cos\theta)$ as a joint probability with respect to ω_1 and ω_3 , using the same method as described earlier for calculating $\theta(\omega_3, \tau_2; \omega_1)$.

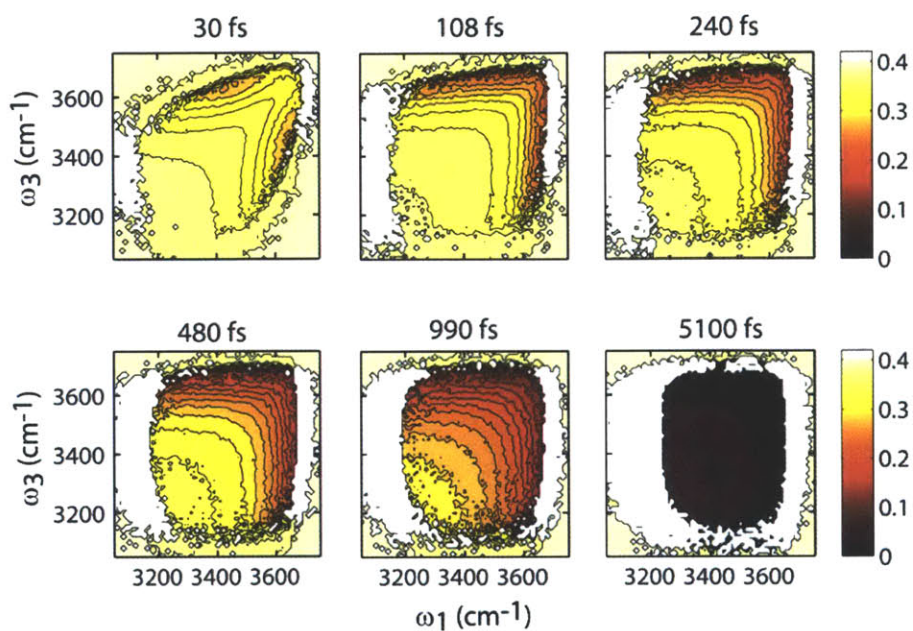


Figure 5-A3: Time-evolution of the second Legendre polynomial orientational correlation function, P_2 , of the OH bond as a function of ω_1 and ω_3 . Here, P_2 is multiplied by 0.4 to convert it into anisotropy units.

Similar to the 2D IR anisotropy spectra calculated from MD simulations, P_2 displays a fast drop in the joint probability representation as well compared to experimental 2D IR anisotropy, and shows similar frequency dependence as seen in the mean angle and standard deviation distributions. Furthermore, all of these joint probability distributions are symmetric about the diagonal like the 2D IR anisotropy calculated for a two-level system. However, while angle-frequency joint probability plots shown in this section are useful for developing an intuition regarding the correlation between OH stretching

frequency and reorientation angle, these calculations do not accurately represent the dynamics. A full response function calculation on the other hand, as described in the main text of this chapter, allows for the incorporation of motional narrowing and non-Condon effects to the spectrum, which better represents the observed orientational dynamics in experiments.

5.B. Appendix: Temperature-dependent pump-probe anisotropy of HOD/D₂O

Temperature-dependent pump-probe anisotropy was performed on HOD/D₂O to extract the dependence of the long timescale on temperature and calculate the activation barrier for hydrogen bond rearrangement. Figure 5-B1 shows the temperature-dependent pump probe anisotropy for detection frequencies integrated across the $\nu = 0$ to 1 transition of the OH stretch, and the corresponding Arrhenius plot for the data. The activation energy obtained from a linear fit to the Arrhenius plot was found to be 3.8 ± 0.2 kcal/mol, which is consistent with previous estimates for the energy barrier for hydrogen bond rearrangement [28].

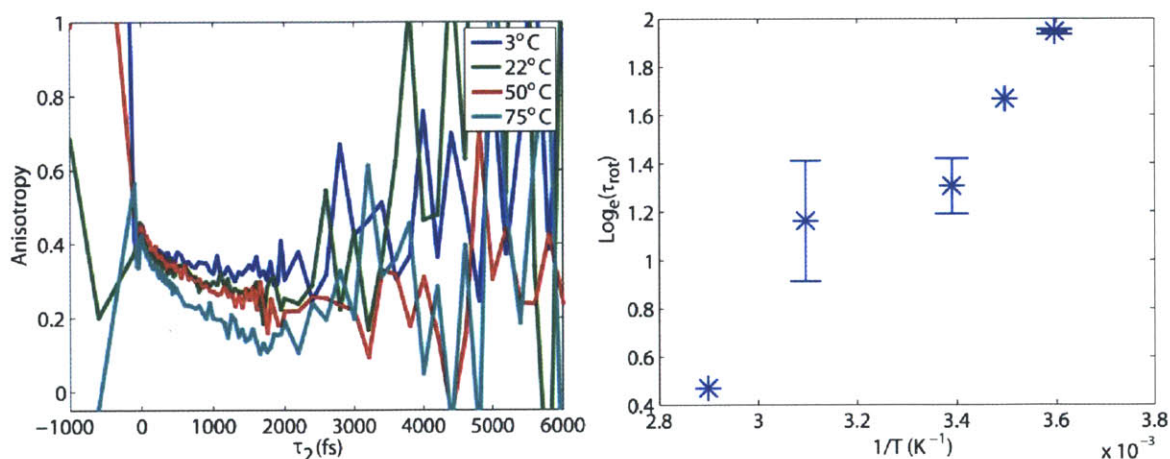


Figure 5-B1: Pump-probe anisotropy of HOD/D₂O at different temperatures (left), calculated for the OH stretch fundamental. The decays were fit to a double exponential plus offset, with long timescales (τ_{rot}) showing the following temperature dependence: 5 °C – 7 ps; 13 °C – 5.3 ps; 22 °C – 3.7 ps; 50 °C – 3.2 ps; 72 °C – 1.6 ps. Arrhenius plot of the temperature dependence of τ_{rot} (in picoseconds) (right), with error bars representing the standard deviation across three independent measurements.

Chapter 6

Generation of ultrafast broadband infrared pulses and measurement of broadband nonlinear spectra

6.1 Introduction

Frequencies, intensities, and lineshapes of vibrational transitions of molecules in solution are sensitive reporters of their local environment [1–3]. Following these vibrations on fast timescales therefore allows us to understand the evolution of molecular configurations such as hydrogen bond rearrangements in water [4–8], aqueous proton transport in acids and bases [9,10] and configurational changes to proteins and peptides [11,12]. Molecular vibrations typically span a wide range of frequencies, from the hydride stretches in the 3 μm region of the mid-infrared to the more delocalized vibrations in the fingerprint region. Correlating the behavior of these spectrally distinct vibrational peaks is crucial to understanding the interplay between local and collective vibrational modes in water and studying how they are influenced by solvent fluctuations. Nonlinear vibrational spectroscopy has proved to be a powerful technique to probe molecular motions in condensed phase on ultrafast timescales due to its high time-

resolution and its sensitivity to nuclear dynamics. These nonlinear experiments require the use of sub-100 fs infrared pulses that can coherently excite all sub-ensembles under broad IR lineshapes and follow their evolution on ultrafast timescales, thus allowing us to characterize spectral diffusion and giving us a glimpse into the structural evolution of the system. We have been able to generate broadband mid-infrared pulses that span the entire mid-infrared region of the spectrum, giving us access to a wide range of vibrational transitions that cannot be accessed with a single measurement using conventional optical parametric amplifiers.

Coupled with the development of ultrafast Ti:sapphire laser systems, optical parametric amplifiers (OPA) have revolutionized the field of ultrafast spectroscopy due to the high fidelity with which they can generate short and intense mid-infrared pulses for nonlinear vibrational spectroscopy. BBO-based OPAs that can generate sub-100 fs pulses have been routinely used in ultrafast infrared spectroscopies in order to study fast vibrational dynamics in a variety of condensed phase systems. Typical OPAs used in two-dimensional and other nonlinear spectroscopies are pumped with the 800 nm sub-100 fs output from ultrafast Ti:sapphire amplifiers [13,14]. A small fraction of the 800 nm beam is first split off to make the white light seed in sapphire, and the remaining 800 nm is used to generate the near-IR signal and idler with the white light after two passes through a BBO. Mid-IR frequencies are then generated by differencing the near-IR signal and idler outputs from the OPA in a crystal like AgGaS₂. Changing the crystal angles and time delays can tune the OPA output spectrum to some degree, but the bandwidth of these pulses is largely constant and is dictated by the duration of the 800 nm pump pulses, the thickness of the nonlinear crystals used in the OPA and the amount of

dispersion the pulses pick up by passing through transmissive optics. The OPA described in Chapter 4 directly generates 3 μm pulses without the difference frequency generation stage [15], and along with the shorter 800 nm pulses and thinner crystals, allows for shorter mid-IR pulses with more bandwidth than the standard BBO-AgGaS₂ based OPAs. However, in general, the bandwidths of the femtosecond OPA outputs range in full-width-half-maximum from around 100 cm^{-1} to 400 cm^{-1} , giving us a very limited window to the vibrational spectrum of many interesting systems in the mid-infrared. Condensed phase systems that have interested many spectroscopists typically display vibrational signatures across the entire mid-infrared region of the spectrum.

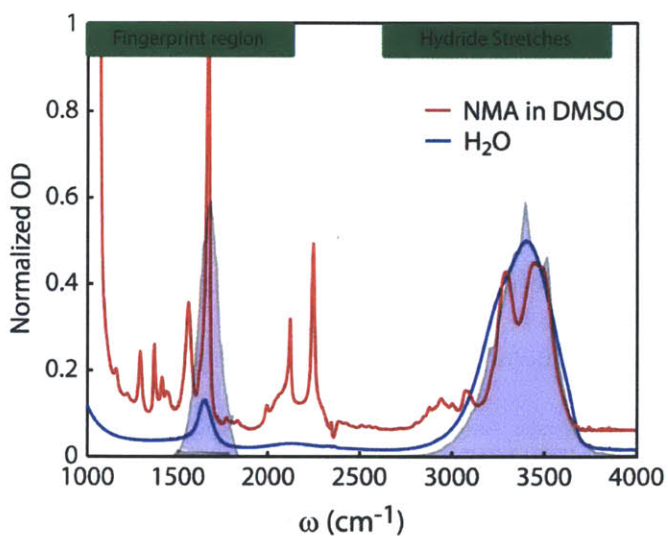


Figure 6-1: Typical spectra from OPAs (shown in purple) compared to the many vibrational features present in H₂O (blue) and N-methylacetamide in dimethyl sulfoxide (red).

These molecules can contain spectrally distinct transitions across many frequencies, from hydride stretch vibrations in the 3 μm region of the infrared spectrum to delocalized polyatomic vibrations in the fingerprint region of the spectrum. As an example, Figure 6-1 shows FTIR spectra of H_2O and N-methylacetamide (NMA) in d-DMSO, along with typical infrared outputs from OPAs.

Broadband mid-IR (BBIR) pulses that span a wide range of frequencies would allow us to study vibrational correlations across distinct transitions, giving us access to a wealth of information on processes that are marked by transitions across the entire mid-IR, such as vibrational relaxation in water, proton transport in acids and bases, vibrational coupling in peptides, and peptide-solvent interactions. Here, our interest lies in understanding proton transport in aqueous HCl, where broad featureless transitions are observed spanning the mid-IR region from 3500 cm^{-1} down to $<500\text{ cm}^{-1}$. Previous simulation work [16–19] and gas phase spectroscopy [20–22] have suggested that these transitions arise from the stretching and bending modes of hydrated proton configurations like H_5O_2^+ and H_9O_4^+ , but experimental evidence for these assignments, and the lifetimes and exchange timescales of the various protonated configurations has been largely absent. Using broadband mid-IR pulses, we studied the timescales and spectral signatures that are unique to these protonated configurations, getting us closer to understanding the underlying dynamics that govern proton transport.

By focusing ultrashort visible pulses in air to create a plasma, we have been able to generate BBIR pulses that range from 4000 cm^{-1} to hundreds of cm^{-1} . We will illustrate the use of these broadband infrared pulses, in conjunction with the 3 μm output from our home-built OPA (described in Chapter 4), to investigate proton transfer dynamics in

concentrated HCl in H₂O (Chapter 8) and vibrational dynamics in H₂O (Chapter 7). In these experiments, we used the 3 μm OPA output to excite the OH stretch vibration, followed by the broadband infrared pulses to probe changes at mid-IR frequencies between 1350 cm⁻¹ and 4000 cm⁻¹. This chapter will first present an overview of the experimental set up used for measuring nonlinear spectra using broadband infrared pulses. The subsequent sections in the chapter will focus on the generation of these broadband pulses, their spectral, temporal, polarization and spatial characteristics, and will describe their application in broadband pump-probe and broadband two-dimensional infrared spectroscopy.

6.2 Overview of the experimental set-up

Figure 6-2 provides an overview of the experimental set-up that is required for the generation of both BBIR pulses and 3 μm pulses, and for acquiring broadband nonlinear infrared spectra. Both the BBIR generation set-up and the 3μm OPA are pumped with a Ti:Sapphire-based laser system. A Femtolasers Femtosource Scientific Pro Ti:Sapphire oscillator (450 mW mode-locked power, 80-100 nm bandwidth at full-width at half-maximum, 10 fs pulse duration, 76 MHz repetition rate), pumped with the 4 W output from a Nd:YVO₄ Spectra Physics Millennia Vs laser, serves as a seed for amplification in the Coherent Legend Elite USX HE regenerative amplifier system. A small portion of the oscillator output is reflected off an uncoated BK7 glass window and sent to a fast photodiode to trigger the Pockels cell in the amplifier.

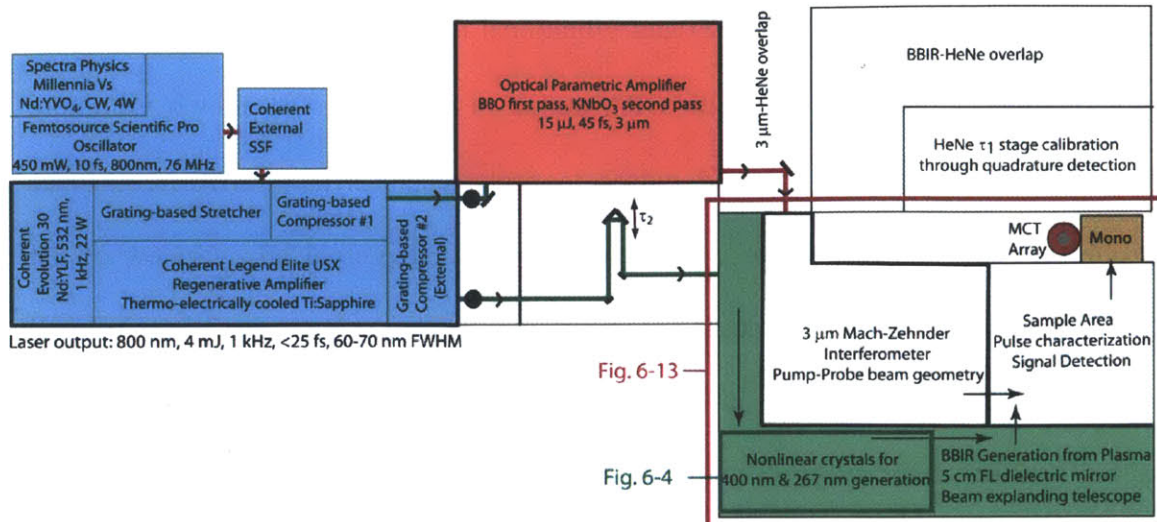


Figure 6-2: Overview of the experimental set-up for measuring broadband nonlinear spectra. Arrows represent the direction of beam propagation and the bold circles are periscopes. Figures 6-13 and 6-4 in this chapter display detailed diagrams of the parts of the set-up indicated above.

The seed pulses from the oscillator are first sent into a spectral filter (Coherent external SSF) that removes intensity from the center of the seed spectrum to pre-compensate for the gain narrowing in the amplifier. Figure 6-3 shows the oscillator spectrum before and after the spectral filter. The shaped seed spectrum is sent into a grating-based stretcher and then into the Ti:Sapphire regenerative amplifier, which contains a thermo-electrically cooled vacuum enclosure for the Ti:Sapphire crystal. The regenerative amplifier is pumped with the ~ 20.5 W output from the Coherent Evolution 30 (1 kHz, 30 W maximum power, 532 nm) laser. The spectra of the 800 nm pulse after the stretcher and after the compressor are also displayed in Figure 6-3.

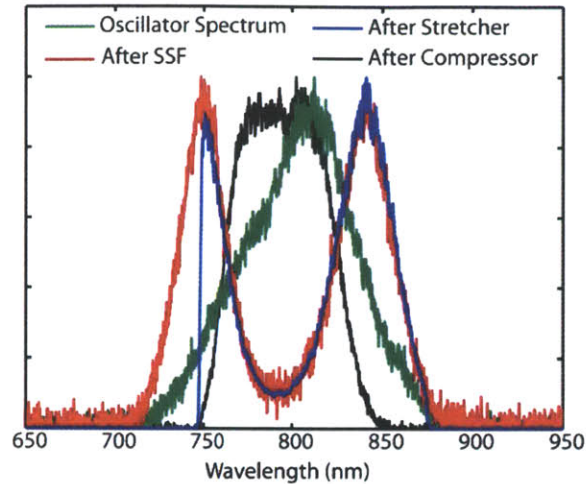


Figure 6-3: Spectra (normalized to maximum intensity) of the 800 nm pulses at various stages in the laser are shown: after the Femtosource Oscillator (green), after the Coherent SSF spectral filter (red), after the stretcher (blue) and the compressed amplified final spectrum (black).

After amplification, the 800 nm beam is split into two arms using a beamsplitter, with ~ 1 mJ/pulse in one arm and ~ 3 mJ/pulse in the other. The 1 mJ arm is sent into an internal grating compressor and then into the OPA. The 3 mJ arm is sent into an external grating compressor and then into the BBIR generation set-up. A $\lambda/2$ waveplate in each arm of the amplified output helps us finely control the 800 nm energy going into the OPA and the BBIR generation set-up, respectively. The compression for both the 800 nm arms can also be controlled independently, allowing us to compensate for the dispersion in the OPA and in the BBIR set-up separately. Overall, we get 4.5 W of power at 1 kHz repetition rate, with <25 fs pulse duration and ~ 65 nm bandwidth FWHM from the laser system. The 800 nm output from the laser is S-polarized.

For the BBIR pulse characterizations described in this chapter and for the experiments detailed in the following chapters, we used the same home-built two-pass OPA as described in Chapter 4 to generate 45 fs 3 μm pulses, upon pumping with 0.5-0.6 mJ of 800 nm from the internal grating compressor of the laser. Briefly, $\sim 1\%$ of the 800 nm pump is focused into a 1.5 mm thick sapphire plate using reflective spherical optics to generate the white light seed, and the intensity of the 800 nm beam is controlled by a $\lambda/2$ waveplate-thin film polarizer combination placed before the sapphire plate. The remaining 800 nm beam is split into two arms for the two passes in the OPA. The first arm is focused into a 1 mm thick Type I β -barium borate (BBO) crystal, and is spatially and temporally overlapped with the white light seed. This process efficiently generates 1.1 μm as signal and 3 μm as idler, but the BBO crystal absorbs the 3 μm idler frequencies. In the second amplification stage of the OPA, the 1.1 μm signal from the first pass is overlapped with the second arm of the 800 nm pump in a 1 mm thick Type II KNbO_3 crystal to generate the 3 μm frequencies. The residual visible and near-IR frequencies are removed by reflecting the output from the second pass off an 800 nm high reflector and then passing it through an anti-reflection coated 2 mm thick germanium plate. The germanium plate also serves to compensate for the pulse dispersion induced by CaF_2 optics in the 2D IR interferometer. The beam is collimated to a diameter of ~ 1 cm upon passing through a transmissive telescope. After spatially overlapping the OPA output with a HeNe tracer for alignment purposes, it is equally split to create a collinear pulse pair in a Mach-Zehnder interferometer.

The BBIR generation set-up on the other hand, is pumped 1.25 mJ to 1.5 mJ of 800 nm from the external compressor. The 800 nm beam from the external compressor travels

first through a transmissive telescope to shrink the beam size from 1.5 cm to $\sim 8 - 9$ mm in diameter in order to comfortably pass through the 1 cm x 1 cm nonlinear crystals that generate the second and third harmonic frequencies of the 800 nm [23]. These beams are then used to create a plasma that emits BBIR pulses. The next section will detail the BBIR generation process and the characteristics of the BBIR pulses. The BBIR then travels through a reflective beam expander, resulting in a nearly collimated beam with ~ 14 -15 mm diameter. The BBIR beam is spatially overlapped with a HeNe tracer on a 400 μm thick Si wafer (MTI Corporation) placed at Brewster's angle, which also serves to filter the visible emission from the plasma and lets wavelengths higher than ~ 1.1 μm pass through. The BBIR and the 3 μm beams are then focused into the sample using an off-axis bare gold parabolic mirror (Janos Tech), and the BBIR along with the resonant third-order signal from the sample are dispersed onto a liquid N_2 cooled HgCdTe array detector (Infrared Systems).

6.3 Generation of BBIR pulses via filamentation in air

Broadband ultraviolet, visible, terahertz and infrared pulses have been successfully generated by focusing ultrafast optical pulses in various gases [24–34]. These broadband pulses have been shown to be sub-50 fs in duration, with excellent mode quality, making them ideal for ultrafast measurements. This process of generating broadband pulses has been attributed to the large nonlinearities in the gas medium due to intense electric field strengths at the focus arising from the high peak power of the ultrafast optical pulses [35]. Under the influence of strong fields, the intensity-dependent refractive index modulation

in a medium like air or nitrogen causes the beam to self-focus. This self-focusing is counteracted by the de-focusing effects of low density plasma that is created from tunneling ionization of the gas medium at the focus [36]. Earlier studies have concluded that this competition between self-focusing and de-focusing effects leads to the formation of several foci along the direction of propagation of the optical beams, a process known as “filamentation”, which results in an increased interaction length between the input optical beams and leads to efficient generation of short broadband pulses [36].

Generation of *high* frequency ultrafast broadband visible, ultraviolet and X-ray pulses by focusing low frequency infrared and near-infrared pulses has been attributed to the process of high harmonic generation. In a classical sense, high harmonic generation can be thought of as a process where electric field oscillations in a short and intense optical pulse severely distort the Coulomb potential of the atoms in the gas medium, thus suppressing the barrier for ionization. In a single electric field oscillation, distortions to the Coulomb potential result in tunneling ionization where the intense electric field pulls an electron away from the nuclear core, followed by a forced re-collision of the electron to the nuclear core, releasing high energy ultrashort broadband pulses in the process [37]. Tunneling ionization has also been used to explain the generation of *low* frequency broadband terahertz pulses upon focusing ultrafast 800 nm and 400 nm pulses in various gases [38,39]. Kim et al. [39] proposed that the two-color input optical pulses cause an asymmetry in the tunnel ionization, where the peaks of the combined electric fields may be different from the peaks of the individual fields, resulting in an interference between two ionization pathways. The authors concluded that this interference would cause a “drift velocity” of the electron resulting in an “electron current” and the emission of

ultrafast broadband terahertz pulses. They proceeded to measure the current at the focal point, and showed a clear dependence of the electron current on the intensity of the 400 nm pulses and the emitted terahertz radiation. This work also demonstrated the dependence of terahertz yield on the ionization rates of various gases.

On the other hand, based on power-dependence measurements of broadband terahertz yield, four-wave rectification that exploits the third-order susceptibility of the gas medium ($\chi^{(3)}$) has been proposed as another mechanism by which terahertz or broadband infrared pulses are generated upon focusing two-color optical pulses in air [24,29,31,32]. While the peak frequencies in a four-wave rectification process add up to zero, broadband THz and infrared frequencies arise from the finite bandwidth associated with the input ultrafast optical input pulses. Cook and Hochstrasser observed a quadratic dependence to the THz energy as a function of the 800 nm input power, leading them to conclude that four-wave mixing is the dominant process for THz generation in air. Kress et al. [31] on the other hand proposed the THz generation mechanism to be driven by the plasma at the focus. The power dependence they extracted corrected for the THz generated in the BBO doubling crystal before the focus, and they found that at low 800 nm input power still higher than the ionization threshold for air, the THz intensity was lower than the predicted quadratic dependence expected for a four-wave mixing process.

Several groups have been able to generate broadband pulses in the terahertz and infrared regimes. By focusing 65 fs 800 nm pulses from a Ti:Sapphire amplifier and its second harmonic at 400 nm in air, Cook and Hochstrasser were able to generate sub-two-cycle THz pulses spanning 1 THz to 6 THz [32]. They empirically estimated the gain in

THz intensities by focusing both the 800 nm and 400 nm beams to be a factor of 4000 greater than focusing just the 800 nm beam in air. Bartel et al. [29] further showed that using a short focal length of 5 cm to focus orthogonally polarized 800 nm and 400 nm pulses produced high intensity THz pulses. Their work also highlighted the role of the 800 nm pulse duration on the bandwidth of the emerging THz pulses. They were able to generate THz pulses that spanned 1 to 8 THz with 25 fs 800 nm pulses, but only 1 to 2 THz for a chirped 300 fs 800 nm input pulses.

Efforts to generate broadband mid-infrared pulses have drawn on these approaches for broadband terahertz pulses generation. Fuji and Suzuki [40] used a $\omega/2\omega$ (800 nm/400 nm) filamentation scheme with 25 fs 800 nm pulse to generate broadband mid-IR pulses that span 1500 cm^{-1} to 4500 cm^{-1} in frequency. In their paper, the 800 nm and 400 nm beams were non-collinearly generated and were timed up using optical delay lines, and focused separately along the same focal region with 75 cm focal length mirrors. The pulse duration of the resulting broadband infrared was measured by upconversion frequency-resolved optical gating (XFROG) with the 800 nm pulses to be sub-20 fs indicating a 1 to 2 cycle pulse. Using pulse shaping techniques, Lassonde et al. [41] were able to generate mildly tunable broadband infrared pulses in a collinear geometry by spectrally shaping 800 nm pulses to contain two spectral components (800+ and 800- for the longer and shorter wavelengths relative to 800 nm, respectively). In their method, only one of the two spectral components (800+) was frequency doubled, which was focused along with the second spectral component (800-) in air to generate broadband infrared pulses. The authors showed that by varying the frequency difference between the second harmonic of the 800+ component and the 800- spectral component, they were able

to control the bandwidth of the broadband pulses, and to some extent, the center frequency as well. The smaller the frequency difference, the broader the bandwidth they generated, thus pushing the bandwidth of the broadband pulses to the far IR region with wavelengths as low as 12 μm . Further, Khalil and co-workers [33], using a $\omega/2\omega$ collinear scheme, showed that the gas medium in which the plasma is generated dictates the energy of the emitted BBIR, with higher intensities reached in Ar than in air or Ne. They also reported that varying the pressure of the gas medium changed the BBIR intensity and stability, and significantly tuned the BBIR spectrum. Both of these observations are consistent with the work by Kim et al. on the influence of the nature and the pressure of the ionizing gas on broadband terahertz yield [39]. For 800 nm input power ranging from 0.2 mJ/pulse to 1 mJ/pulse, Cheng et al. saw a quadratic dependence between the square root of the BBIR intensity and the input 800 nm power, and they concluded that within the energy regime, four-wave mixing was the primary mechanism for BBIR generation [33].

We make use of the method of Petersen and Tokmakoff [23], who adapted the $\omega/2\omega$ BBIR generation scheme to include the third harmonic (3ω) of the 800 nm in a fully collinear geometry, leading to an increase in BBIR production, easier alignment and improved stability by allowing for a compact set-up. Figure 6-4 illustrates the BBIR generation set-up we employed in this study. First, the <25 fs 800 nm pulses from our laser system are frequency doubled to 400 nm by using a Type I β -barium borate (BBO) crystal cut at 29.2° , with 0.2 mm thickness. The fundamental and second harmonic are then summed to generate the third harmonic at 267 nm in another Type I process in a BBO crystal cut at 44.26° , with 0.1 mm thickness. Between the doubling and tripling

crystals, a 2 mm thick BBO crystal cut at 66° is used as a delay plate to pre-compensate for the temporal walk-off between the 800 nm and 400 nm pulses when they travel through the crystals. A waveplate (6.5λ at 800 nm and 14λ at 400 nm) is inserted after the delay plate to rotate the polarization of the S-polarized 800 nm beam onto the P-polarized 400 nm before the tripling process.

The three wavelengths are then incident on a 5 cm focal length dielectric mirror coated for 800 nm and 400 nm, and are focused in air to create a plasma from which BBIR is emitted along the propagation direction of the visible beams. We found that the BBIR emerging from the plasma was slightly vertically displaced relative to the visible frequencies, with the amount of displacement dependent on the alignment on any given day, but is fairly reproducible barring any major realignments to the back end of the apparatus. We placed an iris after the plasma in order to isolate the BBIR part of the emission. The visible emission from the plasma is further filtered on a 400 μm thick high resistivity Si wafer placed close to the Brewster angle at $\sim 70^\circ$, letting only the infrared frequencies through. We found the BBIR to be linearly polarized at $\sim 16^\circ$ off the vertical axis. Petersen and Tokmakoff [23] found that the addition of 3ω to the plasma makes the BBIR linearly polarized, while the $\omega/2\omega$ scheme returned an elliptically polarized BBIR. We also saw that the gain in BBIR energy in the $\omega/2\omega/3\omega$ scheme is roughly 10 times compared to the $\omega/2\omega$ scheme, along with a measurable increase in higher frequencies components ($>3000\text{ cm}^{-1}$) of the BBIR. With the exception of the Si wafer used to filter the visible wavelengths, this set-up uses only reflective optics after the plasma to minimize dispersion of the broadband infrared pulses and maximize the available bandwidth.

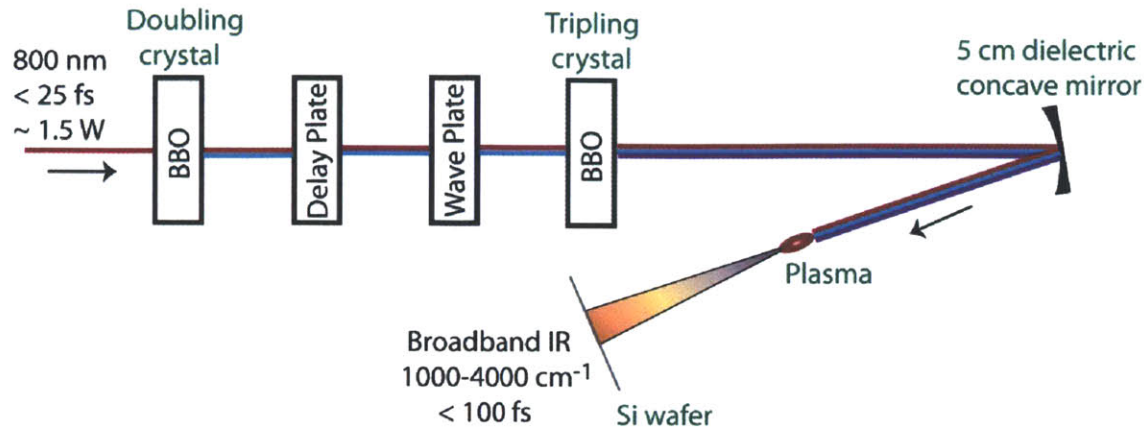


Figure 6-4: The $\omega/2\omega/3\omega$ broadband infrared generation scheme.

We also compared the BBIR spectra generated using 5 cm, 50 cm and 75 cm focal lengths and found that for a given input 800 nm power, the BBIR intensity was larger for shorter focal lengths with more intensity in the higher frequency regions of the spectrum. This observation is reasonable given that concentrating all of the visible pulse energy in a short focus creates a high energy plasma leading to higher BBIR intensity and more high frequency components than with longer focal length plasmas. However, this behavior could also be due to the fact that the 5 cm mirror we used is a dielectric mirror coated for 400 nm and 800 nm with 99% reflectance in the visible, while we used UV enhanced metallic mirrors for longer focal lengths, which have ~85% reflectance at 400 nm and 800 nm and about 90% reflectance at 267 nm. Other groups [23,41–43] have successfully used longer focal length metallic mirrors ($f > 0.5\text{ m}$) to focus the visible beams for generating BBIR pulses. Groups that generate ultraviolet and visible pulses via filamentation in air have also used focal lengths ranging from 50 cm to 4 m. Theberge et al. [44] showed that the spectral broadening of the emerging ultraviolet pulses increased

along the length of the plasma. Using a 82 cm focal length mirror and a 4 m focal length mirror, they showed that the generated broadband ultraviolet pulses broadened from a FWHM of 23 nm (22 fs pulse duration) to a FWHM of 64 nm (9 fs pulse duration), respectively. We have not observed this behavior in the generation of BBIR.

One of the advantages of using longer focal lengths is the higher saturation threshold in pumping the plasma. For a 5 cm focal length, pumping the plasma with more than ~ 1.5 W of 800 nm leads to a drop in the BBIR intensity and a significant increase in the shot-to-shot noise of the BBIR, perhaps due to the excess energy density at the focus. Moreover, using a longer focal length leads to a smaller distortion in the spatial mode of the plasma since the angle of incidence and reflection off the spherical focusing mirror can be closer to 0° . Nevertheless, we used a 5 cm focal length mirror due to a factor of 10 gain in BBIR intensity, the compactness of the set-up and higher intensity at frequencies above 3000 cm^{-1} . Using a 5 cm focal length mirror to focus ultrafast 800 nm, 400 nm and 267 nm pulses in air, we were able to generate plasma that was approximately 2 mm long along the focus. Due to the compactness of the set-up, the mode of the BBIR beam emerging from the collimating mirror is slightly vertically elongated.

We optimized the intensity of the BBIR pulses by iteratively varying the compression of the input 800 nm pulses, the angles of the doubling crystal, the tripling crystal and the delay plate about all three axes, and the setting of the waveplate. We have observed that varying any of these parameters results in many local maxima, and it requires several iterations of varying all these parameters, in any sequence, to find the global maximum in the BBIR intensity.

6.3.1 BBIR spectral and spatial characterizations

The BBIR spectrum from the set-up described above measured on a liquid N₂ cooled 64 element HgCdTe detector is displayed in Figure 6-5. The spectrum spans a wide range of frequencies from hundreds of cm⁻¹ to 4000 cm⁻¹. The spectrum shown in Figure 6-5 trails off at lower frequencies due to limitations in the detector response [23].

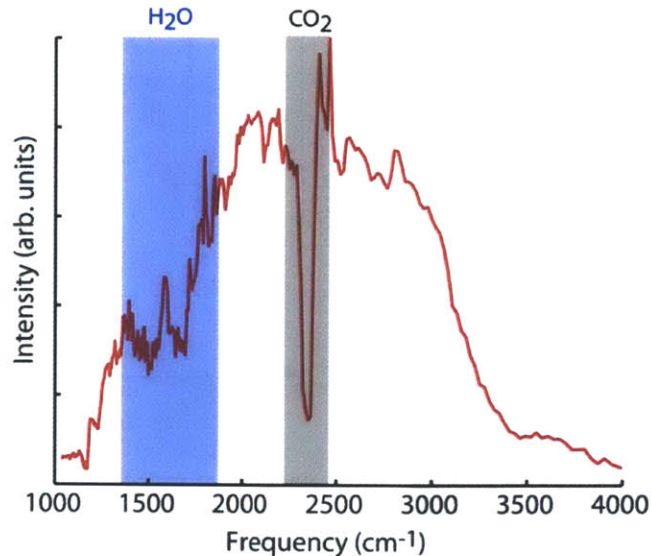


Figure 6-5: Spectrum of the BBIR dispersed onto a 64 element liquid N₂ cooled HgCdTe array detector, with a 6 μm blazed 50 grooves/mm grating. The drop in intensity on the red edge of the spectrum is detector-limited, the feature at approximately 2300 cm⁻¹ is due to absorption from atmospheric CO₂, and absorption lines between 1400 cm⁻¹ and 1800 cm⁻¹ are due to atmospheric H₂O.

We have observed that the intensity at higher frequencies can be varied by rotating the delay plate and the tripling crystal about the vertical axis, and by tuning the

compression of the 800 nm pulses. This suggests that the shorter the 800 nm pulses and the more accurately timed the 400 nm and 800 nm pulses, the hotter the plasma, leading to the generation of more high frequency components in the BBIR. With a 5 cm focal length, the BBIR intensity starts saturating at 1.25 W of input power (Figure 6), and as this saturation limit is reached, the noise in the plasma also increases drastically, especially in the high frequency region.

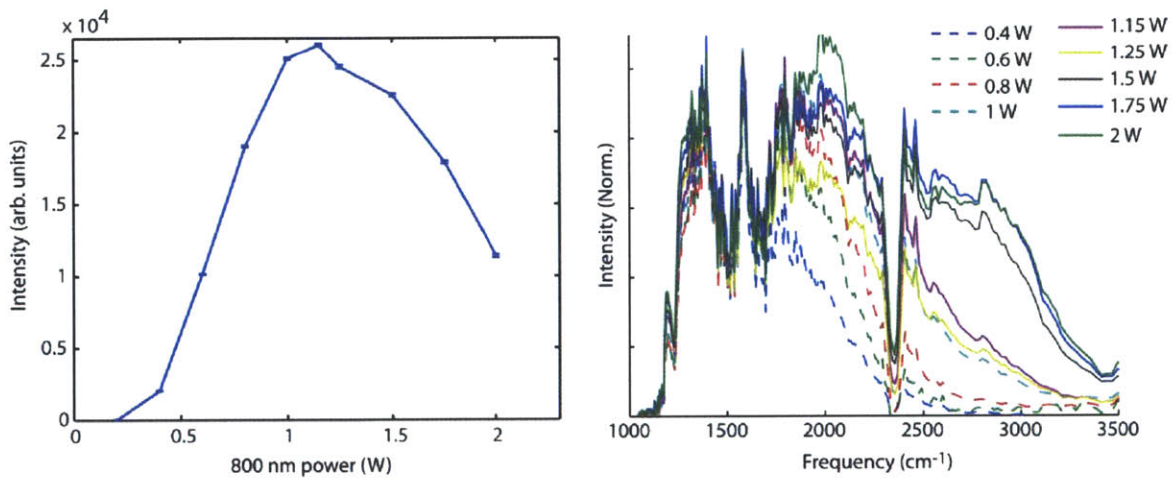


Figure 6-6: Dependence of the BBIR integrated intensity on the 800 nm power (left) for a BBIR spectrum resembling the one displayed in Figure 6-5. Error bars represent the standard deviation. Variation in the BBIR spectrum at different input 800 nm power (right).

The power dependence varies based on whether the spectrum contains more or less of the high frequency components in the 3 μm region. The saturation threshold is higher when the BBIR spectrum contains fewer high frequency components. Figure 6-6 shows the power dependence when the spectrum at 1.25 W contained more high frequency

components, resembling the spectrum displayed in Figure 6-5. Our BBIR experiments on water and acids required the high frequency components in the BBIR in order to comfortably probe the OH stretching region of the spectrum at 3400 cm^{-1} . There is a steep dependence of the intensity of the BBIR at high frequencies on the 800 nm input power. The larger the input power, the more the high frequency components in the BBIR, as displayed in Figure 6-6, since the high input energies of the optical pulses gives rise to a higher energy plasma that can emit higher frequencies. At any given input 800 nm power, the shot-to-shot noise of the higher frequency edge of the BBIR is more than at the peak of the spectrum or at lower frequencies. On most days, purging the plasma with dry air reduces the shot-to-shot noise significantly. However, there was insignificant change in intensity and no change in the BBIR spectrum when Ar was gently flowed through the plasma instead of dry air. Figure 6-7 shows the dependence of the BBIR intensity, noise and the spectrum on the purging medium. This result is different from the observations that Cheng et al. [33] made, perhaps because our plasma is shorter and is in a flow tube instead of being enclosed in a pressure-controlled gas cell like in their work.

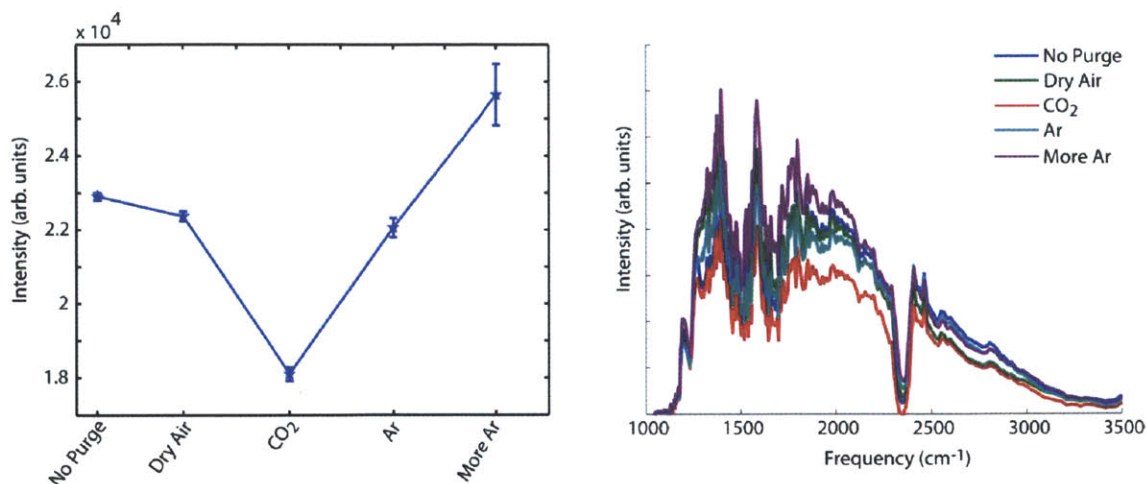


Figure 6-7: Dependence of the BBIR integrated intensity and the noise on the medium used to purge the plasma (left). Error bars represent the standard deviation in the measurements. BBIR spectra taken for different purging conditions, normalized to the BBIR frequency integrated intensity (right).

The spatial chirp of the BBIR was minimal along the focus at the sample position. Figure 6-8 shows the BBIR spectrum through a 50 μm pinhole (BBIR is focused to a spot-size of $\sim 100 \mu\text{m}$ at the sample position) placed at different positions along the focus at the sample, and the spectra look identical. Moving the pinhole orthogonal to the propagation of the beam changes the spectrum slightly probably due to deviations in the alignment into the detector.

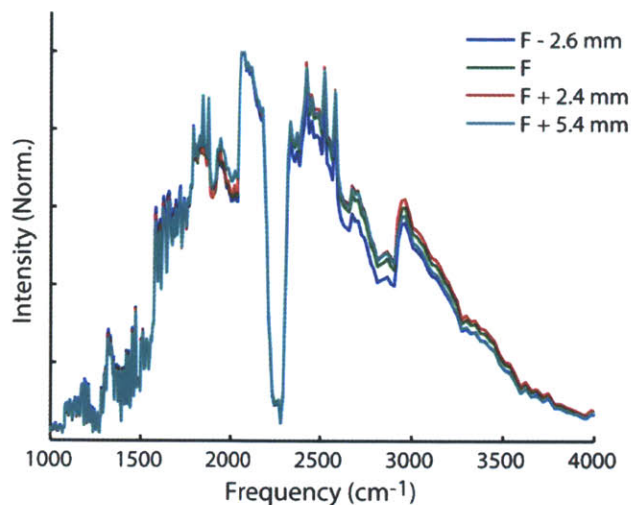


Figure 6-8: BBIR spectrum detected on the HgCdTe array detector after passing through 50 μm pinhole placed at different points about the focal point at the sample position. Here, F is the position of the focus and the number after that indicates the deviation from this position.

6.3.2 BBIR temporal characterization

The temporal width of the BBIR pulse was measured by cross-correlating the BBIR with the known 45 fs 3 μm pulses from the OPA. We used the 3 μm pulses as the pump to cause an above band gap transition in a 500 μm thick InSb wafer (band gap of 7.3 μm), followed by the BBIR probe pulses at different time delays. The cross-correlation, shown in Figure 6-9, looks like a step response since the carriers generated by the 3 μm pulses are long-lived compared to the timescales we can access. However, we can estimate the BBIR pulse duration by fitting the rise of the step response, assuming that the response of the material is shorter than the pulse duration.

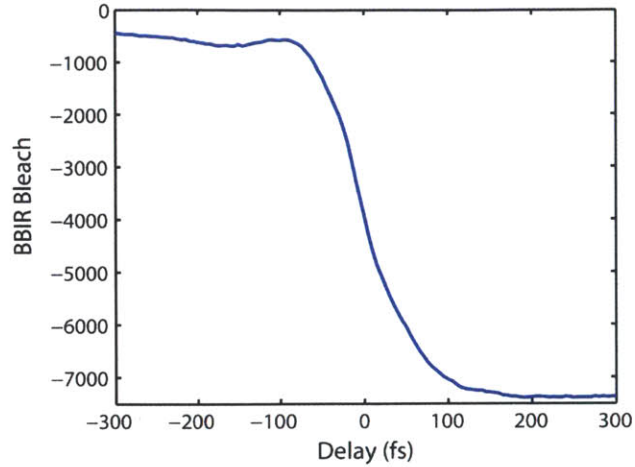


Figure 6-9: Cross-correlation of the BBIR pulses with 45 fs 3 μm pulses in 500 μm thick InSb.

Fitting the step response to an error function yields a sub-70 fs pulse duration for the BBIR pulses, which is in the ball park of earlier estimates of the temporal width [33,40,42,43], but is longer than expected for the large frequency bandwidth of the BBIR pulses. The finite length of the plasma and the use of a 400 μm thick Si wafer for filtering visible frequencies, which has a uniform positive group velocity dispersion across the mid-IR frequencies of about 500 fs^2/mm , probably cause the temporal lengthening of the BBIR pulses. Moreover, the time duration of the BBIR pulses is characterized against a 45 fs 3 μm pulse in a sufficiently thick InSb wafer, resulting in further limitations to the measurement.

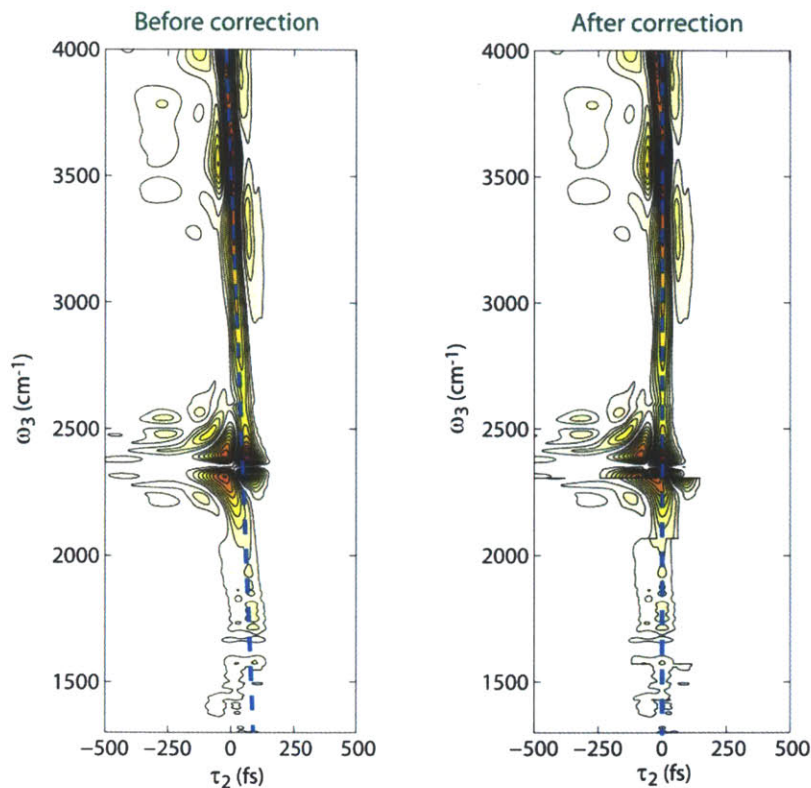


Figure 6-10: Cross-correlation of the BBIR pulses with 3 μm pulses in a 1 mm thick CaF_2 window, showing a linear chirp across the mid-IR (left). The same cross-correlation is shown after numerically correcting for the chirp (right). The dotted blue line tracks the maximum of the cross correlation at every ω_3 to guide the eye.

We also characterized the temporal chirp of these pulses by cross-correlating the BBIR pulses with the 3 μm pulses in a 1 mm thick CaF_2 window and dispersing the signal onto the HgCdTe infrared array detector, shown in Figure 6-10. The chirp in the 1300 cm^{-1} to 3500 cm^{-1} frequency range of the BBIR is approximately 70 fs, and is quite linear across the frequencies. The cross-correlation derived from this data is <70 fs, consistent with the pulse-width measured from resonant cross-correlation in InSb. To correct for the chirp, we interpolated to a fine spacing in the frequency dimension and then shifted the peak of

the time trace at each frequency slice to $\tau_2 = 0$. The right panel of Figure 6-10 shows the cross-correlation after chirp correction. The chirp was very similar to the traces displayed in Figure 6-10 regardless of the degree of enhancement in the high frequency region of the BBIR spectrum. When they measured the cross-correlation between the BBIR pulses and the 267 nm pulses in CaF₂, Petersen and Tokmakoff [23] found that the chirp on the BBIR pulses was minimal between 2000 cm⁻¹ and 4000 cm⁻¹, with a 50 fs chirp at frequencies lower than 2000 cm⁻¹. While our measurements were slightly different from theirs, the extracted chirp of the BBIR agrees reasonably well with their results.

6.3.3 BBIR polarization characterization

The BBIR pulses are close to linearly polarized across the frequency range from 1300 cm⁻¹ to 3500 cm⁻¹. Figure 6-11a shows the BBIR spectrum after passing through a polarizer set to different angles. At an angle of 90° the BBIR intensity is almost extinguished. The polarizations depicted in Figure 6-11 are relative to the polarization of the BBIR pulses. Figure 6-11 also contains a plot of the normalized spectra at different polarization angles, which clearly shows that the spectrum does not change significantly for different polarizations. Figure 6-11b displays the polarization dependence to the intensity at various frequencies, normalized to the value at 0°. From this, it is clear that going from the red side of the BBIR spectrum to the blue side, the polarization of the BBIR pulses changes by $\sim 5^\circ$, which is minimal for our purposes.

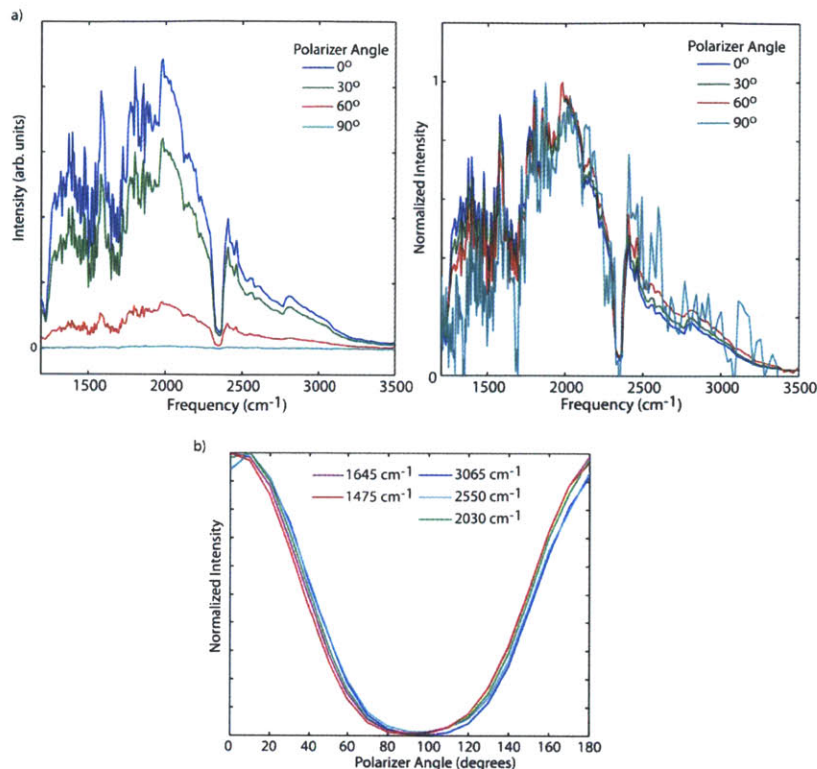


Figure 6-11: a) Spectrum of the broadband IR pulses at different polarization angles, unnormalized (left) and normalized (right). The polarization angles are relative to the polarization of the BBIR. b) Polarization dependence to the intensity of the BBIR at different frequencies, normalized to the value at 0° polarization angle.

6.4 Spectroscopy with broadband infrared pulses

We use third-order nonlinear spectroscopy to study vibrational dynamics in a variety of condensed phase systems. As outlined in chapter 2, third-order spectroscopy involves the sequential interaction of three ultrafast pulses with the sample to resonantly drive the system to emit a third-order polarization. 2D IR spectroscopy is one flavor of third-order spectroscopy that correlates initial and final frequencies of a system and allows us to follow the evolution of this correlation on fast timescales. In these measurements, the

first pulse creates an oscillating coherence between two vibrational states and after a time delay τ_1 , the second pulse creates a population state that decays with the characteristic vibrational lifetime. After a waiting time τ_2 , the third pulse again creates a coherence that oscillates in τ_3 . 2D IR spectroscopy correlates the oscillation frequency in τ_3 with that in τ_1 as a function of τ_2 . Fourier transforming the coherence oscillations in τ_1 and τ_3 gives us a 2D IR spectrum as a function of ω_1 (excitation frequency) and ω_3 (detection frequency) at different waiting times.

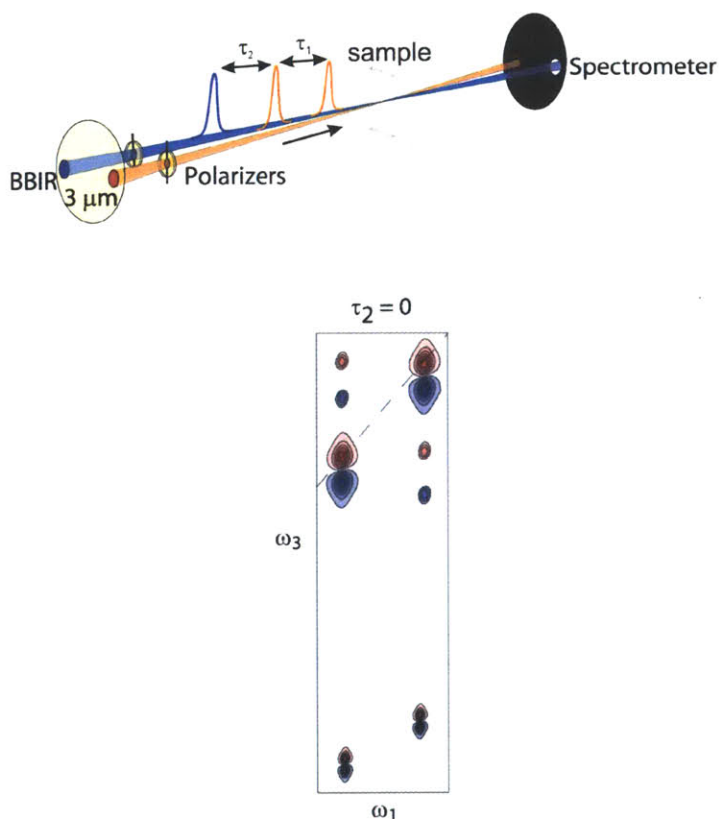


Figure 6-12: Beam diagram for the broadband 2D IR experiment (top). A cartoon of a broadband 2D IR spectrum of coupled oscillators at zero waiting time. The ω_1 dimension is defined by the 3 μm pulses and the ω_3 dimension is determined by the BBIR pulses.

The beam diagram for the broadband 2D IR experiment and an illustrative broadband 2D IR spectrum are shown in Figure 6-12. Such a 2D IR spectrum reflects the joint probability of exciting a vibration in ω_1 and measuring it at ω_3 after a waiting time τ_2 . In the broadband 2D IR experiments (BB 2D IR) that I will describe in this section, the first two interactions are with the 3 μm pulses from our OPA and the third interaction is with the BBIR pulses from the plasma. These experiments can hence correlate the vibrations in the 3 μm region with those at lower frequencies probed by the BBIR. Our BB 2D IR experiments were done in the pump-probe geometry, where the first two (pump) interacting beams are collinear, and the third interaction (probe) also acts as the local oscillator to heterodyne the third-order signal that is emitted in the same direction. The two 3 μm pump pulses are delayed with respect to each other to generate the τ_1 dimension, which is then numerically Fourier transformed to give the ω_1 axis, and the BBIR probe pulse along with the resonant third-order signal is dispersed onto an infrared array detector to generate the ω_3 axis of the BB 2D IR spectrum. In the pump-probe geometry, switching between acquiring broadband 2D IR spectra and collecting broadband pump-probe spectra is as simple as blocking one of the pump beams, and scanning the time delay (τ_2) between the other pump beam and the probe beam. Broadband pump-probe spectroscopy using BBIR pulses generated using methods similar to what was outlined in the previous section has been demonstrated by Petersen and co-workers to study vibrational dynamics in metal carbonyls and strongly hydrogen bonded dimers [43].

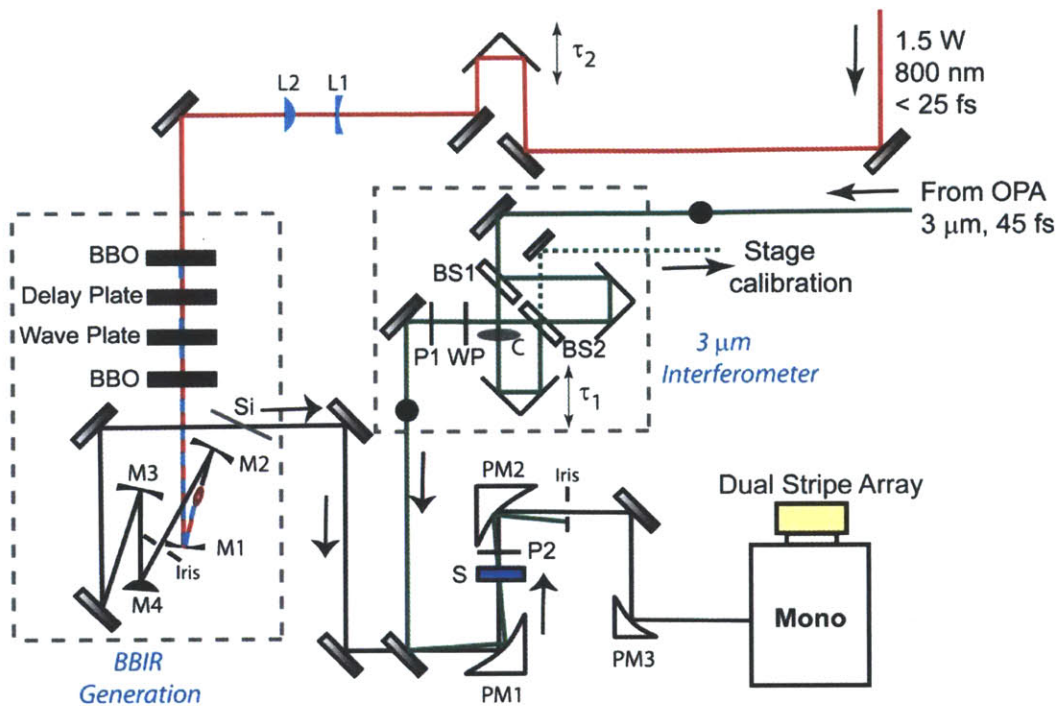


Figure 6-13: The broadband 2D IR experimental set-up. L1 and L2 are 1 in. fused silica lenses; BS1 and BS2 are CaF₂ 50/50 beam-splitters, anti-reflection coated for 3 μm on back face; WP is a λ/2 waveplate; P1 and P2 are CaF₂ wire-grid polarizers; C is chopper; M1 is a 1 in. dielectric curved mirror with $f = 5$ cm coated for 800 nm and 400 nm; M2 is a 1 in. UV enhanced silver mirror with $f = 5$ cm; M3 and M4 are 1 in. protected gold mirrors with $f = +25$ cm and -10 cm, respectively; PM1 and PM2 are 3 in. bare gold off-axis parabolic mirrors with effective focal length of 101.6 mm; PM3 is a 2 in. off-axis gold parabolic mirror with an effective focal length of 200 mm; S is sample. The filled circles represent periscopes. Note: The orientation of this diagram is different from what is shown in Fig. 6-2.

The 3 μm pulse pair for BB 2D IR experiments was created in a Mach-Zehnder interferometer, as shown in Figure 6-13. We first used a 50/50 beamsplitter (BS1, 3 mm thick, CaF₂, anti-reflection coated for 3 μm on one side and beam-splitter coated on the

other) to split the 3 μm output from the OPA into two arms. One arm was sent onto a retro-reflector mounted on a motorized translation stage (Aerotech) to scan the delay between the two arms that makes up the τ_1 dimension, and the other arm was sent onto a fixed retro-reflector and was chopped at half the laser repetition rate. Both the beams were then spatially re-combined on another 50/50 beamsplitter (BS2) and sent through a waveplate (WP) and polarizer (P1) in order to force the polarization of the 3 μm pulse pair to be parallel (or perpendicular) to the BBIR polarization at the sample.

Since the τ_1 axis has to be numerically Fourier transformed to obtain the broadband 2D IR spectra in the frequency domain, it is important to make sure that the error in the τ_1 delays is minimized to avoid side-bands and other artifacts in the Fourier transformed 2D IR spectra. It is therefore imperative that we perform an interferometric stage calibration procedure to correct for errors in the timing between the two arms before Fourier transforming the time-frequency raw data. The errors in stage position are systematic and stem from round-off issues in the stage encoder that tells the stage where to park for every time delay. These systematic errors can be corrected for by calibrating stage position using HeNe quadrature detection as described in Section 4.4.1. To acquire BB 2D IR data on acids and water, the τ_1 axis was scanned in steps of 2 fs from -100 fs to 400 fs to sample the coherence oscillations, which in H₂O-related systems dephases on a 100 fs timescale. After correcting for the stage errors, the oscillations in the τ_1 domain were then numerically Fourier transformed to generate the ω_1 frequency axis of the BB 2D IR spectrum.

For obtaining the BBIR probe beam, the 800 nm beam from the external compressor is first sent to an Aerotech translation stage to allow us to scan the waiting time τ_2 between the BBIR and 3 μm pulses. The beam is then shrunk in size using a telescope, and sent through the nonlinear crystals described in the previous section and onto the 5 cm focusing mirror to generate BBIR in a plasma. The BBIR emerging from the plasma is first incident on a 5 cm focal length concave silver mirror (M1; Newport) to collimate the beam (M2). The beam size at this point is ~ 7 mm in diameter, and is well-collimated. In order to achieve good focusing of the BBIR at the sample, we use a reflective expanding telescope consisting of a concave (M3 = +25 cm FL) and convex (M4 = -10 cm FL) gold mirrors (Edmund Optics) separated by ~ 13 cm, resulting in an increase in the size of the beam to ~ 14 mm-15 mm when collimated. The BBIR beam is then spatially overlapped with a HeNe tracer beam on the Si wafer, to help with subsequent alignment.

The 3 μm and the BBIR beams are parallel and vertically displaced, and are focused into the sample using the same 3 inch diameter off-axis bare gold parabolic mirror, with a reflective effective focal length of 101.6 mm (PM1). The size of the 3 μm beam out of the OPA is about 10 mm in diameter, giving us $\sim 75\%$ - 85% transmission through a 100 μm pinhole placed at the sample position, translating to a spot size of ~ 120 μm . The energy of the 3 μm at the sample is < 5 μJ . In order to find the zero-timing between the 3 μm pulses from the Mach-Zehnder interferometer, we perform interferometric autocorrelation through a 50 μm pinhole, and detect the interferogram on the HgCdTe array detector. We time up the BBIR and the 3 μm pulses by first finding the approximate time-zero in the InSb wafer and then by interferometric cross-correlation through a 50

μm pinhole. The resulting cross-correlation interferogram is shown in Figure 6-14. Since the interference between any two pulses requires spectral overlap, in addition to spatial and temporal overlap, the interferometric cross-correlation accurately times up only the blue side of the BBIR spectrum around 3400 cm^{-1} that is spectrally overlapped with the $3\text{ }\mu\text{m}$ pulses. Since the chirp of the BBIR is $\sim 70\text{ fs}/1500\text{ cm}^{-1}$, the timing of the BBIR pulses at lower frequencies will be delayed by approximately that amount relative to the $3\text{ }\mu\text{m}$ pulses. This is crucial to keep in mind while analyzing BBIR data.

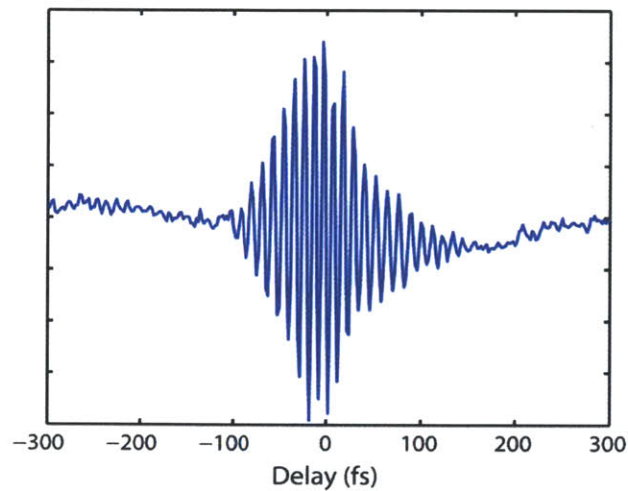


Figure 6-14: Interferometric cross-correlation of the blue side of the BBIR and the $3\text{ }\mu\text{m}$ pulses.

A second off-axis bare gold parabolic mirror (PM2) then collimates the beams after the sample. A pair of irises, one soon after the sample and another after the collimating parabolic, are placed to block the $3\text{ }\mu\text{m}$ beam and let the BBIR beam along with the resonant signal through and to prevent scatter from the pump beam from getting into the

array. We place an analyzing polarizer (P2) soon after the sample, and the angle is set at a value where maximum BBIR intensity is transmitted through the polarizer.

The BBIR beam along with the third-order signal is then focused using another off-axis gold parabolic mirror (PM3; 2 inch diameter, effective focal length ~ 20 cm) into a spectrometer equipped with a 50 grooves/mm grating blazed at $6 \mu\text{m}$ (Jobin Yvon Horiba Triax 190), which spectrally disperses the beam onto the liquid N_2 cooled HgCdTe 64 element array detector to generate the ω_3 dimension. The grating typically provides a spectral range of $\sim 1.5 \mu\text{m}$, with a $0.023 \mu\text{m}/\text{pixel}$ resolution. In order to capture the entire BBIR spectrum on the array detector, we have to scan the spectrometer grating position and stitch the spectra together during post-processing. We calibrated the frequency axis at every grating position by calculating the linear absorption spectrum of the acetic acid dimer in CCl_4 using BBIR pulses, and comparing it to the spectrum measured on a commercial FTIR spectrometer. For acquiring data in the $6\text{-}7 \mu\text{m}$ region, we place a long pass filter in front of the detector, which absorbs wavelengths lower than $4.5 \mu\text{m}$, hence eliminating artifacts associated with higher order diffraction from the gratings in the spectrometer.

For every grating position, the 2D IR spectra are acquired by scanning the non-chopped arm of the $3 \mu\text{m}$ interferometer in steps of 2 fs from -100 fs to 400 fs to create the τ_1 axis at a given τ_2 . After the τ_1 axis is scanned for all waiting times at one grating position, we scan the grating to a different position and acquire the waiting time series, and so on. We have seen that scanning four different grating positions can capture the BBIR spectrum from $\sim 1200 \text{ cm}^{-1}$ to 4200 cm^{-1} . The third-order signal is measured as a

change in absorbance, $\Delta OD = -\log\left(\frac{I_{open}}{I_{close}}\right)$, where I_{open} is the intensity measured on the detector when the chopper is open and I_{close} is the intensity with the chopper closed. In order to facilitate stitching of the spectra in the ω_3 dimension of the dispersed pump-probe and 2D IR data, the four grating positions are scanned such that there is a small region of overlap in frequency between the grating positions. We use these overlap regions to force the signal to be equal within this overlap by adding or subtracting the difference to one of the grating positions. We have found that the amount that we add or subtract is usually $<0.0005 \Delta OD$, which likely arises from slight changes to the alignment of the signal onto the array detector when the grating position is scanned.

The entire set-up is enclosed in a box containing four compartments – one for the transmissive telescope and the nonlinear crystals before the plasma, one for the plasma and curved mirrors, one for the 3 μm interferometer, and another for the sample/detection area. This allowed us to more efficiently purge the set-up with house dry air to minimize dispersion of the pulses due to atmospheric H_2O , and to minimize air currents that lead to fluctuations in BBIR beam pointing.

6.5 Conclusions

The ability to generate ultrafast broadband infrared pulses has opened opportunities to study many interesting systems that were previously studied through a limited window accessed by narrowband infrared pulses from conventional OPAs. Focusing the first, second and third harmonics of the <25 fs 800 nm output from a commercial Ti:Sapphire

amplifier in air has proved to be a robust and reliable way of generating linearly polarized BBIR pulses spanning 4000 cm^{-1} to hundreds of cm^{-1} , with <70 fs temporal duration and minimal chirp across the bandwidth. These pulses are well-suited for use in third-order nonlinear spectroscopy, and can be readily incorporated into 2D IR and pump-probe experiments. While we have characterized many of the features of the BBIR pulses, a lot remains to be understood. For example, we do not know why we see many BBIR intensity maxima while varying any of the parameters that determine the nature of the input visible pulses. Moreover, in the current set-up, the polarization of the third harmonic is orthogonal to that of the second harmonic and the fundamental frequencies. Understanding how changing the relative polarization of the visible beams affects the spectrum, intensity and the polarization of the BBIR pulses will provide us with ways of tuning the BBIR pulses to suit specific experimental requirements. Spatially profiling the BBIR beam is also important, as is finding ways of reducing noise and intensity drifts in the plasma, in order to improve the quality of the BBIR.

We have successfully employed broadband infrared pulses in broadband 2D IR spectroscopy and broadband IR pump-probe spectroscopy for probing processes such as vibrational dynamics in H_2O and proton transfer dynamics in acids, which will be described in detail in the subsequent chapters.

Acknowledgements

I thank Luigi De Marco and Aritra Mandal for their assistance with building the apparatus for broadband mid-infrared spectroscopy. This work was supported by the U.S Department of Energy (DE-FG02-99ER14988).

References

- [1] C. P. Lawrence and J. L. Skinner, *The Journal of Chemical Physics* **118**, 264 (2003).
- [2] K. B. Møller, R. Rey, and J. T. Hynes, *J. Phys. Chem. A* **108**, 1275 (2004).
- [3] Z. Ganim, H. S. Chung, A. W. Smith, L. P. Deflores, K. C. Jones, and A. Tokmakoff, *Acc. Chem. Res.* **41**, 432 (2008).
- [4] S. T. Roberts, K. Ramasesha, and A. Tokmakoff, *Acc. Chem. Res.* **42**, 1239 (2009).
- [5] J. D. Eaves, J. J. Loparo, C. J. Fecko, S. T. Roberts, A. Tokmakoff, and P. L. Geissler, *Proc. Natl. Acad. Sci. U.S.A.* **102**, 13019 (2005).
- [6] J. J. Loparo, C. J. Fecko, J. D. Eaves, S. T. Roberts, and A. Tokmakoff, *Phys. Rev. B* **70**, 1 (2004).
- [7] J. B. Asbury, T. Steinel, C. Stromberg, S. A. Corcelli, C. P. Lawrence, J. L. Skinner, and M. D. Fayer, *J. Phys. Chem. A* **108**, 1107 (2004).
- [8] R. A. Nicodemus, K. Ramasesha, S. T. Roberts, and A. Tokmakoff, *J. Phys. Chem. Lett.* **1**, 1068 (2010).
- [9] S. T. Roberts, P. B. Petersen, K. Ramasesha, A. Tokmakoff, I. S. Ufimtsev, and T. J. Martinez, *Proc. Natl. Acad. Sci. U.S.A.* **106**, 15154 (2009).
- [10] S. T. Roberts, K. Ramasesha, P. B. Petersen, A. Mandal, and A. Tokmakoff, *J. Phys. Chem. A* **115**, 3957 (2011).

- [11] H. S. Chung, A. Shandiz, T. R. Sosnick, and A. Tokmakoff, *Biochemistry* **47**, 13870 (2008).
- [12] A. W. Smith, J. Lessing, Z. Ganim, C. S. Peng, A. Tokmakoff, S. Roy, T. L. C. Jansen, and J. Knoester, *J. Phys. Chem. B* **114**, 10913 (2010).
- [13] G. Schweitzer, L. Xu, B. Craig, and F. C. Deschryver, *Opt. Commun.* **142**, 283 (1997).
- [14] H. S. Chung, M. Khalil, A. W. Smith, and A. Tokmakoff, *Rev. Sci. Instr.* **78**, 063101 (2007).
- [15] C. J. Fecko, J. J. Loparo, and A. Tokmakoff, *Opt. Commun.* **241**, 521 (2004).
- [16] J. Kim, U. W. Schmitt, J. A. Gruetzmacher, G. A. Voth, and N. E. Scherer, *J. Chem. Phys.* **116**, 737 (2002).
- [17] H. Chen, G. A. Voth, and N. Agmon, *J. Phys. Chem. B* **114**, 333 (2010).
- [18] J. Xu, S. Izvekov, and G. A. Voth, *J. Phys. Chem. B* **114**, 9555 (2010).
- [19] D. Borgis, G. Tarjus, and H. Azzouz, *J. Chem. Phys.* **97**, 1390 (1992).
- [20] J. M. Headrick, E. G. Diken, R. S. Walters, N. I. Hammer, R. A. Christie, J. Cui, E. M. Myshakin, M. A. Duncan, M. A. Johnson, and K. D. Jordan, *Science (New York, N.Y.)* **308**, 1765 (2005).
- [21] J.-W. Shin, N. I. Hammer, E. G. Diken, M. A. Johnson, R. S. Walters, T. D. Jaeger, M. A. Duncan, R. A. Christie, and K. D. Jordan, *Science (New York, N.Y.)* **304**, 1137 (2004).
- [22] J. R. Roscioli, L. R. McCunn, and M. A. Johnson, *Science (New York, N.Y.)* **316**, 249 (2007).
- [23] P. B. Petersen and A. Tokmakoff, *Opt. Lett.* **35**, 1962 (2010).
- [24] X. Xie, J. Dai, and X.-C. Zhang, *Phys. Rev. Lett.* **96**, 075005 (2006).
- [25] A. Stepanov, J. Kuhl, I. Kozma, E. Riedle, G. Almási, and J. Hebling, *Opt. Express* **13**, 5762 (2005).
- [26] H. Wen and A. Lindenberg, *Phys. Rev. Lett.* **103**, 023902 (2009).
- [27] N. Karpowicz and X.-C. Zhang, *Phys. Rev. Lett.* **102**, 093001 (2009).
- [28] J. Dai, N. Karpowicz, and X.-C. Zhang, *Phys. Rev. Lett.* **103**, 023001 (2009).

- [29] T. Bartel, P. Gaal, K. Reimann, M. Woerner, and T. Elsaesser, *Opt. Lett.* **30**, 2805 (2005).
- [30] H. Hamster, A. Sullivan, S. Gordon, W. White, and R. W. Falcone, *Phys. Rev. Lett.* **71**, 2725 (1993).
- [31] M. Kress, T. Löffler, S. Eden, M. Thomson, and H. G. Roskos, *Opt. Lett.* **29**, 1120 (2004).
- [32] D. J. Cook and R. M. Hochstrasser, *Opt. Lett.* **25**, 1210 (2000).
- [33] M. Cheng, A. Reynolds, H. Widgren, and M. Khalil, *Opt. Lett.* **37**, 1787 (2012).
- [34] T. Fuji, T. Horio, and T. Suzuki, *Opt. Lett.* **32**, 2481 (2007).
- [35] S. L. Chin, S. A. Hosseini, W. Liu, Q. Luo, F. Théberge, N. Aközbek, A. Becker, V. P. Kandidov, O. G. Kosareva, and H. Schroeder, *Can. J. Phys.* **83**, 863 (2005).
- [36] A. Braun, G. Korn, X. Liu, D. Du, J. Squier, and G. Mourou, *Opt. Lett.* **20**, 73 (1995).
- [37] P. B. Corkum, *Phys. Rev. Lett.* **71**, 1994 (1994).
- [38] K.-Y. Kim, J. H. Glowina, A. J. Taylor, and G. Rodriguez, *Opt. Express* **15**, 4577 (2007).
- [39] K. Y. Kim, A. J. Taylor, J. H. Glowina, and G. Rodriguez, *Nat. Photon.* **2**, 605 (2008).
- [40] T. Fuji and T. Suzuki, *Opt. Lett.* **32**, 3330 (2007).
- [41] P. Lassonde, F. Théberge, S. Payeur, M. Châteauneuf, J. Dubois, and J. Kieffer, *Opt. Express* **19**, 14093 (2011).
- [42] C. R. Baiz and K. J. Kubarych, *Opt. Lett.* **36**, 187 (2011).
- [43] C. Calabrese, A. M. Stingel, L. Shen, and P. B. Petersen, *Opt. Lett.* **37**, 2265 (2012).
- [44] F. Théberge, N. Aközbek, W. Liu, A. Becker, and S. Chin, *Phys. Rev. Lett.* **97**, 1 (2006).
- [45] V. Greco, G. Molesini, and F. Quercioli, *Rev. Sci. Instr.* **66**, 3729 (1995).
- [46] L. Lepetit, G. Chériaux, and M. Joffre, *J. Opt. Soc. Am. B* **12**, 2467 (1995).

[47] S. T. Roberts, J. J. Loparo, K. Ramasesha, and A. Tokmakoff, *Opt. Commun.* **284**, 1062 (2011).

Chapter 7

Water vibrations have strongly mixed intra- and inter-molecular character

7.1 Introduction

Most chemical reactions in nature happen under aqueous conditions, where the ultrafast motions of liquid water play a crucial role in activating reactants and stabilizing reactive intermediates. Solutes dissolved in water are greatly influenced by the vibrational motions of the surrounding water, which include their internal bond vibrations and the orientational and translational motions. Unlike other liquids, water's intermolecular motions span an enormous range of frequencies, making vibrational energy relaxation in liquid H₂O a particularly complex interplay between intra- and inter-molecular relaxation pathways that is influenced by anharmonic vibrational coupling, hydrogen bonding interactions, and dielectric or charge fluctuations. The timescales and pathways for the relaxation of vibrational excitation in H₂O has been the subject of numerous recent experimental [1–11] and theoretical [12–17] investigations. Most of

these studies interpret relaxation processes using a common weak coupling paradigm which effectively decouples the contributions from stretching, bending, and inter-molecular pathways of energy relaxation and leads to cascading downhill energy relaxation from intramolecular vibrations and into the solvent. This picture persists even as recent studies established that the OH stretching vibration of water cannot be described simply as local bond stretching or symmetric/asymmetric vibrations, but as a collective excitation of several molecules [15–17]. Here, we present ultrafast broadband infrared spectroscopy of H₂O which provides evidence for the strongly mixed character of all intra- and inter-molecular vibrations in water.

As displayed in Figure 7-1, the molecular vibrational motions of liquid water contribute to mid-infrared absorption features that span a wide range of frequencies, including OH stretching at 3400 cm⁻¹, the H₂O bend vibration at 1650 cm⁻¹, and intermolecular vibrations such as librations (hindered rotations) between 700-400 cm⁻¹ and hydrogen bond stretching and deformation at even lower frequencies. To properly investigate the couplings and energy transfer between these vibrations therefore requires an experimental technique that can probe the entire mid-infrared spectrum with high time resolution. To now, experiments have either been limited by insufficient time-resolution or limited spectral bandwidth. We have employed a new femtosecond laser plasma source that generates mid-infrared pulses with a bandwidth many times that of traditional sources and a pulse duration of <70 fs, and used these to perform broadband pump-probe and 2D IR experiments on water in which the OH stretch vibration of H₂O was excited and the mid-infrared between 1350-4000 cm⁻¹ was probed. 2D IR measurements allow us to observe vibrational couplings of the OH stretch vibration with other degrees of

freedom, and frequency-dispersed pump-probe experiments monitor vibrational and orientational relaxation processes.

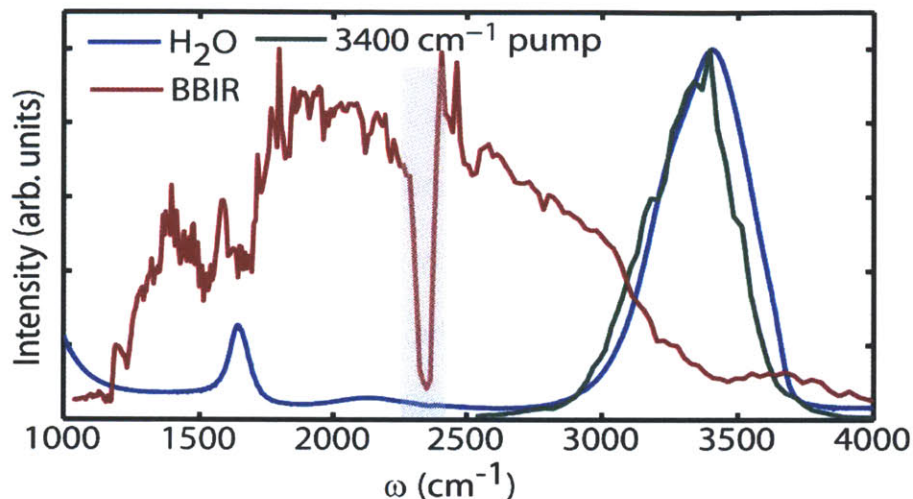


Figure 7-1: Spectra of the 3400 cm^{-1} pump and the broadband infrared probe pulses overlaid on the linear infrared spectrum of H_2O . The dip in the BBIR spectrum at $\sim 2300\text{ cm}^{-1}$ is due to the atmospheric CO_2 .

7.2 Experimental methods

Pump-probe and 2D IR measurements were performed using $\sim 3400\text{ cm}^{-1}$ excitation of the OH stretching region in H_2O , followed by broadband mid-infrared probing. The excitation pulse was the 45 fs output from a home-built BBO/ KNbO_3 based OPA, with the pulse spectrum centered at 3400 cm^{-1} with a $350\text{-}400\text{ cm}^{-1}$ bandwidth at full-width at half-maximum [18]. We used femtosecond broadband mid-infrared (BBIR) pulses that ranged in frequency from $<400\text{ cm}^{-1}$ to 4000 cm^{-1} for probing changes to the mid-infrared region of the H_2O spectrum [19]. Figure 7-1 shows the $3\text{ }\mu\text{m}$ and BBIR pulse spectra

along with the linear infrared spectrum of H₂O. To generate the BBIR pulses we used ~1.25 W of the <25 fs 800 nm output from a 1 kHz commercial Ti:Sapphire regenerative amplifier to generate its second and third harmonic frequencies in Type I BBO crystals. A delay plate and a waveplate between the doubling and tripling crystals were used to compensate for the temporal walk-off and polarization changes, respectively. All three frequencies were then focused in air using a 5 cm focal length dielectric mirror to create a plasma, which radiated short pulses that spanned the mid- to far-IR [19]. The BBIR pulses generated using this method were linearly polarized. The visible output from the plasma was filtered out by passing the beam through a sequence of gold mirrors and a 400 μm thick high-resistivity Si wafer placed at Brewster's angle.

Broadband 2D IR experiments were done in the pump-probe geometry [20], where the first two (pump) interactions are with the spatially overlapped 3 μm excitation pulses, and the third (probe) interaction is with the BBIR pulse that co-propagates with the resonant third-order signal from the sample. The 3 μm pulse pair for the 2D IR experiments was created by splitting the OPA output in a Mach-Zehnder interferometer. One of the two interferometer arms was sent to a finely-controlled and interferometrically calibrated [21–23] translation stage, and the other arm was chopped at half the laser repetition rate. The 3 μm pulses were delayed with respect to each other from -100 fs to 400 fs in steps of 2 fs to trace out the coherence oscillations in τ_1 , which were subsequently numerically Fourier transformed to generate the ω_1 dimension of the 2D IR spectrum. The waiting time (τ_2) was controlled by scanning the 800 nm beam prior to the generation of the BBIR probe. The BBIR and the 3 μm beams were focused into the sample using bare gold off-axis parabolic mirrors. After the sample, the transmitted BBIR

along with the resonant signal was dispersed onto a 64 element liquid nitrogen cooled HgCdTe array detector to generate the ω_3 dimension. The broadband 2D IR and pump-probe spectra in this chapter are plotted from 1350 cm^{-1} to 4000 cm^{-1} , where the low frequency limit is imposed by the detector response. The BBIR pulse was temporally characterized against the known $3\text{ }\mu\text{m}$ pulse through resonant cross-correlation in InSb. This yielded a BBIR pulse duration of $<70\text{ fs}$, which is maintained at all probed frequencies. An average chirp of $\sim 70\text{ fs}$ in the 1350 cm^{-1} to 4000 cm^{-1} region was characterized using non-resonant cross correlation of BBIR and $3\text{ }\mu\text{m}$ pulses in a 1 mm thick CaF_2 window. Time-zero in τ_2 between the BBIR and $3\text{ }\mu\text{m}$ pulses is defined based on the resonant pump-probe signal from H_2O or through resonant cross-correlation in InSb. For 2D IR experiments, the τ_1 time zero between the $3\text{ }\mu\text{m}$ pulse pair is defined using interferometric cross-correlation through a pinhole placed at the sample position, and detected on the array. Small errors in τ_1 timing are corrected by adding a phase factor during post-processing of the acquired broadband 2D IR spectra upon invoking the projection-slice theorem.

For the broadband 2D IR spectra, the polarizations of both the pump and probe pulses were oriented parallel to each other. For pump-probe experiments, we by-passed the Mach-Zehnder interferometer and used the full output of the home-built OPA as the excitation pulse, and the BBIR pulse was used as the probe. We tuned the polarization of the $3\text{ }\mu\text{m}$ beam relative to the BBIR beam using a $\lambda/2$ waveplate–wire-grid polarizer pair. The H_2O sample for these experiments was held between two 1 mm thick CaF_2 windows without a spacer, and the sample was maintained at room temperature of $\sim 25\text{ }^\circ\text{C}$. The optical density of the sample was kept between 0.8 and 1 at the peak of the OH stretch

lineshape at 3400 cm^{-1} for both measurements. This corresponds to an optical density of a little less than 0.3 at the 1650 cm^{-1} H_2O bend transition.

We use a 50 grooves/mm grating to disperse the BBIR probe plus resonant signal onto the HgCdTe array detector. We have found that scanning four different grating positions can capture the BBIR spectrum from $\sim 1250\text{ cm}^{-1}$ to 4200 cm^{-1} . For every grating position, the 2D IR spectra are acquired by scanning the non-chopped arm of the $3\text{ }\mu\text{m}$ interferometer in steps of 2 fs from -100 fs to 400 fs to create the τ_1 axis at a given τ_2 . After the τ_1 axis is scanned for all waiting times at one grating position, we scan the grating to a different position and acquire the waiting time series, and so on. We follow a similar procedure for broadband pump-probe spectroscopy, where we scan all the waiting times at one grating position, and then move the grating to a different position and repeat the process. The third-order signal is measured as a change in absorbance,

$$\Delta OD = -\log\left(\frac{I_{open}}{I_{close}}\right),$$

where I_{open} is the intensity measured on the detector when the

chopper is open and I_{close} is the intensity with the chopper closed. For acquiring data in the $6\text{-}7\text{ }\mu\text{m}$ region, we place a long pass filter in front of the detector, which absorbs wavelengths lower than $4.5\text{ }\mu\text{m}$, hence eliminating artifacts associated with higher order dispersion from the grating. [While all the broadband pump-probe spectra presented in this chapter do not contain artifacts from higher order dispersion, we are currently in the process of implementing this procedure for the broadband 2D IR spectra. While most features in the low frequency region of the 2D IR spectra are not significantly impacted by higher order dispersion due to substantial contribution from resonant signal, the $\omega_3 = 1400\text{ cm}^{-1}$ peak in the 2D IR spectra is an artifact of higher order dispersion, which

should appear as a plateau]. In order to facilitate stitching of the spectra in the ω_3 dimension of the dispersed pump-probe and 2D IR data, the four grating positions are scanned such that there is a small region of overlap in frequency between the grating positions. We use these overlap regions to force the signal to be equal within this overlap by adding or subtracting the difference to one of the grating positions. We have found that the amount that we add or subtract is usually $<0.0005 \Delta OD$, which likely arises from slight changes to the alignment of the signal onto the array detector when the grating position is moved.

The entire set-up is enclosed in a box and is purged with dry air to minimize contribution to the spectrum from atmospheric H_2O . However, atmospheric CO_2 contributes to our signal in the 4 μm region of the BBIR spectrum.

7.3 Results and discussion

Figure 7-2 and 7-3 display the broadband 2D IR spectra of H_2O at different waiting times. A 2D IR spectrum is related to the joint probability of exciting a vibration of frequency ω_1 and detecting it at ω_3 after a waiting time τ_2 . The spectra exhibit cross peak bleaches (blue) and induced absorptions from the excited OH stretch vibration to a continuum of overtone and combination bands (red). Focusing on the earliest waiting time data ($\tau_2=50$ fs in Figure 7-2a), we note that the spectrum is dominated by a bleach on the diagonal axis at the OH stretch frequency $(\omega_1, \omega_3) = (3400 \text{ cm}^{-1}, 3400 \text{ cm}^{-1})$, and a broad induced absorption below it. The diagonal region bears some similarity to results obtained with narrower bandwidth pulses [6,9], but the off-diagonal region reveals far

more extensive vibrational couplings. Upon OH stretch excitation, we also see the immediate appearance of a bleach cross peak with the water bending transition at (3350 cm^{-1} , 1650 cm^{-1}), which is anticipated from the anharmonic couplings reported in pump bend/probe stretch experiments [2]. The presence of cross-peaks in a short waiting time 2D IR spectrum indicates that the coupling of these vibrations is strong enough that excitation exchanges coherently on the timescale of their vibrational periods.

The bend cross peak bleach is superimposed on an induced absorption ridge that stretches from $\omega_3 > 3200\text{ cm}^{-1}$ down below the limits of our detector $< 1350\text{ cm}^{-1}$. The induced absorption ridge is particularly striking because it is peaked at $\omega_3 = 2950\text{ cm}^{-1}$, 450 cm^{-1} below the bleach at 3400 cm^{-1} , and extends as a prominent tail toward and beyond the bend transition. It is qualitatively different from the transient OH stretching spectrum observed after pumping the H₂O bend [2]. Therefore, this band cannot be solely ascribed to transitions to overtone or traditional combination bands, such as those used to describe isotopically dilute ice Ih [24]. These induced absorptions represent vibrational states that have been accessed by two sequential mid-IR photons with energies in the range $3200\text{-}3600\text{ cm}^{-1}$ and $3000\text{-}2600\text{ cm}^{-1}$, although the one-photon absorption spectrum (Fig. 7-2b) is spectrally clear in the corresponding $6000\text{-}6400\text{ cm}^{-1}$ region.

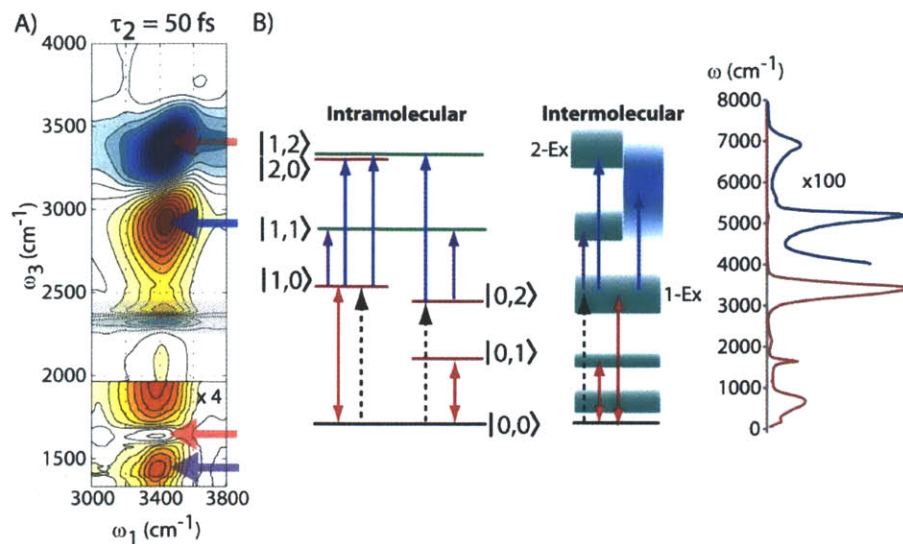


Figure 7-2: a) Broadband 2D IR spectrum of H₂O at $\tau_2 = 50$ fs using excitation pulses centered at 3400 cm^{-1} , with a $\sim 400\text{ cm}^{-1}$ bandwidth. Color-coded arrows represent transitions illustrated in b). The grey bar represents response from atmospheric CO₂. b) Intramolecular and intermolecular energy level diagrams representative of the bend-stretch coupling and vibrational delocalization pictures, respectively. The terms 1-Ex and 2-Ex represent one-exciton and two-exciton manifolds. Infrared spectrum of H₂O from 0-cm^{-1} to 8000 cm^{-1} gives the energy scaling for the transitions illustrated in the energy level diagrams [25].

Rapid and efficient intermolecular transfer of OH vibrational excitation has been described in recent experiments and theory. In some cases, this process has been attributed to resonance energy transfer, a weak interaction between donor and acceptor that results in energy transfer without memory [26]. In other cases, the OH stretch has been described as a delocalized vibration, or exciton, that involves coherent vibrational motion spanning 1-6 water molecules [15–17]. Here also, an OH transition dipole interaction was used for describing the coupling. Explicit modeling of 2D IR spectra with exciton models capture the width of the OH excitation in ω_1 , but do not reproduce the

induced absorption features in ω_3 . Therefore, our data are not described by resonant energy transfer or transition dipole coupling, which are bilinear couplings based only on the energy splitting between donor and acceptor states and the magnitude of their transition dipoles. Instead, the broad induced absorptions in our experiments demonstrate that excitation of the OH stretch alters the energy of the doubly excited states of the coupled system, which requires a nonlinear or anharmonic coupling between exciton states. Excitation of one delocalized OH vibration is coupled strongly enough to other OH vibrations that coherent energy exchange between them allows excitation of the second at much lower energy, as shown in Figure 7-2b. This excitation induced shift is analogous to the frequency shift in electronic systems attributed to the biexciton binding energy.

In addition to delocalization of the OH stretch vibration, there is evidence of strong stretch-bend coupling. Upon forming hydrogen bonds in water the frequency of the OH stretch red-shifts whereas the bend frequency blue-shifts. These effects shift the OH oscillator toward resonance with the bending overtone transition, resulting in an anharmonic Fermi resonance between the $v = 1$ level for strongly hydrogen bonded OH oscillators and the $v = 2$ state of the bending mode, shown in Figure 7-2b. This effect is observed in the 2D IR spectrum through the position of the bend cross-peak bleach. Its peak excitation frequency (ω_1) is red-shifted by $\sim 100 \text{ cm}^{-1}$ relative to the stretching bleach at $\omega_1 = 3400 \text{ cm}^{-1}$. This indicates that the feature at $\omega_3 = 1650 \text{ cm}^{-1}$ is correlated with the red-shifted bend overtone transition at 3250 cm^{-1} , providing evidence that the pump pulse excites vibrations with mixed stretch and bend character by virtue of a Fermi resonance. Therefore, we argue that the bleach at 3400 cm^{-1} is due to contributions both

from stretch and bend overtone excitations, and the separation in frequency between the bleach and induced absorption in the 3 μm region does not directly report on the anharmonicity of a single OH stretch vibration. These findings also suggest that the same Fermi resonance is involved in the debated residual structure at 3250 cm^{-1} in the IR absorption and Raman spectra of H_2O .

Although a clear bleach of the bend fundamental transition is present, there is no clear induced absorption attributable to a distinct stretch-bend combination band. Rather, it seems that the probe transition from the excited stretch to the bend-stretch combination band is a broad background that is continuous with the stretch induced absorption. Fermi resonance between stretch and bend also leads to near-degeneracy between the $|20\rangle$ and $|12\rangle$ vibrations (Figure 7-2b), where the states are represented as $|n_s, n_\delta\rangle$, n_s referring to the stretch quantum number and n_δ referring to the bend quantum number. This near-degeneracy ensures that these states will be strongly mixed by the intermolecular fluctuations that modulate their energy about the degeneracy point. As a result, the mixing of bend and stretch is strong enough that their vibrational character is inextricably intertwined, and strongly influenced by the intermolecular motions that determine the fate of this interaction. Therefore, we believe that the intrinsic vibrational excitations in H_2O are highly mixed and include contributions from the OH stretch, the H_2O bend and the intermolecular vibrations.

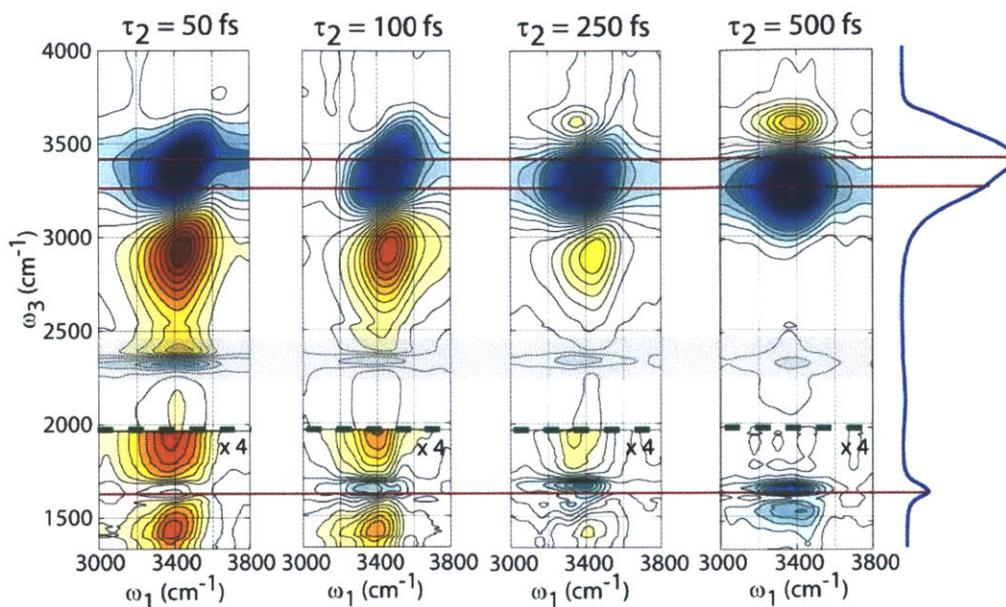


Figure 7-3: Broadband 2D IR spectra at waiting times of 50 fs, 100 fs, 250 fs and 500 fs. The spectra are normalized to the maximum of the 50 fs surface. The low frequency parts of the spectra at $\omega_3 < 2000 \text{ cm}^{-1}$ are magnified by a factor of four. The FTIR spectrum of H_2O is aligned with the ω_3 axis to guide the eye. The feature at $\omega_3 \sim 2300 \text{ cm}^{-1}$ is due to the atmospheric CO_2 .

With these spectral assignments at hand, we examine the waiting time dependence of the 2D IR spectra to describe the dynamics of these excitons. Figure 7-3 shows a series of 2D IR spectra of H_2O at different waiting times. The spectra show a fast loss of frequency correlation in the OH stretch region with a time scale of ~ 250 fs, as seen from the evolution of the slope of the nodal line between the $\omega_3 = 3400 \text{ cm}^{-1}$ and the $\omega_3 = 3000 \text{ cm}^{-1}$ features. Also the induced absorption relaxes with a similar 250 fs time scale in the broadband 2D IR spectra across all frequencies. These observations qualitatively differ from previous 2D IR measurements with narrower spectral bandwidth, where 2D IR

surfaces showed a loss of frequency correlation within 50 fs and the decay of the induced absorption at $\omega_3 = 3000 \text{ cm}^{-1}$ within 100 fs [6,9].

Pump-probe spectroscopy allowed us to track the time-evolution of the spectral features seen in broadband 2D IR spectra. The waiting-time-dependent broadband dispersed pump-probe spectra of H₂O are displayed in Figure 7-4a. We performed constrained singular value decomposition (SVD) [27] between 100-5000 fs to determine distinct characteristic time scales and spectral features in the data. Although the shortest dynamics do not linearly decompose, this analysis does confirm that spectral relaxation after 100 fs can be described in terms of two spectral relaxation components within the data. The first component of the decomposition yields a spectrum that we constrain to match the long time response, and is dominated by the 700 fs to 2 ps rise timescale (Figure 7-4b). The second component resembles the early time spectrum consisting of the continuum response, exhibiting timescales between 200 fs and 300 fs. Although the minimum of the 3400 bleach appears to red-shift with time, also seen in the diagonal peak in 2D IR spectrum, singular value decomposition suggests that the spectrum can be decomposed into primarily two-component consisting of the early time spectrum and the long time spectrum. The long time SVD component spectrum in turn is quantitatively identical to a 3 degree thermal difference spectrum.

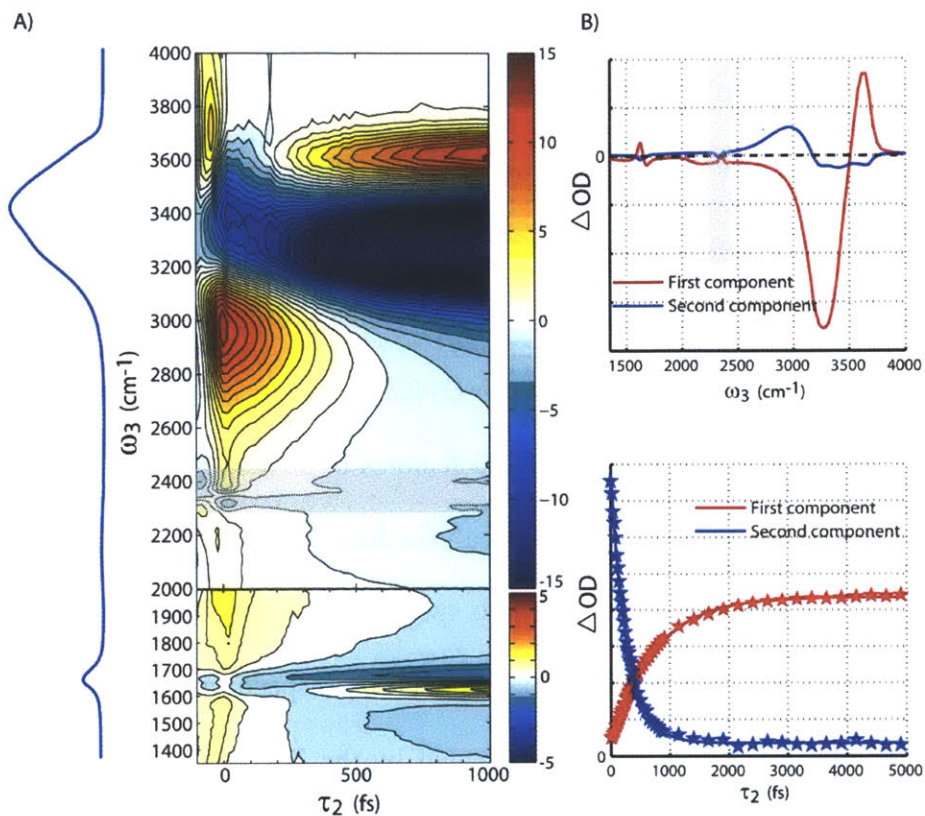


Figure 7-4: a) Broadband dispersed pump-probe spectrum of H₂O taken under magic angle polarization conditions (left). The feature at $\omega_3 \sim 2300 \text{ cm}^{-1}$ is due to the atmospheric CO₂. Color bar represents a change in absorbance in units of ΔmOD . b) The first two components from a constrained singular value decomposition of the data presented in a) from 100 fs to 5 ps. The spectral components are displayed in the top panel, and the time components are displayed in the bottom panel. Lines through the time components represent single exponential fits. The first component yielded a time scale in the range of 700 fs to 2 ps, and the second component was fit to a timescale of 250 fs.

This spectral shifting effect has been observed in a limited spectral range before and our data show that it spans the mid-IR. Due to the correlation with the thermal difference spectrum, the spectral shifting has been ascribed to “heating” of the liquid, in which energy transfer into intermolecular motions leads to a net weakening of hydrogen bonds [28]. It is remarkable that a spectrum of a system that is clearly not at equilibrium

appears identical to an equilibrium measurement. We see that these spectral shifts are prominent at all frequencies on time-scales when memory of the initial OH excitation frequency still exists (250 fs), and shorter than the structural relaxation of the liquid hydrogen bond network (1-2 ps). Relaxation of these intertwined vibrations is slower than OH stretching vibrational periods, but short compared to the intermolecular motions. Indeed the observed picosecond response from the sample appears similar to what one would see from impulsive excitation of low frequency modes in which the response rises with the time-scale of the vibrational period, as seen in the $\omega_3 = 3600 \text{ cm}^{-1}$ slice through the dispersed pump-probe displayed in Figure 7-5. Thus we conclude that this observation is consistent with strong nonlinear coupling of the intermolecular hydrogen bonding motions with the stretch and bend delocalized vibrations. This coupling is strong enough that pumping the OH excitation acts to physically change intermolecular configurations to an extent expected for thermal changes as fast as the collective motion of the molecules allow. These conclusions are consistent with recent theoretical studies that report strong coupling of stretch, bend, and librational modes, in which bend excitation transfers between adjacent molecules in 50 fs, a time-scale comparable to the period of bending vibrations (20 fs) [12].

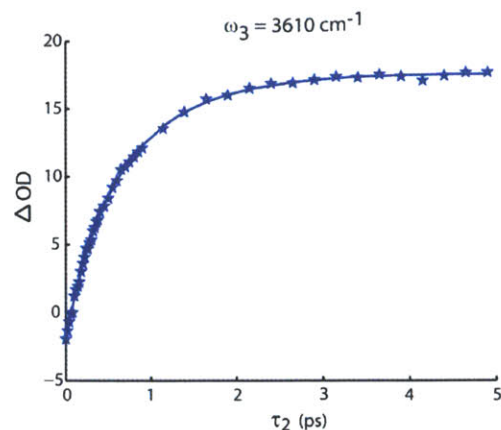


Figure 7-5: Slice at $\omega_3 = 3610 \text{ cm}^{-1}$ through the broadband dispersed pump-probe spectrum of H_2O . The line represents a double exponential fit through the data, which yielded timescales of 250 fs and 1 ps.

Further information on the delocalized stretch-bend excitations is obtained from polarization-dependent pump-probe studies. Figure 7-6 shows the parallel and perpendicular dispersed pump-probe spectra of H_2O , along with the calculated anisotropy between 2900 cm^{-1} and 3000 cm^{-1} . From these spectra, it is clear that the stretch and induced absorption region are polarized. It appears that excitation of OH stretching motion polarizes charges along the constituent hydrogen bonds so that second OH excitation is enabled along the same orientation at much lower energy. The induced absorption has a common anisotropy decay of $\sim 100 \text{ fs}$ at 2900 cm^{-1} to 3000 cm^{-1} , which agrees with the earlier measurements of anisotropy in the OH stretch region [9,26]. The bend bleach, however, is depolarized from zero waiting time, pointing again to the delocalized stretch excitation over several water molecules such that the orientation of the bend transition dipole is uncorrelated with that of the stretch.

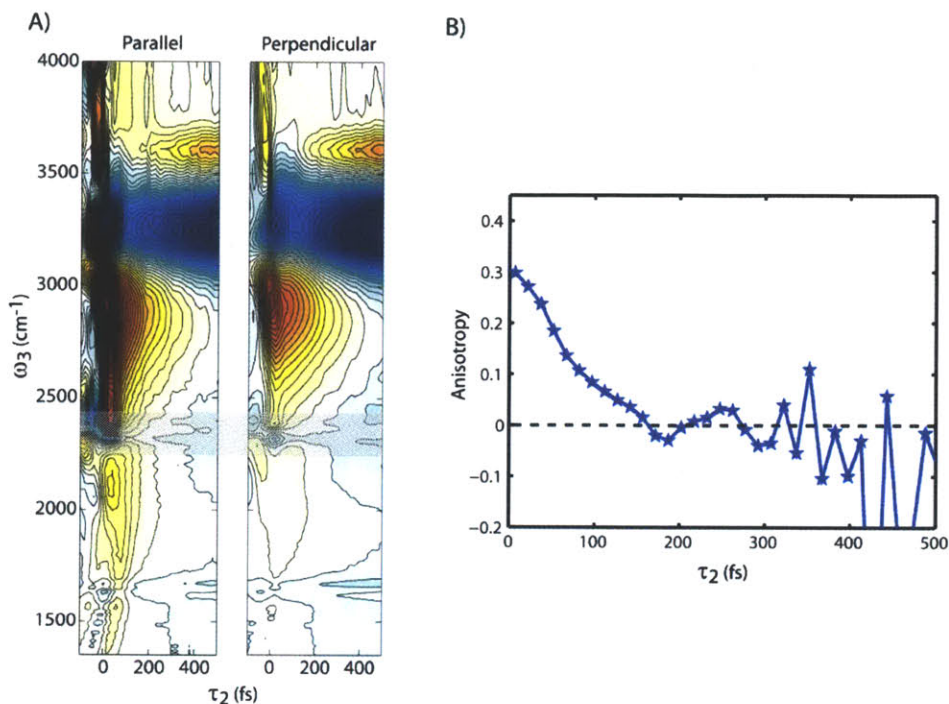


Figure 7-6: a) Broadband dispersed pump-probe spectra of H₂O at parallel and perpendicular polarizations, normalized to the maximum of the parallel spectrum. b) Time trace of pump-probe anisotropy as a function of waiting time integrated in ω_3 between 2900 cm⁻¹ and 3000 cm⁻¹.

These results can be used to propose a molecular picture for energy relaxation and vibrations of the liquid. Infrared excitation of OH stretching transitions creates delocalized states with varying stretch and bend character. These excitons are by no means stationary and are constantly evolving due to the motions of the liquid, resulting in competing ultrafast energy transport and dissipation pathways. Depending on the changing intermolecular configurations within the exciton, it can transfer to lower energy configurations within the exciton band, preferentially moving toward low energy strongly hydrogen bonded traps. Relaxation within the band guides the energy into resonance with the bend overtone, making it the preferred relaxation route. But simultaneously, we

observe that energy relaxation to intermolecular motions acts to shift spectral bands at short times. The stretch/bend exciton also couples into bend and intermolecular motion, which results in the response of the liquid on the timescales of the fastest intermolecular motions. Distributing the 3400 cm^{-1} of energy among the large densities of stretch, bend and intermolecular modes therefore results in numerous channels for energy dissipation.

Our proposal differs considerably from the canonical picture of vibrational relaxation, in which energy flows downhill through a set of weakly coupled intramolecular normal modes and into low-frequency collective intermolecular vibrations of the surroundings. This picture, rooted in perturbation theory, is commonly used to describe relaxation of the OH stretch excitation and the growth of the thermal difference spectrum in water. In previous work it was concluded that upon the excitation of the OH stretch vibration in water, the energy first flows into the overtone or the fundamental transition of the H_2O bend vibration that is either localized on one molecule or across two neighboring water molecules, and then into the collective motions of the liquid [3,8,10,11]. These pictures are appropriate in the case of weak coupling between donor and acceptor, when the timescale of energy exchange and relaxation far exceeds the vibrational periods. Given that the relaxation time-scales are similar to vibrational periods, and occur faster than the reorganization of liquid structure, description of energy transfer in terms of the normal modes or local modes of an H_2O molecule will be unsatisfactory. Vibrational excitation in water is coupled strongly enough that the local intermolecular configuration of the liquid dictates the form of the vibration, and is more accurately described as an exciton with mixed inter- and intra-molecular character.

Highly coupled and collective vibrational motions in water would have significant implications for the way in which we conceive of solutes in water and aqueous chemical reactivity. Traditional ways of thinking about the interaction between a solute and the solvating water molecules, where their interaction is treated as a perturbation, may need to be re-evaluated for the case of aqueous solutes. Given that water vibrations are delocalized, the vibrational eigenstates associated with the solute in water may also be delocalized, with correlations extending over its solvation shell. The extent of coherent vibrational character of coupled solute and solvent also determines the distance scale and mechanism over which concerted bimolecular chemical reactions such as proton transfer can occur. These vibrational motions, in addition to dissipation, are also the origin of activation processes for solution phase chemical reactions. Our results also imply that intermolecular motions can be coupled effectively to intramolecular modes of the system, which may act to funnel energy of collective motion and enhance local reactivity.

7.4 Summary

In this chapter, I have demonstrated the use of broadband infrared spectroscopy techniques to study coupling and vibrational energy relaxation in liquid H₂O. Our data show clear evidence for a vibrationally coupled system, where features seen across the mid-IR in both the 2D IR and pump-probe spectra are a result of transitions to strongly mixed vibrational states that are inherently broadened by their coupling to intermolecular modes. Exciting the OH stretch vibration results in an instantaneous and coherent response from the bend and intermolecular modes of water. These observations suggest

that one cannot separate the contributions from inter- and intra-molecular pathways in describing energy transfer and relaxation in water.

Acknowledgements

I thank Luigi De Marco and Aritra Mandal for their help with setting up the experiment and acquiring data. This work was supported by the U.S Department of Energy (DE-FG02-99ER14988).

References

- [1] A. Pakoulev, Z. Wang, and D. D. Dlott, *Chem. Phys. Lett.* **371**, 594 (2003).
- [2] J. Lindner, D. Cringus, M. S. Pshenichnikov, and P. Vöhringer, *Chem. Phys.* **341**, 326 (2007).
- [3] J. Lindner, P. Vöhringer, M. S. Pshenichnikov, D. Cringus, D. A. Wiersma, and M. Mostovoy, *Chem. Phys. Lett.* **421**, 329 (2006).
- [4] Z. Wang, A. Pakoulev, Y. Pang, and D. D. Dlott, *J. Phys. Chem. A* **108**, 9054 (2004).
- [5] O. F. A. Larsen and S. Woutersen, *J. Chem. Phys.* **121**, 12143 (2004).
- [6] M. L. Cowan, B. D. Bruner, N. Huse, J. R. Dwyer, B. Chugh, E. T. J. Nibbering, T. Elsaesser, and R. J. D. Miller, *Nature* **434**, 199 (2005).
- [7] N. Huse, S. Ashihara, E. T. J. Nibbering, and T. Elsaesser, *Chem. Phys. Lett.* **404**, 389 (2005).
- [8] J. C. Deák, S. T. Rhea, L. K. Iwaki, and D. D. Dlott, *J. Phys. Chem. A* **104**, 4866 (2000).

- [9] D. Kraemer, M. L. Cowan, A. Paarmann, N. Huse, E. T. J. Nibbering, T. Elsaesser, and R. J. D. Miller, *Proc. Natl. Acad. Sci. U.S.A.* **105**, 437 (2008).
- [10] A. J. Lock and H. J. Bakker, *J. Chem. Phys.* **117**, 1708 (2002).
- [11] S. Ashihara, N. Huse, A. Espagne, E. T. J. Nibbering, and T. Elsaesser, *J. Phys. Chem. A* **111**, 743 (2007).
- [12] R. Rey and J. T. Hynes, *Phys. Chem. Chem. Phys.* **14**, 6332 (2012).
- [13] T. L. C. Jansen, B. M. Auer, M. Yang, and J. L. Skinner, *J. Chem. Phys.* **132**, 224503 (2010).
- [14] T. Yagasaki and S. Saito, *J. Chem. Phys.* **134**, 184503 (2011).
- [15] B. M. Auer and J. L. Skinner, *J. Chem. Phys.* **128**, 224511 (2008).
- [16] A. Paarmann, T. Hayashi, S. Mukamel, and R. J. D. Miller, *J. Chem. Phys.* **130**, 204110 (2009).
- [17] C. Falvo, B. Palmieri, and S. Mukamel, *J. Chem. Phys.* **130**, 184501 (2009).
- [18] C. J. Fecko, J. J. Loparo, and A. Tokmakoff, *Opt. Commun.* **241**, 521 (2004).
- [19] P. B. Petersen and A. Tokmakoff, *Opt. Lett.* **35**, 1962 (2010).
- [20] L. P. Deflores, R. A. Nicodemus, and A. Tokmakoff, *Opt. Lett.* **32**, 2966 (2007).
- [21] S. T. Roberts, J. J. Loparo, K. Ramasesha, and A. Tokmakoff, *Opt. Commun.* **284**, 1062 (2011).
- [22] L. Lepetit, G. Chériaux, and M. Joffre, *J. Opt. Soc. Am. B* **12**, 2467 (1995).
- [23] V. Greco, G. Molesini, and F. Quercioli, *Rev. Sci. Instr.* **66**, 3729 (1995).
- [24] F. Perakis, S. Widmer, and P. Hamm, *J. Chem. Phys.* **134**, 204505 (2011).
- [25] G. M. Hale and M. R. Querry, *Appl. Opt.* **12**, 555 (1973).
- [26] S. Woutersen and H. J. Bakker, *Nature* **402**, 507 (1999).
- [27] K. C. Jones, Temperature-jump 2D IR Spectroscopy to Study Protein Conformational Dynamics, Ph.D Thesis, Massachusetts Institute of Technology, 2012.

- [28] F. O. Libnau, O. M. Kvalheim, A. A. Christy, and J. Toft, *Vib. Spec.* **7**, 243 (1994).

Chapter 8

Fleeting excursions of protons in water give rise to the short-lived acid continuum and drive the exchange of Eigen and Zundel configurations

8.1 Introduction

Most chemical reactions in nature occur in aqueous environments where water plays a crucial role in mediating these reactions through its remarkable ability to form structured hydrogen bond networks that can rapidly respond to the motion of solutes. Aqueous reactions that take place under acidic or basic conditions are governed by the transport of protons through liquid water's evolving hydrogen bonding network. Water is an active participant in the transport and stabilization of excess protons in solution since it can undergo ultrafast hydrogen bond rearrangements as well as induce efficient vibrational energy dissipation due to the strong mixing of inter- and intra-molecular vibrations in liquid water. Early measurements of ionic conductance in strong acid and salt solutions showed that protons are several times more mobile in water than Na^+ , K^+

and other cations similar in size to the hydronium ion (H_3O^+) [1]. This phenomenon has been attributed to the Grotthuss hopping mechanism [2], illustrated in Figure 8-1, which describes proton transfer as a process of sequential proton hops from one water molecule to the next, via the cleavage and formation of covalent O-H bonds resulting in long-range charge transport instead of long-range displacement of any particular proton.

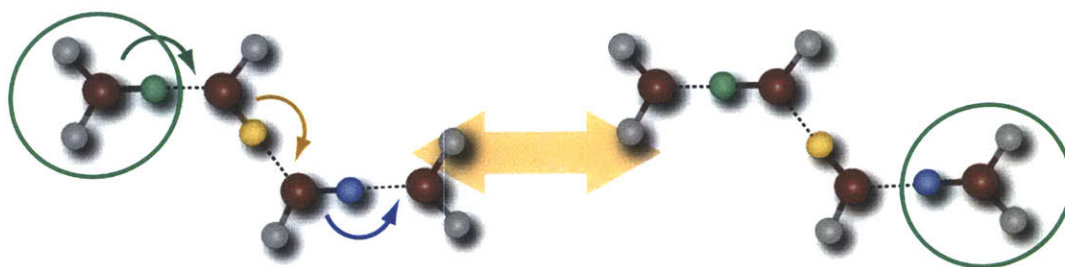


Figure 8-1: Illustration of the Grotthuss proton hopping mechanism. The breaking and forming of O-H covalent bonds along hydrogen bonds results in charge transport rather than long range transport of a single proton.

While the proton hopping mechanism is a widely accepted picture for proton transport in acids and bases, it presents a highly simplistic view of the process since it neglects the participation of solvating water molecules and fails to treat the liquid as dynamic. Several unanswered questions therefore remain regarding the structure of the proton in liquid water and the dynamics of its transport. What are the dominant hydrated proton structures in water and what are their relative stabilities? How do different hydrated proton configurations interconvert during proton transport? What is the role of the surrounding water molecules in the transfer of protons?

The dynamics of proton transfer in strong acids has been the subject of several theoretical studies leading to differing pictures, with few experimental observations to

compare with [3–12]. *Ab initio* and classical empirical valence bond molecular dynamics (MD) simulations have hypothesized two limiting structures for protons in water – the Eigen configuration (H_9O_4^+), which represents a triply solvated hydronium ion, and the Zundel configuration (H_5O_2^+), representing a shared proton structure as shown in Figure 1-4. The Eigen complex [13] consists of a central covalently bonded hydronium ion solvated by three water molecules that accept strong hydrogen bonds from the hydronium core. The O---O separation distance (R_{OO}) between the hydronium ion and any of the three solvating water molecules is approximately 2.6 Å, compared to a distance of approximately 2.8 Å in bulk water [8]. The Zundel structure [4,14] consists of a proton that is equally shared between the oxygens of two water molecules, with an R_{OO} of 2.4 Å [8]. The proton under these conditions has a relatively flat potential between the oxygens, leading to an extended wavefunction and a central O-H-O bond with significant covalent character.

The variation in R_{OO} distances between these structures is small enough that even minor perturbations in the surrounding water can shift configurations so that these structures interconvert. As detailed in Chapter 1, previous theoretical investigations have proposed various mechanisms that each suggests the importance of Zundel or Eigen configurations to describe the dynamics of proton transport, but they differ based on the assumptions that go into the calculations. Discussions about the mechanism for proton transfer have suggested a set of reaction coordinates, most of which focus on the change in the coordination numbers of the proton donor and acceptor molecules. The step-wise mechanism that was outlined in Chapter 1 is described based on the decrease in coordination number of the proton acceptor due to the rupture of a hydrogen bond in the

second solvation shell of the hydronium, which is followed by the proton hop to the acceptor molecule and a subsequent increase in the donor coordination number from the formation of a new hydrogen bond [1,7,8,15]. This picture implies that the Eigen and Zundel configurations are the major players in proton transfer and that they can be defined based on changes to their coordination numbers. On the other hand, electric field of the solvent environment has been suggested [16–18] as a more appropriate reaction coordinate to describe proton transfer, since field fluctuations represent the collective influence of surrounding water molecules on the displacement of the proton. Indeed simulations by Parrinello and co-workers have suggested that solvated protons exist in several configurations that cannot be explicitly identified as either Eigen or Zundel complex [6]. Since the symmetry required to maintain the ideal Zundel or Eigen structure is never present in liquid water, a realistic picture of proton transfer probably involves exchange between a range of different solvated proton configurations that can bear resemblance to the Eigen or the Zundel species. In this chapter, we will therefore use the terms Zundel and Eigen to qualitatively mean the set of configurations about the strictly symmetric Zundel and Eigen limiting structures, which are sampled under equilibrium fluctuations of the liquid.

Experimental investigations of excess protons in water have largely been limited to time-averaged measurements of structure, such as gas phase spectroscopy on hydrated proton clusters [19–22], linear infrared spectroscopy [4] and neutron scattering experiments [23], which do not address the dynamics of proton transfer in liquid water. Time-resolved studies of aqueous proton transfer have in turn been limited by the narrow spectral window offered by conventional mid-infrared optical parametric amplifiers for

probing systems such as acids and bases that inherently display extremely broad spectral transitions [24,25]. Since the structure and the dynamics of the proton cannot be separated, and since these are determined by ultrafast motions giving rise to extraordinarily broad spectral features, there is a dearth of experiments that provide insight into these processes. In this chapter, I report on the application of ultrafast broadband infrared spectroscopy to study the dynamics of proton transfer in concentrated HCl in H₂O. As detailed in Chapter 6, ultrafast broadband infrared spectroscopy provides the time-resolution as well as access to the entire mid-infrared region of the spectrum, which are both necessary to probe the dynamics of aqueous proton transfer. Our results provide experimental evidence for the existence of both Eigen and Zundel configurations of the solvated proton in HCl/H₂O, and show that fleeting excursions of the proton from the Eigen configuration toward the Zundel configuration are stabilized in less than 100 fs by electric field fluctuations of the solvating water molecules.

The infrared spectrum of neat liquid H₂O, shown in Figure 8-2, consists of the broad OH stretch absorption centered at 3400 cm⁻¹ and the H₂O bend vibration at 1650 cm⁻¹. Several changes to the infrared spectrum accompany the addition of strong acids to water. Compared to the infrared spectrum of neat liquid H₂O, HCl/H₂O spectra show strong enhancements on the low frequency side of the OH stretch. In HCl/H₂O, the OH stretch lineshape broadens on the red side and its peak shifts to lower frequencies reflecting the fact that water molecules form stronger hydrogen bonds to protons than to other water molecules. Water molecules directly hydrogen bonded to the chloride ion also contribute to the acid linear infrared spectrum, and their OH stretch vibrations are blue-shifted compared to bulk water due to a weaker hydrogen bonding interaction with the Cl⁻ ion.

The dominant feature in the HCl/H₂O spectrum is a broad “continuum” absorption that spans from ~900 cm⁻¹ to 3400 cm⁻¹ and grows in with increasing acid concentration. Riding on top of the continuum is a shoulder to the blue side of the 1650 cm⁻¹ H₂O bend vibration at 1740 cm⁻¹, reflecting the fact that stronger hydrogen bonds tend to blue-shift the bend frequency. The infrared spectra display another subtle but distinct feature centered at 1200 cm⁻¹, which also grows in with increasing HCl concentration.

Assignments of these spectral features have so far relied on gas phase spectroscopy of protonated clusters aided by DFT calculations and normal mode analysis, and empirical valence bond (EVB) MD simulations of excess protons in water [9,19–22,26–28], both of which have associated these infrared transitions to specific vibrational modes of the Eigen and Zundel limiting forms of the hydrated proton.

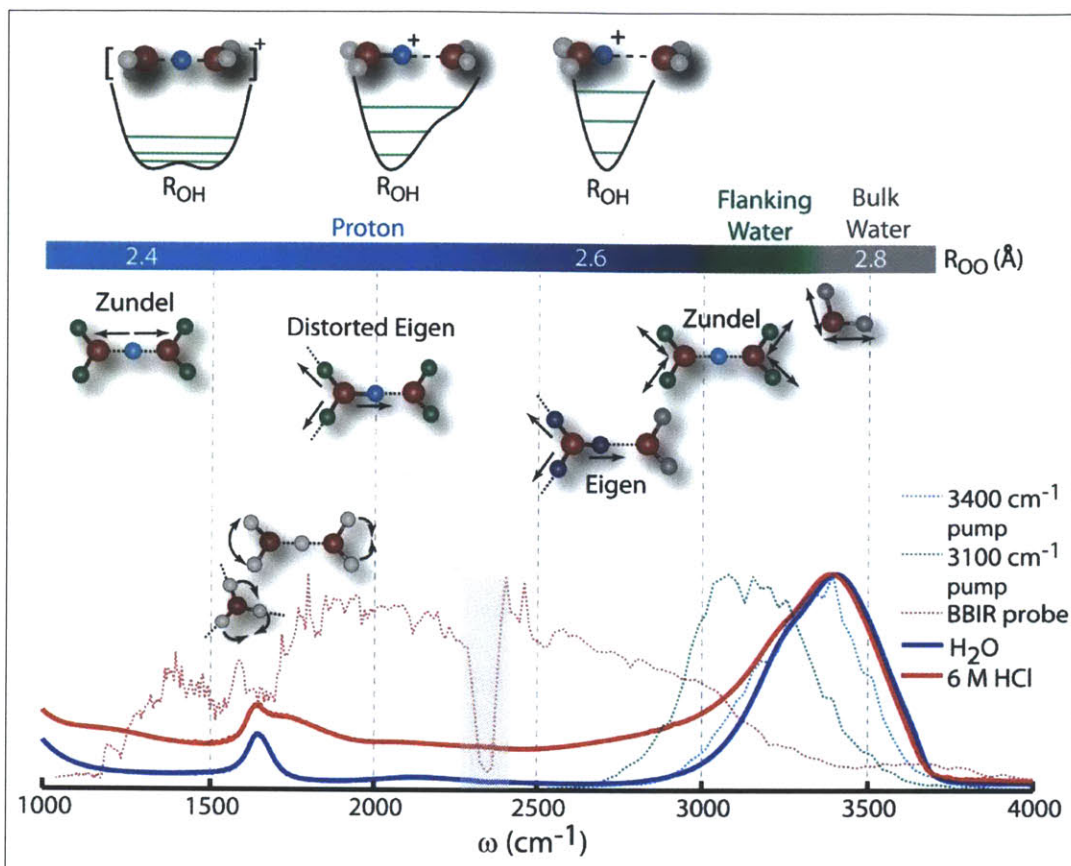


Figure 8-2: Infrared spectra of H₂O and 6M HCl are shown along with spectra of the 3100 cm⁻¹ and 3400 cm⁻¹ excitation pulses and the BBIR probe pulse. Displayed on top of the spectra are cartoons of the Eigen (or hydronium), bend vibrations and the corresponding O---O separation (R_{OO}) distances. Cartoons of double-well proton transfer potentials are shown at the very top to illustrate the correlation between proton displacement and the corresponding vibrational frequencies, as previously described for aqueous hydroxide in Ref. [16]. The gray box represents the absorption of BBIR probe spectrum by atmospheric CO₂.

Gas phase spectroscopy of small hydrated proton clusters has served as a great start for assigning these infrared transitions. These studies have shown that for an isolated Zundel complex, the symmetric and asymmetric OH stretching vibrations of the two water molecules flanking the shared proton display frequencies of ~ 3570 cm⁻¹ and ~ 3680

cm^{-1} , respectively [20]. The frequency of the shared proton oscillation in the Zundel complex was measured to be in the vicinity of 1100 cm^{-1} [20–22], and the out-of-phase bending vibration of the flanking water molecules in the Zundel complex was assigned a frequency of $\sim 1770 \text{ cm}^{-1}$ [29]. With a bigger cluster size consisting of 6 water molecules, the flanking water vibrations red-shift to 3160 cm^{-1} due to hydrogen bond formation, while the shared proton oscillation remains similar. The degenerate asymmetric stretching vibrations of the hydronium core in a full Eigen complex (cluster size of 4 water molecules) were assigned a frequency of 2665 cm^{-1} [20]. With increasing cluster size, the sharp infrared peaks seen in smaller clusters begin to significantly broaden, at which point assigning spectral features to specific vibrational modes of the Eigen and Zundel limiting structures becomes challenging [20].

In acid solutions, the nature of these vibrations changes, since vibrations such as bend and stretch modes undergo significant broadening and shifts in frequency caused by strong hydrogen bonding interactions and inhomogeneity in the molecular environment. Just as the vibrations in neat H_2O are delocalized over several water molecules, vibrations associated with excess protons in liquid water could also be delocalized to varying extents, and the coupling between intra- and intermolecular motions in liquid water would result in significant mixing of vibrational character. It has been suggested that a proton can be delocalized over as many as six water molecules [30]. These factors make spectral assignments of features to vibrations of the excess protons in liquid water rather formidable. Spectral assignments based on MD simulations of excess protons in liquid water exhibit broadening relative to gas phase frequencies. EVB MD simulations have assigned different ranges of frequencies to vibrations of the Eigen and Zundel forms of

the proton. The 3200 cm^{-1} to 3400 cm^{-1} region of the spectrum has been assigned to the OH stretching vibration of the water molecules flanking the shared proton in the Zundel complex ($\nu^{\text{Zun},f}$) [9,26]. The 1740 cm^{-1} feature has been assigned to the bend vibration of the flanking water molecules ($\delta^{\text{Zun},f}$), and the 1200 cm^{-1} feature to the inter-dimer asymmetric stretching mode of the Zundel configuration involving the shuttling of the shared proton ($\nu^{\text{Zun},p}$) [9,31]. Due to the existence of very strong hydrogen bonds between the three solvating water molecules and the hydronium core in the Eigen configuration [32], the OH stretch vibrations of the hydronium (ν^{Eig}) display red-shifted frequencies in the range of 2600 cm^{-1} to 3000 cm^{-1} , while the equatorial bending mode of the H_3O^+ species (δ^{Eig}) is believed to absorb between 1580 cm^{-1} and 1640 cm^{-1} [9,26,33]. The assignments of features within the acid continuum based on gas-phase clusters and computational studies are summarized in Fig. 8.2. Experimental evidence for spectral assignments in acid solutions would provide a valuable benchmark for these assignments, and are essential for determining if the Eigen and Zundel structures are present in liquid water and if so, how long they persist.

Assigning the physical origin of the featureless acid continuum has also come with enormous challenges. Zundel spent much of his career investigating the continuum in strong acids and bases [14], and his work is at the root of the many proposals that have been put forth regarding the origin of the acid continuum [3,4,12,26,34,35]. Using *ab initio* calculations on the H_5O_2^+ Zundel complex, Janoschek et al. proposed the so-called “direct” mechanism for the appearance of the continuum absorption in acids [4]. The direct mechanism suggests that the polarizability of the Zundel complex is directly coupled to the solvent dipole field and to the intermolecular vibrations of the solvent,

leading to the immense broadening of infrared transitions in acids. Using MD simulations and mixed quantum classical modeling of spectroscopy, the direct mechanism was later demonstrated to be one of the primary mechanisms by which extreme broadening in the infrared spectrum of acids can be explained [4,12]. The “indirect” mechanism, on the other hand, suggests that the coupling of the proton motion to the O---O stretching vibration of H_5O_2^+ gives rise to the continuum absorption [31,34]. The acid continuum has also been attributed to the rapid exchange between Eigen and Zundel forms of the proton [3], and more recent EVB MD simulations have suggested that the broadening in the 2000-3000 cm^{-1} region is due to dynamic distortions of the Eigen configuration [26].

Infrared spectral assignments in acids are intimately linked to the dynamics of proton transfer, but experiments so far have not had the time-resolution and the spectral bandwidth required to address the coupled problem of assignments and the underlying dynamics. Due to highly overlapping and extremely broad mid-IR absorption features that are characteristic of solvated protons in liquid water, linear infrared spectroscopy can offer little evidence for assignments of various features to specific solvated proton configurations and how they interconvert. Nonlinear infrared spectroscopy measures time-dependent frequency correlations between different vibrational modes in the system, which can be used to assign infrared spectral features to specific solvated proton configurations and monitor their exchange on ultrafast timescales. Hence, these experimental techniques are well-suited for investigating proton transfer dynamics on femtosecond to picosecond timescales. Due to broad infrared transitions, we performed 3 μm pump-broadband IR probe and mixed 3 μm -broadband two-dimensional infrared (2D IR) spectroscopies on different concentrations of HCl in H_2O in order to correlate acid-

specific transitions across the mid-infrared spectrum and follow their evolution on ultrafast timescales.

8.2 Experimental methods

Broadband pump-probe and 2D IR measurements were performed using 3 μm excitation of the OH stretching vibrations of H_2O and $\text{HCl}/\text{H}_2\text{O}$, followed by broadband mid-infrared probing. The excitation pulses were the 45 fs output from a home-built BBO/ KNbO_3 based OPA [36]. The 3 μm pulse spectra displayed 350-400 cm^{-1} of bandwidth at full-width at half-maximum and were tuned between 3100 cm^{-1} and 3400 cm^{-1} to excite different regions of the broad OH stretch lineshape in $\text{HCl}/\text{H}_2\text{O}$. We used femtosecond broadband mid-infrared (BBIR) pulses that ranged in frequency from <400 cm^{-1} to 4000 cm^{-1} for probing changes to the mid-infrared region of H_2O and $\text{HCl}/\text{H}_2\text{O}$ [37]. BBIR generation and characterization are detailed in Chapter 6.

Broadband 2D IR and pump-probe spectroscopy are described in detail in Chapters 6 and 7. Briefly, broadband 2D IR experiments were done in the pump-probe geometry [38], where the first two (pump) interactions are with the spatially overlapped 3 μm excitation pulses, and the third (probe) interaction is with the BBIR pulse that co-propagates with the resonant third-order signal from the sample. The 3 μm pulse pair for the 2D IR experiments was created in a Mach-Zehnder interferometer. The OPA output was first equally split into two arms. One of the two arms was sent to a finely-controlled and interferometrically calibrated [39–41] translation stage to control the τ_1 time delay, and the other arm was chopped at half the laser repetition rate. The beams were then

recombined on another 50/50 beamsplitter. The coherence oscillations in τ_1 were numerically Fourier transformed to generate the ω_1 dimension of the 2D IR spectrum. The waiting time (τ_2) was controlled by scanning the 800 nm beam prior to the generation of the BBIR probe. The BBIR and the 3 μm beams were focused into the sample using bare gold off-axis parabolic mirrors. After the sample, the transmitted BBIR along with the resonant signal was dispersed onto a 64 element liquid nitrogen cooled HgCdTe array detector to generate the ω_3 dimension. The broadband 2D IR and pump-probe spectra in this chapter are plotted from 1350 cm^{-1} to 4000 cm^{-1} , where the low frequency limit is imposed by the detector response. Time-zero in τ_2 between the BBIR and 3 μm pulses was defined based on the resonant pump-probe signal from H_2O or through resonant cross-correlation in InSb. For 2D IR experiments, the τ_1 time zero between the 3 μm pulse pair was defined using interferometric cross-correlation through a 50 μm pinhole placed at the sample position. Small errors in τ_1 timing are corrected for by adding a phase factor during post-processing of the acquired broadband 2D IR spectra upon invoking the projection-slice theorem [42,43].

The H_2O and $\text{HCl}/\text{H}_2\text{O}$ samples for these experiments were held between two 1 mm thick CaF_2 windows without a spacer, and the samples were maintained at room temperature of $\sim 25\text{ }^\circ\text{C}$. The optical density of the sample was kept between 0.8 and 1 at the peak of the OH stretch absorption at 3400 cm^{-1} for both measurements.

8.3 Results and discussion

Mixed 3 μm -broadband 2D IR spectra correlate vibrations in the OH stretching region of the spectrum with vibrations at all other probed mid-infrared frequencies. Taking slices through these spectra at different ω_1 frequencies allows us monitor how specific frequencies within the OH stretching band are correlated with spectral features at other frequencies as a function of waiting time. Figure 8-3a displays broadband 2D IR spectra of H_2O and 6M HCl at waiting times of 50 fs and 100 fs. Results from broadband infrared spectroscopy of neat liquid H_2O are discussed in detail in Chapter 7, and Figure 8-3 serves to compare and contrast 6M HCl and H_2O spectra.

The OH stretch region of the 2D IR spectra of 6M HCl show tremendous inhomogeneity compared to neat water, pointing to a large distribution of OH stretch frequencies experiencing diverse local environments. Figure 8-4 shows 2D IR spectra of 6M HCl at waiting times from 50 fs to 500 fs. These spectra show that the inhomogeneity in acids persists for > 500 fs, longer than in H_2O , where the OH stretch inhomogeneity decays completely by 500 fs (see Chapter 7). The persistence of inhomogeneity in 6M HCl even at the OH stretch frequency of bulk H_2O suggests that the reorganization dynamics of water slows down, perhaps due to both an the increase in viscosity in acids and the slow-down associated with the presence of Cl^- [44]. This behavior has also been seen in aqueous hydroxide, where the inhomogeneity in the OH stretch region increased monotonically with increasing hydroxide concentration due to significant increase in viscosity with sodium hydroxide concentration [45].

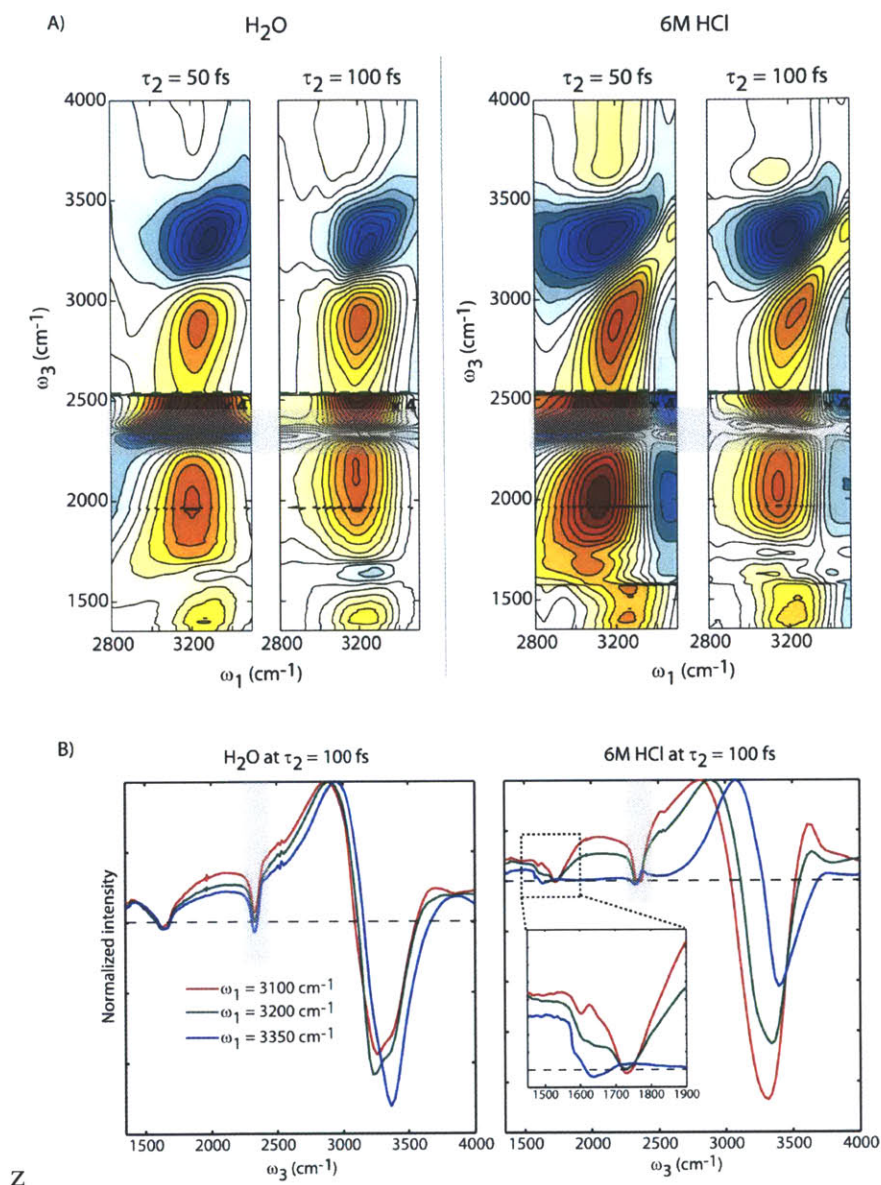


Figure 8-3: a) 2D IR spectra of H₂O (left) and 6M HCl (right) at $\tau_2 = 50$ fs and 100 fs taken for pump pulses centered at 3200 cm⁻¹ with a bandwidth of 400 cm⁻¹. The spectra are normalized to their respective maxima and the contours represent a change in absorbance. A magnification factor of 4 was introduced for clarity when plotting at $\omega_3 < 2500$ cm⁻¹. b) $\omega_1 = 3350$ cm⁻¹, 3200 cm⁻¹ and 3100 cm⁻¹ slices of the 2D IR broadband spectra of H₂O (top) and 6M HCl (bottom) at a waiting time of 100 fs. The slices are normalized to the induced absorption maximum. Inset zooms into the bend region of the 6M HCl spectrum. Spectral regions that are distorted due to atmospheric CO₂ absorption at 2350 cm⁻¹ have been greyed out.

Moreover, the continuum absorption in 6M HCl displays a different profile compared to the tail of the induced absorption in H₂O. The acid continuum extends to >3600 cm⁻¹ and rapidly decays in ~100 fs, which has also been observed in aqueous hydroxides [16]. The H₂O and 6M HCl 2D IR spectra also display some similarities, such as the appearance of an instantaneous bend bleach in the $\omega_3 = 1650\text{-}1750$ cm⁻¹ region upon OH stretch excitation and the absence of any noticeable stretch-bend combination band at $\omega_3 < 1650$ cm⁻¹. The thermal response appears at very early waiting times relative to the structural relaxation timescales for both systems.

Slices through the 2D IR spectra at three different ω_1 frequencies at a waiting time of 100 fs are shown in Figure 8-3b for both H₂O and 6M HCl. The $\omega_1 = 3350$ cm⁻¹ slice of the 2D IR spectrum of 6M HCl shows similar features to those seen in H₂O, since at this ω_1 frequency, we are primarily tagging OH stretch vibrations of bulk water molecules whose dynamics are analogous to our observations in neat H₂O. The $\omega_1 = 3200$ cm⁻¹ slice of 6M HCl displays a prominent bleach at 1740 cm⁻¹, which is not present in H₂O. The OH stretch vibrations of the flanking waters in the Zundel species (ν^{Zundel}) absorb between 3200 cm⁻¹ and 3400 cm⁻¹, and are directly coupled to the bend vibration of the flanking water molecules at 1740 cm⁻¹ through a similar mechanism as seen in neat H₂O, resulting in an instantaneous response at 1740 cm⁻¹ upon 3200 cm⁻¹ excitation. At $\omega_1 = 3100$ cm⁻¹ an additional instantaneous bleach at ~1600 cm⁻¹ appears.

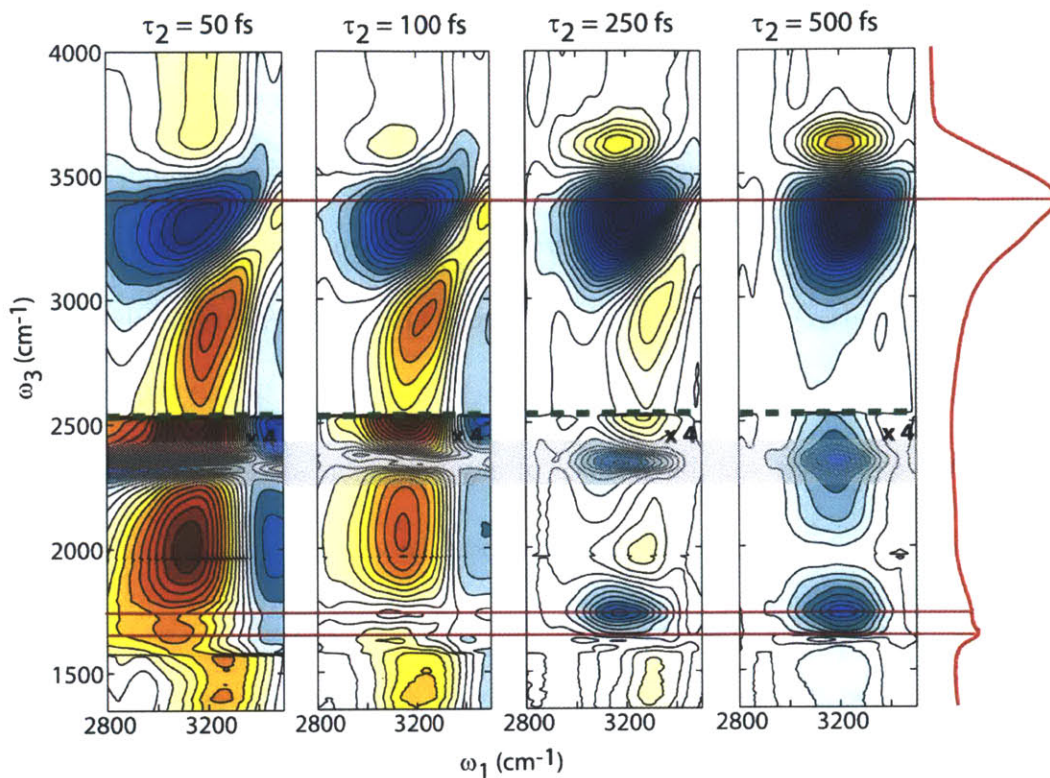


Figure 8-4: 2D IR spectra of 6M HCl at waiting times of 50 fs, 100 fs, 250 fs and 500 fs, for excitation pulse centered at 3200 cm^{-1} , with a bandwidth of 400 cm^{-1} . Regions below $\omega_3 = 2500\text{ cm}^{-1}$ are magnified by a factor of 4 for clarity.

From broadband pump-probe spectroscopy shown in Figure 8-5 for the bend region, we found that this bleach feature grows with acid concentration and is not present when higher OH stretch frequencies are tagged. We therefore assign the 1600 cm^{-1} bleach to the equatorial bending vibration of the hydronium, since exciting the red-shifted hydronium OH stretch vibrations would elicit a simultaneous cross peak bleach at its bend frequency by means of anharmonic bend-stretch coupling.

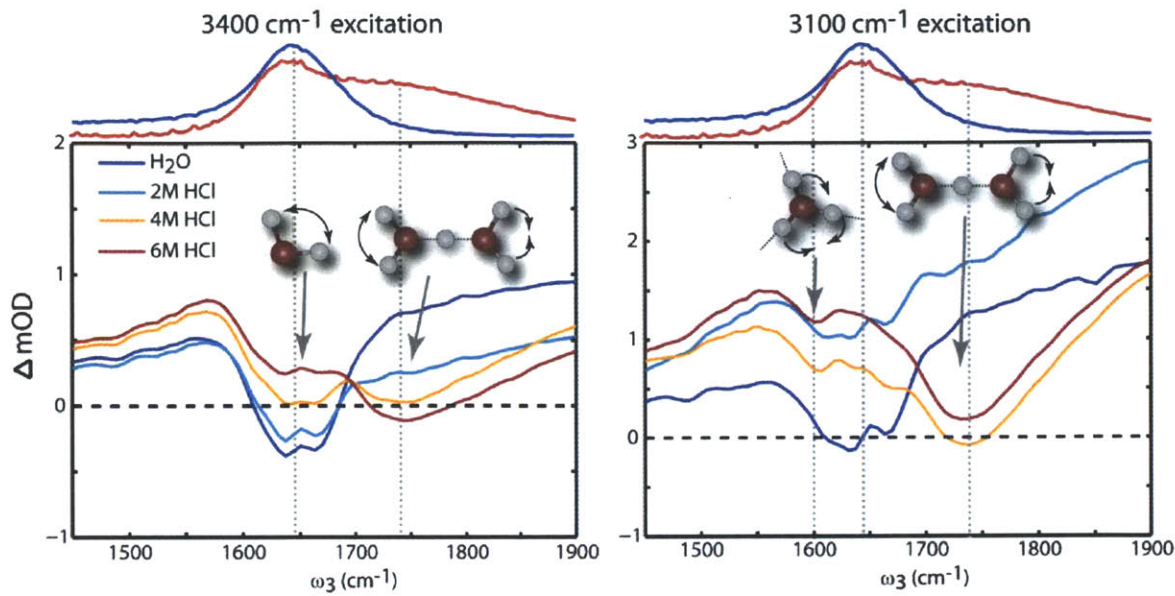


Figure 8-5: Broadband dispersed pump-probe spectra of H₂O, 2M HCl, 4M HCl and 6M HCl using excitation pulses centered at 3400 cm⁻¹ (left) and 3100 cm⁻¹ (right) at $\tau_2 = 60$ fs. The linear infrared spectra of H₂O and 6M HCl, after subtracting the continuum absorption in the 6M HCl spectrum, are plotted on top to guide the eye. The grey dotted lines identify the position of the relevant bend peaks. These spectra display clear dependence on acid concentration, for both the bleach of the Zundel bend vibration at 1740 cm⁻¹ and the bleach of the Eigen bend vibration at 1600 cm⁻¹. While 3400 cm⁻¹ excitation also shows a bleach at 1650 cm⁻¹ from H₂O bend vibration, 3100 cm⁻¹ excitation displays a diminished response from the bulk H₂O bend, consistent with the idea that red-shifted pump frequencies excite water molecules that are primarily associated with protons.

The line widths of the 1600 cm⁻¹ hydronium bend bleach and the 1740 cm⁻¹ bend bleach of the flanking waters in the Zundel complex are 30 cm⁻¹ to 40 cm⁻¹ and ~120 cm⁻¹, respectively. Since the infrared line width itself cannot be used to extract the lifetime of a species due to significant contributions to the width from dephasing, population and orientational relaxation and inhomogeneous broadening that should not be neglected in

this system, we will use the line width to compute only an approximate lower limit to the persistence times of these species under the assumption that all other contributions are negligible. To illustrate, consider the line width under the assumption that line-broadening occurs only as a result of the exchange between proton configurations, k_{ex} . The observed rate in a two state equilibrium in turn is the sum of the forward and reverse reaction rates, $k_{\text{ex}}=k_f+k_r$. In the homogeneous limit, representing the fastest possible kinetics, the transition dipole autocorrelation function can be expected to decay exponentially as $\exp[-k_{\text{ex}}t]$, and the homogeneous line width (FWHM) of the reactant or product will be approximately $k_{\text{ex}}/\pi c$. Within these assumptions, the infrared line widths of the Eigen and Zundel bend transitions provide approximate lower bounds of ~ 800 fs to 1 ps and 250 fs to their persistence times, respectively.

In addition to the presence of distinct peaks in the broadband 2D IR spectra, a strong and featureless induced absorption from the acid continuum appears at $\omega_1 < 3200 \text{ cm}^{-1}$, which intensifies with increasing acid concentration and with decreasing ω_1 frequency. In order to extract the timescales associated with this continuum induced absorption, we performed broadband pump-probe spectroscopy over many waiting times and a range of different concentrations. The concentration-dependent broadband pump-probe spectra, displayed in Figure 8-6 and 8-7, show that the salient acid-related features in the broadband 2D IR and pump-probe spectra of 6M HCl are also present at 2M and 4M HCl and increase monotonically with concentration (see Appendix 8A). Therefore, although ion-pairing occurs at high acid concentrations, these features do not solely stem from ion-pairing effects. Figure 8-6 shows broadband dispersed pump-probe spectra for various concentrations of HCl/H₂O following a 3100 cm^{-1} excitation. The acid spectra show a

pronounced and instantaneous response from the acid continuum for red excitation, which becomes more prominent with increasing acid concentration.

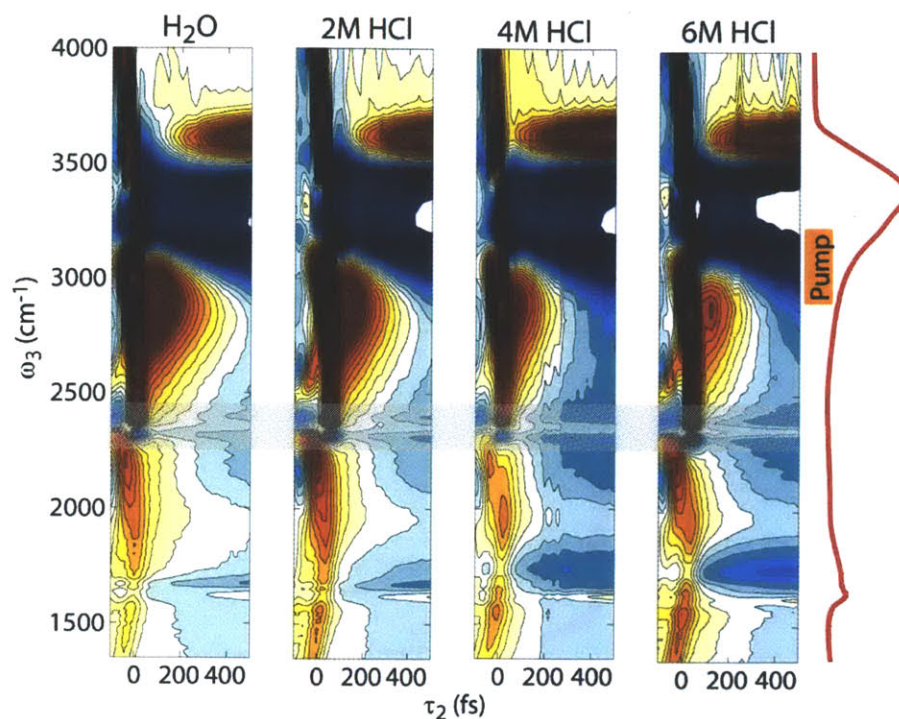


Figure 8-6: Broadband dispersed pump-probe spectra of H₂O, 2M HCl, 4M HCl and 6M HCl plotted from $\tau_2 = -100$ fs to 500 fs, for excitation pulses centered at 3100 cm⁻¹ with 400 cm⁻¹ bandwidth at FWHM. Each spectrum is normalized to the maximum of the induced absorption and the contours are placed between -0.25 and 0.25 at intervals of 0.025.

The acid continuum at all probed frequencies decays very rapidly on a <100 fs timescale, which is within the instrument response time. The time traces at the 3000 cm⁻¹ and 1740 cm⁻¹ for H₂O and 6M HCl for 3100 cm⁻¹ pumping are displayed in Figure 8-7, clearly showing a <100 fs component to the decay timescales associated with a sharp drop in the

continuum induced absorption at two very different probe frequencies. The continuum therefore is not a result of long-lived species, but originates from unstable and fleeting configurations.

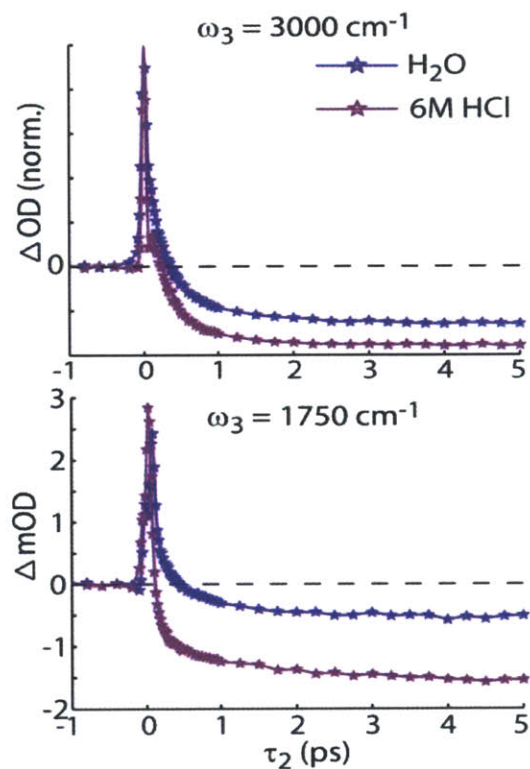


Figure 8-7: Time traces at $\omega_3 = 3000 \text{ cm}^{-1}$ (top) and $\omega_3 = 1750 \text{ cm}^{-1}$ (bottom) of H₂O and 6M HCl for excitation pulses centered at 3100 cm^{-1} .

On the other hand, pumping HCl in H₂O with a pulse centered at 3400 cm^{-1} , as seen in Figure 8-8, does not result in a pronounced response from the acid continuum.

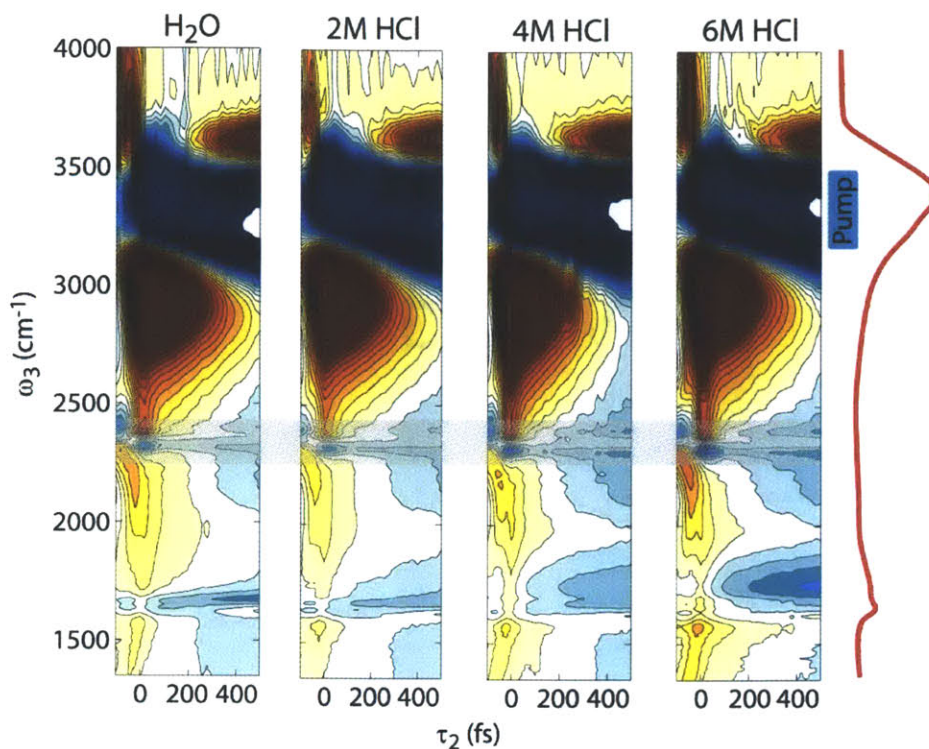


Figure 8-8: Broadband dispersed pump-probe spectra of H₂O, 2M, 4M and 6M HCl solutions plotted from $\tau_2 = -100$ fs to 500 fs, for excitation pulses centered at 3400 cm⁻¹. The spectra are normalized to the maximum of the induced absorption and the contours are placed between -0.25 and 0.25 at intervals of 0.025.

In order to understand the nature of the continuum absorption, we performed polarization-sensitive broadband pump-probe spectroscopy for 3100 cm⁻¹ excitation. Figure 8-9 displays the parallel and perpendicular dispersed pump-probe spectra for 6M HCl and H₂O. These results show that the acid continuum in 6M HCl is most prominent for parallel probing and is greatly diminished at perpendicular polarization. Moreover, the parallel minus perpendicular difference spectrum (Figure 8-9b), which reflects the anisotropy of the system, decays on the same timescale as the continuum induced absorption.

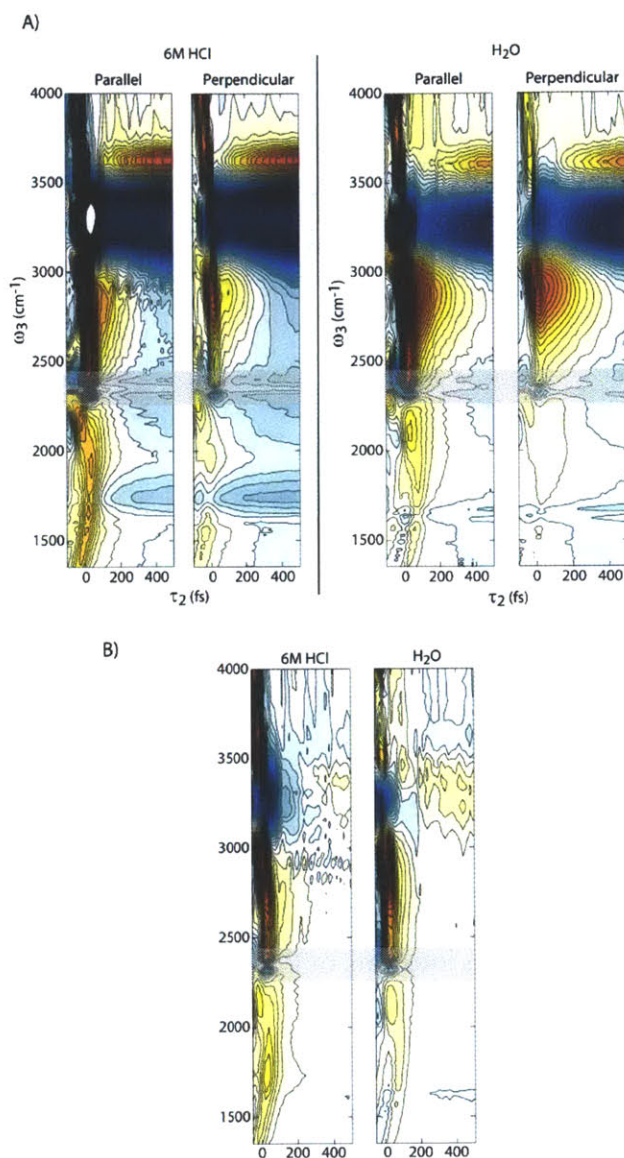


Figure 8-9: a) Polarization dependent dispersed pump-probe of 6M HCl (left) and H₂O (right) using excitation pulses centered at 3100 cm^{-1} , normalized to the maximum of the parallel surfaces, respectively. b) Parallel minus perpendicular difference pump-probe spectra of 6M HCl (left) and H₂O (right). The difference spectra are normalized to their respective maxima.

The growing correlation between OH stretch vibrations at frequencies $<3200 \text{ cm}^{-1}$ and the instantaneous and polarized response from the acid continuum suggests that the

continuum stems from asymmetric distortions of the hydronium ion. Previous simulations have framed these asymmetric distortions in the context of the formation of a “special pair” [3,5,15]. In this picture, fluctuations of the environment introduce asymmetry to the Eigen complex by driving one of the three solvating water molecules towards the hydronium core. The hydronium core and the proximal water molecule in such a distorted Eigen complex form the “special pair”, which is characterized by a shorter O---O distance between the two molecules and a higher propensity for the proton to displace along the special bond to form the Zundel complex. The concept of special pair formation from dynamic asymmetry of the hydronium core allows the proton transfer problem to be described by a pair of water molecules, a proton donor and an acceptor, connected by a strong and linear hydrogen bond. Due to constant fluctuations in the distances between the three water molecules and the hydronium core, the special pair can exchange rapidly between the three solvating water molecules. However, for the sake of simplicity, we will focus on a single special pair to illustrate the associated vibrational degrees of freedom.

Dynamic distortions to the hydronium ion can originate from field-induced perturbations to the proton transfer potential energy curve (Figure 8-2), similar to the ideas proposed by Zundel and co-workers [4]. The electric field fluctuations of the solvent environment can cause the proton transfer potential to evolve from a Morse-like potential to a symmetric double-well potential, while displacing the proton away from a hydronium ion to form a distorted or shared complex. As the proton transfer potential evolves to a double-well potential energy curve, the vibrational transitions experience dramatic shifts to lower frequencies, bringing transitions to overtone and combination bands in resonance with the BBIR probe pulse. Evidence for transitions to overtone states

of the distorted configurations are seen at early waiting time 2D IR surfaces of 6M HCl, where off-diagonal intensity at $\omega_3 \sim 3600 \text{ cm}^{-1}$ in the OH stretch region decays along with the continuum in $<100 \text{ fs}$. A static description of the continuum can be deduced by recognizing that perturbations to the proton transfer potential manifest as changes in barrier height and the relative energies of the donor and acceptor wells, resulting in a distribution of vibrational transitions that give rise to the broad continuum absorption band. The fact that the acid continuum and the polarization anisotropy decay in less than 100 fs indicates that the continuum is dynamically broadened, and the lifetime of the continuum is linked to the fastest intermolecular motions in water – librations and hydrogen bond stretching motion, which exhibit vibrational periods of 50 fs and 180 fs , respectively [46,47]. These low-frequency vibrations give rise to electric field fluctuations that act to rapidly localize a displaced proton, leading to a precipitous decay of the acid continuum on the timescales of these intermolecular motions. The continuum is therefore consistent with a dynamical broadening induced by transient distortions of the Eigen complex towards shared configurations due to fleeting excursions of a hydronium proton, rapidly localized by intermolecular fluctuations of the liquid.

On longer, picosecond timescales, the broadband pump-probe and 2D IR spectra of H_2O and $\text{HCl}/\text{H}_2\text{O}$ look quantitatively identical to the thermal difference spectrum corresponding to a few degree increase in temperature. The thermal difference spectrum reflects changes to the infrared spectrum of H_2O and $\text{HCl}/\text{H}_2\text{O}$ upon the weakening of hydrogen bonds and the resulting shifts to the stretch and bend line shapes when the system equilibrates at a higher temperature. Equilibration at an elevated temperature happens on structural relaxation timescales, which is typically on the order of several

picoseconds in liquid water. However, we see signatures of the thermal difference spectrum as early as 100 fs to 200 fs, depending on the excitation frequency and acid concentration, which is surprisingly even faster than the loss of inhomogeneity in the OH stretch lineshape in acids.

This phenomenon can be explained based on the excitonic nature of vibrations involving protons and H₂O. Previous MD simulations have suggested that the OH stretch vibrations in neat liquid H₂O are delocalized across as many as 6 water molecules [48–50]. Our conclusions from broadband infrared spectroscopy of H₂O further indicated that the vibrational excitons contain both bend and stretch character due to the anharmonic coupling between the stretch fundamental and the bend overtone vibrations. The bend/stretch vibrational excitons in water are not stationary, but are constantly evolving with the intermolecular motions of the liquid. The extent of vibrational delocalization is determined by the strength of the hydrogen bonding interaction as well as the relative contributions from the stretch and bends vibrations, imparting frequency dependence to the degree of vibrational delocalization. Intermolecular motions such as librations and hydrogen bond stretch result in rapid migration and annihilation of vibrational excitons, leading to shifts in vibrational frequencies. Transport and localization of vibrational excitons can result in downhill energy relaxation to strongly hydrogen bonded traps, leading to vibrational energy dissipation primarily through the bend vibrations. Moreover, since the OH stretch and bend vibrations in water are strongly coupled to the intermolecular vibrations of the liquid, exciting the bend/stretch vibrational excitons can also result in the direct excitation of the low frequency intermolecular modes such as librations and translations. Librations and translational modes in water respond to this

excitation on timescales associated with their vibrational periods, leading to rapid changes in the bend and stretch signatures and the appearance of the thermal response in H₂O as early as 200 fs.

Like in H₂O, vibrational excitons may play into the description of the broadband spectroscopy of HCl/H₂O and can explain the fast appearance of the thermal difference spectrum in acids. Such a description for HCl/H₂O requires that we account for the relative extents of vibrational delocalization of the Zundel and Eigen forms of the solvated proton. The OH stretch frequencies of the flanking waters in the Zundel species are resonant with the OH stretch vibrations in bulk water, which may lead to an excitonic character of the $\nu^{Zun.f}$ as well as the $\delta^{Zun.f}$ modes, by virtue of the bend-stretch Fermi resonance. On the other hand, the hydronium stretch vibrations are significantly red-shifted from the OH stretching vibrations of bulk water, which may give rise to more local hydronium stretch modes. Therefore, intermolecular fluctuations that result in the localization of a displaced proton may also cause exciton localization, as the system evolves from a distorted Eigen or Zundel-like species to an Eigen configuration in less than 100 fs. The broadband pump-probe and 2D IR spectra of acids show the appearance of the acid continuum at waiting times >100 fs which may be caused by shifts in the vibrational frequencies of the stretch and bend vibrations in HCl/H₂O on the timescales of librations and translations that also cause the precipitous decay of the acid continuum.

Having established the presence of both hydronium and Zundel species, and the fleeting relaxation of Eigen distortions, we can speculate about their implications for the mechanism of proton transport in water. The simplest explanation for these observations is that proton transfer occurs via an Eigen-to-Zundel-to-Eigen mechanism, in which both

Eigen and Zundel species are present in a ratio given by the equilibrium constant calculated from forward and reverse kinetic rates, $K_{\text{eq}} = 0.28$, which corresponds to a ΔG of 0.75 kcal/mol. Although these values originate from approximated lifetimes, the ratio of these numbers is likely a reasonable measure of the true value. The Eigen and Zundel species exchange rapidly, although they persist longer than the time scale for thermal fluctuations, $\hbar/kT = 160$ fs. In this picture, the distorted Eigen complex lies at the transition state and the Eigen and Zundel species form two minima on either side of the barrier. If we assume that we can describe the system in terms of simple two-state activated kinetics, a gross approximation, then the decay of the continuum marks the lifetime of the transition state (<70 fs), which is a measure of the pre-exponential factor in the rate. If the forward rate from Eigen to Zundel species is 900 fs and the reverse rate from Zundel to Eigen is 250 fs, then we obtain a barrier for the Eigen-to-Zundel process of 1.5 kcal/mol, and a barrier for the Zundel-to-Eigen process of 0.75 kcal/mol, both of which are higher than kT of 0.593 kcal/mol, with the Zundel-to-Eigen process marginally so. Naturally, given that this is a multi-dimensional problem (see Figure 8-10), Eigen-to-Zundel mechanism is only one of several explanations that could be posited by identifying increasingly complex energy landscapes. It is possible that Eigen-to-Eigen and Zundel-to-Zundel transfer processes are also present and that they compete with the Eigen-to-Zundel-to-Eigen mechanism. However, given their small ΔG , it seems unreasonable to assume that they exist in the absence of Eigen-to-Zundel-to-Eigen mechanism.

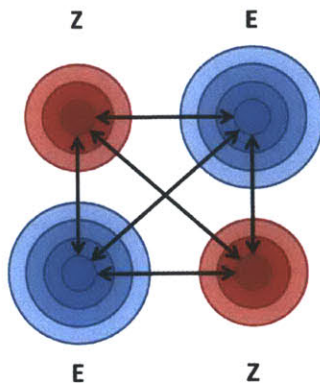


Figure 8-10: A simple illustration to point out the different mechanisms by which the Eigen and Zundel species can exchange. Our data suggest the presence of the Eigen-to-Zundel-to-Eigen mechanism for proton transfer in acids, but does not show evidence for the absence of the Eigen-to-Eigen or Zundel-to-Zundel processes.

The Eigen-to-Zundel-to-Eigen mechanism qualitatively agrees with the proposals for the proton transfer mechanism put forth by Voth and co-workers using EVB MD simulations, where they predicted the lifetime of the Eigen complex to be $\sim 1-2$ ps and that of the Zundel complex to be ~ 370 fs [7]. Our experiments also show evidence for the formation of the “special pair” arising from distortions of the Eigen complex, which agree with EVB simulations by Markovitch et al. [15]. However, our results differ from proposals for proton transfer dynamics based on *ab initio* MD simulations performed by Parrinello and co-workers. Marx et al. predicted that there exist several configurations of the solvated proton that cannot be strictly identified as Eigen or Zundel [6], and that the Eigen and Zundel species are only important as limiting configurations. We have however shown that while distorted complexes do exist in liquid water, they are very short-lived compared to the Eigen and Zundel structures of the solvated proton, which

persist longer than the thermal fluctuations of the liquid. Furthermore, while Marx et al. predicted that the barrier for proton transfer is very negligible at <0.15 kcal/mol [6], our approximations of the barriers for Eigen-to-Zundel and Zundel-to-Eigen exchange indicate that they are on the order of 2.5 kT and 1.25 kT, respectively.

In the end, the calculations of the lifetimes and barriers are by no means definitive since they involve line width approximations that are significant. However, our experimental observations of the Eigen, Zundel and distorted complexes and the timescales associated with these species provide experimental constraints on the dynamics deduced from simulations.

8.4 Conclusions

We have utilized a new broadband mid-infrared source for pump-probe and 2D IR spectroscopy in order to understand the dynamics of aqueous proton transfer in acids. These experiments have provided useful constraints on our understanding of aqueous proton transport. Using spectral correlations derived from broadband 2D IR spectra, we have been able to assign regions of the infrared spectrum of HCl/H₂O to the Zundel, Eigen and distorted Eigen configurations of the solvated proton, and pump-probe spectroscopy has allowed us to measure timescales over which these correlations persist.

The presence of distinct spectral signatures of the bend vibrations of the hydronium ion and the flanking water molecules in the Zundel configuration provide the first direct experimental evidence for the existence of Eigen and Zundel configurations of the solvated proton in liquid water, and provide associated spectroscopic markers to identify

these configurations. While a more direct measure of the persistence times of the Eigen and Zundel configurations is required, we have estimated the lower bounds to their persistence times based on the widths of their bend features to be 800 fs to 1 ps and 250 fs, respectively. The persistence times of these complexes are greater than thermal fluctuations of the liquid, suggesting that the Eigen and Zundel forms of the proton are covalently stabilized.

The polarized response from the acid continuum for $< 3200 \text{ cm}^{-1}$ excitations indicate that the acid continuum arises from asymmetric distortions to the Eigen complex caused by the displacement of a proton towards shared configurations. The acid continuum and its anisotropy decay in less than 100 fs due to symmetry-breaking intermolecular vibrations of the liquid, resulting in electric field fluctuations that rapidly localize the proton on a hydronium ion. We believe that earlier theories for the origin of the acid continuum fundamentally point to the same physics – fast intermolecular vibrations are coupled to proton motion, resulting in the rapid evolution of solvated proton structures and a broad spectral signature. Following the fast decay of the acid continuum, the thermal response immediately appears due to vibrational exciton localization that accompanies the transformation of a distorted Eigen complex to a hydronium ion.

Our observations point to an Eigen-to-Zundel-to-Eigen mechanism for aqueous proton transfer in acids, where the Eigen complex is stable and the Zundel complex is quasi-stable, with distorted species forming the transition state for Eigen-Zundel exchange. Assuming two-state kinetics, we estimated the barriers for the Eigen-to-Zundel and the Zundel-to-Eigen processes, which were both greater than kT . The shorter persistence time of the Zundel complex is consistent with the fact that its large

polarizability makes it more susceptible to electric field fluctuations of the solvent environment that cause rapid localization of the shared proton and a corresponding decay of the Zundel complex. Future experiments probing the 1200 cm^{-1} feature that has been uniquely assigned to the inter-dimer vibration of the Zundel complex following the excitation the OH stretching vibration at different frequencies, can provide the most direct evidence for the exchange timescale and the relative stabilities of the Eigen and Zundel species.

These experiments further confirm that the electric field of the environment is a useful reaction coordinate to describe proton transport in water [16,17]. Geometric coordinates such as O---O separation or the δ parameter, which is the distance from the proton to the mid-point of the O---O distance, do not adequately describe aqueous proton transfer since they cannot account for the collective influence of the solvating water molecules. The solvent electric field is a better measure of the influence of the surrounding water molecules and more accurately represents bond destabilizing fluctuations that displace protons.

Acknowledgements

I would like to thank Luigi De Marco and Aritra Mandal for help with building the experimental set-up for broadband infrared spectroscopy and for assisting with acquiring data on HCl/H₂O. This work was supported by the U.S Department of Energy (DE-FG02-99ER14988).

References

- [1] N. Agmon, Chem. Phys. Lett. **244**, 456 (1995).
- [2] C. J. T. d. Grotthuss, Ann. Chim. LVIII **54**, (1806).
- [3] R. Vuilleumier and D. Borgis, J. Chem. Phys. **111**, 4251 (1999).
- [4] R. Janoschek, E. G. Weidemann, H. Pfeiffer, and G. Zundel, J. Am. Chem. Soc. **94**, 2387 (n.d.).
- [5] M. E. Tuckerman, K. Laasonen, M. Sprik, and M. Parrinello, J. Chem. Phys. **103**, 150 (1995).
- [6] D. Marx, M. E. Tuckerman, J. Hutter, and M. Parrinello, Nature **397**, 601 (1999).
- [7] H. Lapid, N. Agmon, M. K. Petersen, and G. A. Voth, J. Chem. Phys. **122**, 14506 (2005).
- [8] T. J. F. Day, A. V. Soudackov, M. Čuma, U. W. Schmitt, and G. A. Voth, J. Chem. Phys. **117**, 5839 (2002).
- [9] J. Kim, U. W. Schmitt, J. A. Gruetzmacher, G. A. Voth, and N. E. Scherer, J. Chem. Phys. **116**, 737 (2002).
- [10] H. Chen, G. A. Voth, and N. Agmon, J. Phys. Chem. B **114**, 333 (2010).
- [11] A. A. Kornyshev, A. M. Kuznetsov, E. Spohr, and J. Ulstrup, J. Phys. Chem. B **107**, 3351 (2003).
- [12] D. Borgis, G. Tarjus, and H. Azzouz, J. Chem. Phys. **97**, 1390 (1992).
- [13] M. Eigen, Angew. Chem. **3**, 1 (1964).
- [14] G. Zundel, Adv. Chem. Phys. **111**, (2000).
- [15] O. Markovitch, H. Chen, S. Izvekov, F. Paesani, G. A. Voth, and N. Agmon, J. Phys. Chem. B **112**, 9456 (2008).
- [16] S. T. Roberts, P. B. Petersen, K. Ramasesha, A. Tokmakoff, I. S. Ufimtsev, and T. J. Martinez, Proc. Natl. Acad. Sci. U.S.A. **106**, 15154 (2009).

- [17] P. L. Geissler, C. Dellago, D. Chandler, J. Hutter, and M. Parrinello, *Science* (New York, N.Y.) **291**, 2121 (2001).
- [18] W. H. Thompson and J. T. Hynes, *J. Phys. Chem. A* **105**, 2582 (2001).
- [19] J.-W. Shin, N. I. Hammer, E. G. Diken, M. A. Johnson, R. S. Walters, T. D. Jaeger, M. A. Duncan, R. A. Christie, and K. D. Jordan, *Science* (New York, N.Y.) **304**, 1137 (2004).
- [20] J. M. Headrick, E. G. Diken, R. S. Walters, N. I. Hammer, R. A. Christie, J. Cui, E. M. Myshakin, M. A. Duncan, M. A. Johnson, and K. D. Jordan, *Science* (New York, N.Y.) **308**, 1765 (2005).
- [21] J. R. Roscioli, L. R. McCunn, and M. A. Johnson, *Science* (New York, N.Y.) **316**, 249 (2007).
- [22] K. R. Asmis, N. L. Pivonka, G. Santambrogio, M. Brümmer, C. Kaposta, D. M. Neumark, and L. Wöste, *Science* (New York, N.Y.) **299**, 1375 (2003).
- [23] A. Botti, F. Bruni, S. Imberti, M. A. Ricci, and A. K. Soper, *J. Chem. Phys.* **121**, 7840 (2004).
- [24] W. Amir, G. Gallot, F. Hache, S. Bratos, J.-C. Leicknam, and R. Vuilleumier, *J. Chem. Phys.* **126**, 034511 (2007).
- [25] S. Woutersen and H. J. Bakker, *Phys. Rev. Lett.* **96**, 138305 (2006).
- [26] J. Xu, Y. Zhang, and G. A. Voth, *J. Phys. Chem. Lett.* **2**, 81 (2011).
- [27] J. Xu, S. Izvekov, and G. A. Voth, *J. Phys. Chem. B* **114**, 9555 (2010).
- [28] F. Paesani, S. S. Xantheas, and G. A. Voth, *J. Phys. Chem. B* **113**, 13118 (2009).
- [29] J. M. Headrick, J. C. Bopp, and M. A. Johnson, *J. Chem. Phys.* **121**, 11523 (2004).
- [30] E. S. Stoyanov, I. V. Stoyanova, and C. A. Reed, *J. Am. Chem. Soc.* **132**, 1484 (2010).
- [31] N. B. Librovich, V. P. Sakun, and N. D. Sokolov, *Chem. Phys.* **39**, 351 (1979).
- [32] O. Markovitch and N. Agmon, *J. Phys. Chem. A* **111**, 2253 (2007).
- [33] F. Agostini, R. Vuilleumier, and G. Ciccotti, *J. Chem. Phys.* **134**, 084302 (2011).
- [34] G. V. Yukhnevich, E. G. Tarakanova, V. D. Mayorov, and N. B. Librovich, *J. Mol. Struct.* **265**, 237 (1992).

- [35] S. Bratos, *J. Chem. Phys.* **63**, 3499 (1975).
- [36] C. J. Fecko, J. J. Loparo, and A. Tokmakoff, *Opt. Commun.* **241**, 521 (2004).
- [37] P. B. Petersen and A. Tokmakoff, *Opt. Lett.* **35**, 1962 (2010).
- [38] L. P. Deflores, R. A. Nicodemus, and A. Tokmakoff, *Opt. Lett.* **32**, 2966 (2007).
- [39] S. T. Roberts, J. J. Loparo, K. Ramasesha, and A. Tokmakoff, *Opt. Commun.* **284**, 1062 (2011).
- [40] L. Lepetit, G. Chériaux, and M. Joffre, *J. Opt. Soc. Am. B* **12**, 2467 (1995).
- [41] V. Greco, G. Molesini, and F. Quercioli, *Rev. Sci. Instr.* **66**, 3729 (1995).
- [42] J. D. Hybl, A. Albrecht Ferro, and D. M. Jonas, *J. Chem. Phys.* **115**, 6606 (2001).
- [43] M. Khalil, N. Demirdöven, and A. Tokmakoff, *Phys. Rev. Lett.* **90**, 2 (2003).
- [44] M. D. Fayer, D. E. Moilanen, D. Wong, D. E. Rosenfeld, E. E. Fenn, and S. Park, *Acc. Chem. Res.* **42**, 1210 (2009).
- [45] S. T. Roberts, K. Ramasesha, P. B. Petersen, A. Mandal, and A. Tokmakoff, *J. Phys. Chem. A* **115**, 3957 (2011).
- [46] J. J. Loparo, C. J. Fecko, J. D. Eaves, S. T. Roberts, and A. Tokmakoff, *Phys. Rev. B* **70**, 1 (2004).
- [47] C. J. Fecko, J. J. Loparo, S. T. Roberts, and A. Tokmakoff, *J. Chem. Phys.* **122**, 54506 (2005).
- [48] A. Paarmann, T. Hayashi, S. Mukamel, and R. J. D. Miller, *J. Chem. Phys.* **130**, 204110 (2009).
- [49] C. Falvo, B. Palmieri, and S. Mukamel, *J. Chem. Phys.* **130**, 184501 (2009).
- [50] B. M. Auer and J. L. Skinner, *J. Chem. Phys.* **128**, 224511 (2008).

8.A. Appendix: Concentration dependence of third-order signal in HCl/H₂O

Figure 8-A1 shows the concentration dependence of the acid continuum absorption at $\omega_3 = 2000 \text{ cm}^{-1}$ and 1745 cm^{-1} . The signal intensities at these frequencies are normalized to the maximum of the induced absorption, since the optical densities cannot be finely controlled and vary across samples of different concentrations.

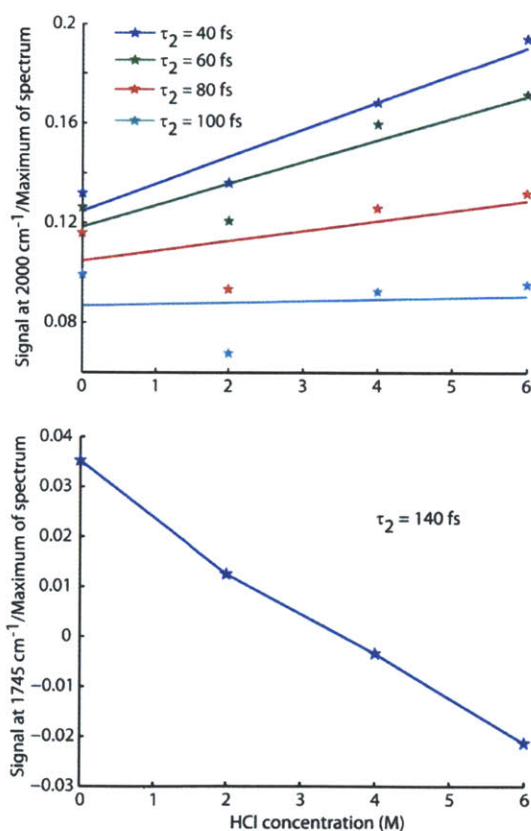


Figure 8-A1: Dispersed pump-probe signals for 3100 cm^{-1} excitation at $\omega_3 = 2000 \text{ cm}^{-1}$ (top) and $\omega_3 = 1745 \text{ cm}^{-1}$ (bottom) as a function of acid concentration, normalized to the maximum of the induced absorption for each concentration, at the specified waiting times. These plots are from one data set, but the concentration dependence is representative of all data taken on the system.

At sub-100 fs waiting times when the acid continuum is most prominent, there is concentration dependence to the continuum signal with respect to the maximum of the induced absorption. At 100 fs, after most of the acid continuum has decayed, the signal at 2000 cm^{-1} is independent of concentration. The $\omega_3 = 1745\text{ cm}^{-1}$ bend bleach of the flanking water molecules in the Zundel complex also shows a clear close-to linear concentration dependence.

Curriculum Vitae

M.I.T Department of Chemistry
32 Vassar St. Room 6-030
Cambridge, MA 02139

Ph: (617) 253-7372
krupa_r@mit.edu

EDUCATION

Doctor of Philosophy (Ph.D) 2006 – 2012

Massachusetts Institute of Technology

Major: Physical Chemistry

GPA 4.7/5.0

Graduate research advisor: Professor Andrei Tokmakoff

Thesis topic: Orientational dynamics of water and aqueous proton transfer dynamics in acids probed with ultrafast nonlinear infrared spectroscopy

Bachelor of Science (B.S.) 2002 – 2006

University of Wisconsin-Madison

Major: Chemistry with 'Honors in Major'

Weighted Cumulative GPA 3.84/4.0

Weighted Chemistry GPA 3.85/4.0

Undergraduate research advisor: Professor F. Fleming Crim

Honors thesis topic: Studies on Photoisomerization Dynamics and Bimolecular Halogen Reactions using Transient Electronic Absorption Spectroscopy

SELECTED AWARDS AND HONORS

- Lester Wolfe Graduate Fellowship, M.I.T Department of Chemistry and G. R. Harrison Spectroscopy Laboratory, 2008
- M.I.T Presidential Graduate Fellowship, M.I.T, 2006-07
- Hertz Fellowship Finalist, Fannie and John Hertz Foundation, 2006
- Honorable Mention, National Science Foundation Graduate Research Fellowship, 2006, 2008
- Dean's List, University of Wisconsin-Madison, 2006, 2002-04
- ACS Daniel Shirk Award for Outstanding Undergraduate Research, Department of Chemistry, UW-Madison, 2006
- Hypercube Scholar: Scholastic Achievement in Chemistry, UW-Madison, 2006
- American Chemical Society Award for Excellence in Physical Chemistry (by the Wisconsin Section), 2005
- Wisconsin/Hilldale Undergraduate/Faculty Research Fellowship (with Professor F. Fleming Crim), UW-Madison, 2005-06
- GE Fund Global Student/Teacher Achievement and Recognition (STAR) Scholarship, General Electric Co., 2002

PROFESSIONAL ACTIVITIES

Research and Teaching experience:

Graduate Research Assistant

November 2006-present

Advisor: Professor Andrei Tokmakoff

Department of Chemistry, Massachusetts Institute of Technology

- Performed ultrafast nonlinear infrared spectroscopy to understand hydrogen bond dynamics of water and its role in aqueous proton transfer dynamics in acids and bases.
- Built a pump-probe 2D IR interferometer with dual stripe acquisition in order to reliably measure 2D IR anisotropy for studying orientational dynamics of water during hydrogen bond exchange.
- Calculated 2D IR anisotropy spectra from molecular dynamics simulations to interpret experimental results.
- Characterized the ultrafast broadband infrared pulses ($\sim 1000\text{ cm}^{-1}$ full-width at half-maximum) generated from a plasma and built a robust set-up to measure broadband pump-probe and broadband 2D IR spectra.
- Took extensive time-resolved broadband infrared pump-probe data on acids and water, including polarization dependence measurements to characterize the broad mid-IR features in acids.

Undergraduate Researcher

March 2003-May 2006

Advisor: Professor F. Fleming Crim

Department of Chemistry, University of Wisconsin-Madison

- Performed transient electronic absorption spectroscopy on microsecond and picosecond timescales to understand halide radical chemistry in solution and photo-isomerization dynamics of stilbene in solution.
- Studied the viscosity-dependence of the photolysis of I_3^- in order to understand solvent cage effects to the formation of photofragments on microsecond timescales.
- Studied halogen radical chemistry in solution upon photodissociation of bromoalkanes and iodine chloride on microsecond timescales.
- Aided in the measurement of ultrafast visible pump-probe spectra to understand the lifetimes and excited state dynamics of cis-stilbene in solution.
- Performed microsecond time-resolved experiments to study the formation of 4a,4b-dihydrophenanthrene upon electronic excitation of cis-stilbene.

Teaching Assistant

Fall 2006-07, Spring 2009

5.33: Chemical Experimentation Laboratory (Undergraduate-level), M.I.T

5.38: Physical Chemistry Laboratory (Undergraduate-level), M.I.T

Grader

Spring 2007

5.74: Introductory Quantum Mechanics II (Graduate-level), M.I.T

Oral and Poster Presentations:

Oral presentations at Conferences and Symposia:

- 1) *Symposium on Molecular Reaction Dynamics to celebrate Prof. F. Fleming Crim's 65th birthday, Madison, WI, May 2012*
Orientational Dynamics of Water Probed with 2D IR Spectral Anisotropy
- 2) *Meeting of the American Physical Society, Boston, MA, March 2012*
Ultrafast Broadband Infrared Source for Nonlinear Infrared Spectroscopy
Krupa Ramasesha, Luigi De Marco, Aritra Mandal and Andrei Tokmakoff
- 3) *17th International Conference on Ultrafast Phenomena, Snowmass Village, CO, July 2010*
Orientational Dynamics of Water probed with 2D-IR Anisotropy Measurements
Krupa Ramasesha, Rebecca A. Nicodemus, Sean T. Roberts, Aritra Mandal and Andrei Tokmakoff
- 4) *16th Annual Argonne Symposium for Undergraduates in Science, Engineering and Mathematics, Argonne National Laboratories, 2005*
Vibrational Relaxation Studies of cis- and trans-Stilbene using Femtosecond Stimulated Raman Spectroscopy
M. Jocelyn Cox, Krupa Ramasesha, Keith A. Zomchek, F. Fleming Crim

Poster presentations at Conferences:

- 1) *6th International Conference on Coherent Multidimensional Spectroscopy, Berlin, Germany, July 2012*
Aqueous Proton Transfer Dynamics probed with Ultrafast Broadband Infrared Pulses
Krupa Ramasesha, Luigi De Marco, Aritra Mandal and Andrei Tokmakoff
- 2) *5th International Conference on Coherent Multidimensional Spectroscopy, Minneapolis, MN, August 2010*
Orientational Dynamics of Water studied with 2D-IR Anisotropy Measurements and Molecular Dynamics Simulations
Krupa Ramasesha, Rebecca A. Nicodemus, Sean T. Roberts, Aritra Mandal and Andrei Tokmakoff
- 3) *14th International Conference on Time-Resolved Vibrational Spectroscopy, Meredith, NH, May 2009*
Anisotropy of Water studied using Molecular Dynamics Simulations
Krupa Ramasesha, Sean T. Roberts, Andrei Tokmakoff
- 4) *Annual Undergraduate Poster Session, Department of Chemistry, UW-Madison, 2006*
Photoisomerization Dynamics of cis-Stilbene and 4a,4b-Dihydrophenanthrene in Solution
Krupa Ramasesha, M. Jocelyn Cox, Katherine A. Freund, F. Fleming Crim

Seminars:

- 1) Modern Optics and Spectroscopy Seminar, George R. Harrison Spectroscopy Laboratory and Department of Chemistry, Massachusetts Institute of Technology, October 2011
Orientational Dynamics of Water Probed with 2D IR Spectral Anisotropy
- 2) Physical Chemistry Seminar, Department of Inorganic and Physical Chemistry, Indian Institute of Science, Bangalore, August 2011
Hydrogen bond Dynamics of Water Studied with Ultrafast Nonlinear Infrared Spectroscopy
- 3) Departmental Seminar, New Chemistry Unit, Jawaharlal Nehru Center for Advanced Scientific Research, Bangalore, August 2011
Hydrogen bond Dynamics of Water Studied with Ultrafast Nonlinear Infrared Spectroscopy

Professional Memberships:

- Women in Science and Engineering (WISE) Residential Program, UW-Madison, 2002-04
- American Chemical Society, Wisconsin Chapter, 2004-06
- Phi Eta Sigma National Honor Society, since 2003
- American Physical Society, 2012-present

PUBLICATIONS

- 1) **Krupa Ramasesha**, Luigi De Marco*, Andrew D. Horning*, Aritra Mandal*, Andrei Tokmakoff; A phenomenological approach to modeling chemical dynamics for nonlinear and two-dimensional spectroscopy, *J. Chem. Phys.* **136** (13), 134507 (2012)
- 2) **Krupa Ramasesha**, Sean T. Roberts, Rebecca A. Nicodemus, Aritra Mandal, Andrei Tokmakoff; Ultrafast 2D IR Anisotropy of Water Reveals Reorientation during Hydrogen-Bond Switching, *J. Chem. Phys.* **135** (5), 054509 (2011)
- 3) Sean T. Roberts, **Krupa Ramasesha**, Poul B. Petersen, Aritra Mandal, Andrei Tokmakoff; Different Stages of Proton Transfer in Aqueous Hydroxide Visualized using Ultrafast Infrared Spectroscopy, *J. Phys. Chem. A* **115** (16), 3957-3972 (2011)
- 4) Sean T. Roberts, Joseph J. Loparo, **Krupa Ramasesha**, Andrei Tokmakoff; A Fast-Scanning Fourier Transform 2D IR Interferometer, *Opt. Comm.* **284** (4), 1062-1066 (2011)
- 5) **Krupa Ramasesha**, Rebecca A. Nicodemus, Sean T. Roberts, Aritra Mandal, Andrei Tokmakoff; "Orientational dynamics of water probed with 2D-IR Anisotropy Measurements" In *Ultrafast Phenomena XVII*, Chergui, M.; Jonas, D.; Riedle, E.; Schloenlein, R.; Taylor, A., (Oxford University Press, 2010), pp. 454-456

- 6) Rebecca A. Nicodemus, **Krupa Ramasesha**, Sean T. Roberts, Andrei Tokmakoff; Hydrogen-bond rearrangements in Water Probed with Temperature-Dependent 2D IR, *J. Phys. Chem. Lett.*, 1 (7), 1068-1072 (2010)
- 7) Sean T. Roberts, **Krupa Ramasesha**, Andrei Tokmakoff; Structural Rearrangements in Water viewed through Two-Dimensional Infrared Spectroscopy, *Acc. Chem. Res.* 42 (9), 1239-1249 (2009)
- 8) Sean T. Roberts, Poul B. Petersen, **Krupa Ramasesha**, Andrei Tokmakoff, Ivan S. Ufimtsev, Todd J. Martinez; Observation of Zundel-like transition state during proton transfer in aqueous hydroxide solutions, *Proc. Natl. Acad. Sci. U.S.A.* 106 (36), 15154-15159 (2009)
- 9) Sean T. Roberts, Poul B. Petersen, **Krupa Ramasesha**, Andrei Tokmakoff; “The dynamics of aqueous hydroxide ion transport probed via ultrafast vibrational echo experiments” In *Ultrafast Phenomena XVI*, Corkum, P.; Silvestri, S. D.; Nelson, K. A.; Riedle, E.; Schoenlein, R. W., (Springer: Berlin, 2009), pp 481-483.
- 10) Poul B. Petersen, Sean T. Roberts, **Krupa Ramasesha**, Daniel G. Nocera, Andrei Tokmakoff; Ultrafast N-H Vibrational Dynamics of Cyclic Doubly Hydrogen-Bonded Homo- and Heterodimers, *J. Phys. Chem. B*, 112 (42), 13167-13171 (2008)

* These authors contributed equally to the work